

**Thermisches und kinetisches Spritzen
von Bronzematerialien
zum Kavitationsschutz im maritimen Umfeld**

Von der Fakultät für Maschinenbau
der Helmut-Schmidt Universität/ Universität der Bundeswehr Hamburg
zur Erlangung des akademischen Grades eines Doktor-Ingenieurs
genehmigte

DISSERTATION

vorgelegt von

Sebastian Krebs
aus Flensburg
Hamburg 2016

Gutachter:

Prof. Dr.-Ing. Thomas Klassen

Prof. Dr.-Ing. Jens Wulfsberg

Prof. Dr.-Ing. Hamid Assadi

Datum der mündlichen Prüfung:

6. Dezember 2016

Institut für Werkstofftechnik

Helmut-Schmidt-University / University der Bundeswehr Hamburg

Zusammenfassung – Dissertation Sebastian Krebs

Herstellung kavitationsbeständiger Bronze-Schichten mittels kinetischen und thermischen Spritzens zum Einsatz im maritimen Umfeld

Mit thermischen und kinetischen Spritzverfahren können stark beanspruchte Bauteile vor Korrosion und Verschleiß geschützt, sowie auftretende Schäden repariert werden. Ein mögliches Beispiel sind Schiffsruder, welche sowohl durch Korrosion als auch erosiven Verschleiß, jedoch überwiegend durch Kavitationserosion beansprucht werden. Die Wechselbelastung durch sich permanent neu bildende und kollabierende Dampfblasen führt schließlich zu Ermüdung, Rissbildung und Materialverlust, der die Funktionalität einschränkt. Um dieses Problem zu minimieren, können Materialien eingesetzt werden, die hohen Widerstand gegenüber plastischer Verformung zeigen. Einige Bronzen erfüllen diese Anforderung und werden bereits für Schiffspropeller eingesetzt. Da Bronzen kostspielig für die Herstellung von Schiffsrudern sind, werden in der Praxis Stahlverkleidungen angebracht, beanspruchte Stellen mittels Auftragsschweißen ausgebessert oder synthetische Schutzschichten aufgetragen. Diese bisherigen Maßnahmen, sowie fluiddynamische Optimierungen der Ruderform bieten bisher keine nachhaltige Lösung zur Vermeidung von Kavitationsschäden.

Ein neuer Lösungsansatz und das Ziel dieser Arbeit besteht darin, Ni-Al-Bronze als eine dichte, oxidarme und gut anhaftende Beschichtung durch Metallspritztechniken aufzubringen, und damit Ruderstandzeiten deutlich zu erhöhen. Dazu wird in dieser Arbeit primär das Kaltgasspritzen angewandt. In Bezug auf verwendete, sehr feste Ni-Al-Bronzen sollten dabei maximal mögliche Grenzbereiche des Kaltgasspritzens evaluiert werden. Zudem enthalten die gasverdünsten Pulver martensitische Strukturen, die die notwendige Verformbarkeit weiter verringern. Um die Schichtqualitäten zu verbessern, werden in dieser Studie neben gasverdünsten Pulvern auch wärmebehandelte und damit martensit-reduzierte Pulver gleicher Zusammensetzung eingesetzt. Zur weiteren Optimierung wurden die Ni-Al-Bronzeschichten ebenfalls einer Wärmebehandlung unterzogen. Als möglicher Kompromiss zwischen Materialeigenschaften und Prozessparametern wurden auch Bronzen mit geringerer Festigkeit gespritzt und entsprechende Schichteigenschaften charakterisiert. Als Alternative für die späteren Anwendungen wurden in dieser Studie zusätzlich die thermischen Spritzverfahren „Warm Spraying“ und „Hochgeschwindigkeits-Flammspritzen“ und entsprechende Konsequenzen für den Schichtaufbau untersucht.

Die unter umfangreicher Variation der Herstellungsparameter kinetisch und thermisch gespritzten, als auch die ausgelagerten Schichten wurden hinsichtlich ihres Gefügebauaufbaus, der kristallographischen Strukturen und möglicher Änderungen der mechanischen und elektrischen Eigenschaften, sowie der Kohäsion zum Bauteilwerkstoff charakterisiert. Zudem wurde das Verformungsverhalten der Beschichtungswerkstoffpartikel beim Aufprall analysiert. Hauptaugenmerk lag hierbei jedoch auf der Charakterisierung der Kavitationsbeständigkeit der Schichten und den zugrunde liegenden Schadensmechanismen.

Die Ergebnisse zeigen, dass alle untersuchten und optimierten Spritzverfahren, sowie Wärmebehandlungen die Herstellung von kavitationsbeständigen Beschichtungen ermöglichen. Neben der Materialauswahl konnte die einzustellende Schichtkohäsion dabei als primärer Schlüssel zur Herstellung kavitationsbeständiger Schichten herausgearbeitet, sowie in allen Verfahren optimiert werden. Jeder der untersuchten Prozesse zeigte jedoch seine speziellen Herausforderungen, die einzeln sowie vergleichend diskutiert werden. Zusätzlich wird erstmalig in der modellmäßigen Beschreibung verfahrensübergreifend die

Aufprallenergie der Beschichtungswerkstoffe als Maß für resultierende Schichteigenschaften quantifiziert. In Summe konnten damit in dieser Arbeit Wege aufgezeigt werden, um mit den verschiedenen Beschichtungsverfahren die Schichtkohäsion zu optimieren und vergleichbar hohe Festigkeiten und Kavitationsbeständigkeiten zu artgleichen Massivmaterialien einzustellen.

**Thermal and Kinetic Spraying
of Bronze Materials for Cavitation Protection
in Marine Environments**

Doctoral Thesis

approved by the

Department of Mechanical Engineering

of the

Helmut-Schmidt-University

University of the German Federal Armed Forces

for obtaining the academic degree of

Doktor Ingenieur (Dr.-Ing.)

presented by

Sebastian Krebs

from Flensburg

Hamburg 2016

Referees:

Prof. Dr.-Ing. Thomas Klassen

Prof. Dr.-Ing. Jens Wulfsberg

Prof. Dr.-Ing. Hamid Assadi

Date of the oral presentation:

6th December 2016

Institute for Materials Engineering

Helmut-Schmidt-University / University of the Federal Armed Forces Hamburg

Acknowledgements

Firstly, I would like to thank Prof. Klassen for his great and continuous support during my academic career. He has accompanied me since 2005, including work on my seminar paper and diploma thesis and who encouraged me to return to university to do my dissertation as a research associate. He has supported my work and given me the opportunity to contribute at international conferences, go abroad for experiments and experience the liberty of research.

I would like to express my gratitude to Dr. Gärtner for his great patience and empathy when assisting and supporting my ideas. It was great discussing with him and experiencing his wide knowledge. That provided me with brilliant inspiration, ideas and remarks to write this thesis. Thank you very much!

Furthermore, I would like to thank my research colleagues for supplying a helpful and pleasant working atmosphere and fruitful discussions: Dr. Maria Villa Vidaller, Kerstin Ernst, Dr. Henning Gutzmann, Alexander List, Ragle Raudsepp, Stephan Theimer and Charline Wolpert.

Many thanks also to Prof. Assadi and Prof. Kreye who were great discussion partners that taught me a lot about science and how to analyse problems from different perspectives.

My particular gratitude is to all engineers and technicians in the Institute for Materials Engineering, who supplied a lot of practical work, patience, helpful advice and inspired working atmosphere: Thomas Breckwoldt, Caroline Hahn, Norbert Németh, Camilla Schulze, Matthias Schulze und Uwe Wagener.

Besides the support from the group, this work comprises many results from students who wrote their scientific thesis. It was always a great pleasure to support them and discuss their ideas and work: Jens Bauer, Timo Baumgart, Patrick Brethack, Jessica Bona, Simon Frede, Martin Graunitz, Tjark Memmert, Marcel Meyer, Lisa Rathje, Christopher Reisgies, Martin Vogel, Oliver Wirth. Thank you very much.

Great thanks also to Dr. Kuroda from the International Institute for Materials Science in Tsukuba / Japan for the opportunity to use their coating facilities and for supplying great guidance in experiments and publications. Additionally, I would like to thank Prof. Katanoda from Kagoshima University / Japan who supply this work with simulation results concerning Warm Spraying and HVOF-Spraying.

I would also like to mention Mr. Krömmer from Linde AG in Unterschleißheim / Germany, who supported this work with his knowledge and the opportunity to use his HVOF spray booth.

I would like to acknowledge the financial support of the German Arbeitsgemeinschaft Industrial Joint Research "Otto von Guericke" e.V., Cologne / Germany (AiF) of the German Federal Ministry of Economic Affairs and Energy in company with the Centre of Maritime Technologies Germany / Hamburg. Moreover I appreciated the collaboration with Michél Hauer from the Fraunhofer Application Centre of Large Structures in Rostock, Germany.

Most of all, I would like to owe my gratitude to my wife Swantje for her great patience and emotional support. She gave me the necessary cover to settle down and to find time frames to forget work and spend time with her and our son Emil Fiete. Finally, I would like to thank my parents and my parents-in-law for supporting me and my work.

Publications

Parts of the following work have been published in scientific journals, conference proceedings or were introduced as oral presentations or posters.

Scientific publications

1. Krebs, S., Kawakita, J., Kuroda, S., Gärtner, F., *Tribology of Titanium Coatings Fabricated by Warm Spray Process with in-situ Zircon Beads Addition*, In: Conference Proceedings, 114th Meeting of the Surface Finishing Society Japan 2006, p.156-157.
2. Kawakita, J., Kuroda, S., Krebs, S., Katanoda, H., *In-Situ Densification of Ti Coatings by the Warm Spray (Two-Stage HVOF) Process*, In: Materials Transactions, Vol. 47, No. 7 (2006), p.1631-1637.
3. Krebs, S., Wirth, O., Gärtner, F., Klassen, T., *Cold Spraying of Cu-Al-Bronze for Cavitation Protection in Marine Environment*, In: Conference Proceedings, 5th International Conference on Spray Deposition and Melt Atomization, Bremen, 2013.
4. Krebs, S., Gärtner, F., Klassen, T., *Cold Spraying of Cu-Al-Bronze for Cavitation Protection in Marine Environments*, In: Conference Proceedings, International Thermal Spray Conference, Barcelona / Spain, 2014, p. 59-64.
5. Krebs, S., Gärtner, F., Klassen, T., *Cold Spraying of Cu-Al-Bronze for Cavitation Protection in Marine Environments*, In: Journal of Thermal Spray Technology, Vol. 24 (2015), p.126-135.
6. Krebs, S., Gärtner, F., Klassen, T., *Cold Spraying of Cu-Al-Bronze for Cavitation Protection in Marine Environments*, In: Materialwissenschaft und Technik Vol. 45, No. 8 (2014), p.708-716.
7. Krebs, S., Gärtner, F., Klassen, T., *Optimizing Cavitation Resistance - An Approach By Cold Spraying Of Several Bronze Materials*, In: Conference Proceedings, International Thermal Spray Conference, Long Beach / USA, 2015, p.1098-1104.
8. Krebs, S., Kuroda, S., Katanoda, H., Gärtner, F., Klassen, T., Araki, H., Frede, S., *Warm Spraying of high strength Ni-Al-bronze for cavitation protection*, In: Conference Proceedings, International Thermal Spray Conference, Shanghai / China, 2016, p.144-150.
9. Hauer, M., Krebs, S., Krömmer, W., *Effect of Traverse Speed on Residual Stress Distribution and Cavitation Erosion Behavior of Arc Sprayed Aluminum Bronze Coatings*, In: Conference Proceedings, International Thermal Spray Conference, Shanghai / China, 2016, p.509-515.
10. Hauer, M., Krebs, S., Krömmer, W., Henkel, K.M., *Effects of Substrate Roughness on Adhesion, Cohesive Properties and Microstructure of Cold Sprayed Nickel Aluminum Bronze Coatings on steel substrates*, In: Journal Thermal Spray Technology, in press 2016.

11. Krebs, S., Kuroda, S., Katanoda, H., Gärtner, F., Klassen, T., Araki, H., Frede, S., *Warm Spraying of High - Strength Ni-Al-bronze: Cavitation Characteristics and Property Prediction*, In: Journal Thermal Spray Technology, in press 10/2016.

Presentations

1. *Tribology of Titanium Coatings Fabricated by Warm Spray Process with in-situ Zircon Beads Addition*, 114th Meeting of the Surface Finishing Society, Sapporo / Japan 2006.
2. *Cold Spraying of Cu-Al-Bronze for Cavitation Protection in Marine Environment*, 5th International Conference on Spray Deposition and Melt Atomization, Bremen / Germany, 2013.
3. *Cold Spraying of Cu-Al-Bronze for Cavitation Protection in Marine Environments*, International Thermal Spray Conference, Barcelona / Spain, 2014.
4. Kaltgasgespritzte Ni-Al-Schichten zum Kavitationsschutz an Schiffsrudern, Arbeitskreis Thermische Spritzen, Unterschleißheim / Germany, 2014.
5. *Optimizing Cavitation Resistance - An Approach By Cold Spraying Of Several Bronze Materials*, International Thermal Spray Conference, Long Beach / USA, 2014.
6. *Warm Spraying of high strength Ni-Al-bronze for cavitation protection*, International Thermal Spray Conference, Young Professionals Session, Shanghai / China, 2016

Poster

1. *Cold-Spraying of Cu-Al-Bronze for Cavitation Protection in Marine Environments*, Meeting Gemeinschaft Thermische Spritzen, Westerborg / Germany 2013.

Summary

By thermal and kinetic spraying, a wide range of coatings can be produced for a variety of different applications. In the mechanical engineering sector, the protection or repair of parts that are highly stressed by corrosion or wear are of particular interest. As one specific example, ship rudders are exposed to such harsh environments, being predominantly stressed by cavitation erosion that restricts functionality and causes costly repairs. The alternating load by the formation and collapse of vapour bubbles deforms the surface and causes material fatigue, resulting in crack formation that finally leads to material loss. To minimize this problem, materials with high resistance against plastic deformation, i.e. materials with a high hardness or strength and high endurance limit, could be deployed to exposed areas. Several bronzes fulfil the requirements and are commonly used for ship propellers. Since bronzes are too expensive for producing complete ship rudders or other massive parts, different alternatives like steel cladding, synthetic protective coatings or fluid dynamic optimizations have been tested so far, but do not provide a satisfactory solution.

In a new approach, this work aims to enhance rudder life times by depositing a Ni-Al-Bronze as dense, almost oxide-free and well adhering coating. In principle, cold gas spraying can provide coatings with similar to bulk properties. However, achievable coating qualities are restricted by the high material strength of the Ni-Al-bronze and accessible spray parameter ranges, since the material requires high process temperatures for sufficient thermal softening. Moreover, as-atomized Ni-Al-bronzes contain martensitic structures that reduce deformability. To tackle these challenges and to enhance coating qualities, the Ni-Al-bronze powder is heat-treated to remove martensitic structures. As a compromise between sprayability and bulk cavitation resistance, bronzes with lower strengths are also investigated.

As alternative approaches to obtain optimum coating qualities, additional coatings were produced by the thermal spray techniques “warm spraying” and “high-velocity oxy-fuel flame spraying” and compared to cold-sprayed coatings.

For wide parameter regimes, the thermally and kinetically sprayed as well as annealed coatings are analysed regarding their microstructure, crystallographic structure, as well as the electrical and mechanical properties. Furthermore, the deformation behaviour of the different bronze materials upon impact is evaluated, and – as main objective – cavitation performance and corresponding damage mechanisms of the different coatings are elucidated.

The results demonstrate that all three spray techniques – under optimized parameter sets – can yield coatings that show similar cavitation resistance as respective bulk material. Apart from the material choice, the coating strength, i.e. internal cohesion, was identified as the key factor for high quality and cavitation resistant coatings, since non-bonded interfaces act as crack nuclei and accelerate cavitation damages. For each of the studied processes, individual challenges are worked out and discussed in this study, allowing for a comprehensive process comparison. A new impact energy based concept is developed that allows for the first time to quantitatively compare different spray techniques regarding coating properties and energy efficiency.

Summing up, the present work presents new solutions to process coatings with a high strength and a cavitation resistance similar to that of cast bronze, based on different spray techniques and heat-treatments. Accordingly, new techniques are available to protect ship rudders or other parts that are exposed against cavitation erosion.

Remarks

The present dissertation was performed in the context of two research projects from the German Arbeitsgemeinschaft Industrial Joint Research "Otto von Guericke" e.V., Cologne / Germany (AiF) of the German Federal Ministry of Economic Affairs and Energy in company with the Center of Maritime Technologies Germany / Hamburg under grant No. IGF-17258 BR and 18449 BG/1. Both research projects were investigated in collaboration with Michél Hauer from the Fraunhofer Application Center of Large Structures in Production Technology / Rostock, Germany.

The warm spray experiments were performed at the National Institute for Materials Science in Tsukuba / Japan. HVOF coatings were sprayed at Linde AG in Unterschleißheim / Germany. The simulation of the warm sprayed and HVOF sprayed impact conditions were calculated by H. Katanoda from Kagoshima University in Kagoshima / Japan.

Furthermore this thesis comprises results of the following published scientific thesis:

Bachelor Thesis:

Patrick Brethack

„Untersuchung des Einflusses von Wärmebehandlungen auf kaltgasgespritzte Bronzeschichten“

Jessica Céolin de Bona

“Analysis of cold sprayed Ni-Al-Bronze coatings applied to cavitation resistance in maritime structures”

Martin Graunitz

„Hochgeschwindigkeitsflammspritzen von Ni-Al-Bronze“

Christopher Reisgies

„Untersuchung des Einflusses der Roboterkinematik auf die Eigenschaften kaltgasgespritzter Bronzeschichten“

Master Thesis

Jens Bauer

„Untersuchung der Kavitationsbeständigkeit kaltgasgespritzter Mn-Bronze und Ni-Sn-Bronze Schichten“

Simon Frede

„Warm Spraying von Ni-Al-Bronze Pulver – eine Untersuchung der Kavitationsbeständigkeit bei unterschiedlichen Spritzparametern“

Marcel Meyer

„Untersuchung des Kavitationsverhaltens kaltgasgespritzter Sn-Bronze-Schichten, sowie Ni-Al-Bronze-Schichten auf Ni-Bond-Coats“

Lisa Rathje

„Untersuchung der Kavitationsbeständigkeit kaltgasgespritzter Ni-Al-Bronze Schichten vor und nach der Wärmebehandlung“

Martin Andreas Vogel

„Untersuchung des Einflusses einer unterschiedlicher Wärmenachbehandlungen von kaltgasgespritzten Ni-Al-Bronzen auf die Kavitationsbeständigkeit“

Oliver Wirth

„Untersuchung des Kavitationsverhaltens kaltgasgespritzter Stahl 316L und Cu-Al-Bronze-Schichten“

The units were reported as SI units, with the exception of the "°C" instead of "Kelvin", to facilitate reading.

Hamburg, December 2016

Sebastian Krebs

Table of Contents

Motivation and Objectives	1
1. Introduction.....	1
1.1. Cavitation.....	1
1.2. Thermal and Kinetic Spray Techniques.....	4
2. Materials and Methods	12
2.1. Substrate and Powder Materials.....	12
2.2. Cold Gas Spray Experiments	13
2.3. Warm Spray Experiments.....	14
2.4. High Velocity Oxy-Fuel Flame Spray Experiments.....	15
2.5. Heat-treatment.....	16
2.6. Flowability, Apparent Density and Particle Size Distribution.....	17
2.7. Optical Microscopy and Porosity Measurements.....	17
2.8. Electrical Conductivity.....	17
2.9. Scanning Electron Microscopy	17
2.10. X-ray Diffraction and Stress Analysis	18
2.11. Determination of Oxygen Contents.....	18
2.12. Determination of Particle Strength.....	18
2.13. Hardness Test	19
2.14. Tensile Testing	20
2.15. Cavitation Erosion Test.....	20
3. Substrate and Powder Properties	21
3.1. Substrate Properties	21
3.2. Powder Microstructures and Properties.....	22
4. Cold Gas Spraying of various Bronze Powders	28
4.1. Calculated Impact Conditions	28
4.2. Particle Impact Behaviour and Deposition Efficiencies.....	32
4.3. Coating Microstructures, Phase Compositions and Residual Stresses.....	39
4.4. Mechanical and Electrical Properties.....	46
4.5. Single Particle and Coating Adhesion	48
4.6. Cavitation Behaviour.....	50
4.7. Annealing of cold sprayed Coatings	56
4.8. Discussion of Cold Gas Spraying of Bronze.....	62
4.8.1. Influence of Spray Parameters and Materials	62
4.8.2. Properties with Influence on Cavitation Performance	64
4.8.3. Influence of the Powder Material Structures of the Ni-Al-Bronze.....	66

4.8.4.	Influence of annealing Time and Temperature on Coating Properties.....	66
5.	Warm Spraying of Ni-Al-Bronze	69
5.1.	Calculated Impact Conditions	69
5.2.	Particle impact Behaviour and Deposition Efficiency.....	71
5.3.	Coating Microstructure, Phase Composition and Residual Stresses.....	75
5.4.	Electrical and Mechanical Properties.....	78
5.5.	Single Particle and Coating Adhesion	80
5.6.	Cavitation Behaviour.....	82
5.7.	Discussion	84
5.7.1.	Influence of the Spray Conditions	84
5.7.2.	Properties with Influence on Cavitation Performance	87
6.	High Velocity Oxy-Fuel Spraying of Ni-Al-Bronze	89
6.1.	Simulation	89
6.2.	Particle impact Behaviour and Deposition Efficiency.....	91
6.3.	Coating Microstructures, Phase Composition and Residual Stresses.....	93
6.4.	Mechanical Properties	98
6.5.	Cavitation Behaviour.....	99
6.6.	Coating Adhesion	101
6.7.	Discussion	102
6.7.1.	Influence of the Spray Conditions	102
6.7.2.	Properties with Influence on Cavitation Performance	104
7.	Comparison between different Spray Techniques and Annealing Conditions.....	106
7.1.	General Aspects	106
7.2.	Energetic Considerations.....	109
8.	Conclusion.....	112
9.	Literature	114

Abbreviations

BCC	cubic body-centred
BSE	Back scattering electrodes
CFD	Computational fluid dynamics
CS	Cold Spray
EIGA	electrode induction-melting gas atomization
et al.	et alii / et aliae
e.g.	exempli gratia (for example)
FCC	cubic face-centred
HP	high pressure
HVOF	High Velocity Oxygen Fuel Spraying
iaw	in accordance with
LP	low pressure
MFT-Test	Micro Flat Tensile Test
MPa	Mega Pascal
N	Newton
NXXX	nitrogen flow-rate of XXX l/min
OM	optical microscopy / microscope
PE	polyethylene
PU	polyurethane
SE	secondary electron
SEM	scanning electron microscopy
SOD	Stand-off Distance
TCT-test	Tubular-Coating-Tensile-test
WS	Warm Spray

Motivation and Objectives

Travelling with high speeds, modern container ships and ferries have to face severe problems of rudder erosion. Most serious is cavitation-erosion that causes serious material removal at stressed areas and thus reduces the rudder functionality as shown in Figure 1 for ship rudders and propeller. In addition, the naval environment leads to high corrosion rates and erosive wear by dispersed sediments. Respective erosive damages at the rudder and stern area of ships mostly result in high costs for repair and can hardly be eliminated completely. As a result, ships need to be docked at least every 5 - 7 years or even earlier to restore the rudder damages. At present, counter measures concern steel claddings, synthetic protective coatings or fluid dynamic optimizations to enlarge rudder life times, but so far do not supply an enduring sustained solution.



Figure 1: Typical cavitation damages of a ship's rudder (a, b) and propeller (c) after operation in marine environments (courtesy of DNV GL).

Thus, for tackling the problem by a completely new approach, the objective of the present study was to develop a kinetically or thermally sprayed metal coating as a dense layer against cavitation erosion in corrosive and abrasive marine environments. Bronzes, particularly nickel aluminium bronze, are identified as promising materials for offering the needed protection. Different spray techniques as cold spraying, high velocity oxy-fuel spraying and warm spraying have to be adapted for processing coatings with optimum properties. Respective influences by spray parameter variation on a variety of properties then could allow for deriving more general descriptions of coating formation.

To supply a rather comprehensive view the thesis is structured as following. More details on the problems caused by cavitation are given in chapter 1, describing the cavitation phenomenon and respective damage mechanisms, and supplying information in state of the art countermeasures, as well as and on the material selection. Furthermore, this chapter describes possible coating techniques and expected benefits for the chosen materials. In chapter 2 the used powder and substrates materials described, as well as the choices of the parameter sets in the used spray methods. Moreover, details on the different methods for coating analyses are given. Chapter 3 presents the results concerning the used substrate materials and feedstock powder properties. The results of cold spray experiments and respective heat-treatments are given and discussed in chapter 4. Warm spray results and HVOF sprayed results are presented in chapter 5 and 6, respectively.

Within each of the chapters 4 to 6 on coating formation by the different spray methods, the deformation behaviour of single splats, the coating microstructures, crystallographic structures, as well as the electrical and mechanical properties are presented under viewpoints on influences on cavitation resistance. Furthermore, these results are individually discussed focusing on influences of the spray parameter sets on coating properties. For cold spraying, additionally, influences of different spray materials and microstructural changes by powder heat-treatments on coating properties are described. Chapter 7 compares the coating properties obtained by the different spray methods for deriving similarities. Based on that, an impact energy based parameter concept is applied that allows for comparing coating properties of different spray methods by one single parameter. Finally, conclusions of this thesis for further applications are summarized in Chapter 8.

1. Introduction

1.1. Cavitation

Principles and Damage Mechanisms

Cavitation is a widely spread phenomenon that occurs when a liquid like e.g. water or oil frequently changes between the liquid and the gaseous state. Within a liquid, vapour, so called cavitation bubbles, form locally by pressure drops or temperatures rises, resulting in lower equilibrium pressure. When these bubbles get to areas with higher pressure or lower temperatures, they implode [BRE13]. The pressure dependent phenomenon arises at technical applications when a liquid stream passes areas with locally higher flow velocities. Typically, ship rudders, propellers, pumps or tubes with cross-sectional changes are affected. Naturally, the bubbles collapse omnidirectional within a liquid. When imploding close to a boundary, they collapse asymmetrically and form a high-speed water jet that causes pressures of up to 1 GPa [MAN02, WOO06]. This water jet is directed towards the boundary as sketched in Figure 2a and b and can cause severe damages on material surfaces by loading and unloading.

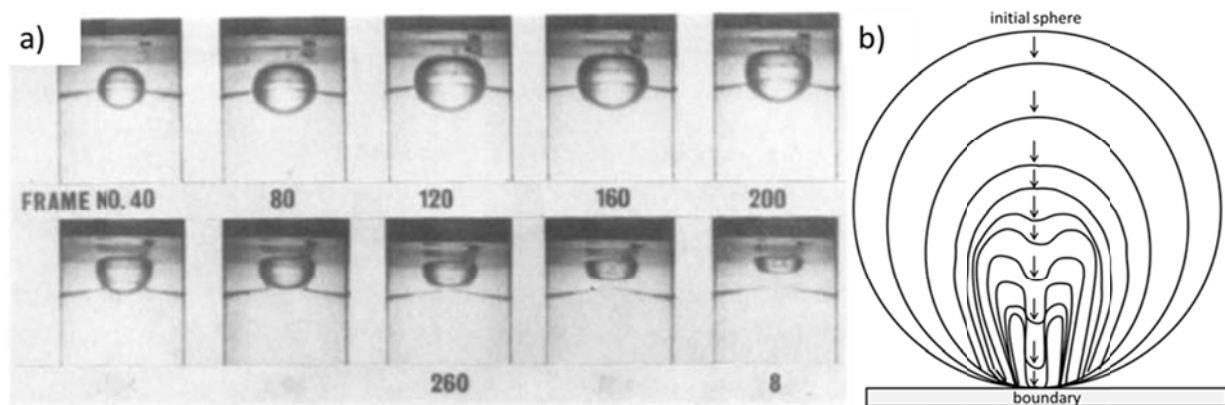


Figure 2: Photograph (a) (with kind permission of the publisher [BLA87]) and simulation (b) (adapted from [PLE71]) of the collapse of a single cavitation bubble near a boundary, demonstrating the formation of a directed micro-jet.

A typical damage development of a coating as introduced in standard ASTM G32-10 is shown in Figure 3 and reveals two linear trends. Typically, after a certain incubation time, the material loss rises and results in a steady state erosion. In contrast to bulk materials, coatings often show a pronounced material loss in the early beginning, since loosely bonded particles on the sample surface are easily removed as illustrated in Figure 3. During the incubation period, metallic materials show plastic deformation that result in typical surface topographies with extrusion-like material assemblies at e.g. grain boundaries or strain hardened areas [VYA77]. The extrusions are highly deformed and could break under further load cycles, similar to low cycle fatigue, and cause continuous material removal after the incubation time [BOU02, SOM10, CZI10, VYA77].

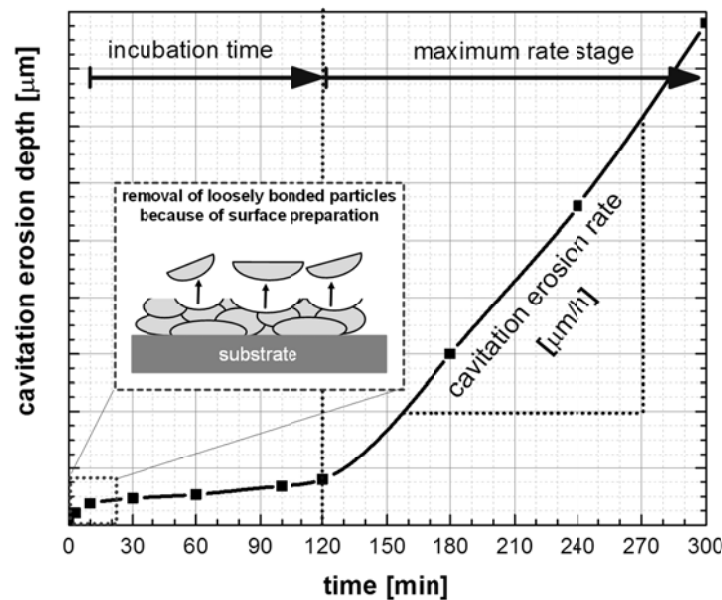


Figure 3: Schematic of the cavitation erosion depth over time for metallic materials iaw ASTM G32-10. As alternative to the cavitation erosion depth [μm], the mass loss [mg] and respectively the cavitation rate [mg/h] can be chosen as a measure for cavitation. As sketched in the insert, in contrast to bulk material, coatings typically show a rise in material loss within the first minutes due to removal of loosely bonded particles after surface preparation.

The damage development is highly material dependent [OER12, BOU02, VYA77, SOM10, CZI10]. Harder metallic materials show enlarged incubation times and less surface damages as compared to softer materials. In contrast, ceramic materials could show cracks on internal interfaces and transcrystalline fracture. [BOU02, CZI10].

Especially, the damages by microcrack initiation reduce the cavitation performance of materials, a matter that particularly affects thermally sprayed coatings. Inhomogeneities like phase boundaries or coating defects like pores, cracks or non-bonded interfaces as well as oxides act as possible crack nuclei and thus enhance material damage [BAR05, TAN03, TAN05, AL-02].

Even for homogeneous materials, the material removal begins at pre-damaged areas. Scratches or cavities at the surface enhance cavitation damage [MAN02]. Hence, the surface quality of exposed areas plays an important role in terms of cavitation resistance. During long term cavitation exposure, the surface roughness increases by high material losses, and might trigger secondary effects [CZI10].

State of the Art Countermeasures and Cavitation resistant Materials

Up to now, metal spray techniques to coat and protect endangered rudder areas by high durable and metallic materials are not in use [KIM10, GEB08]. So far, PU- / PE-based polymers, polymer-metal composites or synthetic rubbers are offered to enhance protection against cavitation-erosion and erosive wear [BEL10, HYD13]. However, scientific confirmations about possible improvements are not available yet. Welding and cladding are common methods in ship-building to enhance part life-times [FAH06, DIL06]. However, applications are still restricted by intermixing and possible embrittlement between the substrate and the welding material. In addition, weld cladding is a rather slow process and

causes high heat input into parts that might affect the mechanical properties of the construction and distortion [FAH06, DIL06].

Other approaches to reduce cavitation damages aim to optimize rudder geometries as well as propeller-rudder interactions. Therefore, hydro-dynamic simulations are conducted by computational fluid dynamics (CFD). Figure 4 shows a typical simulation of the pressure distribution at a rudder. In addition to simulations, small-scale tests within hydrodynamic-cavitation tunnels (HYCAT) are performed [LÜC09, CAR09]. Characteristic countermeasures concern the mounting of twisted rudders or cavitation optimized rudder profiles [TAN05, LÜC09, CAR09]. However, best profiles still cannot avoid cavitation completely.

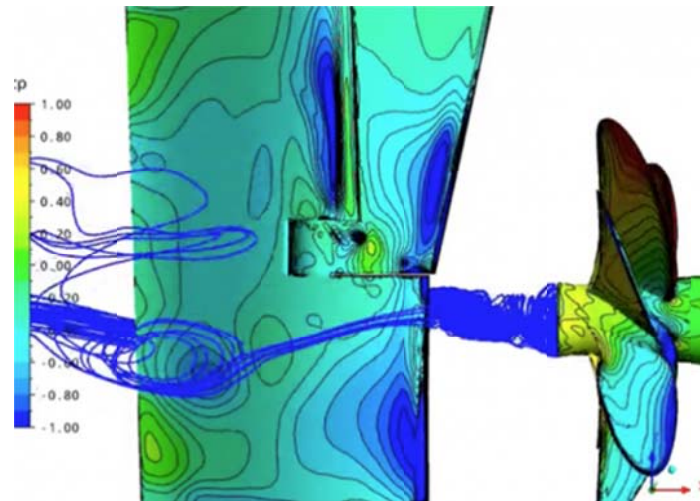


Figure 4: Pressure distribution and the line of flow at ships rudder by courtesy of SVA Potsdam / Germany.

High cavitation resistance of materials is often associated with a high hardness or resistance against plastic deformation [VYA77, HAT04, AST70, NEV01]. Nevertheless, material removal mostly arises by crack growth; hence fatigue characteristics need to be considered as well [RIC97, HAT01]. This description might incorporate the amount of inhomogeneities and local defects densities [HAT07]. Some materials with high endurance limit exhibited longer incubation times and reduced cavitation erosion-rates [RIC97].

Hence, the two criteria - fatigue behaviour and resistance against plastic deformation - might allow for material selection. A corresponding Ashby-map is shown in Figure 5. Within the map, highest cavitation performance is expected for materials in the upper right corner. It should be noted here, that the selection was restricted to materials that show minimum elongation of 10 - 15 % [KLA16], a necessary requisite for coating formation in cold gas spraying. The map demonstrates that bronzes, certain steels and Stellite 6 are candidates for good cavitation performance. Steels exhibit slightly higher fatigue limits, whereas the bronze materials have a higher resistance against plastic deformation. Referring to literature, the following materials are expected to show highest cavitation resistance:

- Ni-Al-bronze [RAV05, RIC97, KOR09B, LAE13, BAR05]
- Co-alloys (Stellite 6) [KUM05, CIN13A, CIN13B]

As an alternative, martensitic transforming superelastic NiTi-alloy or special steels like CaviTec or D-CAV show outrageous cavitation performances [RIC97, HAT07, KUM05, WU00]. Unfortunately, these materials could not be used for cold spraying due to their high strength. In consequence, the present study focuses on analysing coating formation of Ni-Al-bronze by different deposition methods as described in the following chapters. For cold gas

spraying, less hard bronze materials like the Mn-bronze, CuNi15Sn8 and CuSn10 are additionally examined as a compromise between better processability and by lower strength also lower cavitation performance.

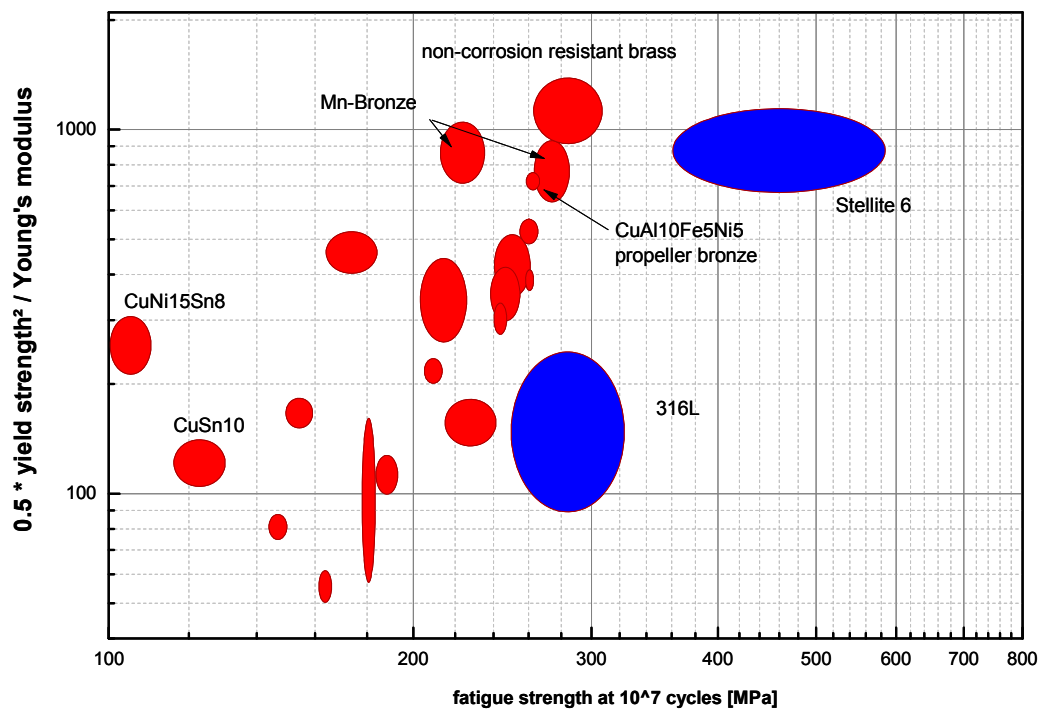


Figure 5: Material selection of deformable metals, showing the relation between the fatigue strength and the resistance against plastic deformation as a measure for cavitation resistant, illustrated by an Ashby - map. The present study focuses on the Ni-Al bronze CuAl10Fe5Ni5, the Mn-bronze CuMn13Al8Fe3Ni3, CuNi15Sn8 and CuSn10.

Apart from the chosen materials, also composites could offer high cavitation resistance by combining the high hardness with the deformability of an elastic binder. However, adhesion between the different components and the size of the hardening component has to be considered [LAM08]. Nevertheless, Hong et al. showed that WC-Co-HVOF sprayed coatings can reach very low cavitation erosion-rates [HON15].

For marine environments, in addition to the cavitation resistance, also the resistance against erosive wear by dispersed sediments or larger obstacles as well as an adequate corrosion resistance are necessary requirements and should be considered [MAN02, WOO06].

1.2. Thermal and Kinetic Spray Techniques

Promising solutions for providing the needed surface protection are offered by thermal spray techniques. As surface engineering tools like thermal or kinetic spray techniques allow for coating formation or repair of damaged parts by depositing molten, semi-molten or solid droplets on a substrate. This provides the opportunity to combine the material properties of the substrate or parts with functional properties of the coating. Well-tuned properties are obtained without substantial heating or even melting or changing the substrate material.

Figure 6 illustrates the general principle of thermal or kinetic spraying and reachable temperature and velocities by various spray techniques. A feedstock material given as a powder or wire can be heated up to 3600 K and / or accelerated up to 1200 m/s depending on the energy source [KUR08]. In thermal spraying combusted gas, plasma, flame or electric arcs can provide sufficient energies to heat and accelerate the feedstock material [FAU14,

KUR08]. For molten feedstocks, droplets deform to splats and rapidly solidify on the substrate [FAU14]. This continuous stream of deposited droplets forms layer by layer building up a coating with thickness of typically a couple of microns. By solidification, microstructures are usually polycrystalline and grain-refined [CRA04].

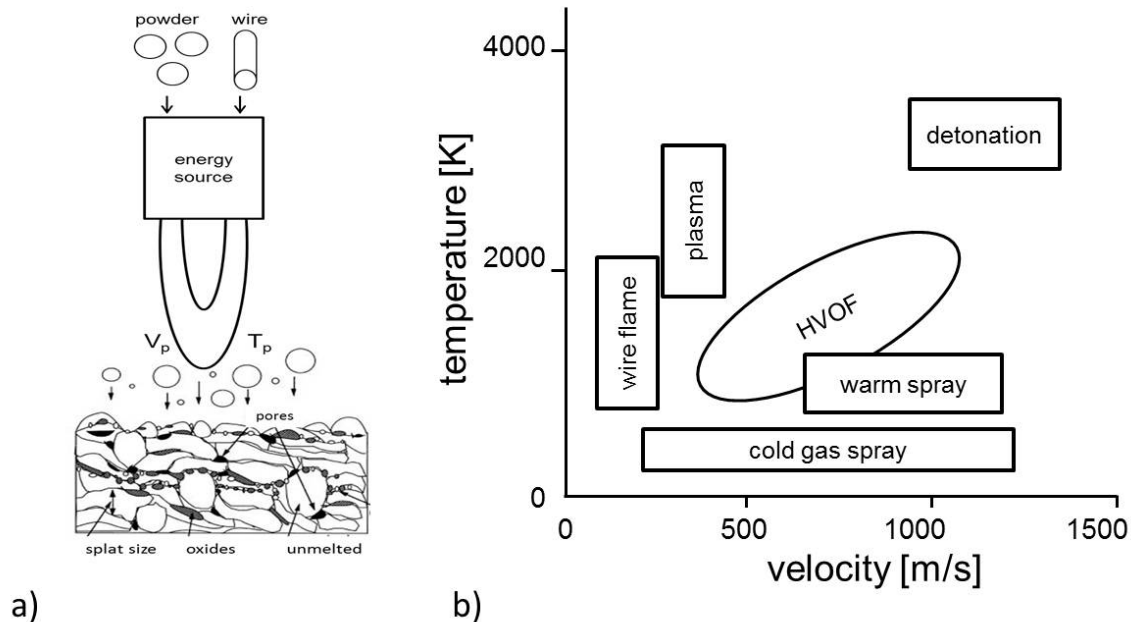


Figure 6: Schematic of thermal or kinetic spraying (a) and assessable temperature and velocity regimes for the different types of thermal and kinetic spray systems as adapted from [FAU14, KUR08].

One of the major advantages of these spray techniques is their wide variety of applicable spray materials. Ceramics or cermets as well as metallic or even polymer based coatings made of pure powders, powder blends, agglomerates or wires can be processed for a wide range of applications. A more detailed overview about possible applications and material combinations is given in [FAU14].

Besides the advantages, depending on the spray technique and material combination, thermal spray techniques may suffer from microstructural changes due to molten and re-solidified droplets. Moreover, oxidation may occur within the spray process. Also residual stresses, both tensile and compressive, depending on impact velocity, might influence surface properties [LON04].

For cavitation protection, thermally sprayed high-strength metals or composites are tested in pumps and water-power plants [HOE11, KUM05]. Co-based alloys like Stellite exhibit already better wear behaviour and better cavitation performances than welded parts [CIN13A, CIN13B]. HVOF-sprayed Ni-Al-coating suffered from cracks at non-bonded and oxidized areas within the coating [BAR05, TAN03, TAN05]. Hence, processing bronze coatings demands for low oxygen contents and high coating purities with as less defects like pores or non-bonded areas as possible [HAN10, KRE15, KRE14, WOO06]. This confines the selection of possible spray techniques and sets focus on more kinetic than thermal spray methods. Hence, this study concentrates on cold gas spraying, warm spraying and an air or nitrogen cooled high velocity oxy-fuel flame spray process.

Besides the coating technique, post-treatments further customize surface properties and are well established processes within surface engineering [LON04]. Typical improvements consider adjusting of the coating microstructure by changes like the grain growth or precipitation hardening, stress relief, reduction of porosity or chemical modifications [LON04]. One main objective is to enhance coating adhesion and cohesion by diffusion during post heat-treatments. Gärtner et al. and Stoltenhoff et al. demonstrated for thermal and cold sprayed copper coatings that cold sprayed coatings show improved mechanical and cohesive properties after heat-treatments [GAE06, STO06]. They claim that diffusion occurs between particles that are under compressed contact and hence allow for closing gaps to reduce the number of potential crack nuclei. In contrast, heat-treatments of thermal sprayed coatings by HVOF or arc spraying alter mainly the oxide distribution within the coating but do not enhance coating properties. Hence, the present study also examines consequences by heat-treatments of cold-sprayed coatings to evaluate possible improvements.

Cold Gas Spraying

Cold gas spraying, also called cold gas-dynamic or kinetic spraying, was invented in the early 1980s in Russia [ASS16, IRI08, ALK90] and attracted growing interest as demonstrated by numbers of patents, publications and industrial applications [ASS16, GAE06A, PAP06, CHA07, WAN13, MOR14, GRI15]. As a solid-state coating technology, it allows for outstanding coating properties by low oxidation and high purity coatings that could reach bulk like properties [KLA16, SIN12, LEE15]. In addition, particles usually keep their original microstructure during the entire process and do not show any major structural changes. Hence, this technology is in use as a protective coating and repair method for bulk materials in aerospace, marine industries, automotive, aircraft industry or electronics [ASS16, KRE15, GAE05, KAY16]. Another market of cold spraying is the usage as a solid-state additive manufacturing process [ASS16].

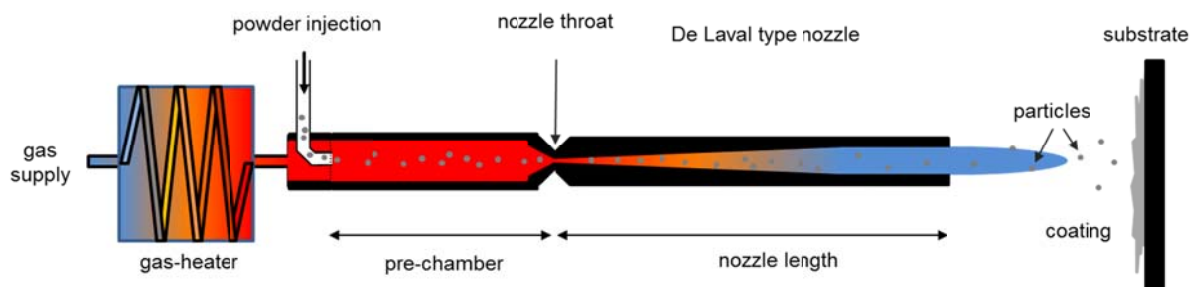


Figure 7: Schematic of the cold gas spray system indicating the gas temperatures within the process (red → hot and blue → cold).

The principle of the cold spray set-up is sketched in Figure 7. An up to 6 MPa pressurized gas, typically nitrogen or helium, is heated within a gas-heater up to 1000 K [ASS16]. With temperature the velocity of sound rises, providing higher particle velocities, and by heating thermally soften [DYK98]. Within the pre-chamber, the hot inert gas stream and powder particles are mixed and fed towards a De-Laval-type (converging/diverging) nozzle [ALK01]. Depending on the pre-chamber length and particle size, particles favourably reach the gas temperature [SCH06A]. Within the nozzle throat, the gas reaches its sound velocity and begins to expand. In consequence, the gas velocity rises and temperature drops [DYK98]. The pre-heated particles are dragged by the hot and fast gas stream and accelerate while reducing their temperature until impacting on the substrate. In cold gas spraying, the particle size ranges from 10 - 50 μm , allowing for acceleration of up to 1200 m/s within the

supersonic gas stream [KRE00A, STO02]. As compared to thermal spray techniques, the particle temperature remains below the melting point. When hitting the substrate, the particles decelerate within less than 100 ns and deform severely [ASS03].

The bonding mechanism of ductile materials is based on this severe plastic deformation [ASS03, ASS11, GIL99]. In detail, particles bond, if conditions are reached that thermal softening by deformation overcompensates work hardening and strain rate hardening effects, resulting in adiabatic shear instabilities [ASS03]. This results in viscous-like material flow at the particle rims and forms typical material jets [ASS03]. This allows for metallurgical bonding. The simulation of Assadi et al. showed that minimum 15 - 25 % of the contact zone should show adiabatic shear instabilities for bonding [ASS03]. By elevated particle velocities or temperatures as well as pre-heated substrates, areas of shear instabilities rise and improve bonding [ASS16, SCH06A, YU13].

Alkimov et al. identified, that a necessary requisite for bonding is that particles exceed a certain critical velocity [ALK90]. Particles below the critical velocity would act abrasive, comparable to grit-blasting. Also too fast particles would show a destructive character [KLI05, SCH06A]. Based on the adiabatic shear instability formation, Assadi et al. describe the critical velocity as given in equation 1 [SCH06A],

$$v_{crit} = \sqrt{\frac{F_1 * 4 * R_m}{\rho} * \left(1 - \frac{T_i - T_r}{T_m - T_r}\right) + F_2 * c_p * (T_m - T_i)} \quad (\text{Eq. 1})$$

with the empirical determined fitting parameters F_1 and F_2 that refer to thermo-mechanical (F_1) and the thermal (F_2) part of the equation. Further the equation considers the heat capacity C_p , the melting temperature T_m , a reference temperature T_r and the particle impact temperature, as well as the particle density ρ_p and the material strength σ . Summing up, equation 1 shows that increased particle temperatures result in lower critical velocities due to improved deformability at elevated particle temperatures.

For supplying a uniform description to compare and correlate different spray conditions, Assadi et al. [ASS03] introduced the coating quality parameter η , as the ratio between the particle velocity and the critical velocity at individual impact temperatures (eq 2). Hence, η should exceed 1 to fulfil the necessary criteria for bonding. Best coating qualities are expected at η -values >1.5 [SCH06A, ASS11].

$$\eta = \frac{v_p}{v_{crit}} \quad (\text{Eq. 2})$$

This parameter assumes that particle and already adhering substrate material have similar mechanical and thermal properties during the moment of impact. Nevertheless, this parameter gives an exclusive opportunity to compare and to predict coating properties. Recent studies describe the impact energies as an alternative to provide a more general basis [KRE16, ASS16]. For cold spraying, the present study compares the different parameter sets on the basis of η .

The cold spray process allows for many opportunities to control and adjust the spray parameter sets and consequently the coating quality parameter by influencing the particle velocity or temperature as well as the critical velocity. Table 1 summarizes possible process variables for cold spraying [ASS16]. The present study focussed on different nozzle contours, pre-chamber lengths, different gas types, temperatures and pressures as well as substrate pre-heating conditions. Except substrate heating influences, all process variables

were used as input to simulations with the software tool KSS (see chapter 2.2). Detailed results and influences of these variables are shown and described in chapter 4.1.

Table 1: Overview about adjustable process variables in cold gas spraying [ASS16].

nozzle	gas	pre-chamber	procedure
length	type (He, N ₂)	length	standoff distance
diameter	pressure		spray angle
expansion ratio	temperature		traverse speed
			powder feed-rate

Apart from the process settings, the effects of the thermal and the mechanical substrate properties as well as the surface roughness could influence coating formation [ASS16, VIL15, HUS09, YU13, ZHA05]. For example, less hard substrates result in slower deceleration and in deeper penetration of particles within the substrate [VIL15]. Also influences by the particle size distribution, particle density and shape are often discussed within the literature [ASS16, JEA14, SCH06A].

Warm Spraying

Warm spraying, also known as two-stage HVOF or modified HVOF spraying, was developed in 1997 at the National Institute for Materials Science in Tsukuba, Japan, comprising the advantages of fast thermal spray techniques and reduced oxidation effects [KUR11]. Hence, dense and corrosion resistant coatings with high purities are the main objectives of this spray technique [KUR08].

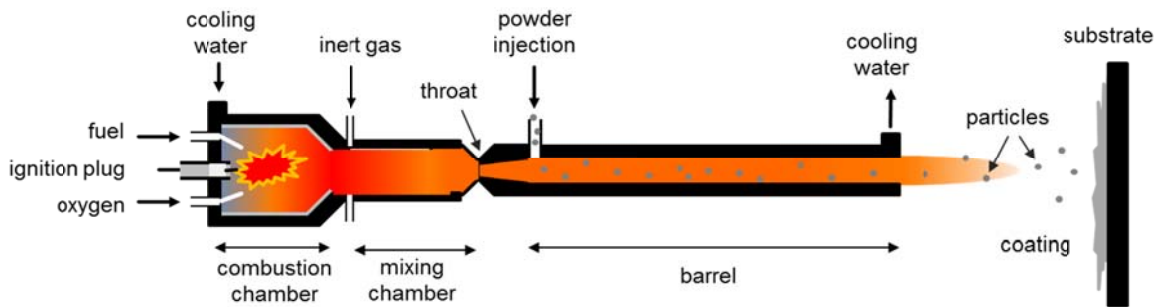


Figure 8: Schematic of the warm spray process.

In warm spraying, kerosene and oxygen are burned at stoichiometric conditions for attaining complete combustion and pre-set a certain combustion pressure [KUR11]. Following the patents of J.A. Browning, after the combustion chamber a so-called mixing chamber is used to blend an inert gas like nitrogen to the combusted gases [BRO94]. Thus, the overall gas stream temperature can be controlled by the nitrogen flow-rates, means high flow-rates would decrease the flame temperature and vice versa [WAT13]. The gun set up allows for operating at two different combustion pressures, 0.9 - 1.0 MPa for low-pressure and 3.9 - 4.2 MPa for high pressure warm spray [KAT13]. After the mixing chamber, the warm gas stream accelerates within a converging/diverging De-Laval-type nozzle to reach supersonic velocities of up to 1100 m/s [MOL13]. Papamoschou et al. identified that the best position to reduce oxidation is to feed the powder to the process behind the nozzle throat [PAP88]. This principle is used in kerosene driven HVOF-systems and in warm spraying. In warm spraying,

the particles begin to heat-up to temperatures between 850 K and 1400 K, depending on the nitrogen flow-rate [KUR11]. Summing up, the warm spray process allows solid impact by operating below the melting point of feedstock but also provides sufficient heat for thermal softening. Parameters can also be adjusted to result in melting or semi-molten droplets [BRO93, WAT13].

Thus, in warm spraying, these highly thermally softened solid particles hit the substrate surface and adhere by metallurgical bonding [KIM09A, KIM09B, KUR11]. Bonding occurs similar to cold gas spraying by the formation of adiabatic shear instabilities as introduced in the previous chapter [KIM09A].

Typically, the results are compared on the basis of the nitrogen flow-rate or the relation between particle velocity and critical velocity [WAT13, MOL13]. New approaches by Assadi et al. to compare coating properties on the basis of an energy based concept, comparable to the coating quality parameter η in cold gas spraying [ASS16]. This concept was used and adapted for the present study and used as a basis for correlations of warm sprayed coating properties. Later, this concept was used as a basis for comparing results from different spray techniques. The relative impact energy summarizes the kinetic and thermal contributions as described in equation 3. The kinetic energy is given by the particle velocity v and the thermal energy as a function of the heat capacity c_p of the particle and the relation between the particle impact temperature T_p and a reference temperature T_{ref} (here 273 K). For the specific heat a simplified expression is used without accounting for temperature dependencies. To eliminate size effects, the formula is divided by the particle mass m .

$$\text{rel } E_{imp} = \frac{1}{m} \left(\frac{1}{2} v^2 + c_p (T_p - T_{ref}) \right) \quad (\text{Eq. 3})$$

Best results on coating performance are expected for higher relative impact energies, whereas an upper limit and thus erosive behaviour has not been considered yet.

For adjusting coating qualities, warm spraying has several opportunities to influence particle velocity and temperature [KIM09A], as summarized in Table 2. The present work considers influences of the nitrogen flow-rate and different combustion pressures. Besides process conditions, also mechanical and thermal properties of the substrate play an important role [KIM09A]. Hence, one parameter-set within this work considers the influences of pre-heated substrates.

Table 2: Adjustable parameters for warm spraying to regulate particle impact velocity and temperatures [KIM09A].

nozzle	gas	procedure	powder
length	nitrogen flow-rate	stand-off distance	density
	combustion pressure	spray angle	size distribution
		traverse speed	morphology
		powder feed-rate	

For calculating respective particle velocities and temperatures, Katanoda et al. developed an algorithm to simulate different warm spray parameter sets [KAT08]. For the present study he simulated the respective spray parameters to study acceleration and heating of the used Ni-Al-bronze. More detailed information is given in chapter 2.3. The simulations were used to compare and understand the coating formation process within this study.

High Velocity Oxy-Fuel Spraying

The high velocity oxy-fuel (HVOF) process was developed in the early 1980s [FAU01] and still has a fast growing market covering applications from aircraft, automotive, paper and turbine industry as well as general mechanical engineering [KRO09, FAU01, GAE06A, FAU14]. Within the process, a gaseous or liquid fuel is combusted with oxygen. The flame heats and accelerates the feedstock powder during the flight through the nozzle and free-jet. Operating at high velocities, HVOF spraying allows for reducing particle or droplet temperatures. Typical applications concern materials as cermets, metals and metal alloys by gaining high coating density, strong adhesion, high cohesive strength and less oxidation as compared to plasma or arc spraying [KRE00B, WIE06].

Within the last decades, three generations of gun systems were developed under the aim to enhance particle velocities and to decrease process temperatures, and then to reduce oxidation [GAE06A]. As compared to previous HVOF-generations, the third generation uses De-Laval-type nozzles that allow for supersonic flame velocities and thus improved particle acceleration of up to 650 m/s for high-density WC-Co [GAE06A, KRE09, KOR09A]. The flame temperature reaches about 2900 °C for ethylene as fuel and respective particle temperatures above 2000 °C [KRE03]. This implies that the process operates well above the melting temperature of many materials and particle impact primary occurs in the molten or semi-molten state [SHI04, KRE96].

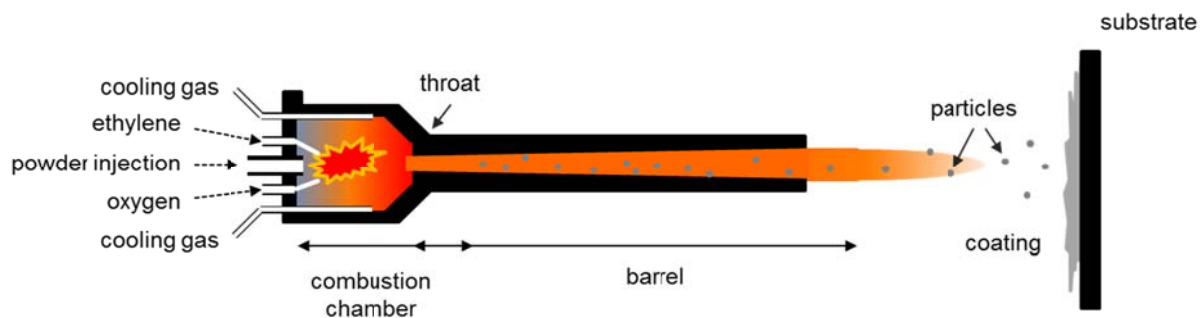


Figure 9: Schematic of about the HVOF gun system Diamond Jet 2700 Hybride (DJ2700).

The Diamond Jet Hybride 2700 gun system (DJ2700) from Sulzer Metco was used in the present study. The schematic is shown in Figure 9. Within the combustion chamber, a gaseous fuel like ethylene or propane is burned with oxygen. Combustion pressures of up to 0.8 MPa are reached depending on the used oxy-fuel ratios [RIC00]. The powder feedstock is fed axially into the combustion chamber to gain sufficient particle heating. A cooling gas - air or nitrogen - is fed along the nozzle walls and around the powder flow to decrease the gas temperatures and thus reduce particle temperatures.

For HVOF spraying, bonding mechanisms are rarely discussed in the literature, whereas [CRA04, RIG04, FAU14] give an overview about possible influences as:

- i. Residual stresses inside the coating
- ii. Localized melting and alloying at the contact zone
- iii. Effects by diffusion of elements through splat boundaries
- iv. Attractive forces at atomic level (van der Waals forces)
- v. Mechanical interlocking

For tuning the spray conditions, Table 3 summarizes typical adjustable process parameters [FAU14, WIE06, SCH06B]. This thesis concentrates on different spray distances, cooling gas types and oxygen-to-fuel ratios.

Table 3: Summary about tuneable parameters in HVOF-spraying.

nozzle	gas	procedure	powder
length	type	standoff distance	density
	combustion pressure	spray angle	size distribution
	oxygen-fuel ratio	traverse speed	morphology
	type of cooling-gas	powder feed-rate	
	flow of cooling-gas		

Especially the oxygen-to-fuel ratio λ gives the opportunity to direct influence the flame temperature [KRE03, FAU14]. Figure 10 shows attainable flame temperatures as a function of λ -values for various fuel types. The stoichiometric conditions are at $\lambda = 1$, means equilibrium combustion. Highest flame temperatures are achieved at λ around 0.7 to 0.8, since by dissociation reactions [KRE03].

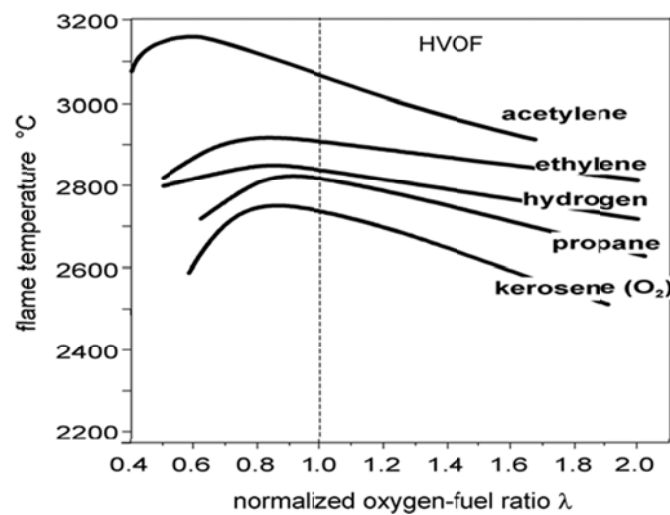


Figure 10: Attainable flame temperatures as a function of the normalized oxygen-fuel ratio λ for different spray fuels [KRE03].

Within the collaboration, Katanoda developed an algorithm to calculate the particle impact velocities and temperatures of the used bronze powder in HVOF spraying. More detailed information is given in chapter 2.4. His simulations were used to compare and to understand the coating formation process within this study.

2. Materials and Methods

2.1. Substrate and Powder Materials

The present study investigates cavitation resistant bronze coatings for applications on a ship rudder. Typically, the ship-building steel GL-A, which is comparable to steel S235, is used as rudder material and thus served as substrate for coating experiments. The mechanical and thermal properties of GL-A are summarized in Table 4 [GL09, GL12].

Table 4: Mechanical and thermal properties of ship-building steel GL-A [GL09].

material	yield strength	ultimate tensile strength	elongation to failure	thermal expansion coefficient	density	melting temperature	effusivity
	[MPa]	[MPa]	[%]	[$\mu\text{strain}/^\circ\text{C}$]	[g/cm ³]	[$^\circ\text{C}$]	[kJ/Km ² √s]
steel GL-A (S235)	>235	>440	>22	13	7.86	1250 - 1460	13

Rectangular substrates (50 x 70 mm) with a thickness of 5 or 15 mm were used. For tubular-tensile tests and adhesion tests (compare 2.14), the cylindrical sample has a height of 25 mm and a diameter of 25 mm. The substrate surfaces were grit-blasted with Al₂O₃ and resulted in a surface roughness of $R_a = 5.6$ for cold spraying, $R_a = 12 \mu\text{m}$ for warm spraying and $R_a = 10 \mu\text{m}$ for HVOF experiments. For analysing single particle impact morphologies, mirror polished substrates with a size of 20 x 70 x 5 mm were used.

As coating materials Ni-Al-bronze, Mn-bronze, CuNi15Sn8 and CuSn10 were chosen. Powders were specially processed for this project according to HSU definitions. The mechanical, thermal and electrical properties of the respective bulk bronze materials are summarized in Table 5 and are sorted with decreasing material strength. All materials have a similar melting temperature and coefficient of thermal expansion but different densities. Elongation to failure is above 10 %, which is favourable for cold gas spraying [KLA16].

Table 5: Overview about the mechanical, thermal and electrical properties of the different bulk bronze material [MEI00, MAT16, INS16, DEU16].

material	melting point	ultimate tensile strength	endurance limit	elongation to failure	density	coefficient of thermal expansion	electrical conductivity
	[$^\circ\text{C}$]	[MPa]	[MPa]	[%]	[g/cm ³]	[$\mu\text{strain}/^\circ\text{C}$]	[MS/m]
CuMn13Al8Fe3Ni3	1030 - 1050	650 - 730	273	18 - 35	7.28	17.7 - 21.3	1.74
CuAl10Fe5Ni5	1040 - 1060	650 - 680	247	18 - 20	7.65	16.3	5.2
CuNi15Sn8	950 - 1115	440 - 590	97	32	8.9	16.4	4 - 6
CuSn10	840 - 1020	260	170	10 - 18	8.7	18.2 - 15.5	7

With respect to possible impact calculations and deformation behaviour, also the temperature dependency of the material strength, as shown in Figure 11 should be considered. The low strength CuSn-bronze and the substrate material have a linear softening behaviour, the high strength Ni-Al-bronze and the Mn-bronze show a low reduction of strength until reaching a temperature of about 300 °C.

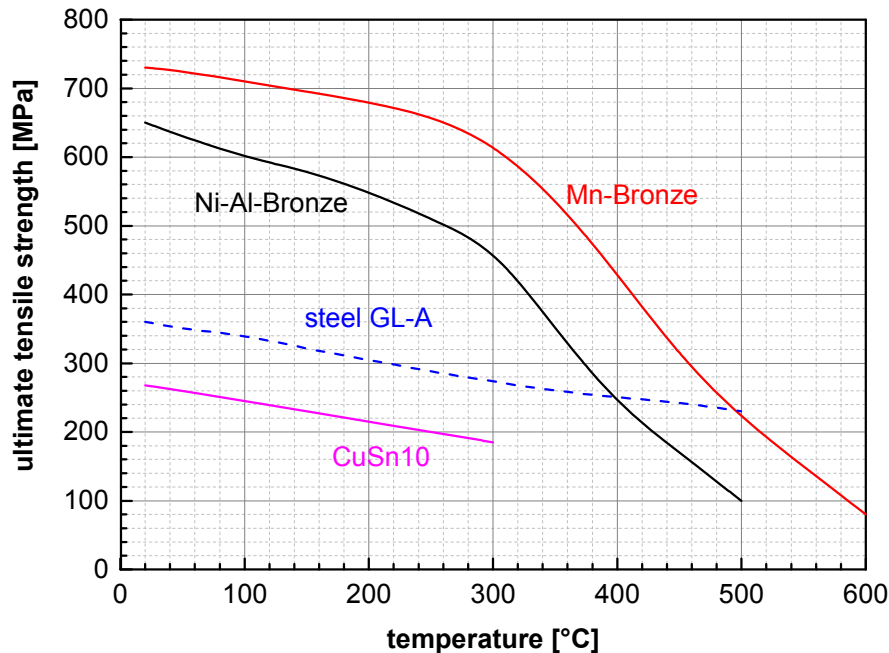


Figure 11: Material strength as a function of the temperature for the different bulk bronzes and the substrate material.

2.2. Cold Gas Spray Experiments

The cold spray experiments were performed by using a modified cold spray system HSU 8000-X, as shown in Figure 12. This equipment allows for gas pressures of about 60 bar and gas temperatures up to 1000 °C by using nitrogen as process gas. Most spray experiments were performed using nitrogen as process gas. Helium as process gas was only used in few selected reference spray experiments. The gas was pre-heated to gas temperatures of up to 680 °C. Additional heating was supplied by a filament heater within the gun. This set-up allows for gas flow-rates of up to 150 Nm³/h per process line (two available). The powder was fed into the process by a high-pressure powder feeder of type PF 4000 Comfort from CGT (Ampfing / Germany). The spray experiments in this study were performed with a feed-rate of 2.15 kg/h. Prior, means up-stream to the nozzle, a pre-chamber of 60 or 180 mm length was fixed. For particle acceleration, the nozzle types 24, 41, 50 and 51 were used. In chapter 4.1 more details on the influences of the different pre-chamber lengths and nozzle types, as well as nozzle dimensions are given.



Figure 12: Assembly of the cold spray gun system at the Helmut-Schmidt University, University of the Federal Armed Forces Hamburg / Germany.

The robot kinematic was set to a traverse speed of 400 mm/s, a line spacing of 2 mm and a spray distance of 60 mm. For analysing single particle impacts, so-called wipe-tests were performed. Therefore the powder feed-rate was lowered to 0.36 kg/h and the gun velocity increased to 1500 mm/s.

For experiments with increased substrate temperature, an induction heater of type EkoHeat from Ambrell (Rijssen / Netherland) with a power of up to 15 kW was used.

Prior to spraying, the software package KSS® from Kinetic Spray Solutions (Germany) was used to estimate optimum powder size distributions, particle impact conditions like the particle impact velocity and temperature as well as the critical velocities and the coating quality parameter η . The calculations are based on fluid dynamic calculations as introduced by Stoltenhoff et al. [STO01, SCH06A].

2.3. Warm Spray Experiments

The warm spray equipment, as shown in Figure 13, is based on a modified conventional HVOF JP5000 equipment from Praxair Technology (USA). This system combusts kerosene and oxygen at stoichiometric conditions and can work at two different combustion pressures. In low-pressure warm spray (LP-WS), the system operates at 1 MPa operates with a barrel length of 200 mm. High - pressure warm spray (HP - WS) works at a higher combustion



Figure 13: Warm spray equipment of the National Institute for Materials Science in Tsukuba / Japan showing a modified JP5000 gun system.

pressures of 4 MPa, under the use of a barrel length of 250 mm. After the combustion chamber, the mixing chamber is installed, which allows for feeding nitrogen into the process.

Table 6 gives an overview of the used gas flow-rates and respective pressures. The pressure reduces slightly with increasing nitrogen flow-rate due to limitations of the kerosene pump system. The powder was fed to the gun system into the straight barrel behind the nozzle throat. A feed-rate of 62 g/min was realized within a carrier gas-flow of 10 l/min.

Table 6: Gas flow-rates and pressures of the warm spray experiments for high and low combustion pressures and various nitrogen flow-rates.

nitrogen [l/min]	low pressure			high-pressure		
	pressure [MPa]	oxygen [l/min]	kerosene [ml/min]	pressure [MPa]	oxygen [l/min]	kerosene [ml/min]
1000	0.90	714	34 7	4.0	380	780
750	0.95	760	369	-	-	-
500	1.00	805	391	4.0	480	980

The robot traverse speed was kept at 700 mm/s with a spray distance of 200 mm. The line spacing was set to 4 mm.

To pre-heat the substrates, two resistance heaters were installed on the back side and regulated at 300 °C substrate temperature for coatings and 200 °C for wipe tests. Coatings sprayed without pre-heating are cooled from the backside to reduce the substrate temperatures.

For better process understanding and prediction, Katanoda et al. introduced an algorithm to calculate particle impact conditions for warm spraying by using a 1D-model [WAT13, KAT11, KAT09, MOR13, IVO06]. Within the collaboration, he simulated respective bronze spray conditions for this study. This model determines the particle velocity and temperature as well as the mass-based molten fraction of a particle.

2.4. High Velocity Oxy-Fuel Flame Spray Experiments

HVOF experiments were conducted by using the water-cooled gun system Diamond Jet 2700 (DJ2700) Hybride from Oerlikon Metco (Wohlen / Switzerland) (Figure 14). This system allows for using gaseous fuels like ethylene, propane and propylene mixed with oxygen. The spray experiments were done using ethylene as fuel at a combustion pressure of about 7 MPa. To influence the flame temperature as explained in chapter 1.2, the stoichiometric conditions between ethylene and oxygen were varied. The different parameter sets are summarized in Figure 14.

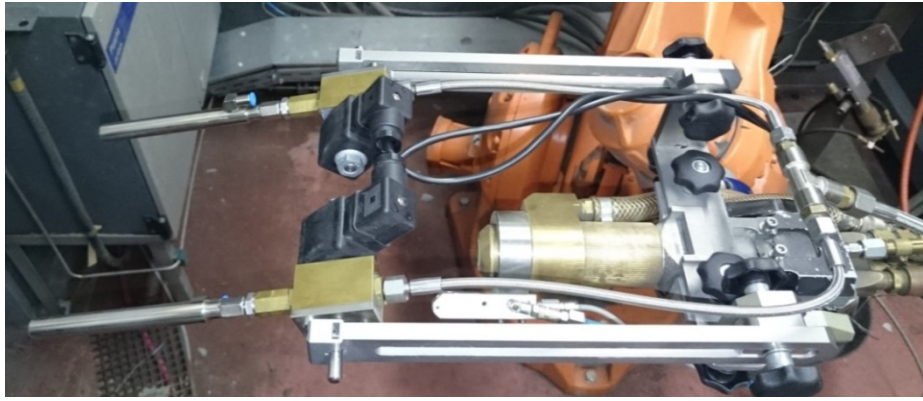


Figure 14: HVOF equipment at Linde Gas AG in Unterschleißheim / Germany showing a gun system of type DJ2700 Hybride with attached CO₂-cooling system.

Table 7: Stoichiometric conditions and related gas flow-rates of the HVOF experiments by using the DJ200 Hybrid gun system at different cooling-gases.

cooling gas	air 360 l/min		nitrogen 360 l/min	
λ	oxygen	ethylene	oxygen	ethylene
-	[l/min]	[l/min]	[l/min]	[l/min]
0,5	-	-	164	110
0,63	137	110	208	110
0,7	160	110	232	110
0,8	192	110	264	110

Nitrogen or air were used as cooling gases to reduce the particle temperature and to cool the combustion chamber. For air as cooling gas, the flow-rate of pure oxygen was reduced due to the assumption that about 20 % of oxygen might participate in the combustion. The powder was fed axial through the combustion chamber. The experiments were performed at feed-rates of 4.5 kg/h. The carrier gas-flow was set to 13 l/min. For particle acceleration, a convergent-divergent nozzle with a length of 203 mm (8 inch) was used. The influence of the stand-off distance (SOD) was analysed for spray distances of 250, 300 and 350 mm.

To understand the influences of the different spray parameter sets, the particle impact conditions were calculated by Hiroshi Katanoda, Kagoshima University, Japan. The calculation was performed for the oxy-fuel ratio of $\lambda = 0.63$ for air and nitrogen as cooling gas and three different spray distances. As a basis, he used the 1D-model introduced in [KAT03, KAT06A, KAT06B], comparable to that of warm spraying (compare the previous chapter).

2.5. Heat-treatment

Powder and coating heat-treatments were performed by using a high-vacuum oven type VHT8/18-KE from Nabertherm (Lilienthal / Germany) at a vacuum of $2 \cdot 10^{-5}$ bar. The heating- and cooling rates were set to 10 °C/min. NAB-powder heat-treatments were performed at a

temperature of 600 °C for 1 h (NAB medium) and for 7 h (NAB soft), NAB coatings were annealed at 500 °C and 650 °C for 0.3 h, 0.6 h, 1 h, 2 h or 4 h.

2.6. Flowability, Apparent Density and Particle Size Distribution

The flowability for each powder type was measured in accordance with DIN EN ISO 13517. 50 g powder had to pass a 2.5 mm wide funnel exit while the flow time was measured. If no powder passes the funnel, the powder is declared as “not flowable”.

The apparent density was determined in accordance with DIN ISO 3923. The powder was sent through a 2.5 mm wide Gustavsson-flowmeter (funnel) and caught within a cylinder of $25 \pm 0.05 \text{ cm}^3$. The respective powder mass within the cylinder was measured and set in relation to the bulk mass. Typical values are between 50 - 60 %.

The particle sizes distribution was determined by laser scattering, using an instrumental type LA-910 from Ltd. Horiba (Japan).

2.7. Optical Microscopy and Porosity Measurements

For analysing powder and coating microstructures, crack formation during cavitation tests as well as investigating the coating-substrate interface, an optical microscope (OM) of type DMRM with Axio-Vision® software from Leica (Germany) was used.

Furthermore, the porosity was determined by analysing optical micrographs according to ASTM-Standard E2109-1 using the software KS300 from Zeiss (Germany).

2.8. Electrical Conductivity

The electrical conductivity of the coatings and the bulk materials were determined by using a Sigmascope® SMP10-HF and measuring sensor ES40HF from Helmut Fischer GmbH (Germany). The experiments were conducted in accordance with ASTM-standard E1004 using an inductive method, operating at a frequency of 1250 kHz to ensure low skin depth. The coatings were polished to reduce influences of surface topographies. Coating thickness was at least 300 µm to avoid influences by the substrate. For better comparability within this study, the measured coating electrical conductivity was set in relation to the bulk conductivity.

2.9. Scanning Electron Microscopy

Scanning electron microscopy (SEM) investigations were performed with a Quanta 650 from FEI (Czech Republic), equipped with a secondary (SE) and back-scattering electron (BSE) detector, as well as a NORAN 7 system from ThermoFisher (USA) for energy dispersive x-ray analyses (EDX). Powder sizes and morphologies as well as detailed surface topographies from wipe tests or coating surfaces were analysed in the SE-mode. Detailed

images of coating microstructures and their respective semi-quantitative composition were observed in the BSE-mode. Detailed material compositions were determined by EDX.

2.10. X-ray Diffraction and Stress Analysis

X-ray diffraction (XRD) measurements were performed by using a XRD3000 PTS X-ray diffractometer from Seifert (Germany) operating at an acceleration voltage of 40 kV and current of 40 mA using a cobalt x-ray tube. Experiments were conducted with a primary collimator diameter of 2.5 mm and a secondary aperture width of 0.5 mm. Resulting XRD pattern for structure determination and stress examinations were analysed with the software package Rayflex Analyse Version 2.503 from Seifert (Germany). Residual stresses were determined at single peaks of the 222- and 311-lattice plane in tilt steps of $\pm 15^\circ$ from 0° to 60° . For determining the Young's modulus and the Poisson ratio of the different bronze types for respective lattice planes, the global values were set in relation to those of pure copper. The resulting calibration factors were then used to estimate the Young's modulus and Poisson ratio of bronzes.

2.11. Determination of Oxygen Contents

Powder and coating oxygen contents were measured by using an analyser type G8 Galileo from Bruker (Germany). For analyses by inert gas fusion, coatings had to be detached from the substrate and crashed into small pieces. Melting occurs in a graphite crucible, CO_2 as a measure for oxygen content can be detected by a mass spectrometer.

2.12. Determination of Particle Strength

For calculating critical velocities, and in consequence using the coating quality parameter η as measure for evaluating different coating qualities, knowledge about the powder deformability, means their strength, is needed. Due to finer grain sizes by the fast quenching rates during atomization, the mechanical strength of particles is higher than that of respective bulk materials [ASS15]. Moreover, the high cooling rate could result in formation of metastable phases with completely different properties as compared to the bulk material.

Ordinary tensile tests are not applicable for powder sizes of 25 – 45 μm . Assadi et al. developed a method to determine particle strength by using a powder compression test [ASS15]. The experiments were performed by using a modified Nanoindenter NHT² from CSM Instruments (Switzerland) with a flat indentation tip (compare Figure 15). Single particles are positioned on a cermet plate. In the test, within 120 sec the indenter compresses the particles at constant rate up to a force of 500 mN. Before and after compression testing, the particle shape and height were determined for additional calibration by using a confocal microscopy of type VK-X200 from KEYENCE GmbH (Germany), as shown in Figure 15.

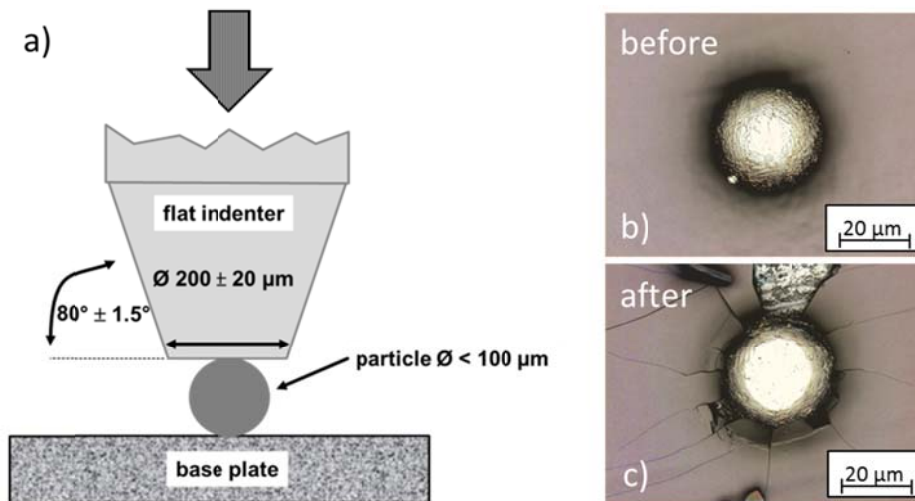


Figure 15: Schematic of the compression test set-up (a) and a NAB - hard particle before (b) and after (c) compression test. The observable cracks in (c) result from the broken thin film of a marker for particle positioning.

Following the procedures in literature, the results of the force-displacement-curve were transformed into a nominal stress-strain-curve (σ and ε) and adjusted to a parametric description from simulation based on the Johnson-Cook-model [CX02].

At the best fit between the experimental results and the finite element method, the constants A, B and n from the Johnson-Cook-model can be determined by optical means as shown in Figure 16. The respective values can be transferred into the material strength.

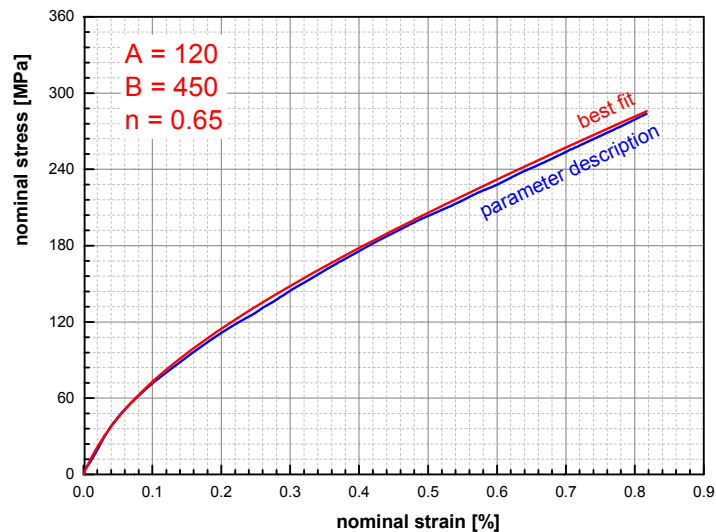


Figure 16: Example for determining mechanical data of a NAB hard particle.

2.13. Hardness Test

Coating hardness was measured with a Miniload II from Leitz (Germany) according to the ASTM E384-10-standard on polished coating cross-sections with a proof load of 2.942 N (HV0.3).

2.14. Tensile Testing

Tensile testing machine from Zwick/Roell (Germany) was used for getting information on mechanical properties as gained by micro-flat tensile, tubular-coating tensile and bond strength tests.

Micro-flat tensile (MFT) test

As compared to usual macro tensile test specimen, the MFT-specimens are smaller, having a thickness of 0.5 mm, with a gauge length of 12 mm and gauge width of 2 mm. The specimens were manufactured by wire spark erosion. The pulling velocity was adjusted to 2 N/sec. The experiments allow for determining coating strain and tensile strengths. For copper alloys, sizes effects could be neglected and results are comparable to those of macro tensile tests [GAE06].

Tubular-Coating-Tensile (TCT) Test

The tubular-coating-tensile test was conducted according to DIN-standard 3253. In contrast to the MFT-Test, the TCT-test does not supply information on coating strain. Moreover, typically a notch factor between the cylinders of about 1.5 to 1.7 has to be considered. The surface of the connected cylinders is typically coated in a thickness of 0.3 – 0.6 mm.

Bond Strength Test

The coating adhesion strength was measured according to the DIN EN-standard 10002 part 1 on roughened surfaces. The coated specimen (\varnothing 25 x 25 mm) were glued to a counter-body using Ultrabond 100 glue and the pulled with a velocity of 2 N/sec.

2.15. Cavitation Erosion Test

Cavitation testing was conducted in accordance with the ASTM-standard G32-10 indirect mode by using a test rig of type BK101Z from KLN Ultraschall GmbH (Germany). The schematic is shown in Figure 17. For testing, the sample surface is placed in a distance of 0.5 mm to the sonotrode. As medium, distilled water at a constant temperature of 22 °C is used to reduce side reactions by e.g. corrosion. The sonotrode has a diameter of 15 mm and works at an amplitude of 25 μ m and a frequency of 20 kHz. This configuration generates cavitation bubbles that implode on the sample surface and cause respective damage.

Polished bulk and coating samples were exposed to cavitation for up to 300 min. The sample surface topography and mass loss were recorded after defined time steps. The mass loss was converted into an erosion depth in μ m and the cavitation rates in μ m/h to obtain a comparable standard for different materials.

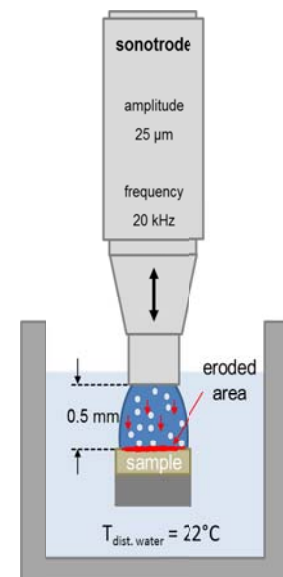


Figure 17: Cavitation erosion test iaw. ASTM G32-10 indirect method.

Wipetest samples were exposed to cavitation up to 120 sec, being regularly interrupted to record the amount of adhering particles by SEM as described by Villa et al. [VIL15].

3. Substrate and Powder Properties

3.1. Substrate Properties

For all spray experiments the ship-building steel GL-A - comparable to steel S235 - was used as substrate material. Ship yards from the project consortium supplied different batches of substrate that were separately analysed regarding their mechanical properties to evaluate probable influences on coating build-up. All supplied GL-A substrates had a thickness of 4 mm, except batch 1 which had a thickness of 15 mm. Annealed S235 substrates were used for adhesion and TCT-test specimen. The mechanical properties of the different substrate types are summarized in Table 4. The hardness for all substrates batches differ within a narrow regime around 135 ± 21 HV0.3. The tensile strengths and elongation to failure show larger differences. This might be due to slightly varying amounts of alloying elements, unknown degree of work hardening or different heat-treatments. All substrates types fulfil the criteria for ship-building steel GL-A [GL09A].

Table 8: Mechanical properties of the substrate material.

material	remarks	hardness	hardness	yield strength	ultimate tensile strength	elongation to failure
		[HV0.3]	[HV2.0]	[MPa]	[MPa]	[%]
steel GL-A (S235)	batch 1	148 ± 8	117 ± 5	303	455	34
steel GL-A (S235)	batch 2	150 ± 1	119 ± 4	339	424	51
steel GL-A (S235)	batch 3	131 ± 5	102 ± 5	414	499	36
S235 900°C annealed	-	127 ± 3	99 ± 3	235	353	47

In addition, the cavitation performance of the substrate material was determined to serve as a reference to sprayed coatings. The result is illustrated in Figure 18. The curve shows an incubation time of about 100 min until reaching the area of steady state cavitation erosion. The steady state cavitation erosion-rate was determined to $26 \mu\text{m/h}$. The surface topography after 100 min cavitation testing, as shown in Figure 18, shows typical low cycle fatigue damage profile as described in literature [BOU02, SOM10, CZI10, VYA77]. Plastic deformation due to static cavitation treatment forms craters and small pores. During the steady state cavitation stage, these microstructural defects accumulate and cause the high material losses by mainly fatigue failure.

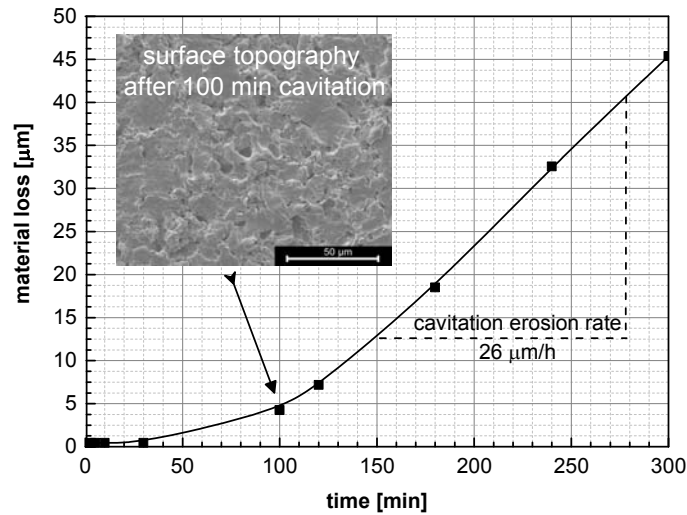


Figure 18: Development of the mass-loss during cavitation testing of the substrate material ship-building steel GL-A and respective damage topographies by SEM analyses.

3.2. Powder Microstructures and Properties

The different bronze powder materials were analysed in detail regarding their flowability, size distribution, microstructure and mechanical properties to gain information on the deformation behaviour and thus coating formation. The powders were produced by electrode induction-melting gas atomization (EIGA) by TLS-Technik (Bitterfeld/Germany) in nitrogen atmosphere. Different batch types were processed and considered separately due to slightly differing compositions and thus slightly different properties.

Table 9: Overview about the different bronze powder compositions, designations, annealing states, particle size distributions and oxygen contents.

material	shortcut	batch	annealing	size distribution			oxygen content
				d10	d50	d90	
		no		[μm]			[ppm]
		1295		19	31	48	
CuAl10Fe5Ni5	NAB hard	1334	none	23	36	59	350 ± 20
		1214		19	31	48	
CuAl10Fe5Ni5	NAB medium	1256	1 h - 600 °C	20	30	45	400 ± 10
		1261		28	38	53	
CuAl10Fe5Ni5	NAB soft	1278	7 h - 600 °C	22	31	48	410 ± 10
		1337		23	36	59	
CuMn13Al8Fe3Ni3	MAB	1284	none	16	27	43	380 ± 110
CuNi15Sn8	CuNi15Sn8	1282	none	10	23	46	2000 ± 20
CuSn10	CuSn10	1293	none	22	32	48	240 ± 30

As introduced in chapter 1.1, the powders CuAl10Fe5Ni5, CuMn13Al8Fe3Ni3, CuNi15Sn8 and CuSn10 alloys were analysed in the as as-atomized state and only the CuAl10Fe5Ni5 powder was additionally heat-treated. The respective powder material abbreviations, batch numbers, annealing conditions and particle size distributions are summarized in Table 9. All particle size distributions lay within a narrow regime and meet the required size ranges of 25 - 45 μm for the different kinetic and thermal spray process. All powders exhibit a good flowability between 17 to 27 s/50g and apparent densities between 55 to 60 %. The oxygen content of most powders was comparably low in ranges between 240 to 410 ppm. Except the CuNi15Sn8 powder showed an up to four times higher oxygen content probably due to long storage times.

The powder morphologies, microstructures and crystallographic structures of each powder type were analysed to gain information regarding sprayability and possible spray parameter sets. The results are summarized in Figure 19 to Figure 23.

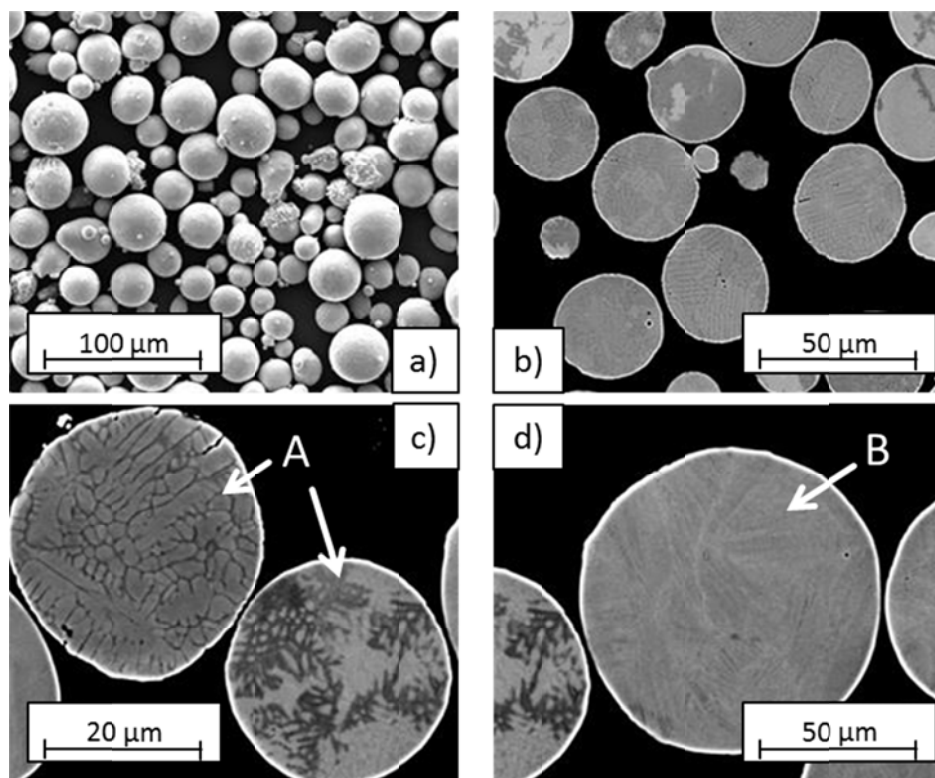


Figure 19: Powder morphologies (a) and microstructures (b - d) of as-atomized CuAl10Fe5Ni5 (NAB hard) powder showing three different types of microstructures. The particles contain dendritic (A) and martensitic (C) structures.

The morphology of as -atomized NAB powder in Figure 19 displays almost spherical shaped particles with very low amounts of satellites and fines. The powder cross-sections reveal, that the powder microstructures are not uniform and vary from particle to particle. The overview in (b) demonstrates that mainly two different types of microstructures (A and B) are obtainable following the definitions given in literature [NOR97, ZAM98]. The dendritic and the grain refined microstructures of type A are assumed to be well deformable during coating formation. In contrast, microstructures of type B show martensite needles that arise from rapid cooling during the gas-atomization process. These martensite fractions would probably reduce powder deformability and thus hinder coating formation [KRE14, KRE15].

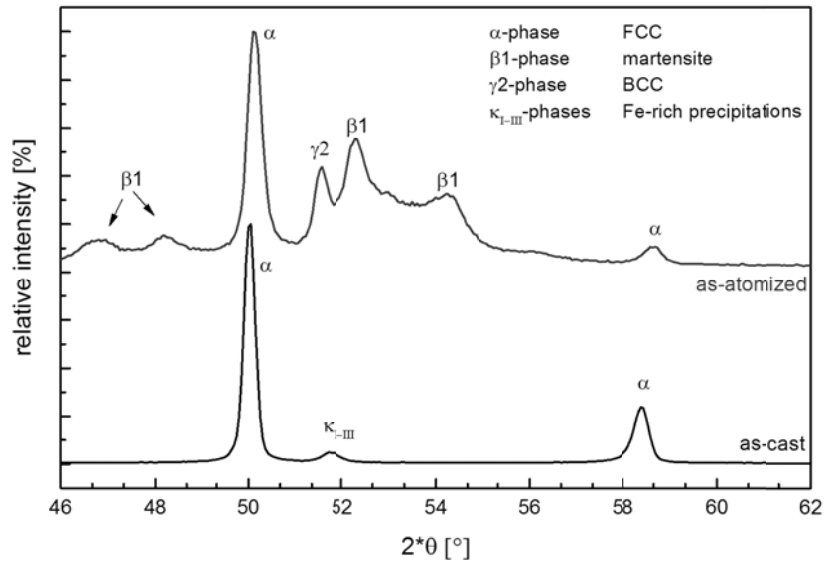


Figure 20: XRD-pattern of as-atomized Ni-Al-Bronze showing high amounts of martensite phases as a result of rapid solidification during powder processing.

The phase-contents of the as-atomized powder in comparison to cast NAB are shown in Figure 20. The cast material contains mainly the α -phase solid-solution and some Fe-rich κ_{I-III} -phases. The XRD-pattern of the as-atomized NAB hard powder confirms the microstructural observations. The XRD-pattern reveal that the cubic face centred α -phases, and to minor contents of the body centred γ_2 -phase, should allow for good deformability. IN addition, higher amounts of martensitically transformed meta-stable high-temperature β_1 -structures are detectable.

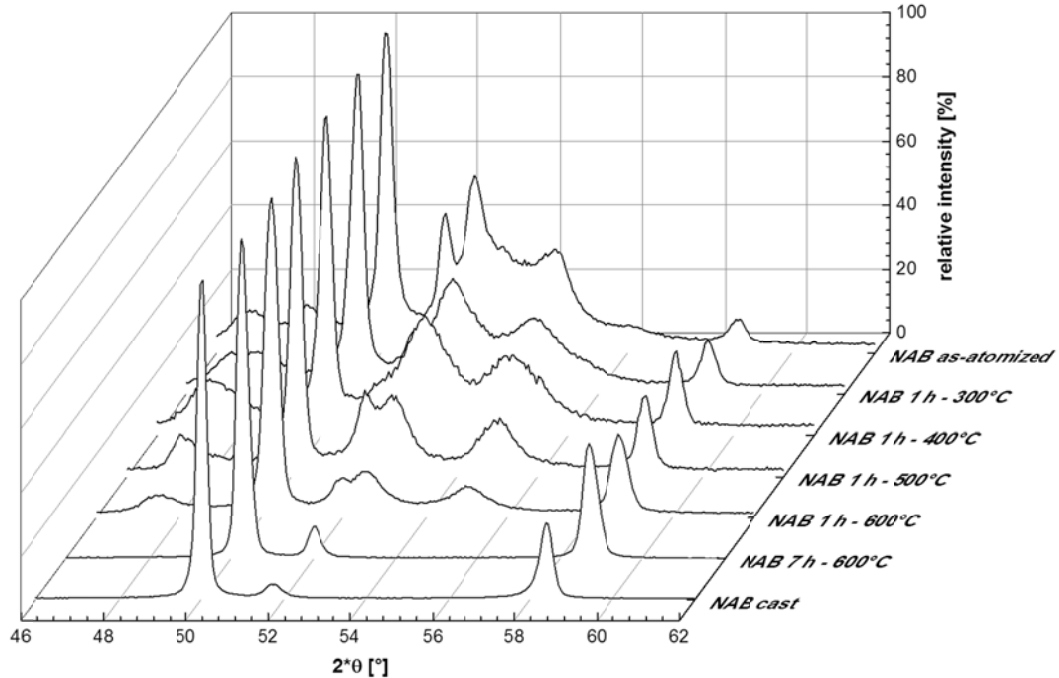


Figure 21: XRD-pattern of NAB powder for different annealing treatments in comparison to cast bulk material showing the decline of martensite for increased annealing time and temperature.

To reduce the martensitic structures within the powder, several annealing treatments were applied. Figure 21 summarizes results on the decline of martensite and γ_2 -phase during respective annealing procedures. As a benchmark, the graph includes the pattern of as cast and martensite-free NAB as bulk material. The martensite fractions transform to the α -phase

at temperatures above 600 °C and after 7 h of heat-treatment reach a martensite-free state, promising bulk-like properties.

Figure 22 shows the morphology (a) and microstructures (b-d) of the NAB powder after 7 h annealing at 600 °C. Annealing of the NAB powder preserves its spherical shape but changes its microstructures. The cross-sections reveal that the microstructure gets more homogeneous with less segregation pattern from dendritic solidification. To some extent, the patterns of former martensite needles are preserved within the microstructures. In addition, Fe-rich κ_{I-III} -phases precipitations – given in the darker contrast - grow at the vicinity of grain boundaries. Such microstructure might probably improve material deformability as compared to that of as-atomized powder.

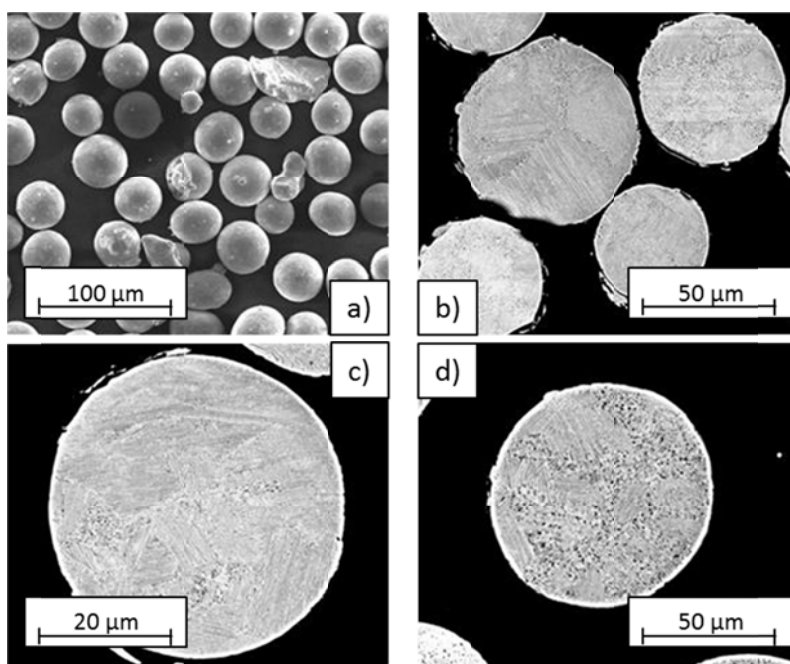


Figure 22: Powder morphologies and microstructures of 7 h at 600°C annealed CuAl10Fe5Ni5 powder (NAB soft) showing mainly homogeneous α -phase, some pattern of former martensite needles and of Fe-rich κ_{I-III} precipitations.

The powder morphologies, microstructures and XRD-pattern of the high-tensile MAB and the low-tensile CuNi15Sn8 and CuSn10 bronzes are summarized in Figure 23. All three bronze powders show spherical shapes and only few fines. Comparing the different powder microstructures, the MAB and the CuNi15Sn8 powder are mainly grain refined, whereas CuSn10 powders appear to be more dendritic, following the definitions in literature [NOR97, ZAM98].

The XRD-pattern of the three powder materials are shown in Figure 23i to k. The pattern of the MAB shows mainly β - and α -phases but also a minor content of martensitic β_1 -structures, not being visible in the powder microstructures. Associated higher strength might negatively influence particle deformability and thus coating formation [KRE14, KRE15]. In contrast, the CuNi15Sn8 and CuSn10 bronzes contain mainly the well deformable cubic face centred (fcc) or cubic body centred (bcc) structures.

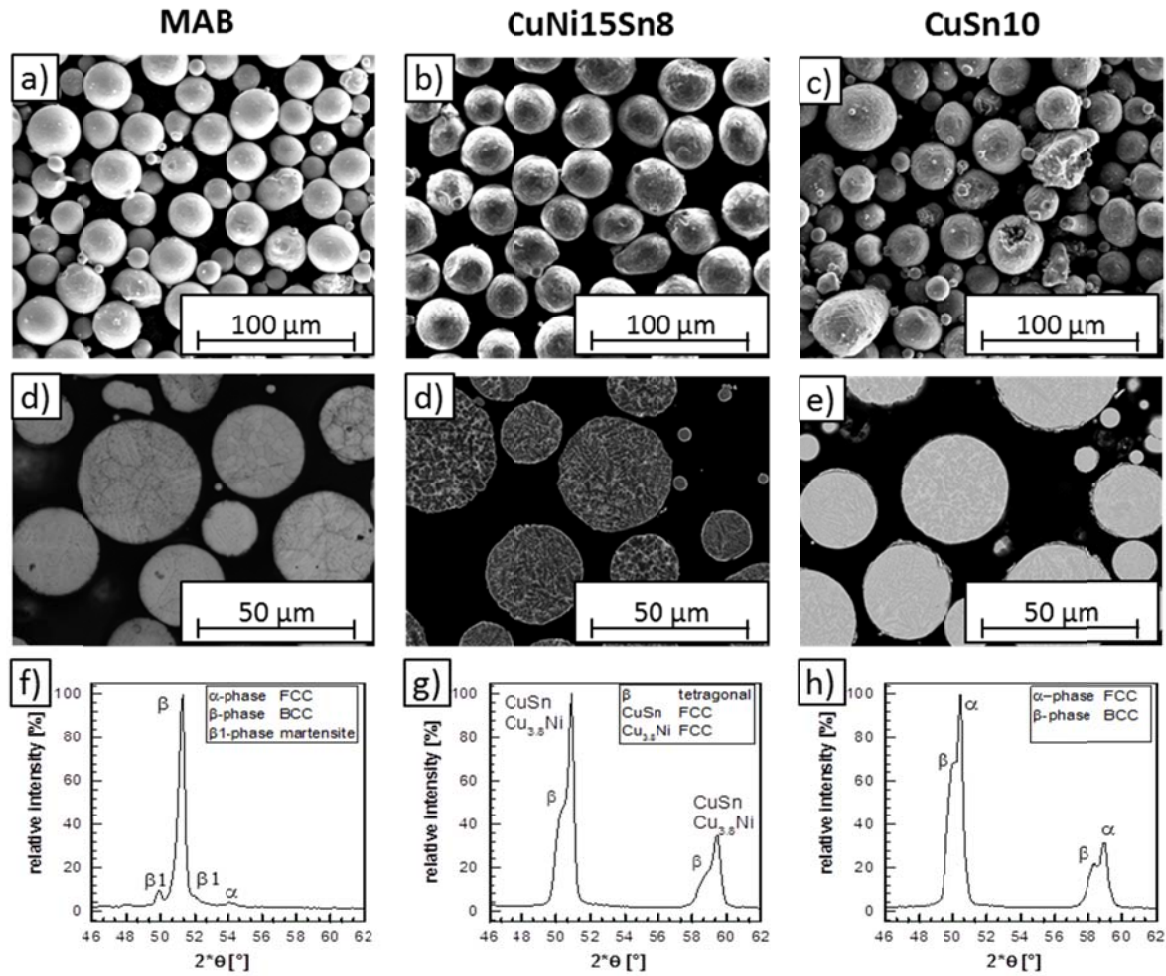


Figure 23: Powder morphologies, microstructures and XRD-pattern of the MAB, CuNi15Sn8 and CuSn10 bronzes.

For calculating the coating quality parameter η , data on materials strength is a necessary pre-requisite. Figure 24 shows the ultimate tensile strengths of the different bronze materials in comparison to the respective bulk material. All bronze powders were analysed in the as-atomized state. In addition, the NAB powder strength was determined after different annealing stages (hard – medium – soft) to obtain information regarding the consequences of the martensite reduction in powder strength. Data for each powder batch was considered separately to calculate the critical velocities and the coating quality parameter as exact as possible. Figure 24 shows that almost all as-atomized powders have a higher strength than respective bulk bronzes. High cooling-rates during the gas-atomization process could hinder the formation of equilibrium states and promote high-temperature phases and martensite formation. Except the CuNi15Sn8 bronze exhibits a lower strength as compared to the bulk material. This powder has been stored for a long-term and might show a strength reduction by aging, as reported for bulk CuNi15Sn8 in literature [SHI05]. At the different annealing stages, the originally high strength of the NAB hard powder is reduced with increasing heat-treatment durations. By adjusting the annealing parameters to 7 h at 600°C, the strength of the NAB soft powder can be tuned to that of as cast bulk NAB material. With respect to cold gas spraying, this reduction of strength should highly influence particle deformability and thus coating formation.

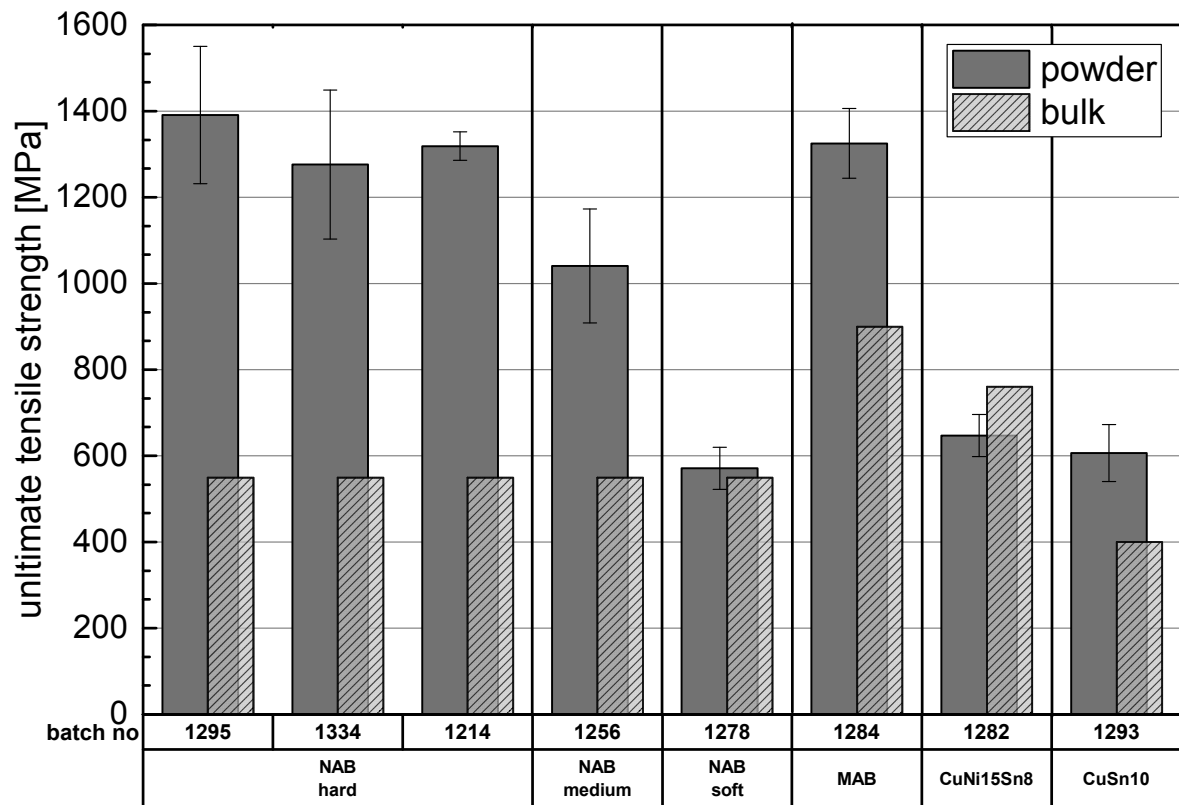


Figure 24: Comparison between the bulk tensile strength and the powder strengths for the different bronze feedstocks. The results show that the powder strength in the as-atomized state is up to 2.5 times higher as compared to that of the bulk material. Only the CuNi15Sn8 powder shows a slightly lower strength than the bulk material. Heat treatment of the NAB (medium → 1 h at 600 °C and soft → 7 h at 600 °C) can reduce powder strengths to similar values for cast bulk material.

4. Cold Gas Spraying of various Bronze Powders

4.1. Calculated Impact Conditions

This study aimed to find optimum spray parameter sets for coating formation of cavitation resistant bronze materials. For better understanding and adjusting the spray parameter sets, the optimum particle size distribution and the Window of Deposition as introduced by Schmidt et al. [SCH06A] and respective impact conditions were simulated and evaluated.

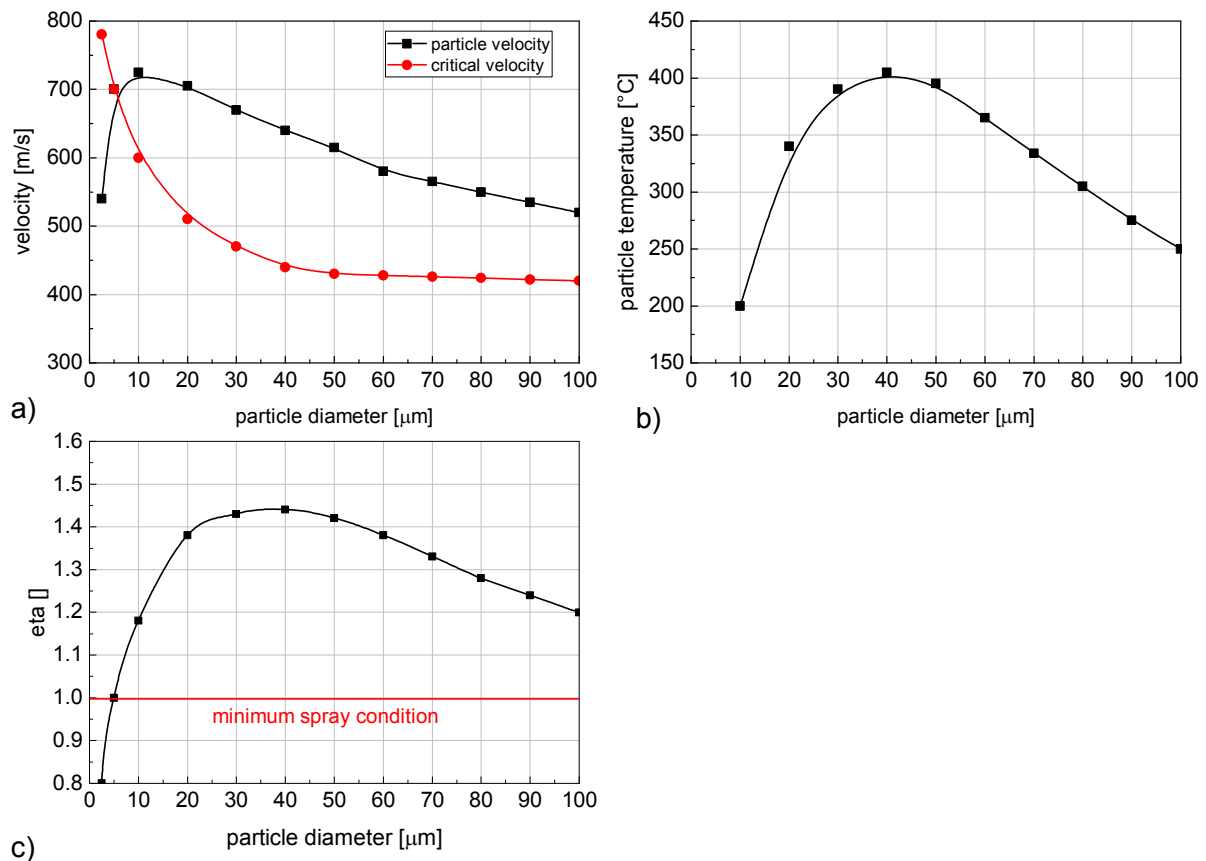


Figure 25: Overview about the influence of the particle size of NAB soft powder in cold gas spraying on particle and critical velocity (a), the particle impact temperature (b) and the resulting coating quality parameter η . The figure shows calculations for a spray set-up of nozzle type 51, 40 bar and 650 $^{\circ}\text{C}$.

The particle size distribution plays a major role in cold gas spraying since small particles are faster and colder due to their lower kinetic and thermal inertia. These particles accelerate and heat-up quickly, but cool down significantly within the cold gas stream. In contrast, large particles reach lower velocities but remain rather hot than smaller particles [KLA16, SCH09]. Furthermore, a wide particle size range would lead to collisions between large but slow and small but fast particles. These crashes divert the smaller particles towards the nozzle wall and can cause nozzle clogging and thus negatively influence the spray conditions. Consequently, the influence of the particle size distribution on velocity and temperature was simulated and respective results are shown in Figure 25. As exemplary cold gas set-up, the nozzle type 51, a gas pressure of 40 bar and a gas temperature of 650 $^{\circ}\text{C}$ were chosen. Figure 25a shows the particle and critical velocity of NAB soft powder as a function of the particle diameter. The critical velocity decreases monotonically with increasing particle

diameter whereas the particle velocity shows a maximum at sizes of about 10 μm . In general, the particle velocity should exceed the critical velocity to achieve the conditions for bonding [ASS03]. Thus, particle sizes have to be adjusted with respect to sufficient particle velocities exceeding the critical velocity. Figure 25b illustrates the dependency of the particle temperature and the particle diameter. At about 35 μm , the curve displays a maximum. Too large particles cannot heat-up sufficiently within the pre-chamber and too small particles loose their heat within the expanding cold gas stream. The resulting coating quality parameter η , as shown in Figure 25c, summarizes the kinetic and thermal influences and exhibits a broad maximum between 25 to 45 μm of particle diameter, hence highlighting the optimum particle sizes distribution for cold gas spray experiments. Respective calculations were performed for all bronze materials used in this study. Simulations of other bronze materials and changes of the spray parameters resulted in variations of the absolute values of particle velocity and η but due to similar densities in only negligible shifts of the maximum with respect to particle sizes of 25 – 45 μm .

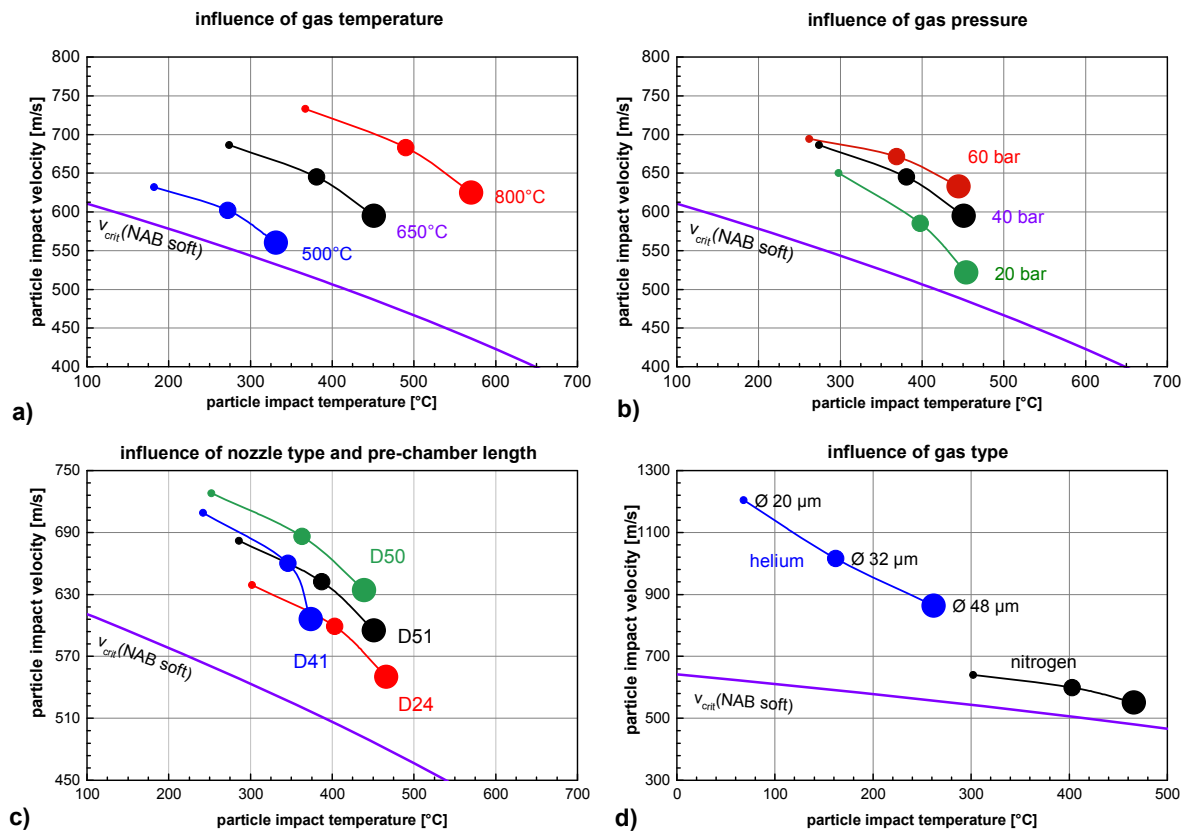


Figure 26: Overview about the different adjustable variables in cold gas spraying. The black curve (D51, 40 bar, 650°C, nitrogen sprayed) serves as a reference, showing the maximum spray parameter. The different symbol sizes indicate impact conditions for small ($d_{10} = 25 \mu\text{m}$), medium ($d_{50} = 32 \mu\text{m}$) and large ($d_{90} = 45 \mu\text{m}$) particle sizes.

Figure 26 describes the influences of the cold spray parameter sets on the respective impact conditions and the window of deposition as introduced by Assadi et al. [ASS11]. It shows the particle impact velocity as a function of the particle temperature for each spray parameter set for small (25 μm), medium (32 μm) and large (45 μm) particles. Besides, the temperature dependent critical velocity is shown. The impact conditions of spherical Ni-Al bronze powder sprayed with nozzle type 51, 40 bar, 650 °C, nitrogen, spray distance 60 mm and a pre-chamber length of 180 mm (black) can be taken as a reference for the different variations. The coloured curves and following descriptions emphasize the changes of the impact

conditions when changing one of the influencing factors like gas temperature (a) or pressure (b), the nozzle type or pre-chamber length (c) or the gas type (d).

Influence of the gas temperature (Figure 26a):

An increased gas temperature leads to higher particle temperatures and velocities. In ideal cases, particles are heated within the pre-chamber until reaching the gas temperature which would support softening. Since the expanding gas stream cools down after passing the nozzle throat, also the particles temperature drop. However, bigger particles by higher thermal inertia retain more heat than smaller particles. Furthermore, a higher gas temperature leads to a higher sound velocity of the gas within the nozzle throat and thus causes higher particle acceleration [DYK98]. This affects mainly the smaller and less heavy particles than larger inertial particles. In summary, particle velocities and temperatures for the given particle sizes increase with increasing gas temperatures of the different spray parameter sets.

Influence of the gas pressure (Figure 26b):

The gas pressure mainly affects the particle velocity due to a higher acceleration within the nozzle. As indicated by higher gas flow-rates at higher gas pressures, more molecules are available to interact with the spray particles [ALK94] and result in a higher drag force that, as shown in Figure 26b, improves particle acceleration. Despite the better heat transfer between particle and gas causing cooling, the particle temperature increases probably due to the shorter dwell time in the expanding regime. This effect is more prominent for larger particles.

Table 10: Used nozzle types and respective nozzle shapes within this study.

nozzle type	Radius nozzle throat	length divergent nozzle part	expansion ratio
	[mm]	[mm]	
24	2.7	130	5.6
41	2.7	230	8.9
50	3.8	238	7.5
513.3	182	6.35	

Influence of the nozzle type and the pre-chamber length (Figure 26c):

The nozzle types comprise different components - nozzle length, throat diameter and expansion ratio together with the pre-chamber length that determines particle impact conditions (Table 10). As compared to nozzle type 24, wider nozzle throats and larger expansion ratios of nozzles type 41, 50 and 51 cause higher particle acceleration. A wider nozzle diameter causes less friction between the gas and the nozzle wall. An elongated expanding nozzle regime allows for longer particle acceleration within the gas stream. Nozzle type 41 has the same throat diameter as type 24, a rather high length and the highest expansion ration within this comparison. The higher expansion ratio increases the gas velocity and thus causes a higher acceleration. This results in as high particle velocities as for nozzle type 51. As compared to the other nozzle types, the particle temperatures are lower due to more efficient cooling in the expanding regime (see small particles) and the use of a shorter pre-chamber (120 mm instead of 180 mm) which prevents large particle to heat through.

Influence of the gas type (Figure 26d):

The simulations for the gas types helium and nitrogen reveal that helium provides much higher particle velocities but lower particle impact temperatures than nitrogen. The velocity of sound that is reached at the nozzle throat of helium is 981 m/s at room temperature, whereas the sound velocity of nitrogen is 333 m/s [ZUC02]. Accordingly, the particles are more accelerated within the helium gas stream although the drag forces are much lower due to a reduced gas density [WON11]. As compared to the use of nitrogen, the lower particle impact temperature is due to more efficient cooling within the expanding helium gas stream.

Windows of deposition and particle impact conditions are shown in Figure 27 for a mean particle diameter of 30 μm . Each dot corresponds to one spray parameter set based on varied nozzle types, gas pressures, temperatures or types. The colours designate the used bronze types. Critical velocities are shown for each bronze material of the present study. The critical velocities are lower for materials of lower strength and decrease with increasing particle temperature. Both aspects determine the particle strength upon impact. Hard materials require more thermal softening to allow for suitable deformation. A necessary pre-requisite for bonding is that the particle impact velocity should exceed the critical velocity [ASS03]. When examining the different spray parameters for each powder type, Figure 27 illustrates that for CuSn10 and CuNi15Sn8 bronze this criterion is fulfilled easily. In contrast, the high-strength bronze NAB hard and MAB reveal that most spray parameter sets result in impact conditions below the critical velocity, not allowing for formation of decent coating quality.

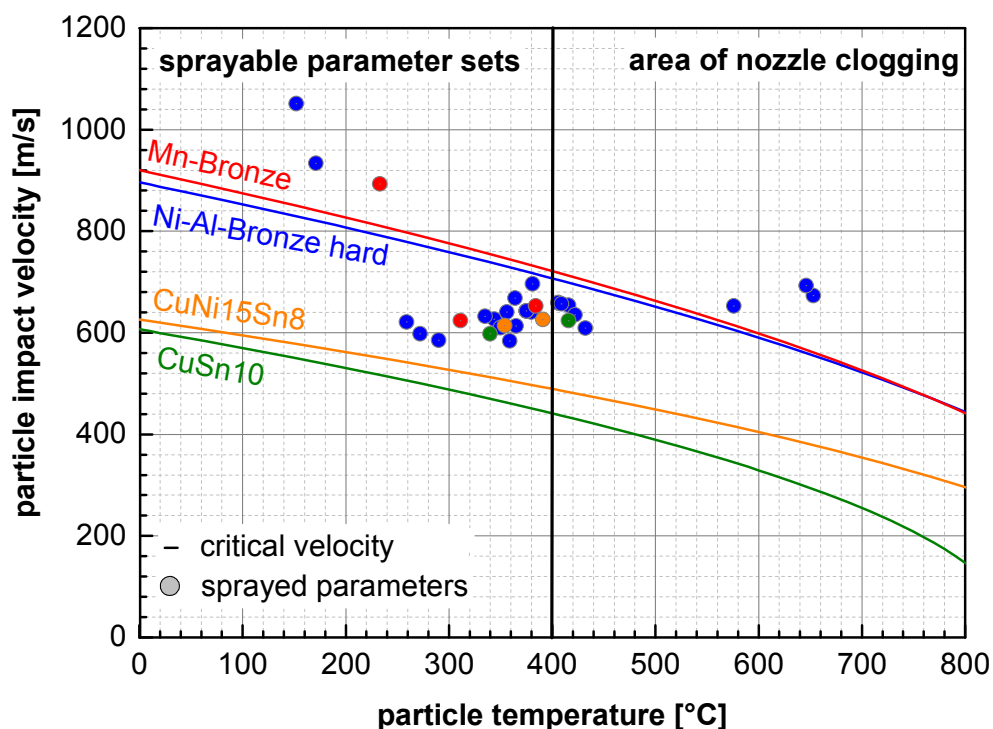


Figure 27: Window of deposition for the different bronze materials of the present study and impact conditions for particle sizes of 30 μm attainable by variation of spray parameter sets. In addition, restrictions due to nozzle clogging at particle temperatures above 400°C are indicated. The solid curves define the critical velocities of the different spray materials. For the hard Ni-Al-bronze and Mn-bronze most parameter sets are slightly below the critical conditions.

Besides boundaries being obvious by the simulation, the cold spray process was practically limited to maximum temperatures of 650 °C, since thermal softening of the particles caused nozzle clogging. The parameter regime of nozzle clogging is also marked in Figure 27 and illustrates that coatings sprayed with too hot spray conditions could not be evaluated experimentally.

To bypass problems with too rigid powders, the NAB hard particles were heat-treated, as introduced in chapter 3.2, to reduce particle strengths and in consequence also the critical velocity. Figure 28 shows the development of the critical velocity of NAB for reduced particle strength by different annealing conditions. By lowered critical velocities, the spray conditions match regimes that are well above critical conditions, particularly when using NAB soft powders.

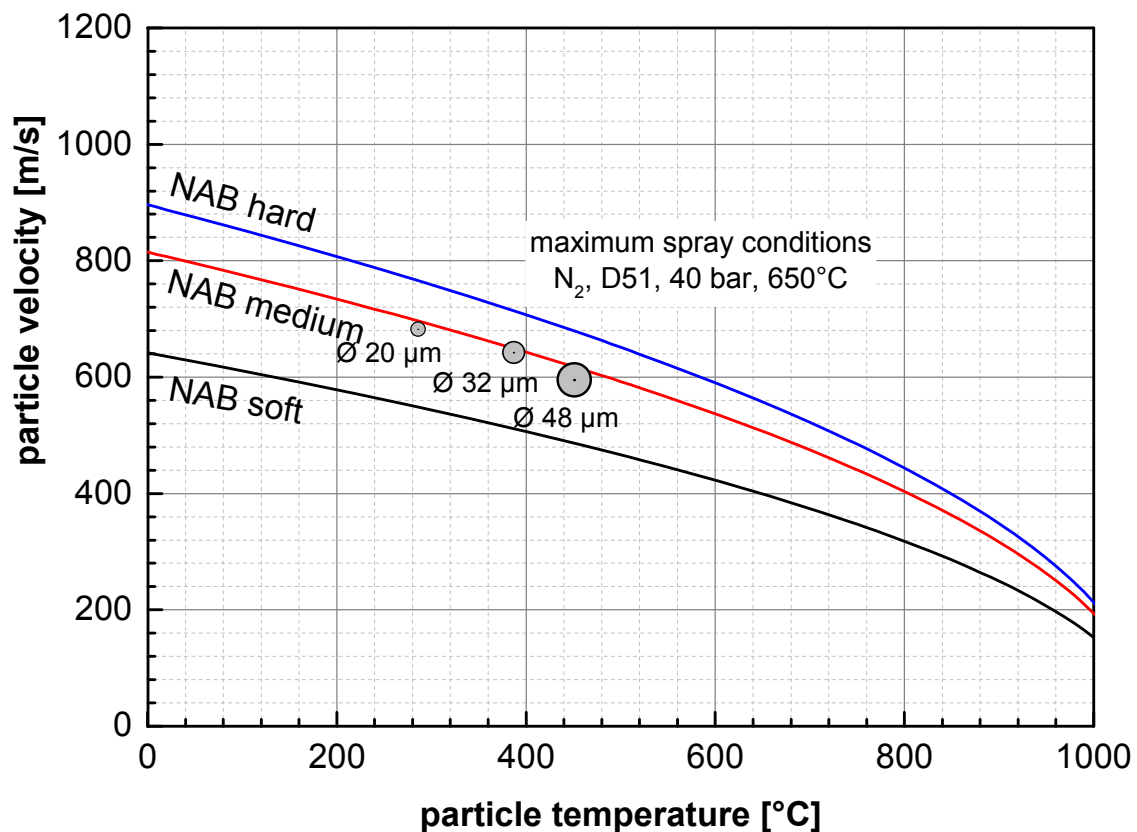


Figure 28: The window of deposition for Ni-Al-Bronze powder for the as-atomized (hard) conditions and after 1 h (medium) and 7 h (soft) annealing at 600 °C. Heat treatment reduces the critical velocity. The spray experiments can be performed well above the critical velocity.

4.2. Particle Impact Behaviour and Deposition Efficiencies

Single particle impact morphologies as obtained by wipe tests supply vital information on the deformation behaviour and bonding conditions. For quantification, different types of deformation were studied, classified and finally statistically evaluated for each bronze type and for various spray conditions. The study of single impact phenomena could also reveal differences by particle deceleration by spraying on different materials or heated substrates, which are not predictable by simulation.

Overviews of typical particle impact morphologies of the as-atomized NAB hard and the heat-treated NAB soft powders are shown in Figure 29 and exhibit particles sprayed on steel GL-A with a low (a, d) and a high (b, e) parameter on room temperature substrates and for high parameters sets on a pre-heated substrate (c, f).

The SEM micrograph of the NAB hard sprayed with low parameters in Figure 29a indicates mainly craters and few adhering particles. The adhering particles show low flattening ratios and almost no material jets around the particles. When spraying with higher spray conditions (Figure 29b), the amount of craters reduces and the particles show a higher degree of deformation. An increased substrate temperature reduces substrate strength and thus allows for better deformation of the substrate. Accordingly, the particles show slightly lower flattening ratios due to less deceleration upon impact and can penetrate deeper within the substrate than on non-pre-heated substrates.

The influence of the spray parameters on the impact morphologies of NAB soft bronze is almost analogous to that of NAB hard. However, Figure 29d - e emphasize that the heat-treated NAB soft powders show a higher flattening ratio as compared to NAB hard. The lower particle strength improves deformability and the formation of shear instabilities, as visible by material jets that provide better adhesion especially at lower spray parameter sets.

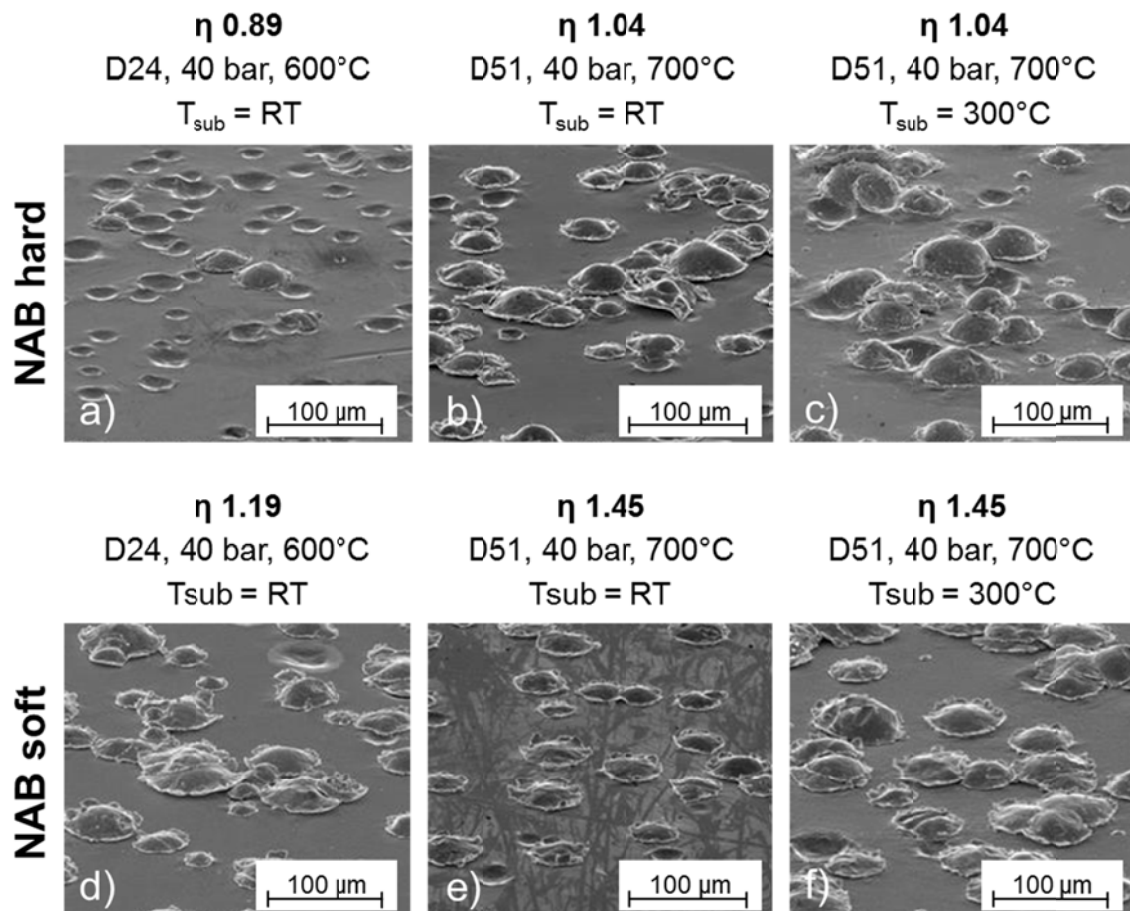


Figure 29: Impact morphologies (angular view) of cold gas sprayed NAB hard and NAB soft particles on steel GL-A for a low (a, d) and a high (b, e) parameter set on substrates at room temperature and for high parameter sets on pre-heated substrates (c, f).

Figure 30 shows the impact morphologies of the highest parameter set using helium as process gas for NAB soft. The overview (a) shows that almost no empty craters are left on the surface and that the impacted particles are highly deformed and deeply penetrated into

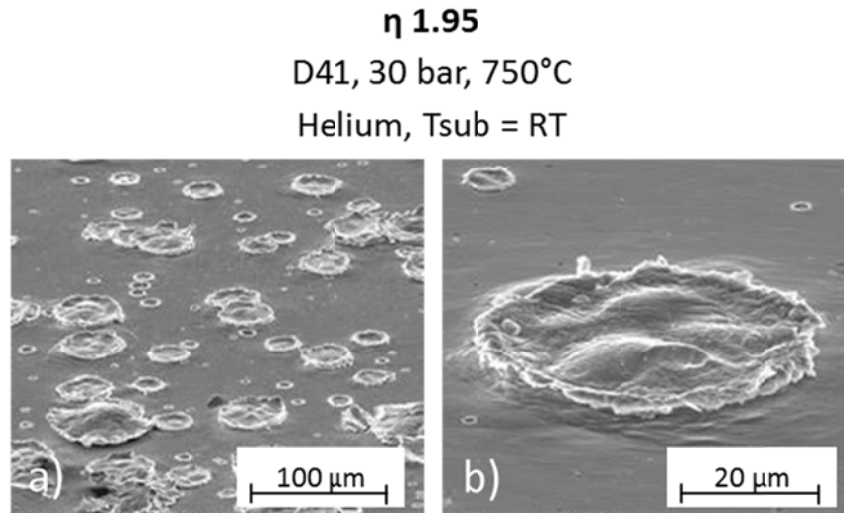


Figure 30: Impact morphologies (angular view) of NAB soft particles on steel GL-A sprayed with helium as process gas showing a very high degree of deformation.

the substrate. The very high particle impact velocity of about 1060 m/s allows for substantial particle deformation. Figure 30b shows more details and illustrates that the whole particle is completely embedded within the substrate and highly flattened. The high kinetic but low thermal energy impact causes sufficient plastic deformation of the particle and the substrate. Thus, a thin common material jet between particle and substrate can be observed. This necessary pre-requisite for shear instabilities is a proof for excellent bonding between particle and substrate.

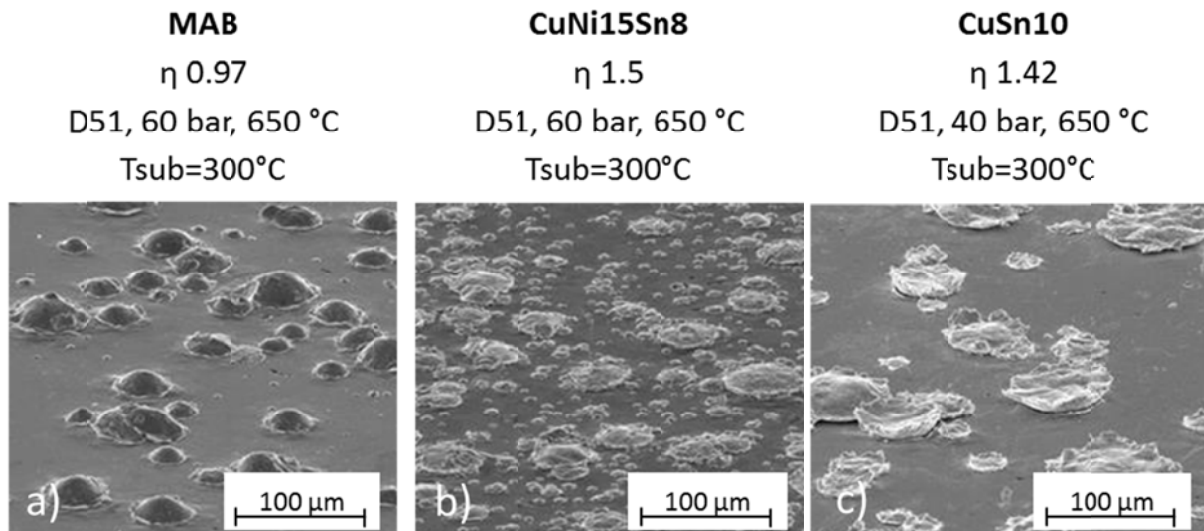


Figure 31: Impact morphologies of MAB, CuNi15Sn8 and CuSn10 powders for selected high spray parameter sets onto pre-heated steel GL-A substrates.

The deformation behaviour of the high-strength MAB and the low-strength CuNi15Sn8 and CuSn10 bronzes are summarized in Figure 31a - c. For this comparison highest η -values and pre-heated substrates were selected. The impact morphologies of the MAB (a) show that no craters are obtainable. Though, the particles exhibit very low flattening ratios but high amounts of desired material jets are present. The CuNi15Sn8 particles show a much higher flattening ratio due to lower particle strength. Nonetheless, material jets are formed to great extent and particles might show good adhesion. The CuSn10 bronze with lowest strength

appears to have the highest flattening ratios and the particle rims tend to bend upwards. Almost all particles seem to adhere on the pre-heated substrate which seems to show only little deformation.

For quantitative evaluation, the particle impact morphologies were systematically categorized and classified into three categories described as “hole”, “low deformation” and “high deformation”. Examples for these classes of characteristic impact events are given in Figure 32.

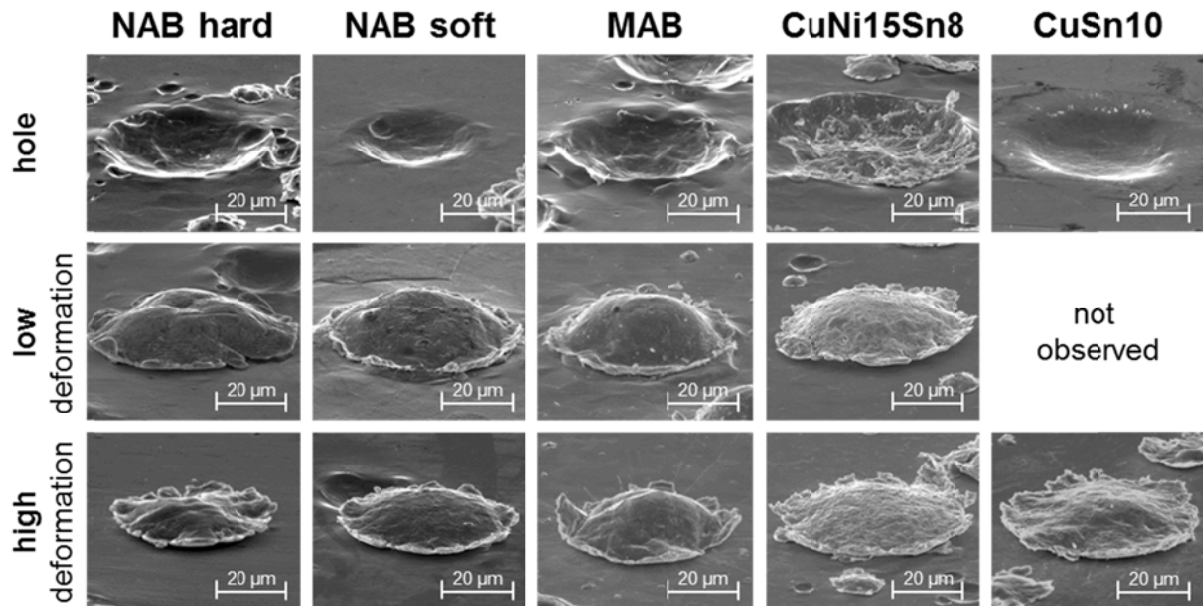


Figure 32: Impact categories of the different bronze types showing similar deformation behaviour for each bronze and category. Only the NAB hard powder reveals non-uniform deformation behaviour.

Category “Hole” (Figure 32a-e)

This category shows a crater left by rebound particles that deformed the substrate. The necessary pre-requisite for bonding of solid particles, the occurrence of shear instabilities due to high deformation-rates between a particle and the substrate, apparently was not fulfilled to needed extent. Thus, the particle did not adhere on the substrate and was rebound by elastic forces [WU06]. In some craters, vein-like patterns are detectable and indicate rupture under viscous flow and thus the occurrence of shear instabilities. However, these shear instabilities did not provide sufficient adherence for the particles to remain on the substrate. This phenomenon appears to happen mainly for high strength bronze materials like NAB hard and MAB. However, such vein-pattern could also be detected for bronzes with lower strength. EDX analyses reveal that these patterns correspond to the powder material.

Category “low deformation” (Figure 32f-j)

This category shows adhering particles that deform when impacting on the hard substrate. These particles illustrate material jets along the contact zone, which can be viewed as a proof for the formation of shear instabilities and indicate good adhesion [ASS03]. Investigation of the material jets by EDX-analyses shows that these jets arise mainly from bronze particles. However, the particles do not penetrate deeply into the substrate. Thus, deformation and possible shear instabilities mainly occurs on particle sides. The flattening ratio is comparably low, leaving a hemisphere particle on the surface. Interestingly, the deformation of the NAB hard powder shows more inhomogeneous deformation behaviour

(Figure 32f) than the other bronze types. Here, the particles show internal topographies and to some extent seem to be internally broken or to deform by locally different mechanisms. For the soft CuSn10 powder, category “low deformation” could not be detected.

Category “high deformation” (Figure 32k-o)

This category describes impact morphologies, where the particles adhere on the substrate but the particle rim is mainly not in contact with the substrate. Consequently, arising shear instabilities are not to full extent contributing to particle adhesion. Furthermore, the flattening ratio appears much higher as compared to category “low deformation”. The extent of plastic deformation of the substrate could not be evaluated. This type of impact occurs at higher particle impact velocities and temperatures than category “low deformation”. The deformation behaviour of the different bronzes under this class is very similar and uniform. Only the NAB hard powder appears to deform more inhomogeneously (Figure 32k). The highly deformed outer rims of the NAB hard particles disintegrate and form particle surface topographies with humps and valleys, all that being more prominent closer to the rim.

The different classes of particle impact morphologies were statistically evaluated for various spray parameter set to predict probable coating formation by analysing about 100 single events. The results for NAB hard and soft are summarized in Figure 33 and for MAB, CuNi15Sn8 and CuSn10 in Figure 34.

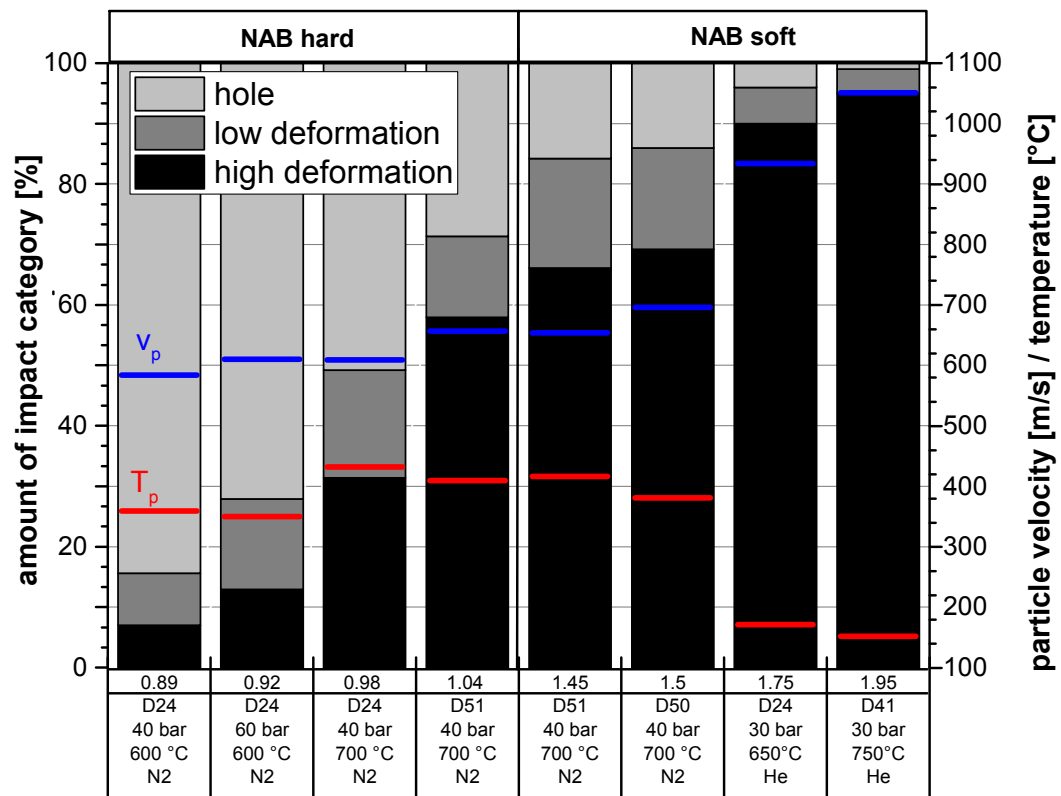


Figure 33: Statistical evaluation of the determined particle impact categories for NAB hard and NAB soft sprayed at different cold spray parameter sets.

Figure 33 shows the percentage of each impact category for NAB hard (left) and NAB soft (right) for various spray conditions. The figure is sorted according to an increasing η -value. In addition, the particle impact temperatures (red) and velocities (blue) are given within the diagram. The results indicate a general trend that higher η -values enhance deformation and thus particle adhesion (category “low deformation” and “high deformation”) for both bronze

materials. Especially the category “high deformation” is highly influenced by increasing η -values and shows the highest amount of adhering particles for the spray conditions with helium as process gas. This means that an enhanced kinetic or thermal energy influences the deformability and formation of shear instabilities. For all conditions, the amount of adhering particles for NAB soft is higher than for NAB hard, although spraying with similar spray parameter sets like the nozzle type, the gas pressure, temperature and type. By lower strength, the critical velocities of the NAB soft are lowered and allow for easier formation of shear instabilities upon impact. Looking into more detail, an increased gas pressure (compare NAB hard $\eta = 0.89$ and $\eta = 0.92$) decreases particle temperatures but enhances particle velocities. A similar observation can be made when comparing wipe tests sprayed with different nozzle types but identical gas conditions (T , p , type) as shown at experiments with $\eta = 0.98$ and $\eta = 1.04$. The particle-substrate combination occurs to be sensitive for particle velocities whereas the particle temperature may not be neglected. Considering the tests sprayed with $\eta = 0.89$ and $\eta = 0.98$, an increasing gas temperature results in slightly higher particle velocities and much higher particle temperatures and consequently in an improved particle adhesion, demonstrated by less holes.

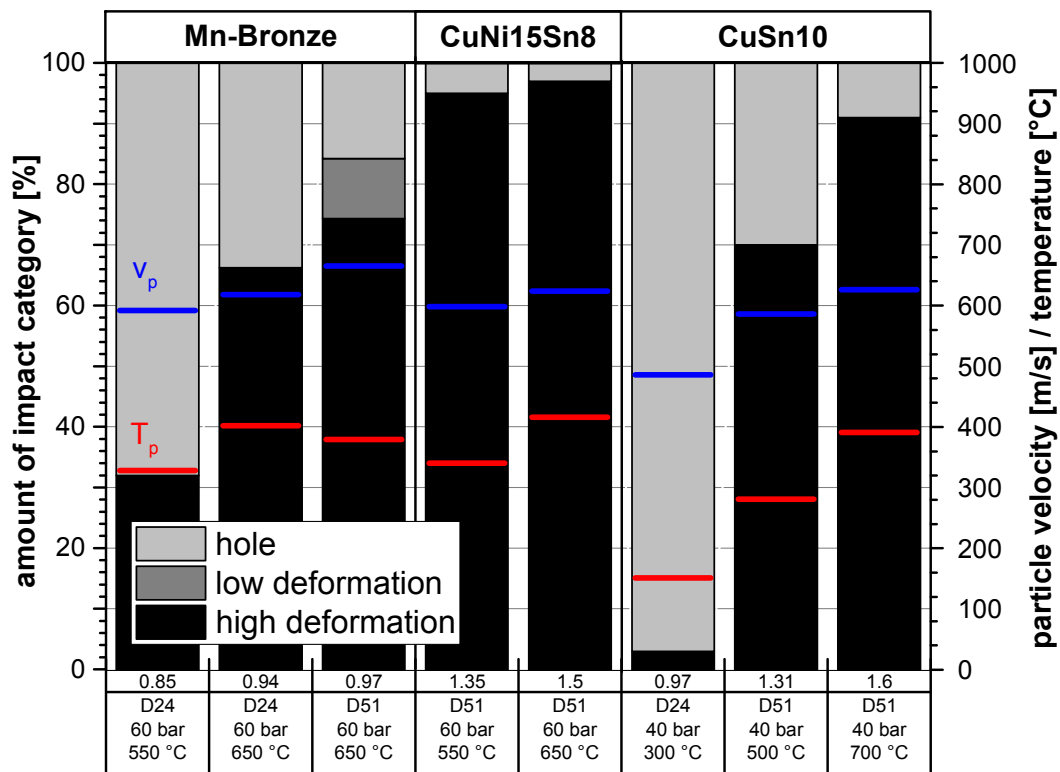


Figure 34: Statistical evaluation of the determined particle impact categories for hard and soft bronze materials sprayed at different cold spray parameter sets.

The statistic evaluation of the MAB, the CuNi15Sn8 and the CuSn10 bronzes are displayed in Figure 34 and are sorted according to decreasing feedstock strength. As for NAB-bronze inputs, also for these materials higher η -values increase the amount of adhering particles (Figure 33). The bronze with lower strength deforms 100 % to category “high deformation”. This might be attributed to the lower strength and higher deformability upon impact. Only the high strength bronze MAB shows particle morphologies of type “low deformation”. When impacting on the hard steel substrate, the softer bronzes decelerate faster and the deformation is more adiabatic than for harder bronze particles.

When comparing the results for different bronzes at similar η -values in Figure 33 and Figure 34, the results vary. It should be noted here that the coating quality parameter η provides information about particle-particle bonding of one material at a given temperature. For the first particles sprayed onto a harder substrate being at ambient temperature, the situation is different, concentrating the deformation mainly to particle sides. Moreover, the description of the critical velocity assumes a close to linear thermal softening behaviour [SCH06A]. If the thermal softening would show anomalies (compare Figure 11), the particle temperature could get a more prominent influence on bonding than the particle velocity [SCH09].

The analyses of the single impact morphologies show that particles of categories “low deformation” and “high deformation” would positively contribute to coating formation. The inhomogeneous deformation behaviour of NAB hard may influence coating formation and thus coating properties. However, the categories and statistical evaluation show that these bronze materials are suitable for cold gas spraying.

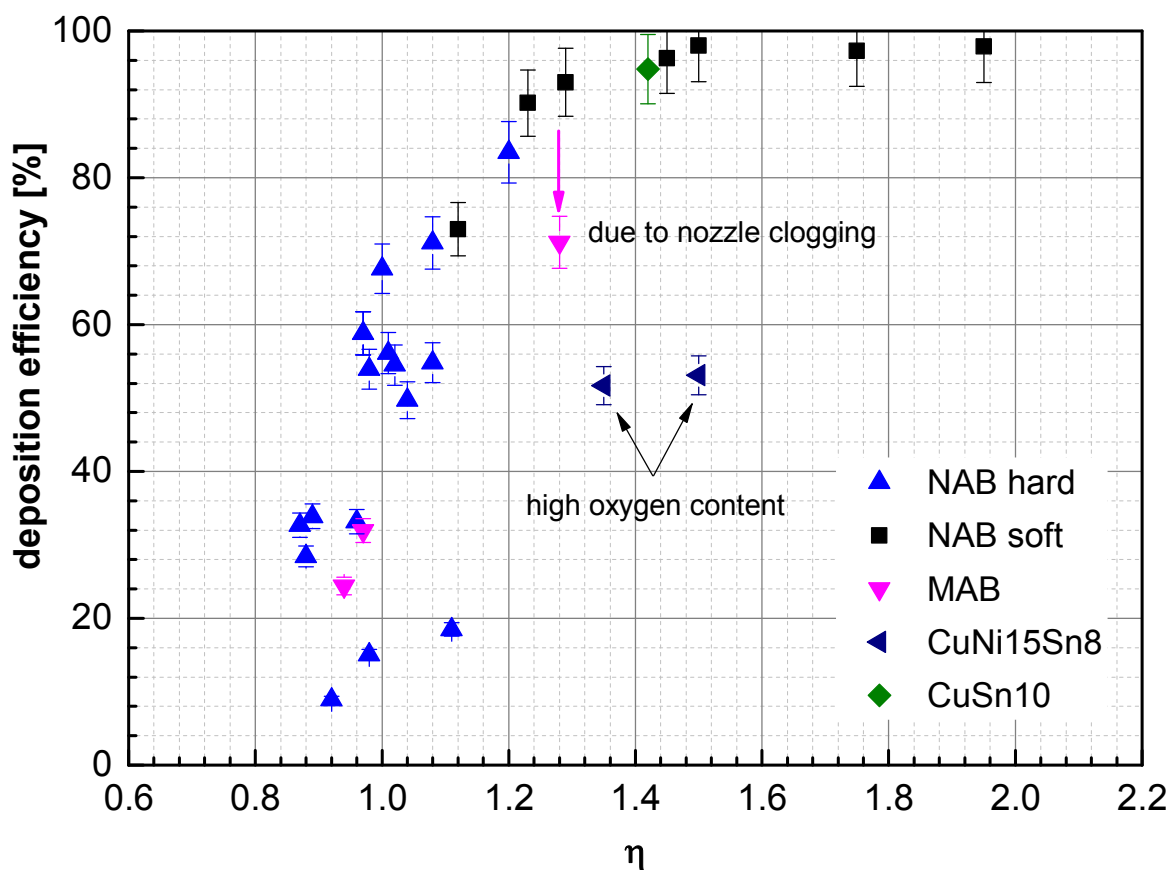


Figure 35: Coating deposition efficiencies of different bronze coatings as a function of the coating quality parameter η .

Figure 35 illustrates the deposition efficiencies during cold spraying of different bronze coatings versus the coating quality parameter η . The results show the expected typical trend with a steep rise at about $\eta = 1$ and a saturation regime at $\eta = 1.2$ [ASS11]. Within this comparison, only the CuNi15Sn8 shows a lower deposition efficiency. This bronze powder contained up to 10-times higher oxygen amounts than the other bronze materials. This increases the critical velocity significantly and thus reduces deposition efficiencies as described in literature [LI09]. Further, Figure 35 also illustrates the decline of deposition efficiency of MAB when the nozzle shape is changed due to nozzle clogging. By lower gas and particle velocities, the real η -value was reduced.

In summary, the results concerning deposition efficiency agree well with the single impact statistics. For similar impact conditions, the coating deposition efficiency correlates well to the amount of adhering particles.

4.3. Coating Microstructures, Phase Compositions and Residual Stresses

Coating microstructures were analysed to determine process influences on particle deformation and cohesion as well as on coating defects like porosity and oxygen content. Additionally, the coating structures and residual stresses were examined.

Figure 36 shows selected coating microstructures as overviews (a-c) and in detail (d-e) of selected cold sprayed NAB hard coatings sprayed with a low (a, d) and a high parameter set (b, e) and a coating sprayed with a high parameter set but onto a pre-heated substrate (c, f).

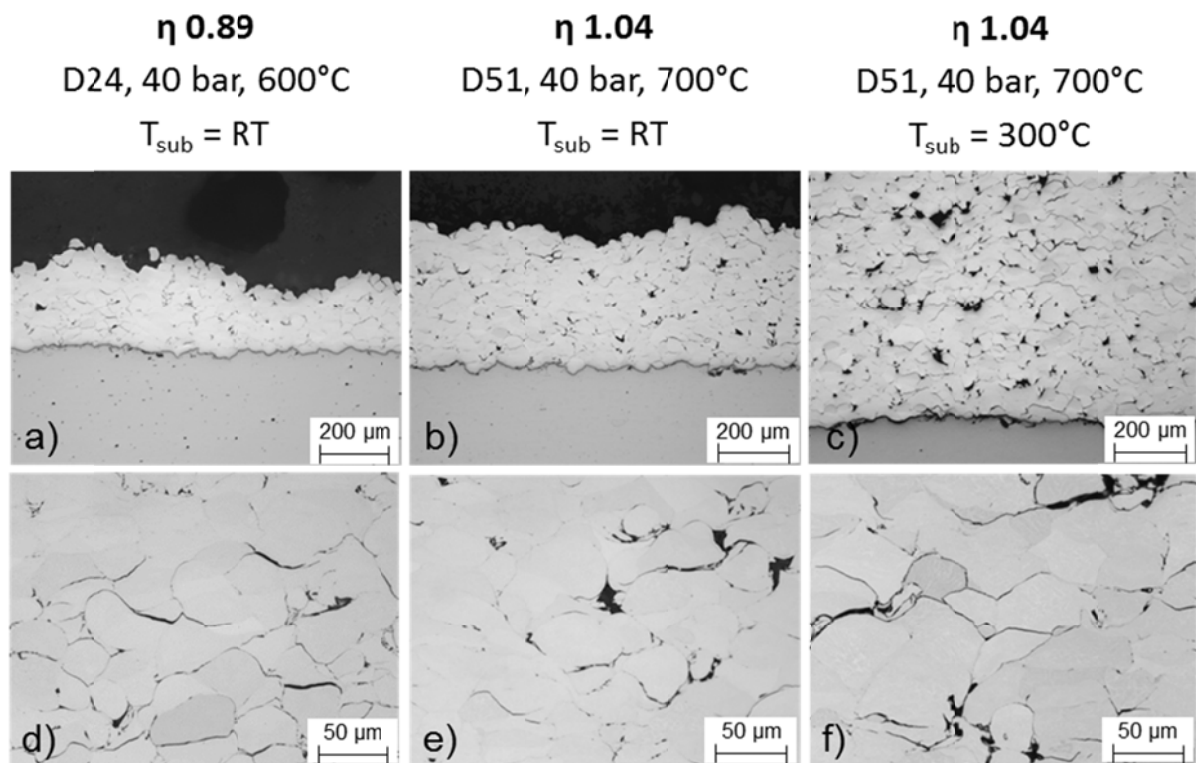


Figure 36: Coating microstructures of cold gas spray NAB hard powder on steel GL-A at different spray parameters and substrate temperatures. The different coating thickness is mainly due to the varied number of spray layers, thus do not correlate to the deposition efficiency.

The coating sprayed with a low spray parameter set has a comparatively rough surface. Within the coating, many non-bonded areas like pores and gaps at particle-particle interfaces can be detected. In addition, the higher resolution in Figure 36d reveals that particles are deformed only to a lower extent and are often surrounded by cracks and gaps around these particles. The interface between coating and substrate appears crack-free, the dark line mainly results from sample preparation due to different wear behaviours. In comparison, the coating sprayed with higher spray parameter shows a less rough surface and slightly less defects like pores and cracks. Particles show slightly more deformation and fewer cracks and non-bonded areas at internal interfaces than those processed at low spray parameter sets.

Nevertheless, porosity is still high. The interface between coating and substrate is similar to that of the low parameter set coating. The coating sprayed on a pre-heated substrate is more porous than the one on not pre-heated substrates, although spraying with the same high parameter sets. Due to thermal softening, the strength of the substrate and already adhering spray layers is lower and allows for larger particles to bond to the substrate or the previous layer. Large and less deformable particles and a lower deceleration upon impact hinder the necessary deformation to close gaps and form a dense coating. Consequently, pores arise and particle-particle cohesion reduces. The coating-substrate interface shows minor gaps, which could arise from residual stresses upon cooling or due to sample preparation.

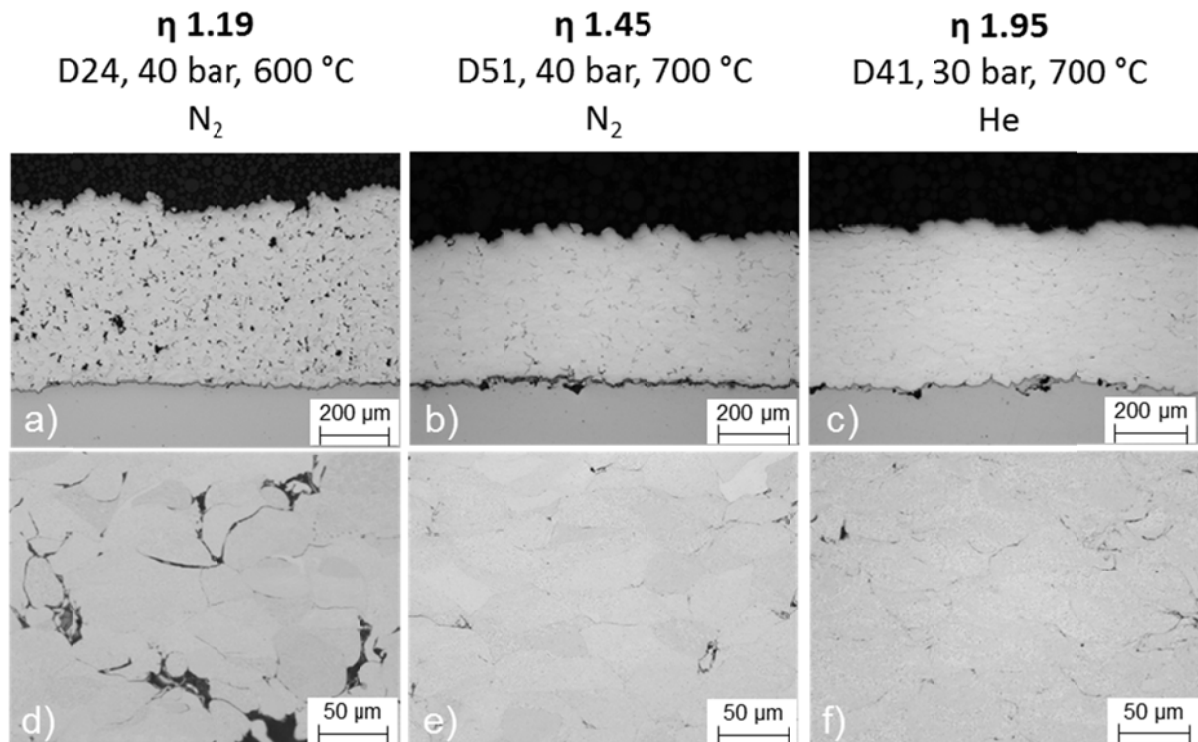


Figure 37: Coating microstructures of cold gas spray NAB soft powder on steel GL-A at different spray parameters.

Similar observations are obtainable in Figure 37 for cold gas sprayed coatings fabricated with the heat-treated NAB soft feedstock powder. Here, the same spray conditions as for NAB hard were realized for this soft powder resulting in higher η -values. For example of using He as process gas, η is much higher. The lower powder strength results in better particle deformation upon impact generating denser and less porous coatings. However, the coating sprayed with low spray conditions ($\eta = 1.19$) still shows pores and non-bonded interfaces. For higher spray parameter sets with nitrogen as process-gas, the coating microstructure becomes almost dense and only minor amounts of pores are observed. The coating-substrate interface shows a larger gap and possibly indicates lower adhesion. Probably, the lower particle strength hinders deep particle penetration into the substrate surface and the formation of shear instabilities on the substrate side. As shown in chapter 4.2, impacting particles of low strength bronze powders can barely deform the substrate and thus shear instabilities occur mainly on particle side. On rather rigid substrates, adiabatic shear instabilities on particle sides to high content might not be in contact to the substrate, thus not contribute to adhesion [ERN13]. When using highest spray conditions with helium as process gas (Figure 37c and f), the coating appears dense and does not show any defects like pores or non-bonded areas.

The cold-sprayed coatings of the high strength MAB and the low strength CuNi15Sn8 and CuSn10 bronzes were optimized regarding their microstructure and porosity by tuning the spray parameter sets for each bronze powder as well as by adjusting the substrate temperature. An overview about selected and optimized microstructures of the bronze coatings sprayed with the highest possible η -value on pre-heated substrates is shown in Figure 38. In comparison to NAB hard, the high strength MAB shows fewer pores and more bonded particle-particle interfaces. Nevertheless, various cracks and non-bonded interfaces are visible within the microstructure. These cracks spread mainly parallel to the coating surface along marginal deformed particles. Coatings on the basis of better deformable feedstock powders (CuNi15Sn10 and CuSn10) show very few cracks and denser microstructures. The interfaces between substrate and coatings show almost no cracks or non-bonded areas thus indicating good adhesion. Spraying these coatings on non-pre-heated substrates (not shown), resulted in large detached areas by poor adhesion (not shown).

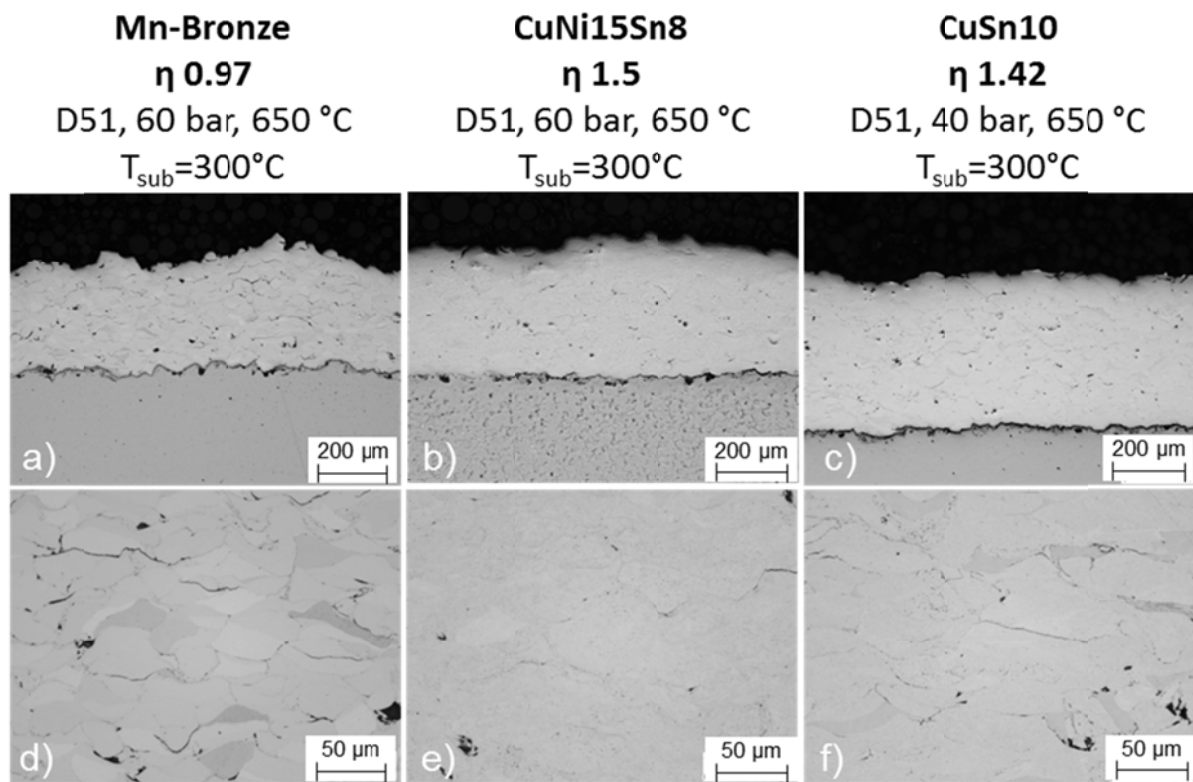


Figure 38: Microstructures of different cold gas sprayed bronze coatings. The micrographs show results of coating sprayed at optimized spray conditions (highest possible η , use of on pre-heated substrate)

As compared to the feedstock powder, the cold sprayed coatings showed only a minor gain in oxygen content during the spray process. The oxygen content of the cold gas sprayed NAB and CuSn10 coatings rose from 240 – 410 ppm (powder) to 700 – 900 ppm (coating). The CuNi15Sn8 bronze oxygen content rose from 2000 ppm to 4500 ppm. For all these results, no significant trend between spray parameters sets and impurity content could be identified.

The condensed results of the porosity measurements as a function of the coating quality parameter η are summarized in Figure 39. The experimental data show that all non-martensitic coatings (NAB soft, MAB, CuNi15Sn8 and CuSn10) reveal a clear trend with respect to η . High parameter sets result in lower porosities due to improved particle

deformability. Enhanced kinetic and/or thermal particle impact energies allow to close gaps and to decrease porosity. Only the martensitic and thus hardly deformable NAB hard coatings show high scatter of the porosity data between 0.2 to 4.8 % for $\eta \sim 1.0$. Here no explicit trend can be determined.

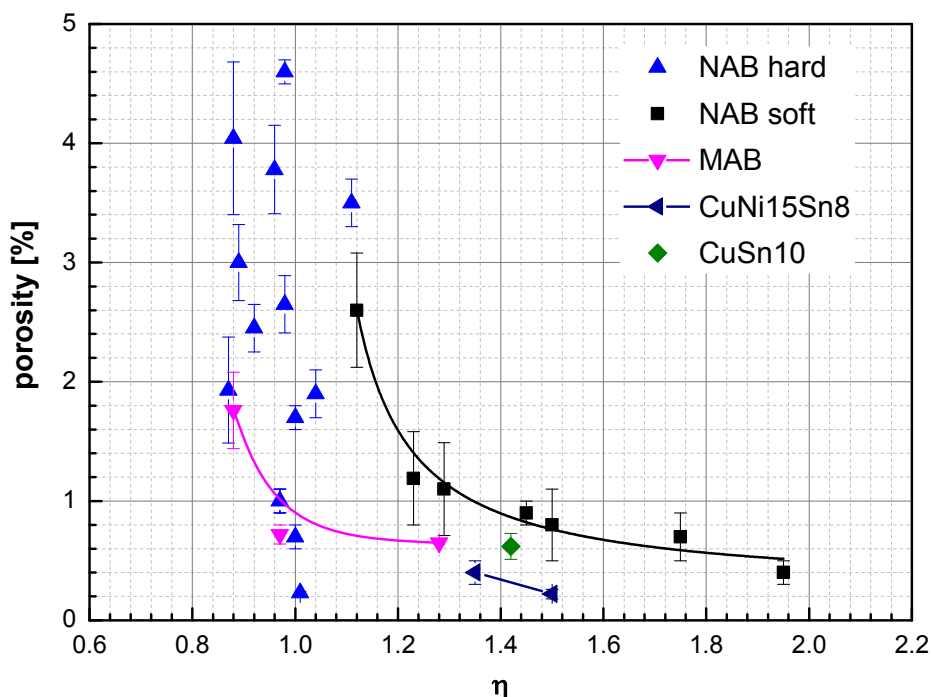


Figure 39: Coating porosity as a function of the coating quality parameters η showing a clear trend for non-martensitic bronze coatings. Only the martensitic NAB hard coatings show typical scatter at η -values around 1.

Besides microstructural investigations, XRD-analysis were used to determine the phase composition of the bronze coatings in comparison to that of the feedstock powder. In addition, XRD was employed to investigate macro-stresses of the different coatings.

Figure 40 compares the XRD-pattern of the NAB hard and NAB soft powder with corresponding cold-sprayed coatings. The selected patterns of the coatings are representative for all cold sprayed coatings; the different spray conditions did not reveal any alterations except stress related peak shifts. The residual stresses were analysed and are considered subsequently in the following section. The XRD-pattern of the NAB hard powder (bottom) illustrates that the powder contains, besides the α -phase, martensitic- and γ_2 -phases. By cold spraying, the peaks of the α -phase widen due to the formation of dislocations and structural failure and shift to the left due to residual (compressive) stresses. The martensite and γ_2 peaks almost disappear and only minor, fairly broad peaks of these phases remain detectable. In contrast, the NAB soft powder with no martensite, retains its structure and shows no phase transformation. Only a peak widening and slight shift to lower angles can be observed. More details will be discussed in the discussion in chapter 4.8.3.

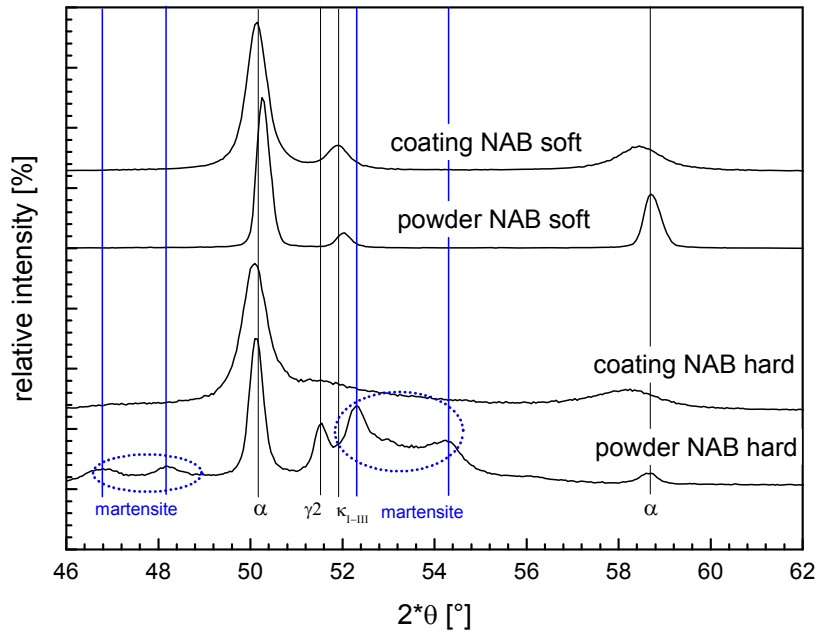


Figure 40: XRD-pattern of the NAB coatings sprayed with as-atomized hard and 7 h annealed NAB soft powder in comparison to the pattern of the feedstock powder. The XRD-pattern of as-atomized powder reveals a phase transformation by cold spraying from martensitic- and Y2-structure to the α -phase. Differences between the various spray parameter sets were not distinguishable.

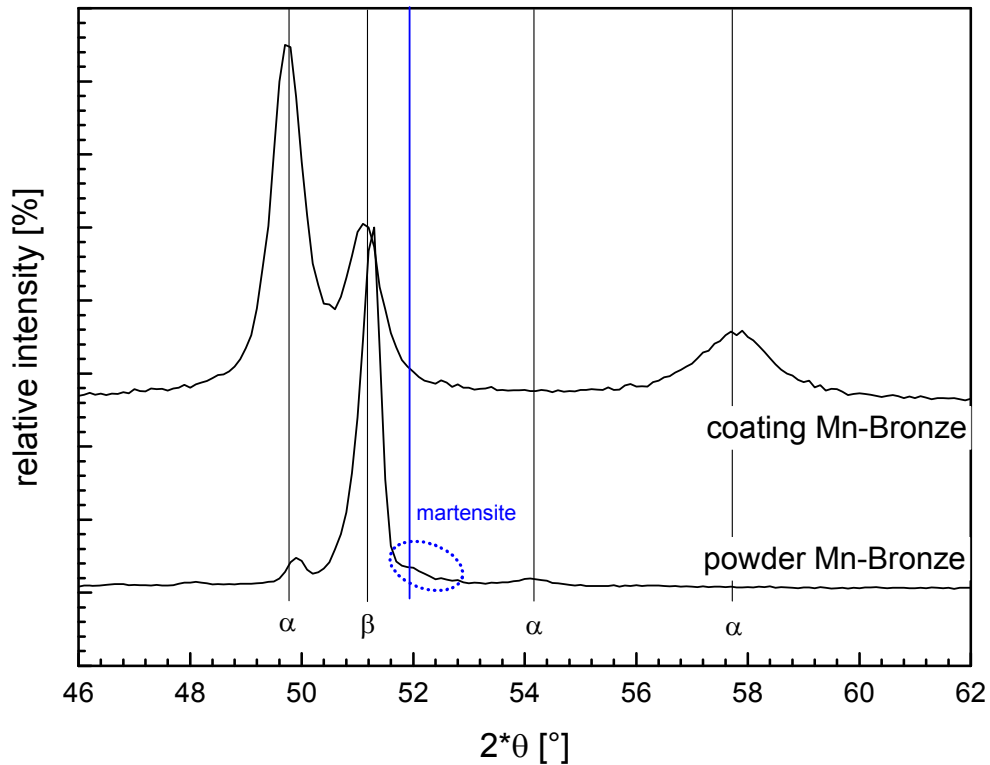


Figure 41: Comparison of XRD-pattern of the feedstock powder and cold sprayed MAB coatings. The powder transforms during cold gas spraying from mainly bcc (β) to fcc (α) phases.

Figure 41 shows the XRD-pattern of the MAB as feedstock powder and the respective cold sprayed coating. The feedstock powder contains mainly cubic body-centred β -phases and minor contents of martensite. By cold spraying, the amounts of β -phases are reduced by the transformation to the cubic face-centred α -structure. The martensitic phases vanish by cold spraying. As for the NAB-feedstock, peak widths of coatings are broader than those of the powder and by macro-stresses show shifts to lower angles.

The XRD-pattern of the martensite-free bronzes CuNi15Sn8 (a) and CuSn10 (b) are displayed in Figure 42. The comparison between the as-atomized powder and the coating phase composition shows that no phase transformation occurs. The differences only concern peak broadening and shifts to lower angles.

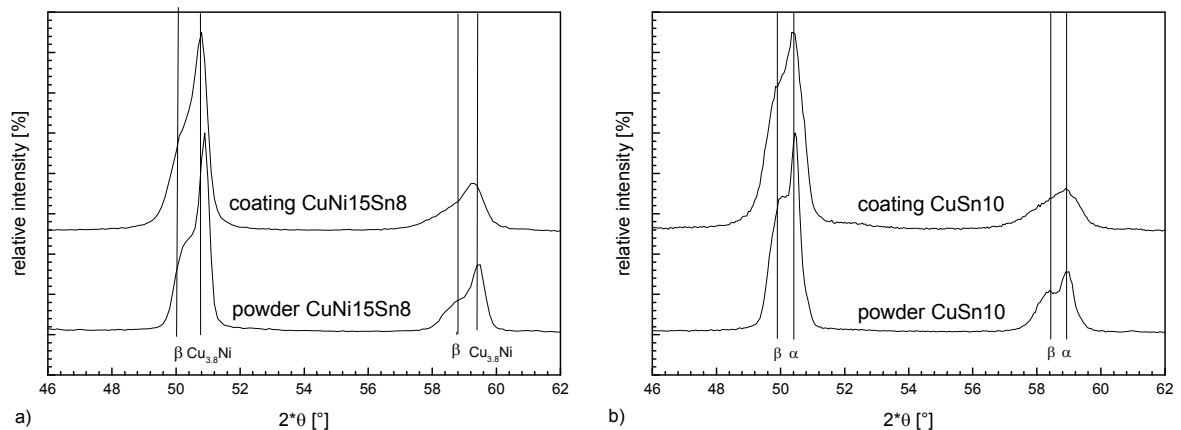


Figure 42: XRD-pattern of a) CuNi15Sn8 and b) CuSn10 showing no phase transformation but peak widening due to a high degree of deformation.

The residual stresses were analysed by evaluating the peak shift of the XRD-pattern by sample tilting. Figure 43 relates the residual compressive stresses of the cold sprayed bronze coatings towards the coating quality parameter η . The relation indicates a clear trend that increasing η -values reduce the compressive residual stresses. Although the particles deform to a higher extent and thus compressive stresses arise, also more heat is generated at higher impact conditions. This allows for reducing the mechanical stresses probably due to local recrystallization effects. Furthermore, it must be considered that the measurements result from superimposing mechanical and thermal effects. The latter is attributed to the thermal mismatch of the thermal expansion ratios between the bronze coating and the steel substrate.

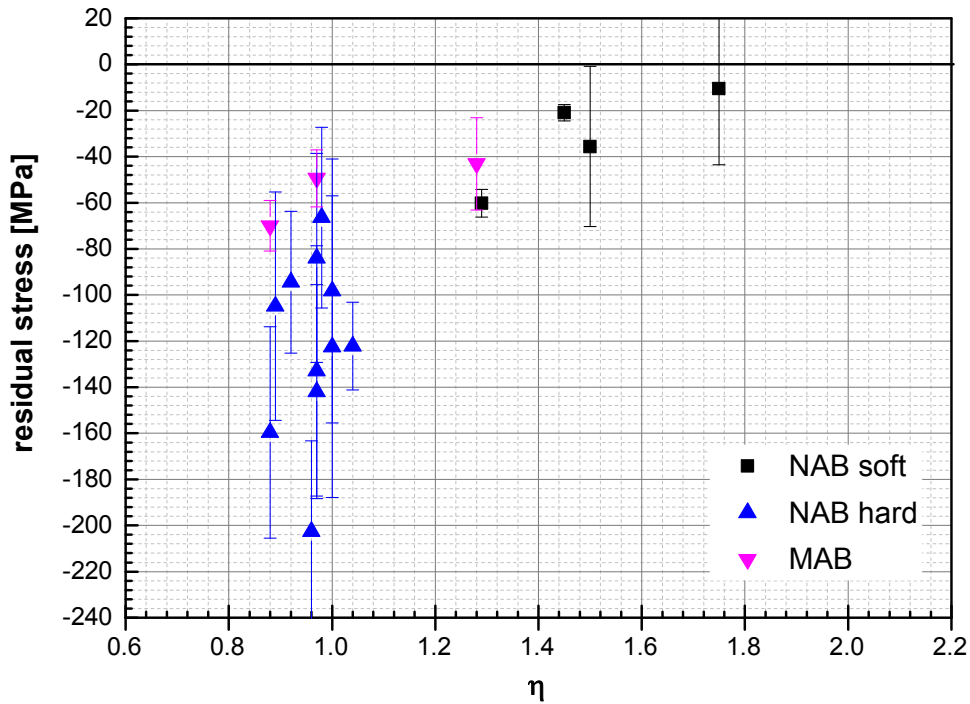


Figure 43: Residual stresses of cold sprayed coatings as a function of the coating quality parameter η . The figure shows that the compressive stresses can be reduced when the spray parameter with respect to particle impact velocity and temperature increases.

Figure 44 highlights the influence of pre-heated substrates on coating residual stresses. The figure illustrates that instead of the compressive stress at room temperature substrates, tensile stresses are formed in coatings on pre-heated substrates. These original residual mechanical stresses reduce due to a substrate temperature above the recrystallization temperature of 240 °C. It might be that less deformation by spraying with lower η -values result in higher recrystallization temperatures, and thus not complete recrystallization at given substrate/coating temperatures. After complete recrystallization, the remaining stresses would derive from the thermal mismatch of substrate and coating [ARA13].

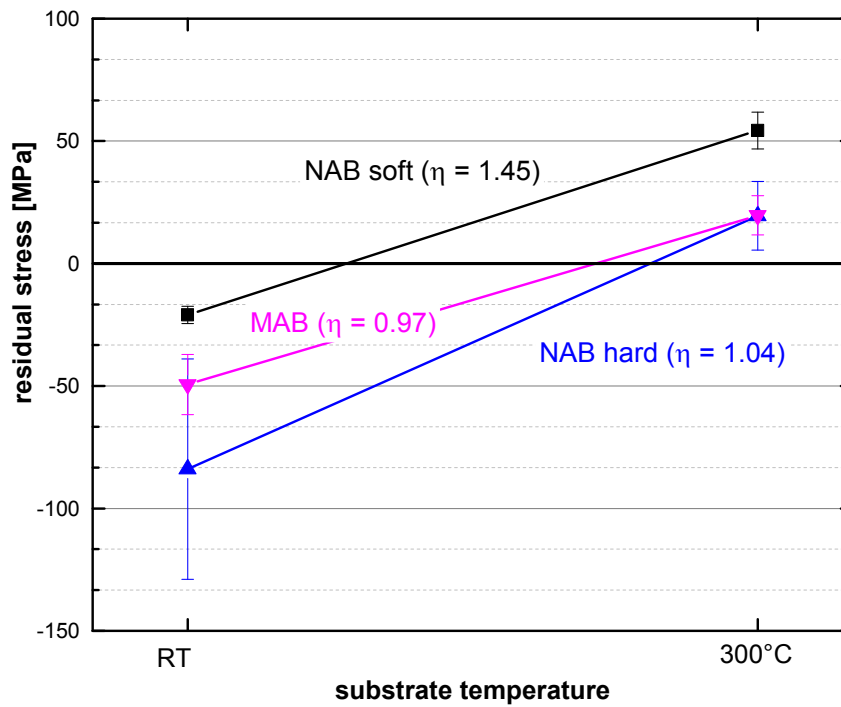


Figure 44: Residual stress of the coatings sprayed with similar spray conditions for each bronze but on pre-heated and non-pre-heated substrates.

4.4. Mechanical and Electrical Properties

The mechanical and electrical properties provide direct information on coating integrity, the different methods being sensitive on individual defects. Hardness measurements record the resistance against compression, being sensitive on porosity. Electron mobility and thus electrical conductivity is affected by all sorts of defects, but most prominently on non-bonded interfaces. The coating strength is mainly dependent on joint interfaces, means bonded interfaces. In the following respective results from different methods are illustrated to supply more information on influences for optimizing coating quality.

Figure 45 gives an overview about coating hardness of the cold sprayed bronze coatings as a function of the spray conditions on the basis of the coating quality parameter η . The results show that coating hardness ranges within a narrow regime between 260 HV0.3 and 400 HV0.3. Maximum attainable coating hardness roughly scales with the strength of the feedstock powder (compare Figure 24) or hardness. Accordingly, the low strength bronze CuSn10 coating has the lowest hardness within the comparison. Furthermore, the coating hardness for the different spray powders rises with increasing η -values. Only the as-atomized and martensitic NAB hard coatings do not show an obvious trend and illustrate a wide hardness range from 280 HV0.3 to 380 HV0.3 at comparable η -values at about 1. The increase of hardness with spray conditions can be explained by reduced porosity.

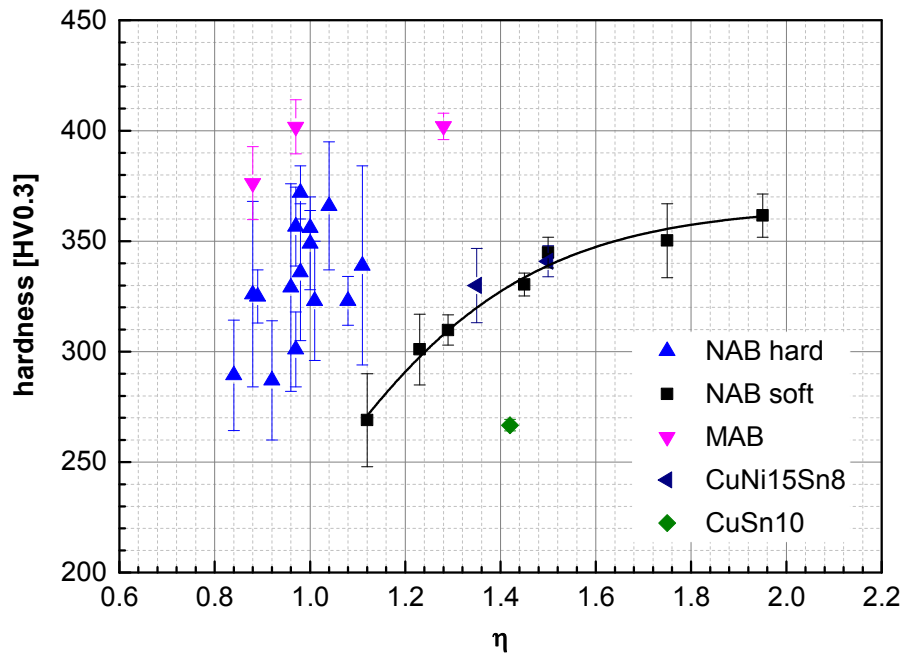


Figure 45: Overview about the coating hardness on the basis of the coating quality parameter η showing a clear trend for bronze materials, except the NAB hard coatings.

Figure 46 shows the results concerning coating tensile strength as obtained by TCT (a) and MFT (b) tests. Both diagrams illustrate coating strength as a function of the coating quality parameter η and indicate a rising strength with increasing η for NAB soft, CuNi15Sn8 and CuSn10. The trends of these three bronze types are comparable. In contrast, the martensitic NAB hard bronze does not offer any clear correlation within the rather narrow regime of η -values about unity. The results demonstrate that coating cohesion, means amounts of bonded areas, is rather constant at η -values about unity. A significant improvement can be obtained for $\eta > 1.2$. However, comparing the TCT and MFT results, TCT strength is unexpectedly higher than the ultimate tensile strength measured by MFT. Probably higher effective surface temperatures at TCT-tests may improve bonding and heal poorly bonded particle-particle interfaces and consequently enhance coating strength.

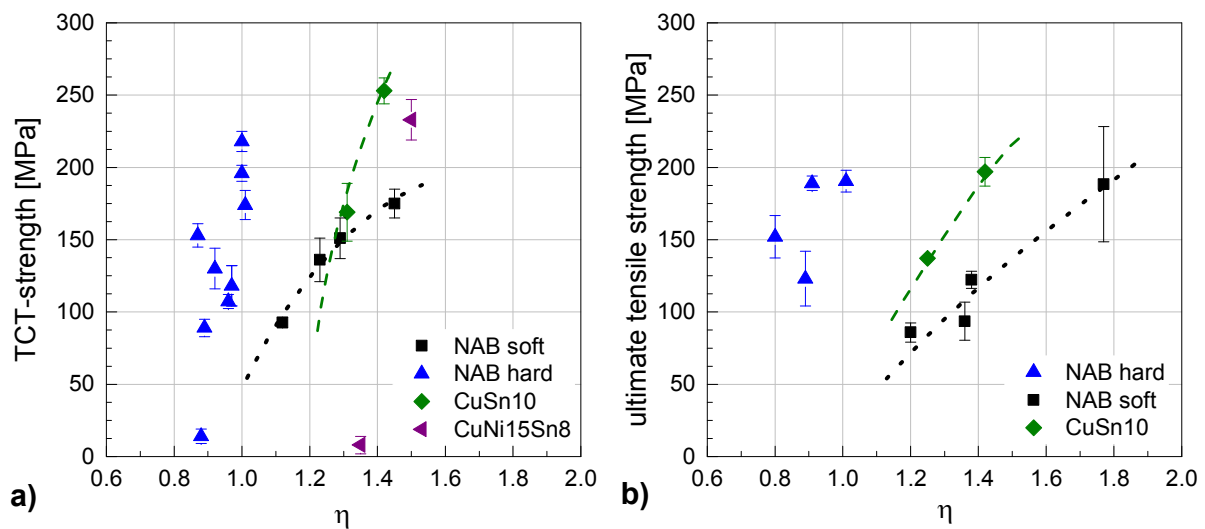


Figure 46: Overview about the cohesive coating properties measured as TCT-strength (a) and ultimate tensile strength (b). For TCT-test results the original data without a notch factor was used.

The measurement of the electrical conductivity provides information about coating integrity. This means that the electrical conductivity allows for summarizing the influences of several sorts of coating defects as porosity, non-bonded interfaces, cracks and oxides as well as impurity contents or dislocation densities. Low porosity and enhanced cohesion improve coating integrity and thus electrical conductivity. In contrast, high oxide contents decrease the electrical conductivity. Figure 47 summarizes the measured relative electrical conductivities as a function of η . The results show a clear trend that higher η values reduce the amount of defects and thus improve coating integrity. A saturation regime can be achieved for $\eta > 1.6$ for NAB soft, CuNi15Sn8 and CuSn10. Trends for MAB are shifted to lower η -values, reaching saturation at $\eta = 1.4$. NAB hard coatings show the typical scatter, expected for conditions at $\eta \sim 1$.

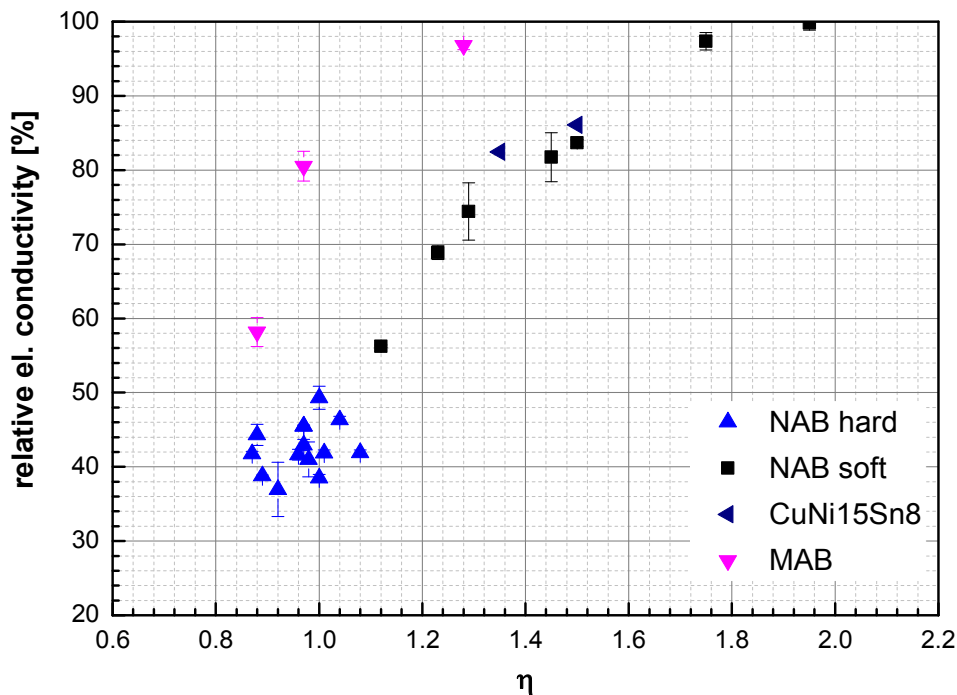


Figure 47: Electrical conductivity as a function of the coating quality parameter η of the cold sprayed bronze. The data are normalized to conductivities of respective bulk material.

4.5. Single Particle and Coating Adhesion

Investigations on adhesion were performed on single particles and on coatings. Single particle adhesion was tested by using the cavitation test. For providing quantitative data, the amount of adhering particles was statistically evaluated and determined after defined time intervals. The results are summarized in Figure 48 and show the particle loss as a function of the cavitation time for each bronze type and for different spray parameters sets. The different spray conditions are displayed in terms of η and of substrate pre-heating. The results show that all bronze powder impacts except for the NAB soft show clear correlations with the spray conditions. Higher spray parameter sets result in better adhesion. The adhesion is improved by substrate pre-heating. The differences might be explained by the complex interplay between particle and substrate deformation, and amounts of bonded areas by shear instabilities.

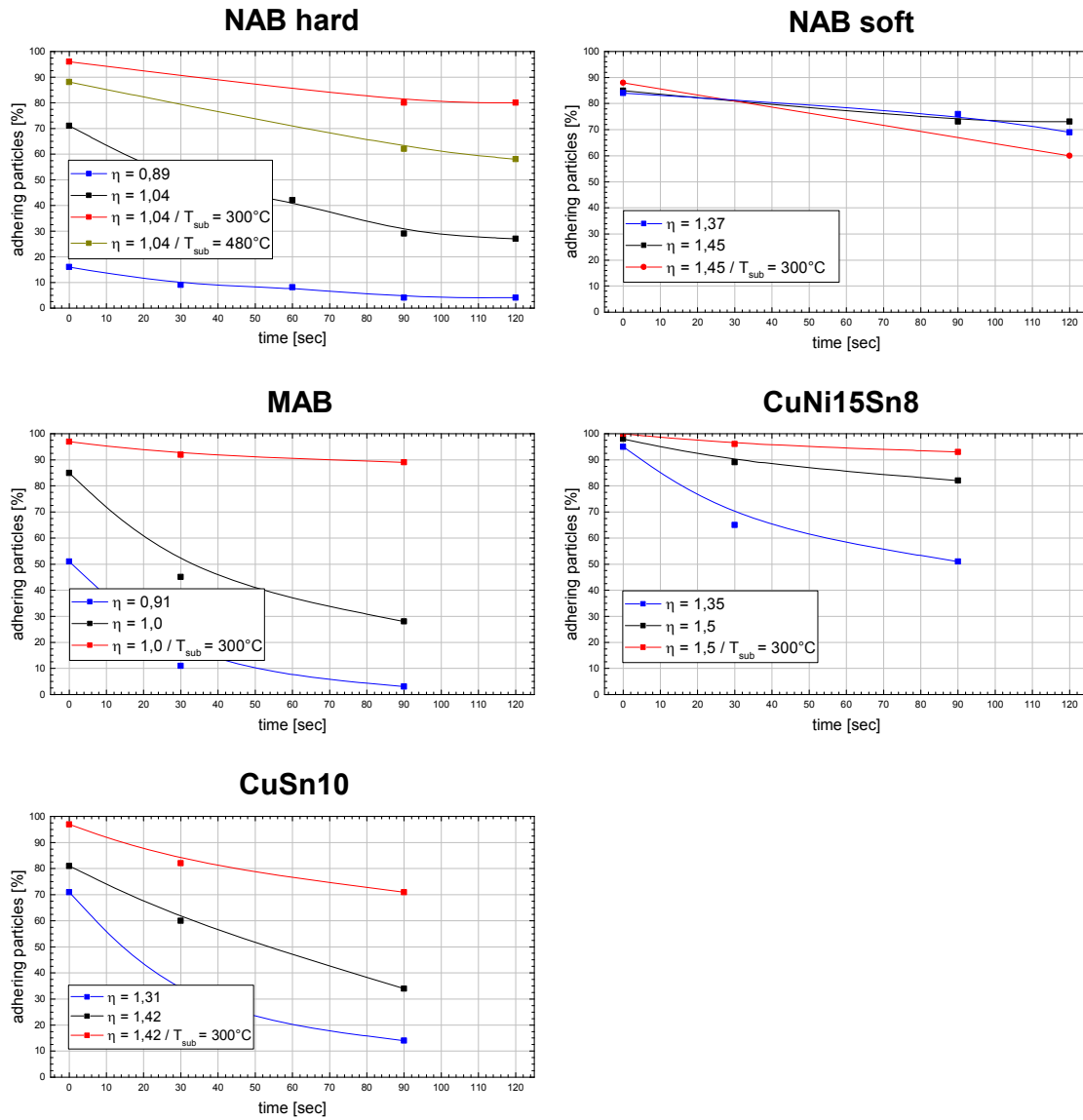


Figure 48: Amount of adhering particles after cavitation treatment showing increased adhesion when particles are sprayed with higher parameter sets with respect to η and on to pre-heated substrates. Only the cold-sprayed NAB soft particles show no remarkable influence by spray conditions.

The results of the coating adhesion test are merged in Figure 49 and show the relation between coating adhesion and the coating quality parameter η . The bond strength values vary between about 5 and 30 MPa. The martensitic NAB hard shows again the high scatter in properties around $\eta = 1,0$, whereas the bond strength of the NAB soft improves with increasing η -values. The NAB soft coating sprayed with helium as process gas shows a lower adhesion than expected. The low bond strength of CuSn10 coating could be due to marginal substrate deformation and thus shape adoption by this rather soft powder. However, the adhesion results should be considered carefully due to influences by the substrate roughness and temperature. In addition, the coating quality parameter η assumes similar strengths of powder and underlying material upon impact. For applying the first spray layer on cold substrates with different properties, no uniform η can be defined for providing an estimate for bonding quality at the interface. Moreover, during the spray experiments several cold sprayed coatings partly or completely detached from the adhesion test samples due to residual stresses during and after spraying. As for single particle events, spraying onto pre-heated substrates might enhance coating adhesion.

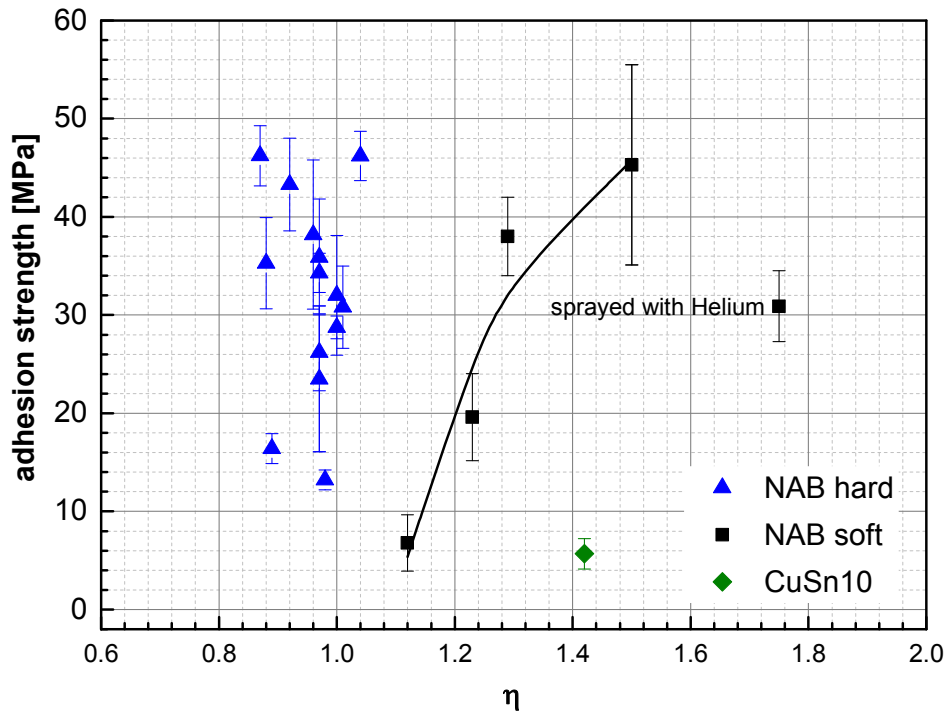


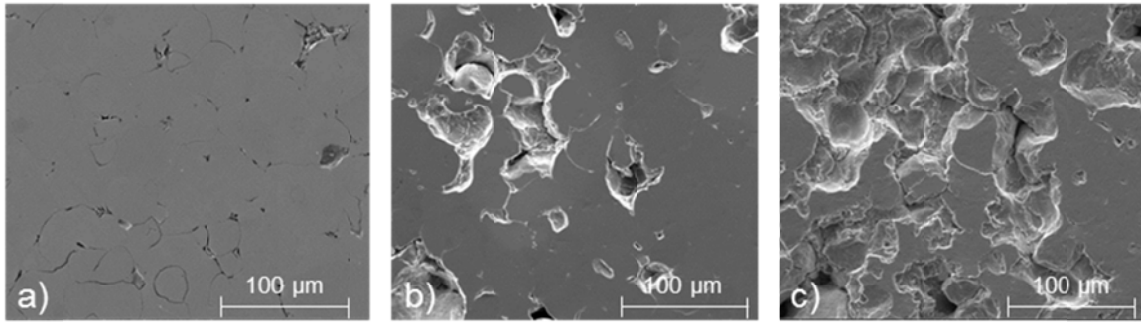
Figure 49: Results of the coating adhesion test plotted as a function of the coating quality parameter η for different bronze types.

4.6. Cavitation Behaviour

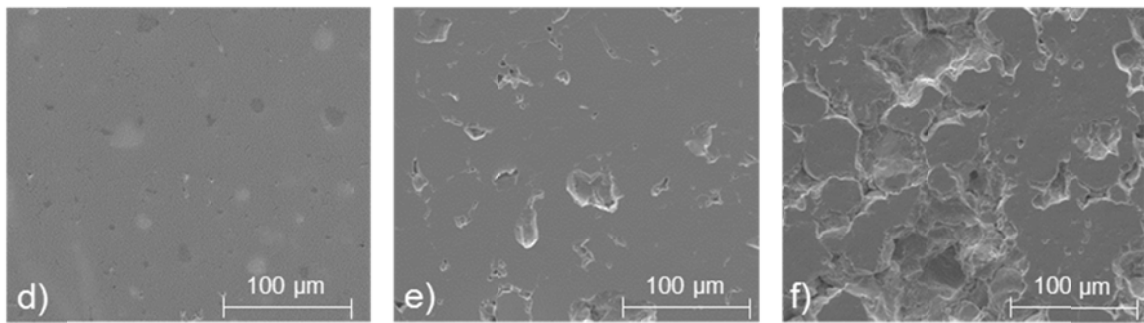
Cavitation erosion was tested in accordance with ASTM G32-10 by using the indirect method. Failure topographies of the cold sprayed bronze coatings were analysed by SEM. Here, after 0 min, 3 min and after 100 min cavitation treatment, the previously polished surface was examined at the same position. Respective surface morphologies are summarized in Figure 50, Figure 51 and Figure 53 for the different bronze types and under diverse spray conditions.

Selected surface morphologies of the NAB hard coatings are shown in Figure 50a to f, showing the failure topographies for cold spraying with a low and a high parameter set after different times of cavitation testing. The coating surface morphology of the coating processed at the low parameter set in Figure 50a in the initial condition shows several pores and non-bonded areas between single particles as indicated by dark rims around these particles. After 3 min of testing (Figure 50b), half-moon shaped particle fractions are removed, probably due to damages by the surface preparation. The non-bonded interfaces at particle-particle boundaries seem to act as crack nuclei. After 100 min cavitation testing (Figure 50c), the surface roughness increases, but still some originally polished surface areas are detectable. At that stage, whole particles seem to be removed from the coating. The bonded interfaces reveal mainly brittle failure and almost no areas of plastic deformation with vain-pattern can be found, details are not shown here. The coating processed with higher spray conditions (Figure 50d, e, f) indicates less non-bonded areas and pores in the as-sprayed state and less particle removal after 3 min of testing. Moreover, as compared to low parameter sets, after 100 min of testing, a higher amount of polished surfaces remains. At areas of removed particles, to some extent vain-pattern due to plastic deformation can be detected. Nevertheless, the main damage mechanism still occurs by the removal of weak bonded particles.

η 0.89 D24, 40 bar, 600°C, $T_{\text{sub}} = \text{RT}$



η 1.04 D51, 40 bar, 700°C, $T_{\text{sub}} = \text{RT}$

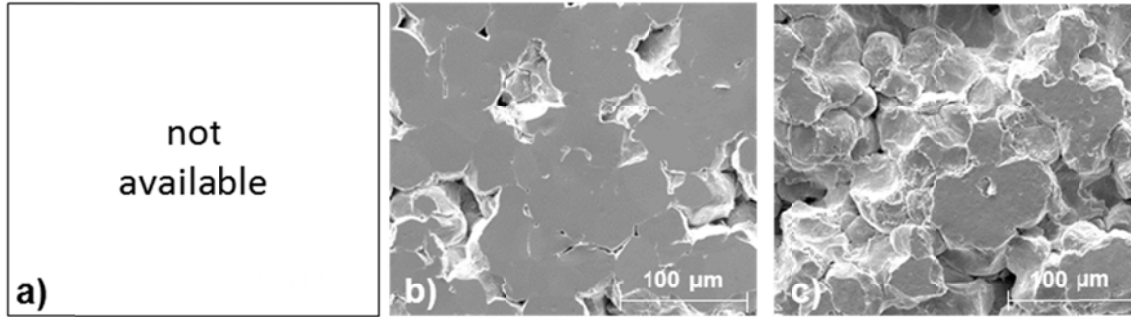


0 min \longrightarrow **3 min** \longrightarrow **100 min**

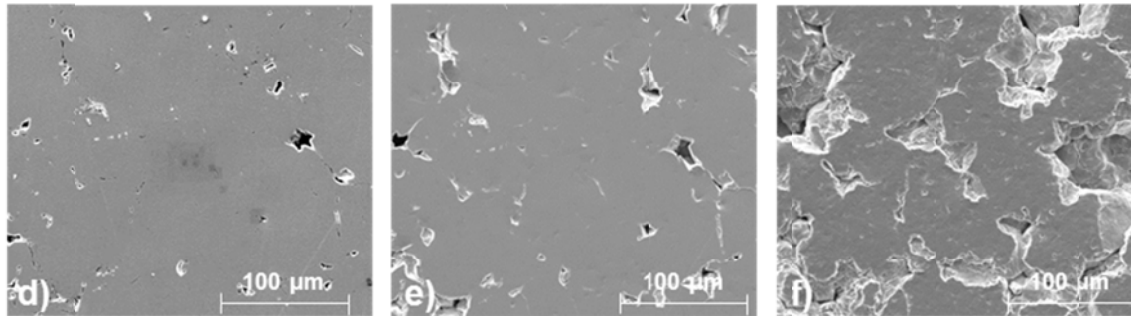
Figure 50: Surface morphologies after different times of cavitation treatment of cold gas sprayed NAB hard coatings.

The cavitation damages of the cold sprayed NAB soft coatings are displayed in Figure 51. From the coating sprayed with the lowest η -value of $\eta = 1.12$ mainly whole particles are detached after cavitation times of 3 and 100 min. In contrast to NAB hard, some areas with vein -pattern by plastic failure are apparent. This indicates better bonding at particle-particle interfaces. Nevertheless, as compared to NAB hard, the higher surface roughness indicates worse cavitation performance. For coatings sprayed with higher parameter sets, the cavitation mechanism changes. Before testing, several cracks and pores are detectable (Figure 51b) that might seem to act as crack nuclei. But after 3 min of testing, only particle fractions are removed. After 100 min of testing, still a high amount of the polished surface remains. Only to some extent whole particles are removed in contrast to NAB hard and lower spray conditions. For the coating sprayed with highest spray condition with helium as process gas (Figure 51c, f, i), only very few material is removed from the surface. After 100 min of testing, material is removed at local sites, similar to fatigue failure of bulk material.

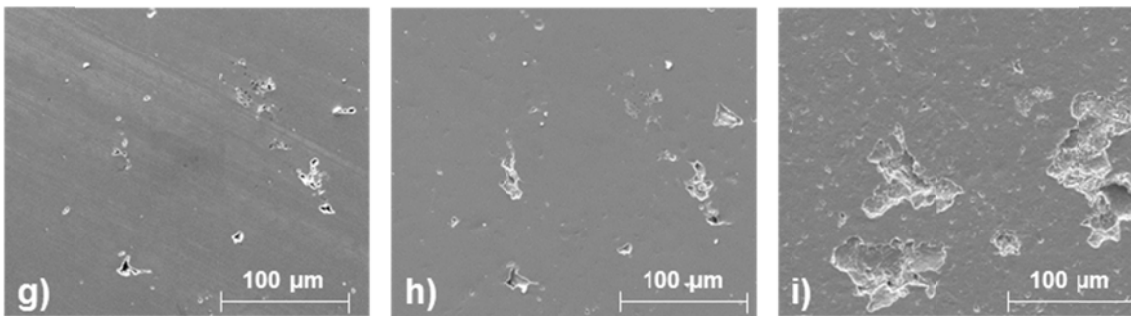
η 1.12 D51, 40 bar, 500°C, Nitrogen



η 1.45 D51, 40 bar, 700 °C, Nitrogen



η 1.75 , D24, 30 bar, 650°C , Helium



0 min 3 min 100 min

Figure 51: Surface morphologies of cold gas sprayed NAB soft coatings after 100 min cavitation treatment with increasing spray parameters the surface damage mode changes from single particle removal towards localized fatigue failure of the bronze material. Especially, the coating sprayed with helium as process gas shows almost bulk like appearance.

Cross sections reveal more details on crack formation and material removal as shown in Figure 52 for cold sprayed NAB soft coatings sprayed with $\eta = 1.45$ and $\eta = 1.75$. The cross-sections compare the initial state (a, d) with that after 100 min of testing (b, c, e, f). The coating sprayed with $\eta = 1.45$ shows some cracks between particle-particle interfaces and few pores. During cavitation testing, failure promotes along weakly bonded particle-particle interfaces parallel to the surface and results in cracks. Some areas suffer from more material removal than others and show increased surface roughness. In the initial state, the coating sprayed with the high $\eta = 1.75$ parameter shows almost no pores or coating failures. Consequently, the cavitation exposure does not cause inter-particle failure by massive cracks. Coating damage is mainly due to trans-particle crack growth and thus fatigue properties of the coating material.

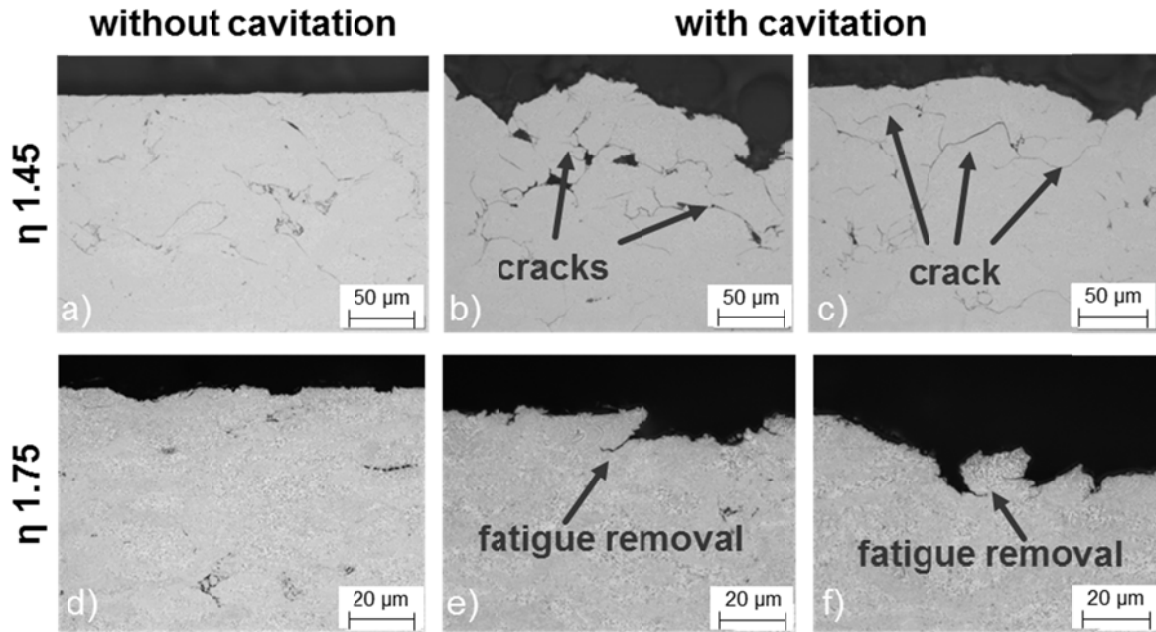
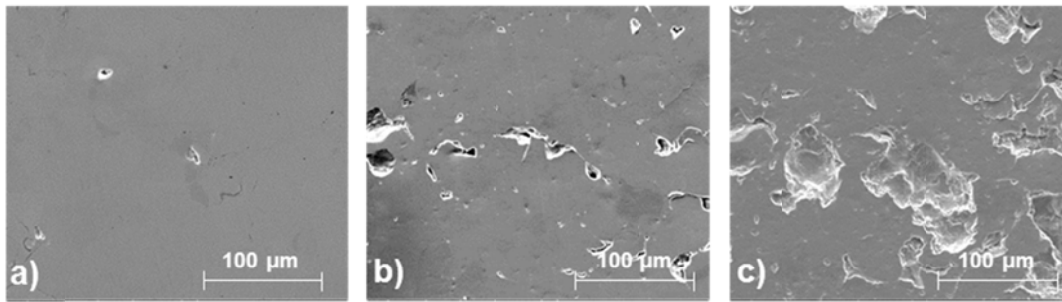


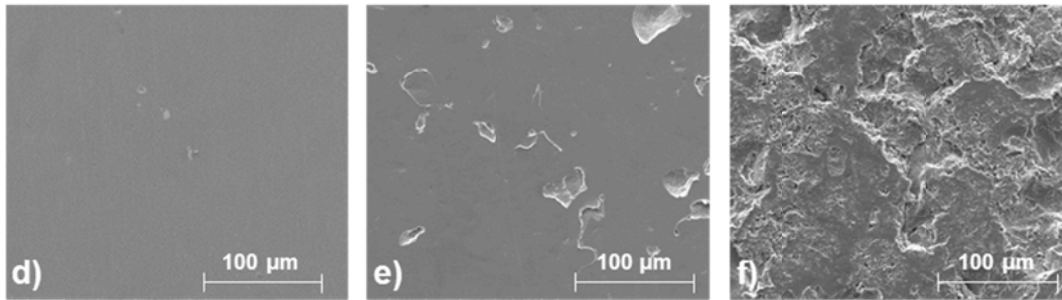
Figure 52: Cross-sections of cold sprayed NAB soft coatings in the initial state and after 100 min of cavitation treatment. The coating sprayed with a low spray parameter set ($\eta = 1.45$) shows crack formation parallel to the surface and mainly at particle-particle boundaries. In contrast, the coating sprayed with the high spray parameter set ($\eta = 1.75$) shows almost no inter-particle cracks. Here material removal occurs by trans-particle crack growth, similar to fatigue damage of bulk material.

Apart from NAB hard and NAB soft coatings, also the cavitation performance of the high strength MAB and the low strength CuNi15Sn8 and CuSn10 bronze coatings were analysed. The comparison in Figure 53 considers the coatings sprayed with the highest parameter sets on pre-heated substrates. The MAB coating shows comparable damage failures, as the cold sprayed NAB hard coatings, with mostly removal of whole particles but to lesser extent. In contrast, the low strength coatings show plastic deformation on the polished surfaces already after 3 min of testing with a wavelike morphology by impacting water jets. In addition, localized material loss occurs at particle-particle boundaries. During 100 min of testing, material is removed by detaching whole particles over inter-particle rupture and very local, mainly ductile, trans-particle failures, similar to fatigue damages. The slightly harder CuNi15Sn8 bronze demonstrates better cavitation performance than the CuSn10 bronze.

MAB η 0.97, D51, 50 bar, 650 °C, $T_{\text{sub}}=300^\circ\text{C}$



CuNi15Sn8, η 1.5, D51, 50 bar, 650 °C, $T_{\text{sub}}=300^\circ\text{C}$



CuSn10, η 1.42, D51, 40 bar, 650 °C, $T_{\text{sub}}=300^\circ\text{C}$

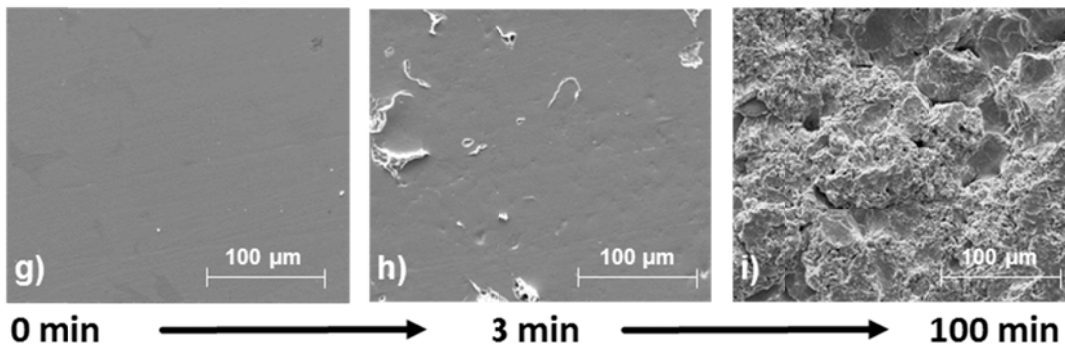


Figure 53: Surface morphologies of different bronze materials cold-sprayed with optimized conditions (η) on pre-heated substrates after 100 min of cavitation treatments. For decreasing powder strength and thus increasing η -values from MAB to CuSn10, the cavitation mode changes from single particle removal towards localized failures.

Figure 54 summarizes the cavitation erosion rates of the different cold sprayed bronze coatings over η . As reference, also cavitation rates of bulk (cast) NAB as well as of the steel GL-A substrate are given. The results demonstrate that higher η -values result in improved cavitation resistance and thus lower cavitation rates. When comparing the different bronze materials, NAB hard, does not follow the mentioned trend and reveals a high scatter around $\eta = 1$. The NAB soft, the MAB and the CuNi15Sn8 bronze coatings show similar trends whereas the absolute values correlate with the feedstock strength. For higher feedstock strength, lower cavitation rates are obtained at similar η -values. The MAB coatings shows already good performance at low η -values. All sprayed coatings offer an already better cavitation resistance than the steel substrate. At high spray parameter sets, MAB and NAB soft coatings reach almost a similar cavitation resistance as the cast NAB bulk material.

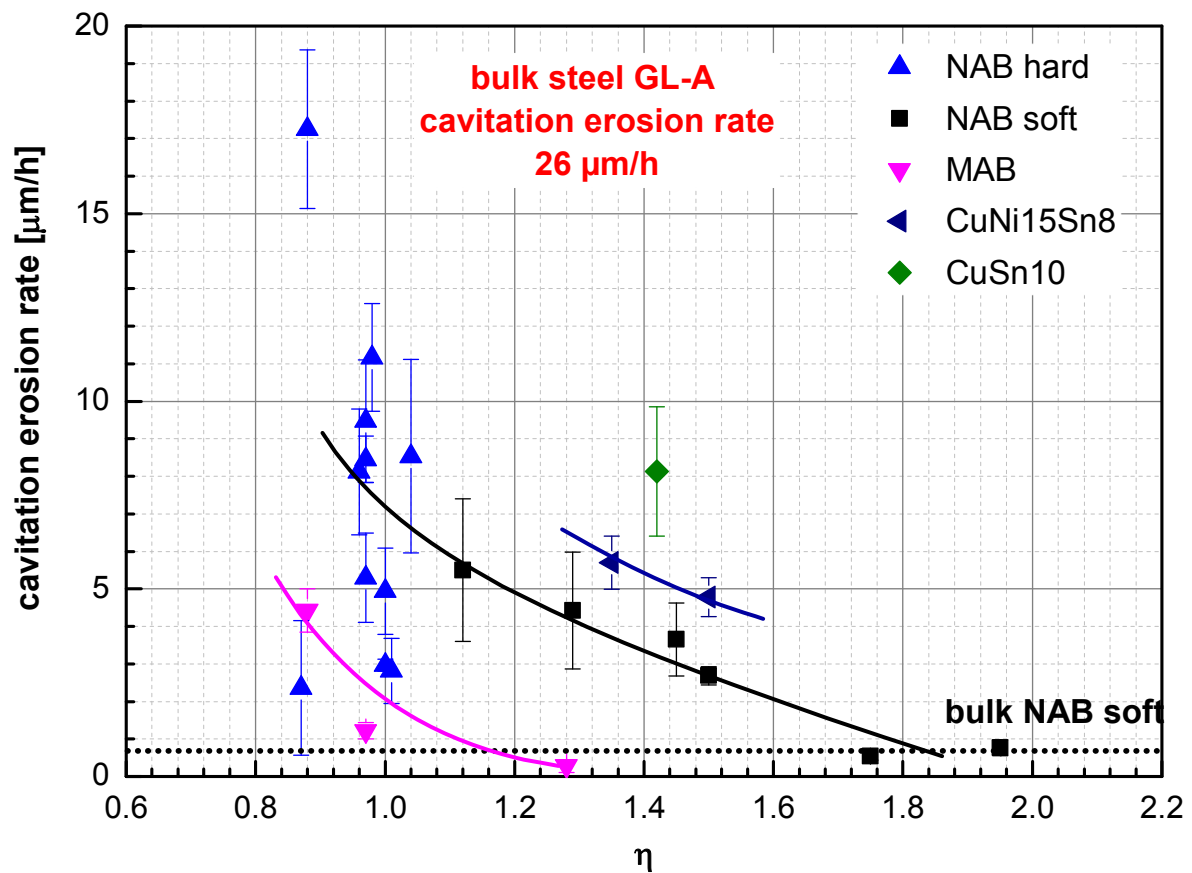


Figure 54: The trend of the cavitation erosion rate shows that increased spray parameter sets regarding particle impact velocity and temperature improve cavitation resistance, only the coatings sprayed with NAB hard powder show no clear trend. However, all coatings show a better performance than bulk steel GL-A. Moreover, high spray parameter sets allow for qualities similar to those of respective bulk material.

4.7. Annealing of cold sprayed Coatings

The results of the cold sprayed coatings so far showed that coating cohesion plays an important role for attainable cavitation resistance. Cohesion could be enhanced by annealing of the NAB hard powder, thus reducing martensite fractions. For Cu-coatings, literature reports improved particle-particle bonding by subsequent heat-treatments [GAE06, STO06]. To investigate the best improvements, the best possible spray conditions (40 bar, 650 °C, nozzle type D51) with nitrogen as process gas were chosen for the feedstocks NAB hard and NAB soft. After spraying, the coatings were annealed at 500 °C or 650 °C for different time scales of up to 4 hours. The annealing temperatures were chosen in accordance to the phase diagram of NAB in Figure 55 to distinguish influences by the formation of γ_2 -phases and reduction of β' -martensite structures [MEI00]. Higher annealing temperatures would enhance oxidation effects at real rudders or propellers. For research purposes, annealing was performed within a high-vacuum oven to avoid oxidation effects, which is probably not needed in later applications.

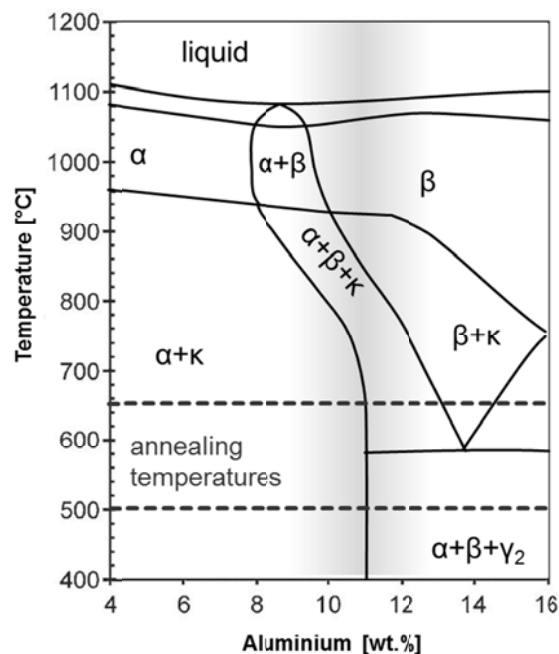


Figure 55: Phase diagram section of CuAl10Fe5Ni5 illustrating the transformation temperatures and the chosen heat-treatments [MEI00]. The blue shaded regime indicates nominal powder composition.

Coating microstructure

Figure 56 compares the coating microstructures of cold sprayed NAB soft and NAB hard coatings in the as-sprayed state and after 2 h of heat-treatment at 500 °C and 650 °C. The microstructure of the as-sprayed NAB hard (a) shows deformed particle, bonded and non-bonded particle-particle interfaces, and most prominently one phase (dendritic) in the particle interior. When annealing NAB hard for 2 h at 500 °C, the microstructure seems not to alter. Neither better particle-particle bonding nor any precipitations can be detected. But when annealing for 2 h at 650 °C, the coating microstructure shows homogeneously distributed dark spots that can be determined as Fe-rich κ -phases. The non-bonded areas seem to diminish. The as-sprayed NAB soft coating shows less non-bonded areas than the NAB hard and precipitations by powder annealing. No major changes occur by annealing at 500 °C.

When annealing at 650 °C the non-bonded areas seem to reduce and the contrast of the κ -precipitations gets more distinct, probably by growth.

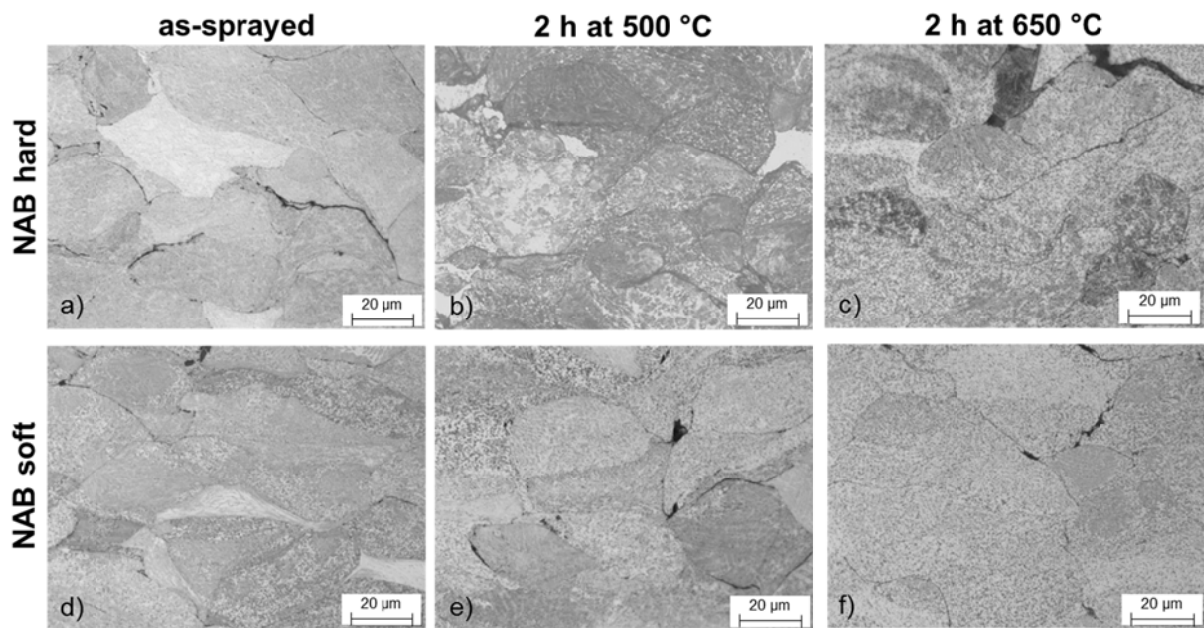


Figure 56: OM-micrographs showing coating microstructures of cold sprayed NAB soft and NAB hard coatings in the as-sprayed state and after 2 h of heat-treatment at 500 °C and 650 °C. The cross-sections were etched for achieving higher contrasts.

Coating hardness

The results of coating hardness are summarized in Table 11. The results indicate influences by recrystallization that reduce hardness and influences by precipitation hardening. Within the first 40 to 60 minutes coating hardness reduces from about 305 HV0.3 to 250 HV0.3. At the annealing temperature of 500 °C longer annealing times ($t > 60$ min) seem to result in a hardness increase by precipitation hardening. Coatings annealed at 650 °C preserve the descending trend.

Table 11: Coating hardness after different annealing times and temperatures showing a drop of about 60 HV0.3 after 40 min for each heat-treatment set.

NAB type	annealing temperature	hardness after			
		0 min	40 min	60 min	120 min
hard	500°C	302 ± 17	-	252 ± 35	267 ± 6
	650°C	302 ± 17	243 ± 18	245 ± 11	235 ± 9
soft	500°C	310 ± 7	252 ± 6	279 ± 15	269 ± 8
	650°C	310 ± 7	244 ± 7	240 ± 10	231 ± 12

Coating structures and residual stress

Figure 57 displays the development of the coating structure for NAB hard (a) and NAB soft (b) at different annealing temperatures and times. The as-sprayed condition is shown in black whereas the red colour refers to an annealing temperature of 650 °C and the blue colour to 500 °C. The graphs show that all structural changes occur within the first 20 minutes of annealing, both at 500 °C and at 650 °C, respectively. The martensite fractions diminish completely by annealing at a temperature of 650 °C whereas at 500 °C minor fractions remain within the coating. Additionally by annealing, the peaks sharpen. Recrystallization reduces dislocation densities and associated micro-strain. However, the graphs give no indication of precipitations, probably due to too low amounts that are not detectable by XRD.

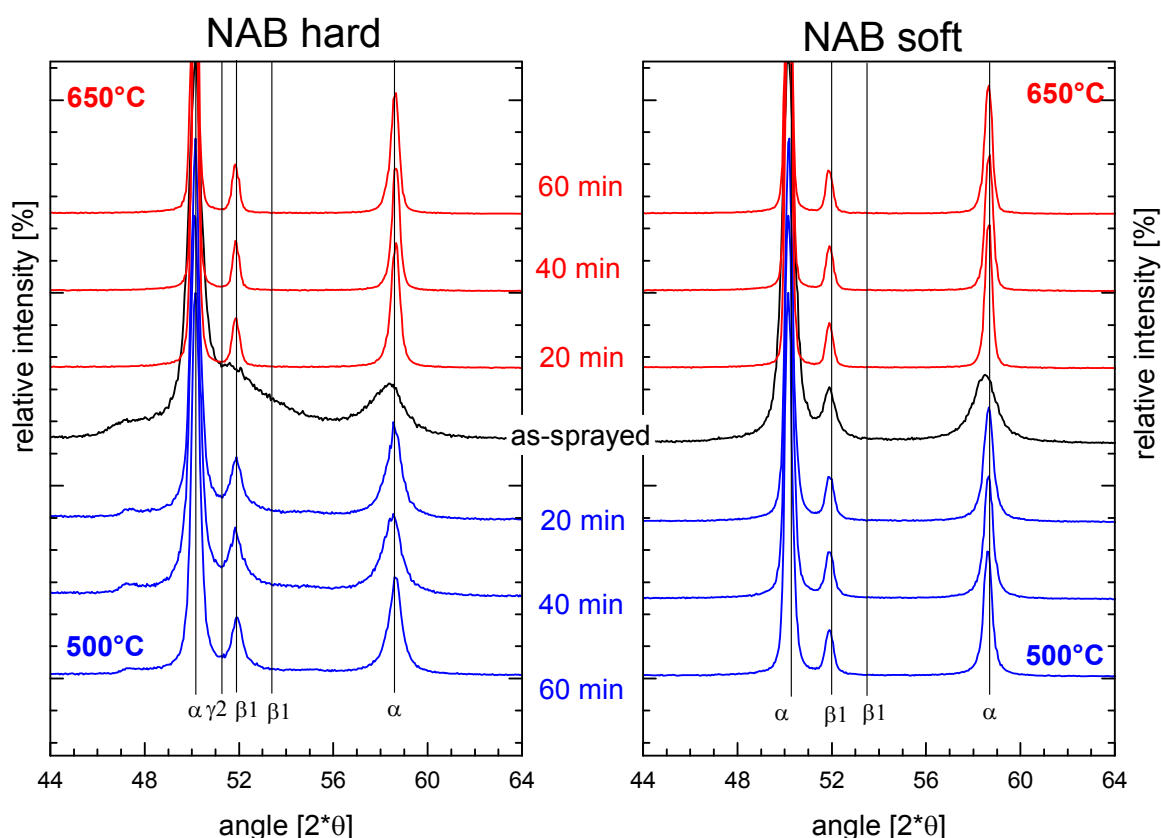


Figure 57: XRD-diffraction pattern of as-sprayed and annealed coatings at 500 °C and 650°C for different annealing times.

Other indications for the influence of recrystallization can be observed by residual stress analyses. Figure 58 illustrates the development of residual stress of the cold-sprayed NAB hard and soft coatings at different annealing times and temperatures. As for the development of the hardness, major changes are observed within the first 20 minutes of annealing, changing the stresses from compressive to tensile. For longer annealing times, the stresses reduce slightly to a certain range probably due to cooling stresses and different thermal expansion ratios of the coating and the substrate. Interestingly, the coatings annealed at lower temperature show higher peak stresses at the beginning.

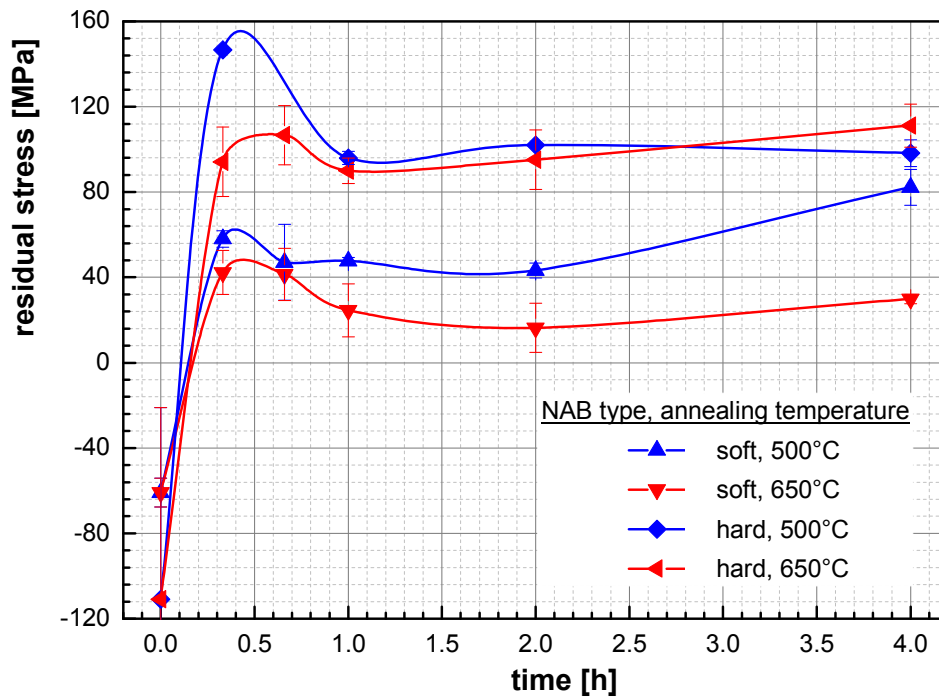


Figure 58: Residual stress as a function of the annealing time for the NAB hard and NAB soft bronze coatings annealed at 500 °C or 650 °.

Electrical Conductivity

The electrical conductivity is supposed to give good information about coating integrity and summarizes influences by coating cohesion, oxide content and the amount of dislocations, as well as porosity, changes by material composition, structure and further coating defects. Due to similar spray conditions and material, most influences are secondary and mainly the coating cohesion and structural changes due to the heat-treatment might affect the measurement of the electrical conductivity. Figure 59 gives an overview about the measured electrical conductivity of the different coatings and annealing temperatures as a function of the annealing time.

For all coatings, the electrical conductivity significantly rises within the first 20 minutes of annealing and settles within saturation regime for the respective spray powder treatment. For NAB soft powder, attainable coating conductivities are slightly higher than for NAB hard. For the different annealing temperatures, the NAB soft shows no difference between the two annealing temperatures. In contrast, NAB hard only for higher annealing temperature of 650 °C reaches the saturation regime within short time scales, for 500 °C more than 2 h are needed. When comparing absolute values, the annealed NAB soft already in the as-sprayed state shows about twice as high conductivity than NAB hard, probably due to better coating integrity. In consequence, improvements by coating annealing are higher for NAB hard.

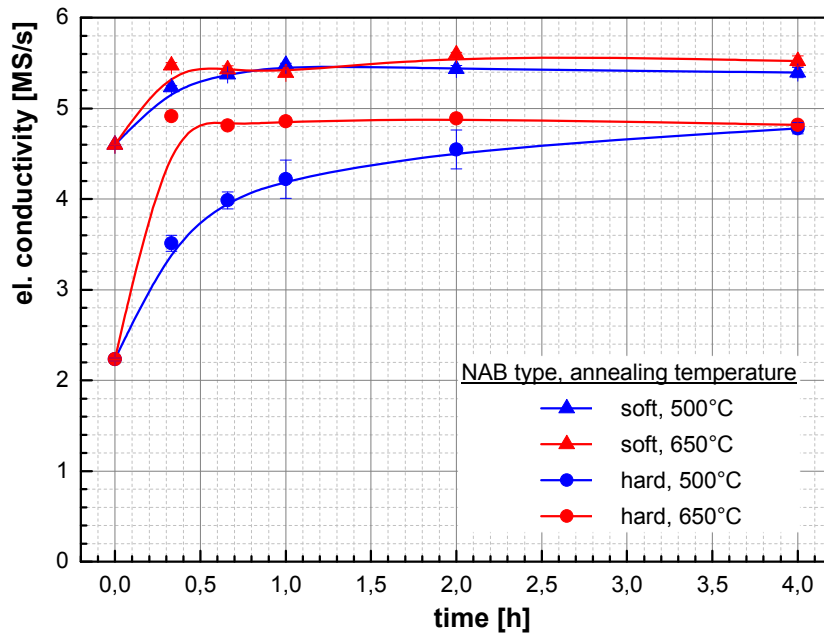


Figure 59: Electrical conductivity over annealing time for NAB hard and NAB soft cold sprayed coatings for annealing temperatures of 500 °C and 650 °C.

Coating strength

The results of the TCT- and MFT-test are summarized in Figure 60. The TCT-strength (continuous lines) was measured for most annealing conditions and types of NAB (hard and soft) whereas the ultimate tensile strength (dashed line) was only measured exemplary for the coatings sprayed with NAB hard in as-sprayed and heat-treated at 500 °C conditions.

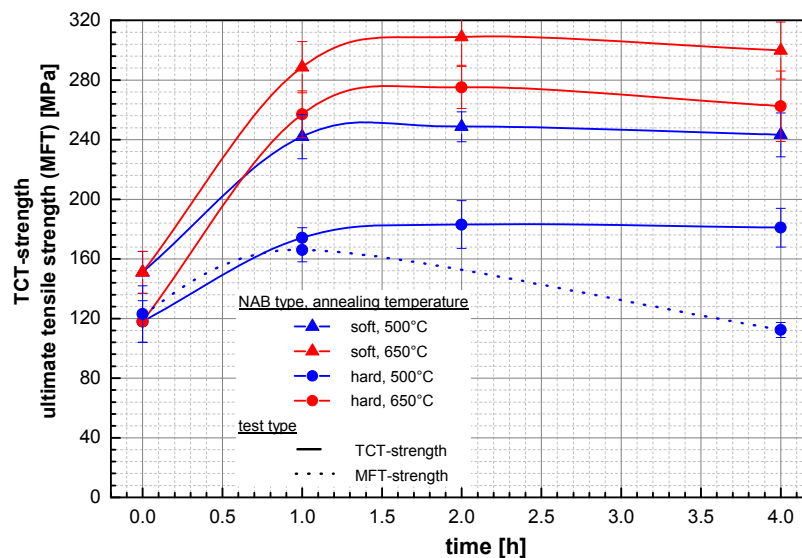


Figure 60: Influence of heat-treatment parameters on coating cohesion (solid lines: TCT-strength / dotted line: MFT-strength). Most strength improvements are obtained within the first 60 minutes of annealing.

When considering the TCT-strengths, all coatings show a high rise in strength within 1 h annealing time. Higher annealing temperatures result in higher strength as compared to lower temperatures. For the same annealing conditions, NAB soft coatings always show

higher strength than NAB hard. For longer annealing times the strength remains within a narrow range but decreases slowly. A similar trend can be observed for the MFT-test results of NAB hard, but the strength seems to decrease stronger for 4 h annealing.

Cavitation behaviour

The results of the cavitation erosion test are shown in Figure 61 and reveal similar trends as the tensile test results. The cavitation rate drops rapidly within the first hour of annealing. For the NAB soft coating annealed for 1 h at 500 °C, similar performance as for respective bulk material was obtained. After this drop, the cavitation rate of NAB soft coatings increases with annealing time. For both annealing temperatures, the cavitation rates of NAB hard show steady decrease with annealing time. Interestingly, the influence of annealing temperature on cavitation is different for NAB hard and soft coatings, the higher temperature being more beneficial for the hard coatings, the lower one being better for the soft coatings.

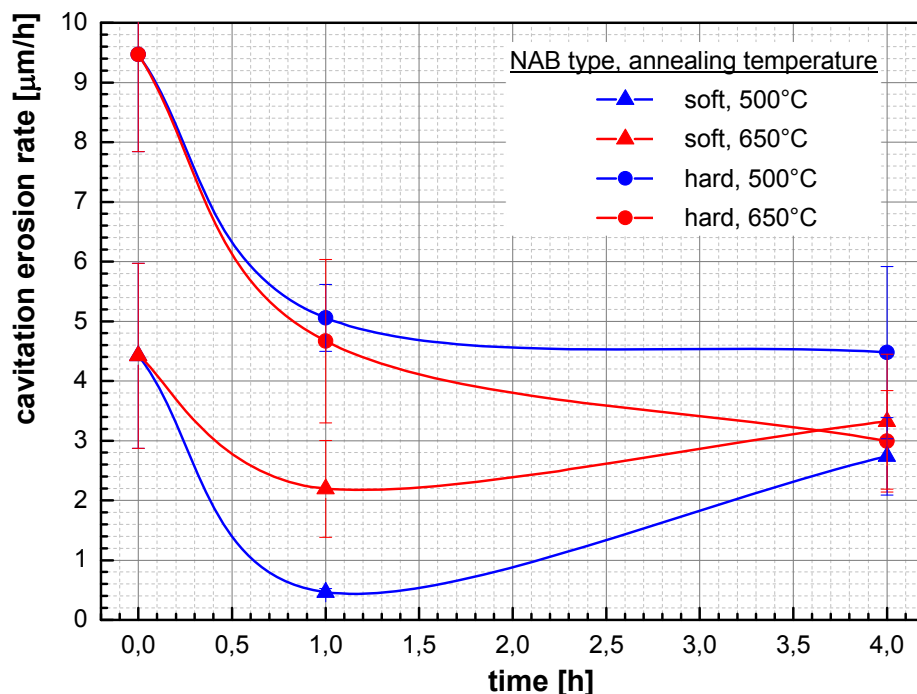


Figure 61: Cavitation erosion-rate of the cold sprayed NAB soft and hard coatings annealed at 500 °C and 650 °C for different time scales.

The surface morphologies after 100 min cavitation testing are shown in Figure 62. When considering the NAB hard coatings annealed at 500 °C, after 1 h annealing only minor changes as compared to the as-sprayed state are visible. Mainly whole particles are removed, most prominently by brittle failure. After 4 h annealing at 500 °C, the cavitation mechanism seems to change. Less complete particles are removed and polished surfaces show traces of plastic deformation and localized pits indicating material loss. The higher annealing temperature of 650 °C significantly improves the plasticity of the NAB hard coating, with most prominently ductile vein-pattern, failure at particle boundaries, a stronger deformed surface and more pits occurring after cavitation testing. For the annealing temperature of 650 °C, the surface damage by cavitation does not differ for the annealing times of 1 h and 4 h. The NAB soft coatings show a more ductile behaviour for all treatment states. Trends are the same with the coating annealed for 1 h at 500 °C showing less deformation and pits at the surface. For longer annealing times, particularly at the annealing temperature of

650 °C material removal gets more selective at medium length scales, indicating inhomogeneities within particles.

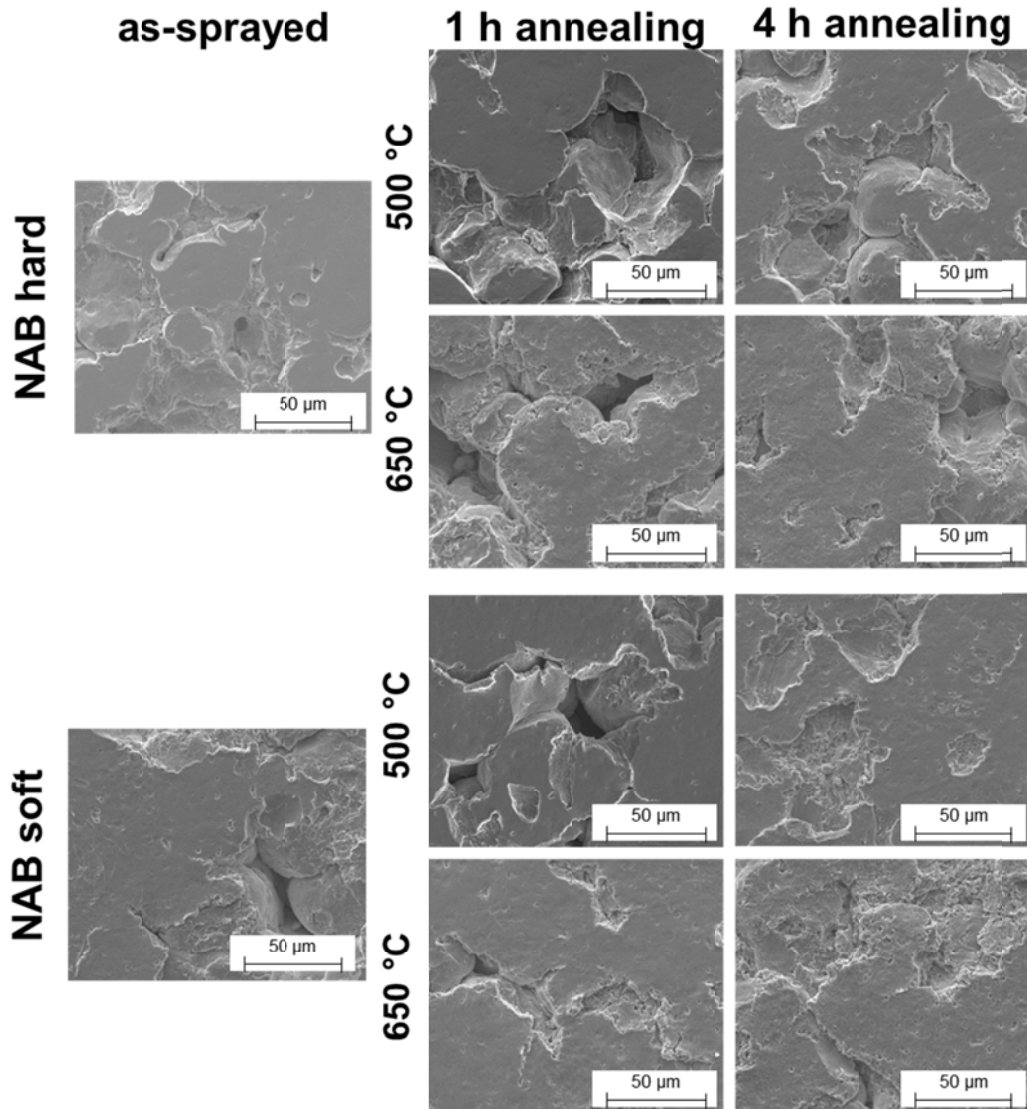


Figure 62: Surface morphologies of cold-sprayed and annealed NAB hard and NAB soft coatings after 100 min cavitation test. The coatings were annealed for 1 h and 4 h at 500 °C or 650 °C, respectively.

4.8. Discussion of Cold Gas Spraying of Bronze

4.8.1. Influence of Spray Parameters and Materials

The results demonstrate that coating properties can significantly be influenced and improved by enhancing cold spray parameter sets with respect to the coating quality parameter η . The attainable η -values depend on bulk material properties, in particular the material's flow stress that play a major role for particle deformation and coating formation, and hence also affect possible cavitation performances.

Consequently, correlating the results with η illustrates that coating formation starts at η -values near unity. Around this $\eta = 1$ regime, coating properties scatter and no clear trends can be observed. This is particularly prominent for the NAB hard coatings, which do not allow

for adjusting sufficiently high η -values due to their high powder strength. Martensitic structures and limited process gas temperatures by nozzle clogging restrict the needed deformability. These influences will be discussed in chapter 4.8.3. Hence, exploring dependencies in terms of η focusses on the bronze powder materials NAB soft, MAB, CuNi15Sn8 and CuSn10. For cold spraying these bronze coatings with η -values above unity, clear trends and correlations get obvious in agreement to dependencies reported in literature [SCH06A, ASS03, ASS11].

By increasing the coating quality parameter η , particles contain higher kinetic and / or thermal energy that allows for enhanced deformability upon impact. This results in reduced porosity and better bonding between particles. For higher η -values, single particle impact morphologies revealed higher flattening ratios and improved material jet formation at particle rims. More prominent jets indicate enlarged areas of adiabatic shear instabilities at particle-substrate and particle-particle interfaces [ASS16, SCH06A]. In consequence, adhesion and cohesion increase with growing amount of bonded interfaces, as proven by higher tensile strength and higher electrical conductivity for higher η -values. Taking electrical conductivity as a measure, almost bulk-like conductivities should be achievable for coatings sprayed with η -values above 1.5. Interestingly, the residual stress reduces from highly compressive to an almost stress-free state with increasing η . Higher thermal and kinetic impact conditions result in elevated local temperatures due to higher deformation. By better deformability, the generated heat turns to be less adiabatic and spreads over larger coating volume, causing a stress relief [ASS16]. When using pre-heated substrates, a change of sign towards tensile stresses is observed. Here, the thermal misfit between the steel substrate and bronze coating becomes more prominent. Further recrystallization at temperatures above 240 °C releases compressive stresses in the deposited bronze coatings. In addition, pre-heated substrates enhance coating adhesion as shown by cavitated wipe-test samples. For single powder impact, sufficient thermally softened materials allow for better deformation and formation of adiabatic shear instabilities. By substrate pre-heating, part of overall deformation is shifted towards the substrate side and enhances adhesion [ASS16].

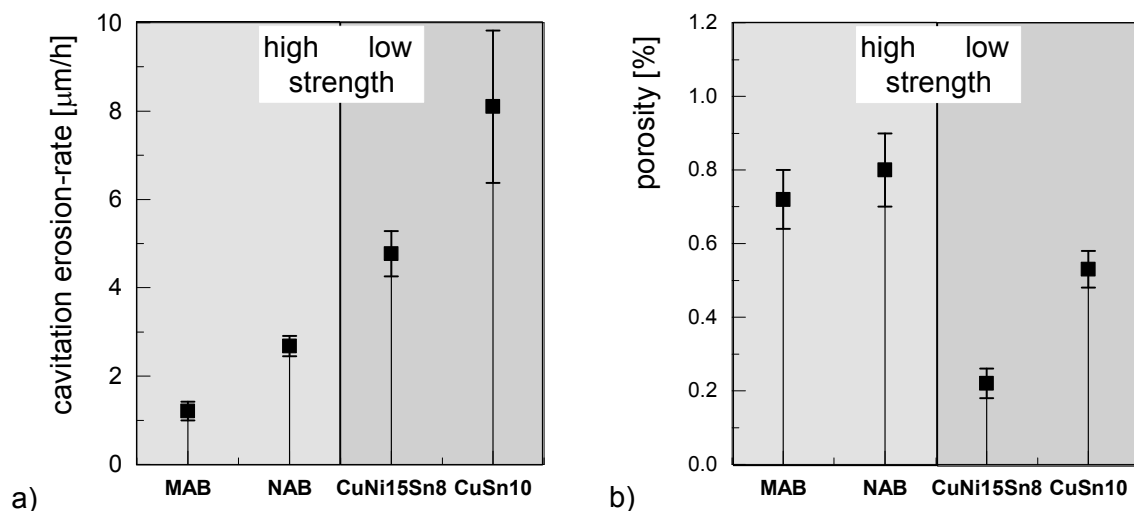


Figure 63: Comparison of the best cavitation performance of each bronze coating type and the respective non-bonded areas within the coatings – here represented by the porosity.

With respect to the cavitation performance of the optimized and maximum cold spray conditions with nitrogen as process gas, different influences can be distinguished as illustrated in Figure 63. The main trends regarding material and coating properties concern the following:

1. Coatings of bronze material with a high strength (MAB and NAB soft) sprayed with low η -values

These coatings can show a low cavitation-rate but due to the lower particle deformability suffer from high amounts of non-bonded areas and pores (compare Figure 63). Considering the morphology of the coating surfaces after cavitation testing, the damage affects mainly poorly bonded interfaces and particles. As mentioned earlier, the limit in gas temperature due to nozzle clogging hinders the use of higher spray parameter sets and thus sufficient formation of shear instabilities ensuring good coating cohesion. On the one hand, the non-bonded areas act as crack nuclei and promote mass loss by whole particle removal. On the other hand, for high strength bronzes lower amounts of bonded interfaces can be sufficient to withstand the loads for particle removal by cavitation. Moreover, the high hardness and high fatigue limit of the high strength bronzes prevent intra-particle cracking, thus partial removal of particle fractions. The superposition of these affects causes the unexpected low cavitation-rates.

2. Coatings of less hard bronze material (CuNi15Sn8 and CuSn10) sprayed with high η -values

The softer bronzes sprayed with η -values above 1.5 showed almost bulk like electrical conductivities and low amounts of non-bonded areas as well as low porosities but high cavitation rates (compare Figure 63). This is most probably due to intrinsic material properties. Cold spray coatings of lower strength bronzes under optimum conditions show a performance similar to bulk material. Only few less bonded areas are present that act as crack nuclei and would affect particle removal during cavitation. Comparing the results of the surface morphologies after cavitation testing, failure sites show ductile fracture at particle-particle boundaries and most prominently fatigue within the particles.

Summing up, on the one hand the coating performance for each bronze type is highly dependent on the spray parameter. Enhanced spray conditions allow for improved deformation and thus enhanced coating performances. Besides the spray conditions, the intrinsic material properties play an important role. The results show that using materials with reduced strengths to enhance coating formation not necessarily reach the outstanding cavitation resistance of high strength bronzes. Thus, when comparing different bronze types, independent from the spray conditions, the material properties seem to dominate.

4.8.2. Properties with Influence on Cavitation Performance

For better understanding the mechanisms of cold-sprayed coatings in terms of cavitation performance, the results are summarized and correlated between the cavitation erosion-rate and various coating properties. The correlations are shown in Figure 64a-d, detectable trends are highlighted. The individual correlations indicate that the cavitation rate decreases with increasing (i) strength, (ii) hardness, (iii) conductivity and decreasing (iv) porosity. Nevertheless, absolute values and thresholds can be different for the coating materials under investigation. When comparing the curves between CuSn10 and NAB soft in Figure 64a, both bronzes exhibit similar coating strengths but the cavitation-rate of CuSn10 is by 10 $\mu\text{m}/\text{h}$ higher than that of NAB soft. This can be explained by the different material properties as introduced in chapter 4.8.1. As described before, the coatings sprayed with NAB hard do not follow any consistent trend and data-points are widely spread. Nevertheless, the results are included to stress this unexpected phenomenon, which will be discussed in chapter 4.8.3.

Figure 64a proves that the coating strength and thus coating cohesion plays an important role for cavitation resistance. As previously mentioned, larger bonded areas reduce the amount of crack nuclei and avoid particle removal. This is underlined by the correlation of the electrical conductivity and porosity in Figure 64c and d, which both represent non-bonded interfaces. As a measure of resistance against plastic deformation, Figure 64d describes the relation between coating hardness and the cavitation erosion-rate. Higher hardness by higher resistance against deformation allows for reduced cavitation rates, which is well in line with results in literature [VYA77, HAT04, AST70, NEV01]. The oxygen content was not considered in this comparison due to too low contamination within cold gas spraying.

With respect to good cavitation resistance, the coating cohesion seems to play the major role, both for high strength bronzes and for low strength bronze materials. Good coating cohesion can be obtained only for low porosity. At high porosity levels, the amount of bonded interfaces barely varies since most of the higher impact energy mainly improves deposition efficiency and flattening [SCH06A]. For a significant improvement of bonding quality, porosity must fall short below certain thresholds.

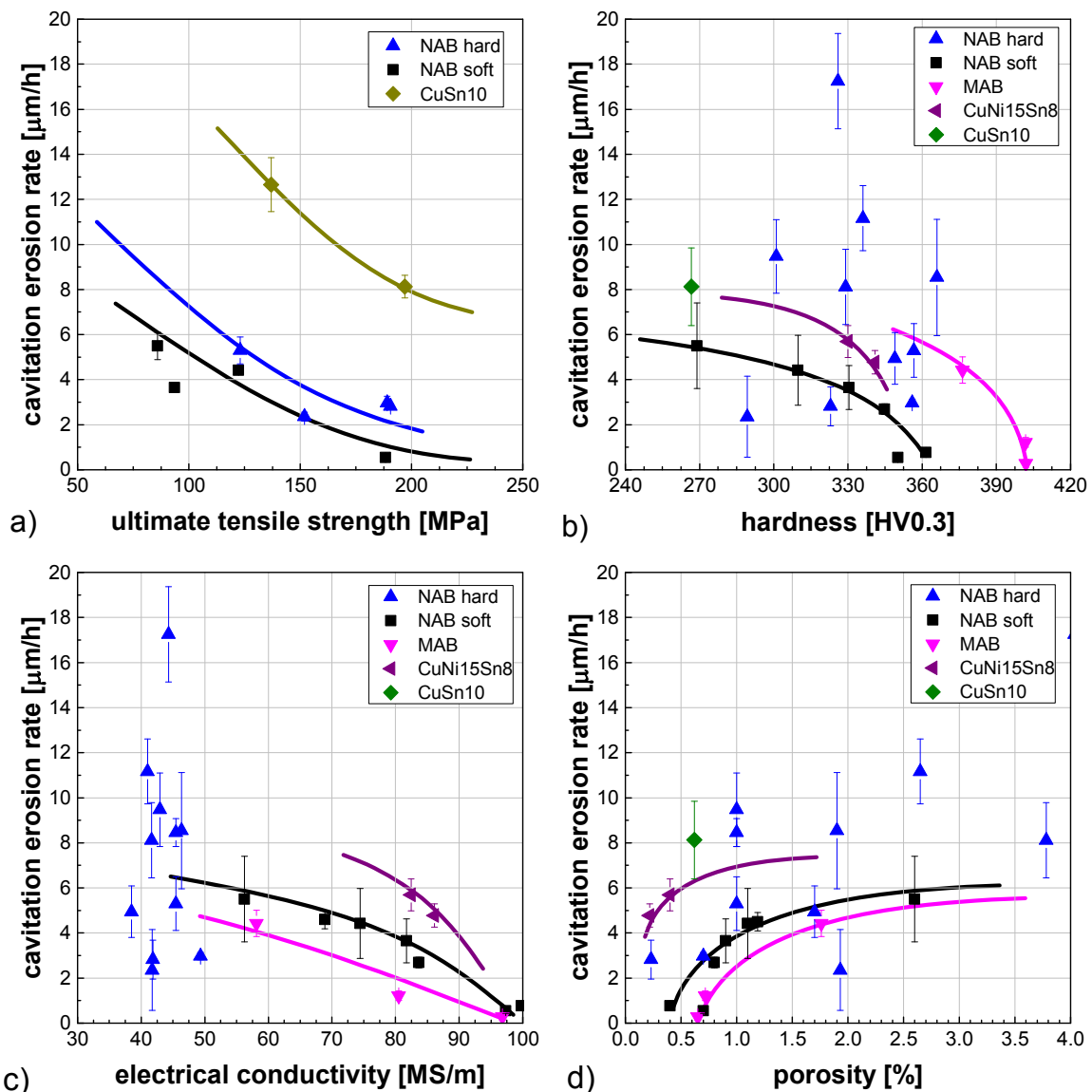


Figure 64: Correlation between the cavitation erosion-rate and selected coating properties of cold sprayed bronze coatings.

4.8.3. Influence of the Powder Material Structures of the Ni-Al-Bronze

The used Ni-Al-bronze contains four different materials (Cu / Al / Ni / Fe) that allow forming several phases and precipitations and consequently determine material properties since the properties are highly sensitive towards material composition variations [MEI00]. Processed as powder, the material contains an α -matrix with β_1 martensitic structures and κ_{I-III} iron-rich and κ_{IV} Ni-rich precipitations. The powder is produced by the so-called EIGA-process that allows for high cooling-rates, the solidification resulting in metastable high temperature β -phases that transform to the martensitic β_1 -structure. As measured, the NAB hard particles contain about 10-15 atm% martensite, which is randomly spread within the powder distribution and within single particles. The microstructures revealed that some particles consist of almost 100 % of martensite needles whereas other particles showed only minor fractions. Within this study, no differences in martensite content between larger and smaller particles due to different cooling rates could be detected. Probably, slightly variation of the material composition – especially of the Al-content - mainly determines martensite formation [XU16]. The martensite causes elevated powder strength. The highly tensed martensite needles are surrounded by an α -matrix, due to volume changes by the phase transformation containing high amounts of dislocations. This might additionally strengthen the powder particle and explain the irregular deformation behaviour as shown in Figure 20. These hardening mechanisms and the limited deformability of martensite restrict particle deformability and raise the critical conditions for bonding ($\eta > 1.00$) [ASS16]. Thus, impact conditions with η around unity are limiting attainable coating qualities. Moreover, the non-uniform martensite distribution might cause the high scatter of coating properties at η -values around 1.00.

Interestingly, as compared to the powders, XRD-pattern of the coatings reveal a visible reduction of martensite [XIO04]. As observed for steel 316L [BOR08] and MCrAlY [BOR14], a strain-induced transformation might occur since the cubic face-centred α -phase is the equilibrium disordered phase in NAB [MEI00]. Such phase transformation might supply further heat by an enthalpy change to the coating and thus enhance coating formation. It can be assumed that the transformation occurs at supersonic speed. This is probably due to the fact that stress concentrations within impacting particles vary and not always exceed thresholds to trigger the martensite to α transformation. A ductile deformation of α also might reduce local stresses.

The remaining martensite might also explain the high cavitation performance of some cold gas sprayed NAB hard coatings. Martensite and the related lattice shearing as known for superplastic NiTi alloys could allow for damping of the incoming water jets from cavitation [RIC97, STE06].

In contrast, the NAB soft powder, which was annealed above 550 °C, contained completely transformed martensite and thus almost dislocation-free α -phase and κ -precipitations [LV15]. The pre-dominantly cubic face-centred structure of NAB soft allows for uniform deformation, as shown by the single particle impact morphologies and more uniform deformed particles within the cold-sprayed coatings.

4.8.4. Influence of annealing Time and Temperature on Coating Properties

The cold sprayed NAB hard and NAB soft coatings were heat-treated at 500 °C and 650 °C up to 4 hours. The results show that coating attainable properties are highly dependent on

the used powder, the time and temperature of annealing, as discussed in the following paragraphs.

Independent from the annealing temperature and the type of used NAB powder, the annealing time plays a major role and determines coating performances in terms of cavitation protection. The main determining time dependent influences are summarized in Figure 65. The cavitation performance (black) is the resultant from the cohesive properties (blue) and the microstructural changes (red). On the one hand, the cohesive properties represent the development of the rising TCT-strength and of the electrical conductivity, due to closing of non-bonded internal interfaces. The microstructural changes within the coating include recrystallization and precipitation hardening as indicated by hardness and XRD measurements. Both curves are further influenced by different diffusion processes that allow for fusing non-well-bonded particle-particle interfaces and dislocations [STO06, DAV04]. Thus, both follow individual dependencies, influencing the coating cavitation properties, as observed. Especially the cohesive properties are affected by the heat-treatments and can be explained by surface diffusion along internal gaps within the coating. As compared to volume diffusion, surface diffusion is significantly faster and thus determines the first annealing period [BUT73], while the microstructural processes related to bulk diffusion kick in for longer annealing times.

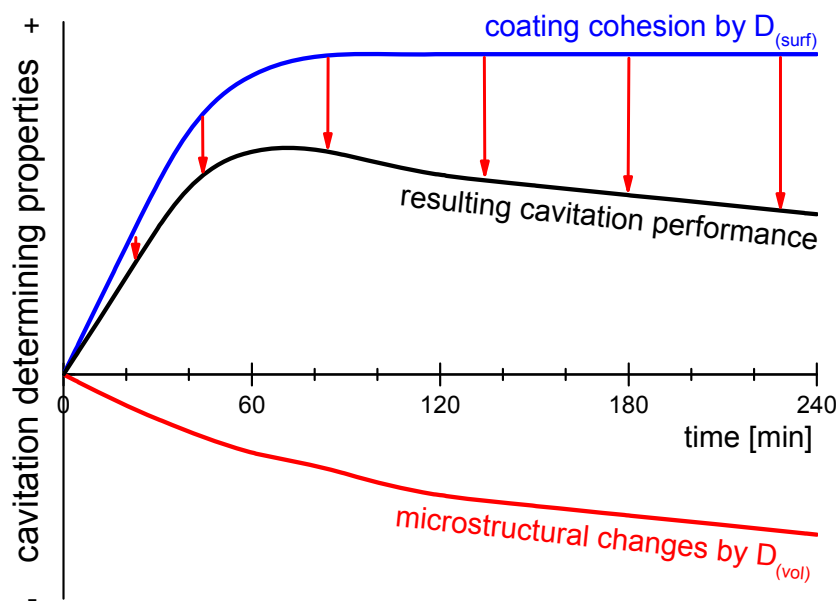


Figure 65: Schematic of property contributions to cavitation performance determining coating properties. The different contributions are mainly determined by surface ($D_{(surf)}$) and volume ($D_{(vol)}$) diffusion processes during annealing. The black curve describes the resulting cavitation performance between enhanced coating cohesion (blue) and microstructural changes (red).

By high diffusion-rates, material is transported on internally open surfaces or grain boundaries towards energetic more favourable positions within the coating. Furthermore, the high degree of dislocations near particle surfaces could promote additional diffusion velocities. At triple points like pore-edges, the atomic bonding is better than at free surfaces and traps diffusing particles to re-settle in these positions. In short words, minimizing internal surface energy, arising from cracks and non-bonded interfaces, leads to spherical pores. This enlarges bonded areas and consequently improves coating cohesion [MEN11]. In parallel, volume diffusion starts and causes recrystallization, reducing coating hardness and

compressive residual stresses. In case of stresses, the final state represents the thermal mismatch between coating and substrate material [MEN11, LI06]. Furthermore, structural changes by diffusion begin to reduce martensite fractions. This meta-stable phase transforms to the cubic-face-centred α -phase and the γ 2-phase. Later, also κ -precipitations grow, as observed in coating microstructures. The associated loss in strength might negatively influence coating cavitation properties. Referring to literature, martensitic structures exhibit outstanding cavitation performances like NiTi-alloys or steel UNSS42000 [RIC97, STE06, WU00, KWO00].

The results show that higher annealing temperatures enhance the diffusion processes. As compared to annealing at lower temperature, this results in slightly higher coating strengths but comparable electrical conductivities and coating hardness. This is mainly affected by recrystallization and different coating microstructures. The phase diagram exhibits the formation of γ 2-phases at 500 °C and the formation of κ -precipitations at 650 °C. The γ 2-phase is known to offer excellent wear properties, but to be corrosion-prone [LV15]. Additionally, this phase suffers from brittleness and thus of compressive loads like cavitation [MEI00]. Within the first 60 min of annealing, the formation of γ 2-phase occurs to be less prominent than after 240 min. Hence, the cavitation performance could reduce and lower tensile strength as compared to higher annealing temperatures without the formation of γ 2-phase can be achieved. In contrast, the coatings annealed at 650 °C show the formation of κ -precipitations [AL-02]. At long annealing times; the microstructure reveals growing amounts of these precipitations that can be observed by OM or SEM. Meigh et al. report that higher amounts and particularly larger κ -precipitations promote crack formation and corrosion, and hence reduce cavitation performances [SHA95, MEI00, HAN10].

The two different NAB powders (hard and soft) are both sprayed with identical spray parameters in terms of gun equipment, gas pressure and gas temperature, but as discussed in chapter 4.8.1 and 4.8.3, result in different coating properties. The NAB hard coatings contain martensitic phases and suffer from high amounts of non-bonded interfaces and pores. In contrast, the NAB soft coatings are free of martensite and show good cohesive properties. The microstructure contains larger Fe-rich precipitations from previous powder heat-treatments. These conditions determine the development of coating properties during the annealing process. The results show that identical heat-treatments cannot heal out all initial coating defects. This was proven by results concerning TCT-strength and electrical conductivity. As compared to coatings sprayed with NAB soft, annealing of NAB hard caused larger rises in TCT-strength, electrical conductivity and cavitation resistance, due to the reaction of non-bonded interfaces. NAB hard coatings show enhanced surface self-diffusion due to numerous non-bonded areas and pores that can heal during annealing and thus improve cohesion to a higher extent, as shown for Cu by Stoltenhoff et al. [STO06]. Interestingly the NAB hard coatings demonstrate larger compressive stresses in the as-sprayed state and after heat-treatment than NAB soft coatings. That might be attributed to less thermal recrystallization during coating deposition. Besides recrystallization, the decreased amount of martensite leads to a volume reduction that increases tensile stresses.

5. Warm Spraying of Ni-Al-Bronze

5.1. Calculated Impact Conditions

Modelling of the particle impact conditions using computational fluid dynamic – codes was performed by Prof Katanoda, Kagoshima University, Kagoshima / Japan. The results were adopted into a similar scheme as for cold spraying. As before for cold spraying, as well for warm spraying, the respective particle impact conditions and window of deposition were simulated for a better understanding of the coating formation and to derive significant influences on coating properties. Later on, coating properties are correlated with impact energies, following a concept by Assadi et al., to include particle impact temperatures close to the melting point [ASS16]. The particle impact energy can be calculated from particle impact velocity and temperature.

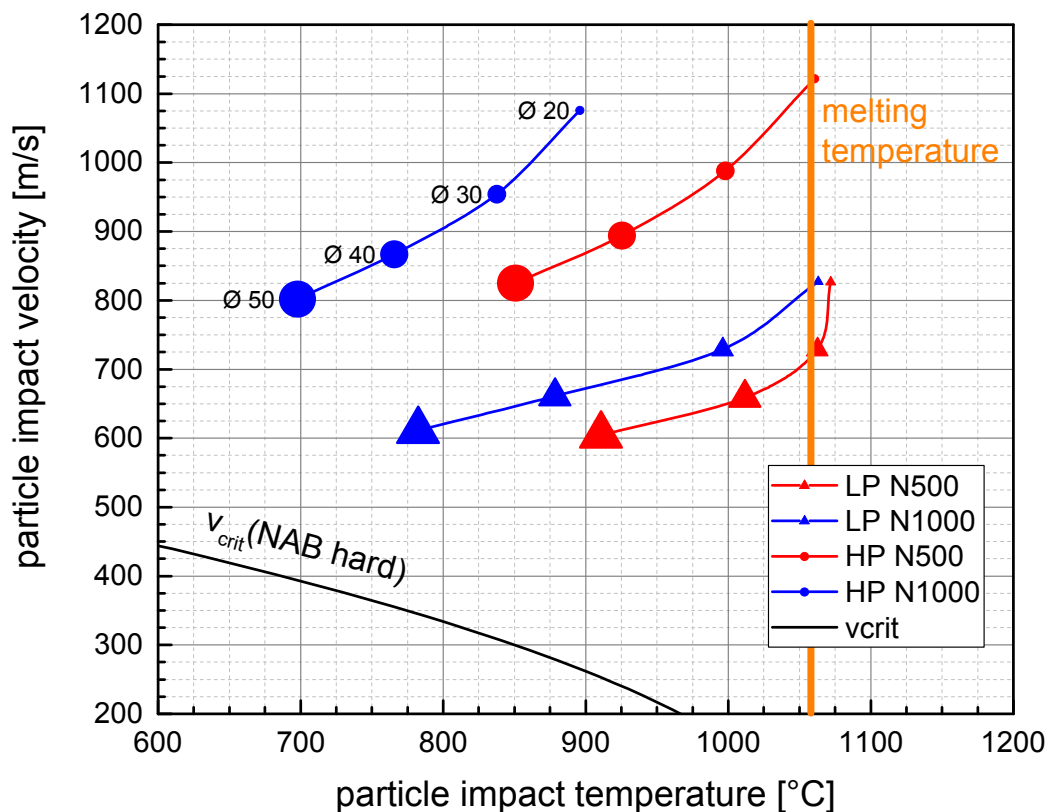


Figure 66: Impact conditions and critical conditions for bonding for the different warm spray parameter sets of this study. The results show that smaller particles are also hotter than bigger particles, in contrast to cold gas spraying.

Figure 66 shows the particle impact conditions and the window of deposition for the NAB hard feedstock powder and for the used warm spray parameter sets. The comparison illustrates that all particle impact conditions are well above the critical velocity. The consideration of the particle sizes emphasize that larger particles remain much colder and are less accelerated than smaller particles within the hot gas stream. A higher thermal and kinetic inertia hinders heating and acceleration within the process. But in contrast to cold spraying, by less gas expansion, small particles are less cooled during the flight through the parallel nozzle and free jet and retain more heat, thus impact at higher temperatures, even at a spray distance of 200 mm, as assumed in the calculations. Therefore, small particles can reach the melting temperature and impact in partially molten states, as for nitrogen flow-rates

below 750 l/min. In contrast, elevated nitrogen flow rates result in colder gas and particle temperatures. The gas pressure mainly affects the particle velocity. Increasing the combustion pressure from about 1 MPa (low pressure) to 4 MPa (high pressure) can yield about 200 m/s to 300 m/s higher particle velocities. The pressure increase is associated with a drop in particle impact temperatures. Smaller particles are more affected by the enhanced combustion pressure than larger ones by showing reduced temperatures but elevated velocities. The lower mass allows for improved acceleration but also less heating due to shorter dwell times. The effect, that an increased gas pressure reduces particle temperatures, is surprisingly more pronounced for high nitrogen flow rates.

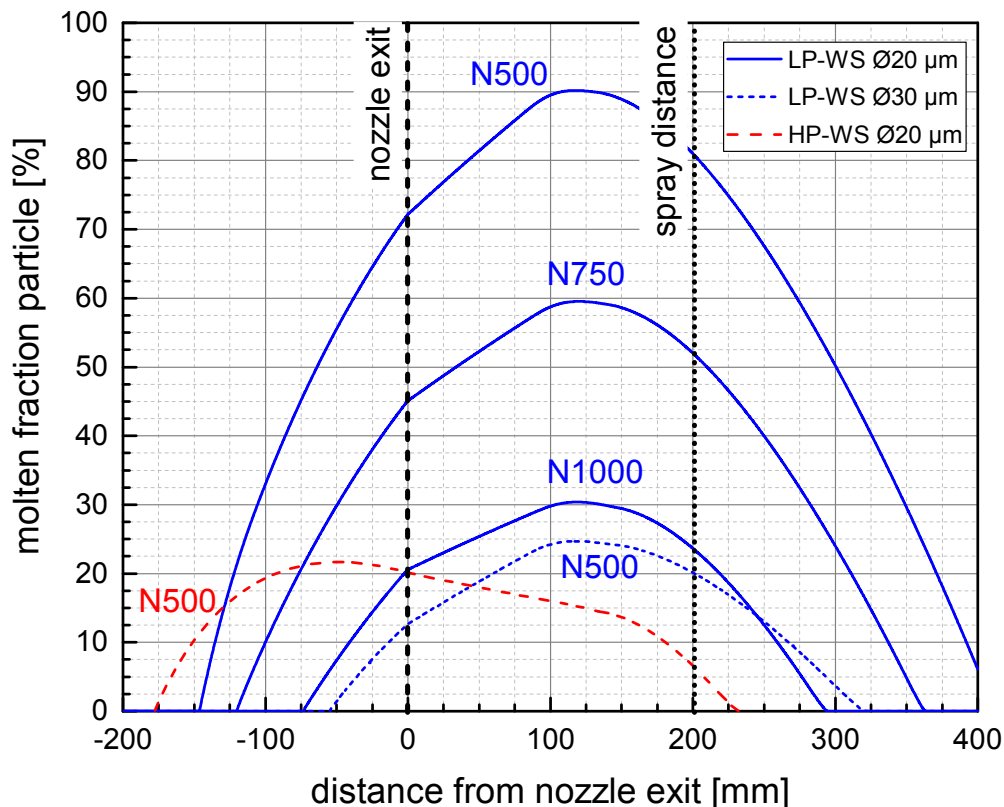


Figure 67: Calculated molten fractions of a particle of warm-sprayed NAB particles for different spray conditions and powder sizes over their axial path through the spray nozzle and free jet.

Figure 67 illustrates the impact conditions under the focus of the molten fraction of a particle. The molten fraction of a particle is calculated over the axial way through the gun system including the free jet. It shows that particles already heat up and begin to liquefy within the spray gun or nozzle. For low-pressure warm spray, maximum fractions are reached in the free jet at a spray distance of about 100 mm from the nozzle exit (0 mm), before solidification starts by reduced gas temperatures. Smaller particles are more sensitive to melting due to the lower mass than larger ones. Even at nitrogen flow-rates of 1000 l/min for low-pressure and 500 l/min for high-pressure warm spray result in partly molten fractions. Particle sizes above 30 µm show partial melting only at nitrogen flow-rates below 500 l/min. At a typical spray distance of 200 mm, most particles are re-solidified. Only particles with sizes smaller than 20 µm at nitrogen flow-rates below 750 l/min show semi-solid impacts. In summary, the simulations show that the impact conditions and in consequence coating properties are highly sensitive to the spray distance.

5.2. Particle Impact Behaviour and Deposition Efficiency

In addition to the simulation results, analyses of single particle impact events from wipe-tests were qualitative and quantitative analysed. The deformation behaviour of single particles (splats) impacted on polished steel substrates were investigated by SEM and classified into different categories to allow for statistical evaluation of the different spray parameter sets.

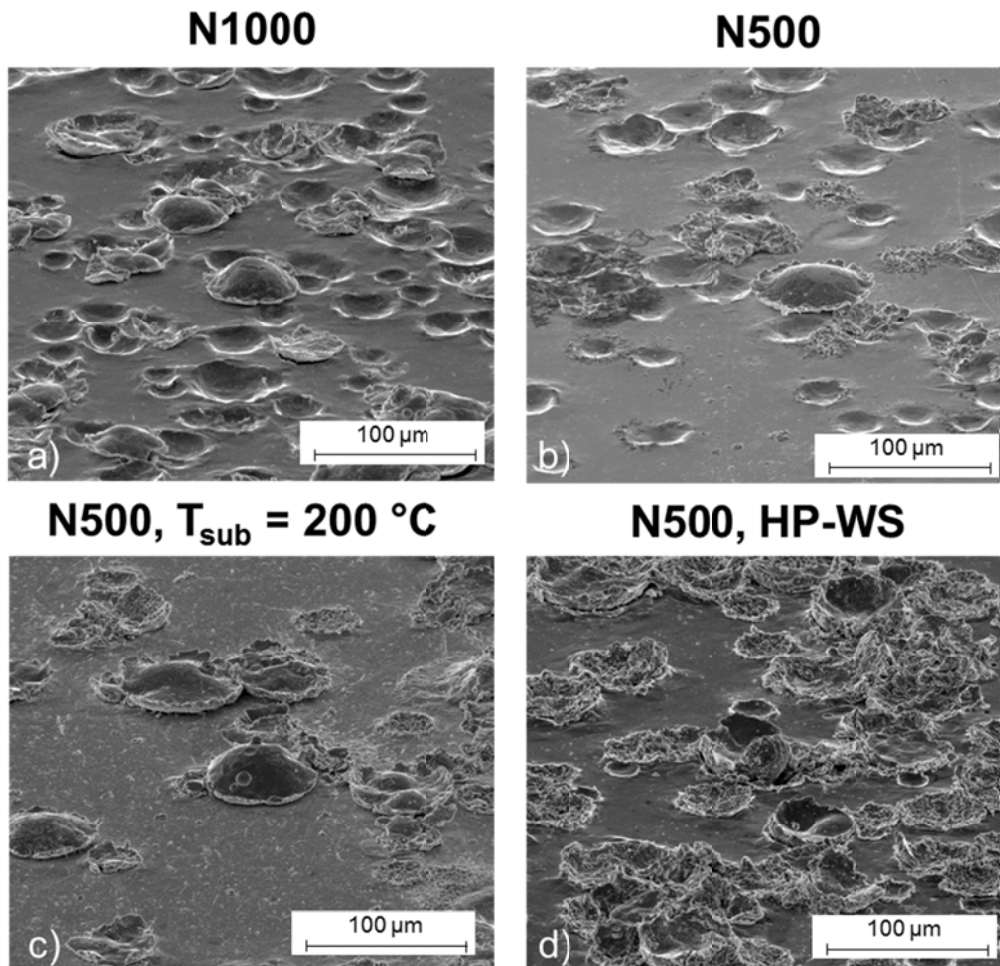


Figure 68: Typical particle impact morphologies of warm sprayed NAB hard bronze particles on polished steel GL-A substrates at different spray conditions.

Overviews of the impact behaviour of NAB hard at different warm spray parameter sets are given in Figure 68 for a cold (a: N1000) and a hot (b: N500) condition on room-temperature substrates, a hot condition on pre-heated substrate (c: N500 – $T_{\text{sub}} = 200\text{ °C}$) and a hot condition at elevated gas pressure on room-temperature substrates (d: N500 - HP-WS). All adhering particles show viscous flow as material jet around their contact zone to the substrate. The impact morphologies show that by spraying with cold conditions on room-temperature substrates (a) the minority of particles adheres on the substrate. Larger adhering particles are less flattened than smaller ones. Smaller particles – moreover – seem to be prone to disintegration. For a lower nitrogen flow-rate and thus higher particle temperatures (b), slightly more particles adhere on the substrate. The flattening ratio is higher than for colder spray conditions, and smaller particles show more semi-molten or partly broken shapes. When spraying with the hot condition on pre-heated substrates (c), the flattening ratio is lower than on not-pre-heated substrates. Moreover, almost all particles adhere, including the smaller and hotter ones. The smaller ones, as for spraying on room

temperature substrates, are more prone to partial melting and disintegration. Highest degrees of deformation can be observed at low nitrogen flow-rates at elevated combustion pressures (d). Occurring material jets are often detached from the substrate surface. Most of the particles seem to disintegrate or to fracture.

The overviews allow for distinguishing three typical impact morphologies (Figure 69) and for defining further statistical analysis and process understanding.

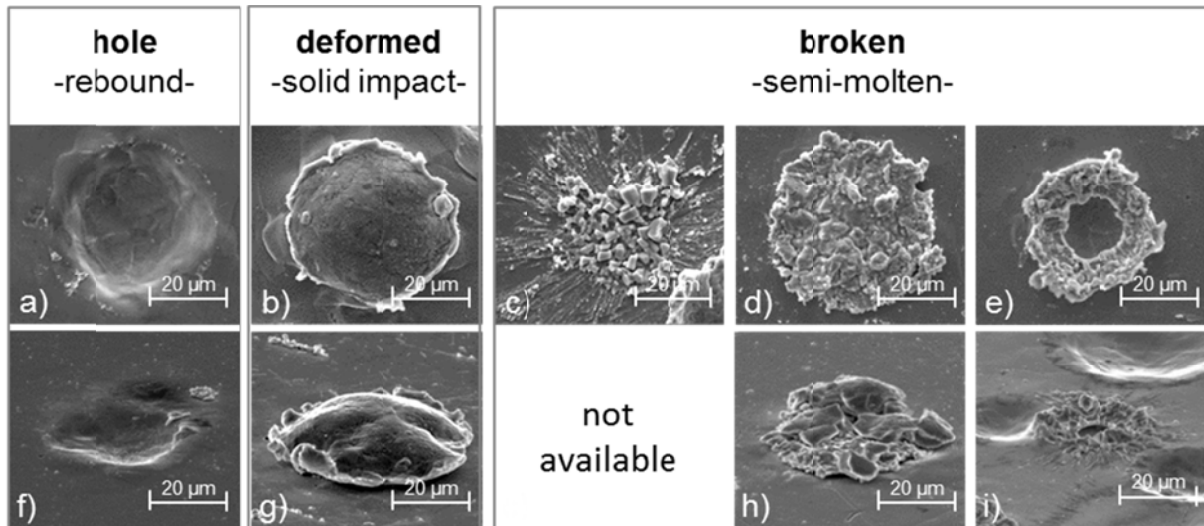


Figure 69: Classes of particle impact morphologies of warm sprayed NAB hard particles on steel GL-A.

Category “hole”

This category shows a crater where non-molten particles rebounded after deforming the substrate. The necessary pre-requisite for bonding of solid particles, i.e. the occurrence of shear instabilities due to high deformation-rates between a particle and the substrate [ASS03], apparently was not fulfilled, and thus the particle did not adhere on the substrate. In some of the craters, vein-like pattern are detectable and are considered as an evidence of minor amounts of occurring shear instabilities, which in these cases did not provide sufficient adherence for particles to remain on the substrate.

Category “deformed”

This category shows highly flattened particles. These particles show material jets around the contact zone to the substrate, which can be viewed as a proof for the formation of shear instabilities and indicate good adhesion [ASS03]. More detailed investigations of the material jets by EDX-analyses show that these jets arise mainly from the bronze particles.

Category “broken”

This category shows different shapes and deformation behaviours than the previous ones. Mainly three subtypes of these semi-molten impacts could be detected and are distinguished in Figure 69c) to e). Broken impact scenarios appear quite inhomogeneous indicating the presence of different phases. Some morphologies show a disintegration of solid and liquid fractions with molten parts spreading in several directions upon impact (c). Such impact scenarios are similar to those observed for HVOF-spraying of metal-ceramic composites as WC-Co [FAU14]. Also Figure 69d) shows soft or viscous and solid constituents but no distributed particle fractions around the particle on the substrate surface. These particles are

highly flattened. One of the phases within the impacting particle may have been liquid at the time of impact, leading to the deposition of individual solid phase particulates in a liquid-like splat. The substrate itself does not show any stronger deformation. In addition, ring-shaped impact morphologies (e) could be detected. Probably outer parts of the particle were partly fused to the substrate and the solid kernel was ejected by elastic rebound forces [ASS16]. The separation of particle parts is probably due to constituents of substantially lower strength, in extreme highly softened, viscous-like or even liquid phases.

For more quantitative analyses, the different morphologies were statistically evaluated for different spray parameter sets, distinguishing influences by the nitrogen flow-rate, the substrate temperature and the combustion pressure. The results are summarized in Figure 70. Considering the influence of the gas temperature, the results show that lower nitrogen flow-rates and thus hotter spray conditions slightly increase the amount of overall adhering particles, whereas the type of adhering particles changes. For hotter conditions, less particles are deformed and more particles labelled “broken” do adhere. When comparing morphologies sprayed onto pre-heated and not-heated substrates, the amount of particles of category “deformed” significantly increases with substrate temperature, in the present case resulting in more than twice as much particles of this type adhering on the substrate. This may be explained by a higher fraction of shear instabilities on the substrate itself due to thermal softening, meaning a lower substrate strength at elevated temperatures. This allows slower and colder particles to bond on the substrate. The amount of category “broken” is less affected by substrate temperature. Also the increase of the combustion pressure improves the amount of adhering particles. Interestingly, the amount of “broken” particles is comparatively high at hot conditions. Probably the softer phase deforms or breaks more easily under impact conditions of higher kinetic energy.

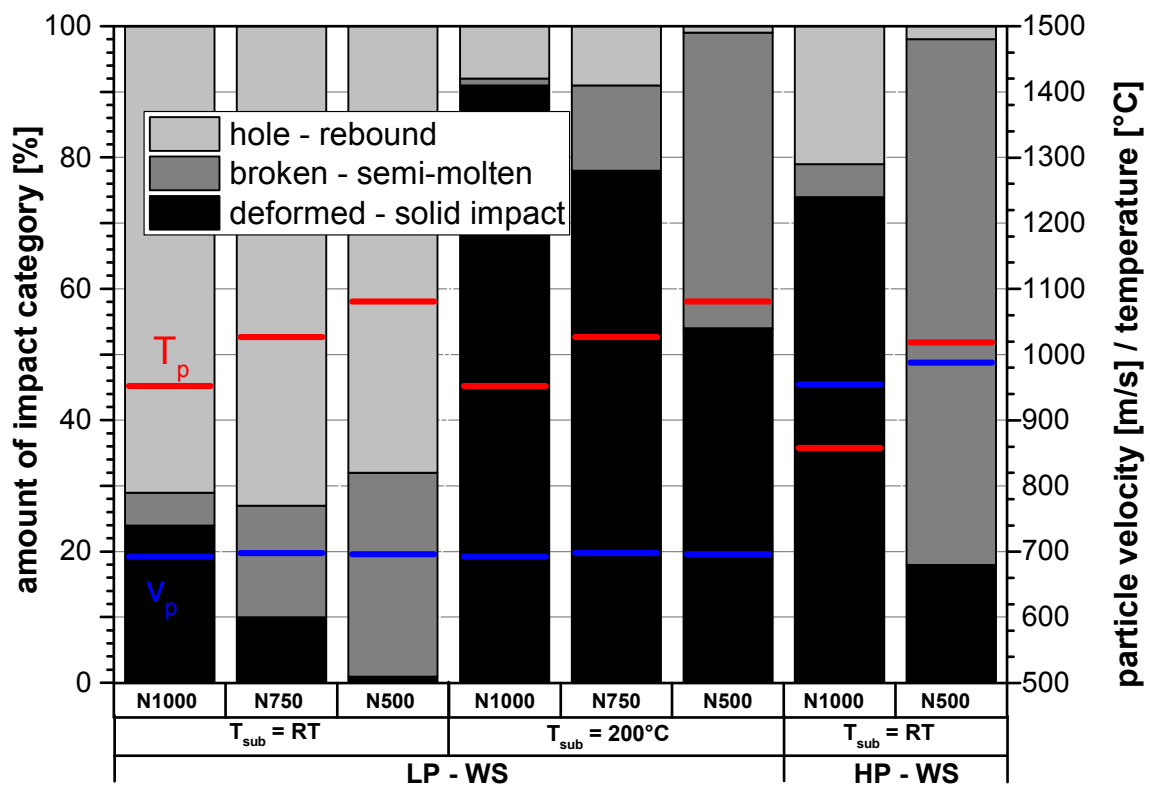


Figure 70: Statistics of single impact morphology classes for different warm spray conditions.

The experimental observations confirm the simulation results with respect to the molten fraction of particles and the influence of the impact velocity. Categories “deformed” and

“broken” are both expected to contribute to coating formation. In addition to the results from simulation, the experiments prove significant influences of substrate temperature on particle adhesion.

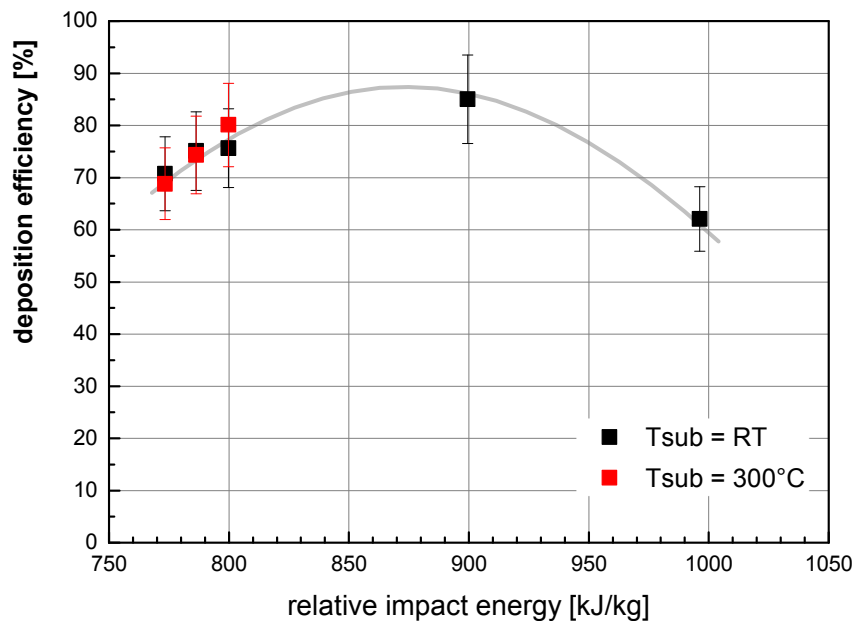


Figure 71: Coating deposition efficiency as a function of the particle impact energy. The decrease at higher impact energies can be explained by semi-molten fractions that splash aside upon impact and not contributes to coating build up.

Coating deposition efficiencies are summarized in Figure 71 as a function of the relative impact energies. The results show that highest deposition efficiencies are obtainable at relative impact energies between about 850 and 950 kJ/kg. Below too low impact energies thresholds for bonding are not exceeded in sufficiently high amounts. Too high impact energies cause severe impact conditions that spread soft or viscous particle fractions aside. As example, Figure 72 shows an adhesion test sample that by such effects was coated at the side by spread and diverted remnants of bronze particles. These particle fractions did not contribute to coating formation and thus reduce coating deposition efficiencies. In contrast to results from single impacts, the deposition efficiency during coating formation is only marginally influenced by substrate temperature.

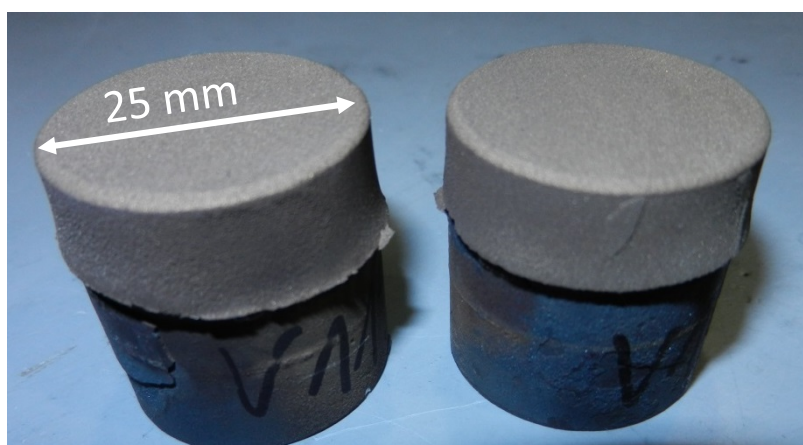


Figure 72: Adhesion test sample covered from the side by spread and diverted fractions of bronze particles at high impact conditions (HP N500).

5.3. Coating Microstructure, Phase Composition and Residual Stresses

Microstructures of warm sprayed coatings were investigated to gain information on the coating formation process with focus on particle deformation and coating cohesion, as well as on coating defects like porosity and oxygen content. In addition, the coating structures and residual stresses were examined.

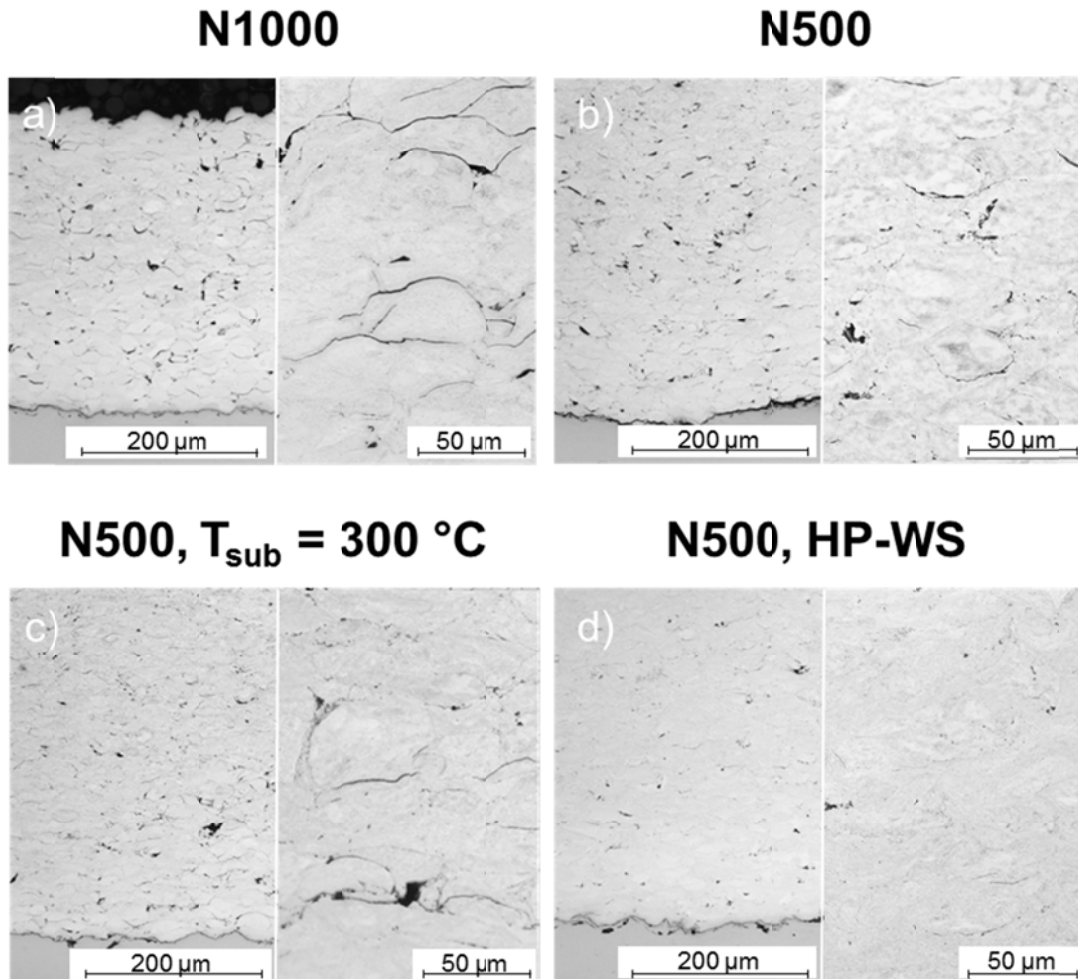


Figure 73: Microstructures as obtained by optical microscopy of selected warm sprayed coatings for different spray conditions as overviews and in detail.

Figure 73 shows the coating microstructures of selected warm sprayed coatings. The microstructure of a coating sprayed with a high nitrogen flow-rate and thus cold spray conditions is shown in Figure 73a. The microstructure shows non negligible non-bonded areas that are visible as micro-cracks between embedded larger particles. Generally, the coating occurs inhomogeneous with regard to particle deformation. Larger and negligibly deformed particles are surrounded by highly deformed smaller ones. The interface between coating and substrates shows no cracks or gaps that might represent poor bonding. When spraying with lower nitrogen flow-rates and thus hotter spray conditions, see Figure 73b, the microstructure displays less pores and non-bonded areas. Particle deformation demonstrates a more homogeneous distribution with regard to different particle sizes. Especially larger particles show a higher flattening ratio as compared to those obtained by colder spray conditions. In contrast to the colder spray parameter sets, several cracks along the coating to substrate interface are detectable. Analysing the same hot spray conditions on a pre-heated

substrate, as shown in Figure 73c, the coating displays a comparable microstructure as without pre-heating in Figure 73b. The most prominent difference is that almost no cracks or non-bonded interfaces between substrate and coating are detectable for substrate pre-heating. Figure 73d displays the microstructure of a coating sprayed with a low nitrogen flow-rate but with an increased combustion pressure. Here the microstructure appears almost dense with only minor defects. Bonding between coating and substrate reveals no cracks or other non-bonded interfaces.

The results of the porosity and oxygen content measurements are summarized in Figure 74a and b. The coating porosities demonstrate a strong correlation to the relative particle impact energy. Enhanced impact energies result in reduced porosities. Higher impact energies allow for improved particle deformation and thus closing of pores, gaps and cracks within the coating. Comparing coatings sprayed on substrates at room temperature with those sprayed on pre-heated ones, the results indicate a slightly lower porosity on pre-heated substrate for coatings sprayed with lower impact energies. Probably impacting particles might enable to deform the thermally softened already adhering particles and to close pores. At higher relative impact energies, the trend could change and highly thermally softened impacting particles could not close gaps below or aside of adhering particles. Available impact energy causes mainly deformation of the incoming particle itself.

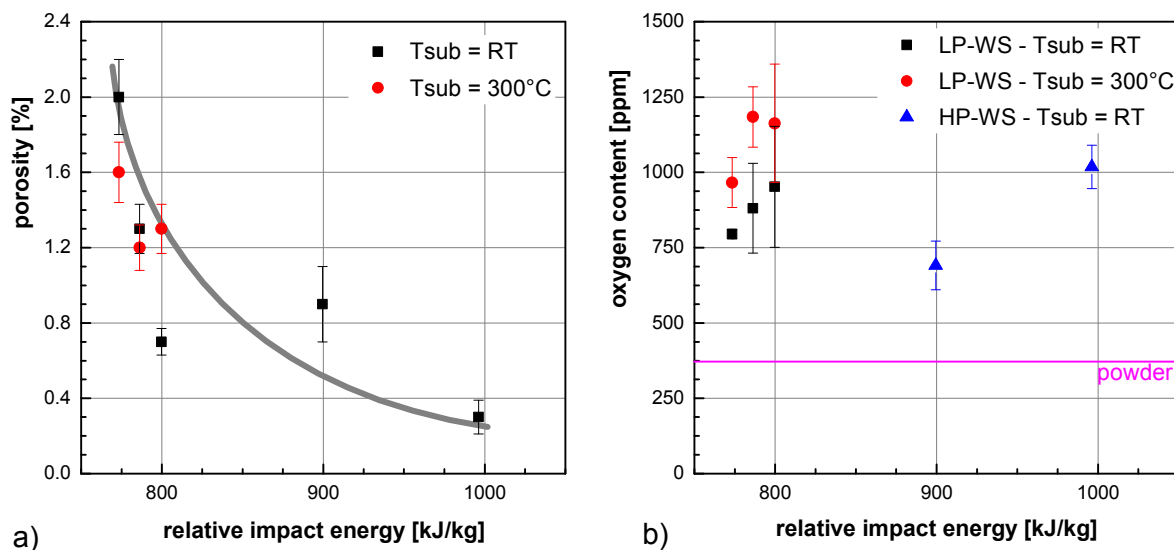


Figure 74: Coating porosity and oxygen content as a function of the relative particle impact energies.

Figure 74 shows the oxygen content of the different warm sprayed coatings as a function of the relative particle impact energies. The oxygen content of the coating is three times higher than that of the powder and 1.5 times higher than for cold spraying. In contrast to the porosity measurements, the results indicate different trends. Individual differences concern influences by enhanced oxidation at elevated impact energies, the substrate temperature and the elevated combustion pressure. Coatings sprayed on pre-heated substrates oxidize more than those on not-pre-heated ones. As described in literature for copper alloys, oxidation of occurs not only within the hot gas stream but also on the hot substrate [DAV14]. The coatings processed by high pressure warm spraying indicate comparable oxygen contents as those of the low pressure ones, since both spray parameter sets operate in similar temperature regimes.

Besides microstructural investigations, the phase compositions of the bronze coatings were investigated and compared to those of the powder feedstock. Respectively, XRD-analysis was also used to determine coating stresses. Figure 75 shows XRD-plots of the feedstock powder in comparison to selected warm sprayed coatings covering a representative angular range. Warm spraying does not affect the presence of the α - and the γ_2 -phase. They only show peak broadening due to lattice defects by deformation. Furthermore, minor shifts to lower angles due to compressive residual stresses can be observed. As compared to the powder, the coating shows a significant reduction of the martensite fraction.

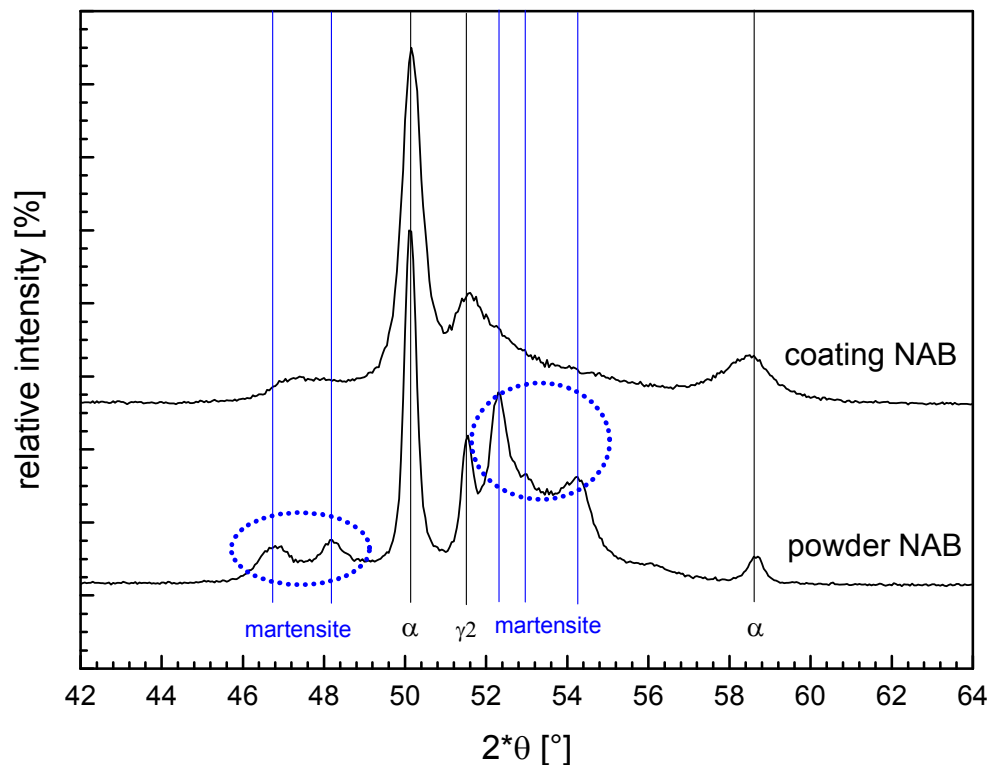


Figure 75: XRD-pattern showing the phase contents of as-atomized powder and a representative warm sprayed coating. By the spray process the peaks widen and the amount of martensite phases reduces.

The residual stresses are summarized in Figure 76. The figure compares the influences of the nitrogen flow-rate for pre-heated and not pre-heated substrates of low and high pressure warm spraying. For low-pressure warm spraying, the results indicate mainly tensile stresses whereas for high pressure conditions an almost stress-free state or even slightly compressive stresses can be observed. For spraying onto non-heated substrates, low pressure warm spray at lower nitrogen flow-rates and thus hotter spray conditions result in tensile stresses up to 90 MPa. There is a slight trend of increased tensile stresses by spraying with lower nitrogen flow-rates, means hotter impact conditions. When spraying onto pre-heated substrates, stresses reach a level of 90 to 100 MPa. An increased combustion pressure and thus much higher particle velocities decrease the residual stresses drastically and could result in slightly compressive stresses by mainly mechanical influences upon particle impact. In contrast to low pressure warm spray, stresses are less tensile for lower N_2 -flow-rates.

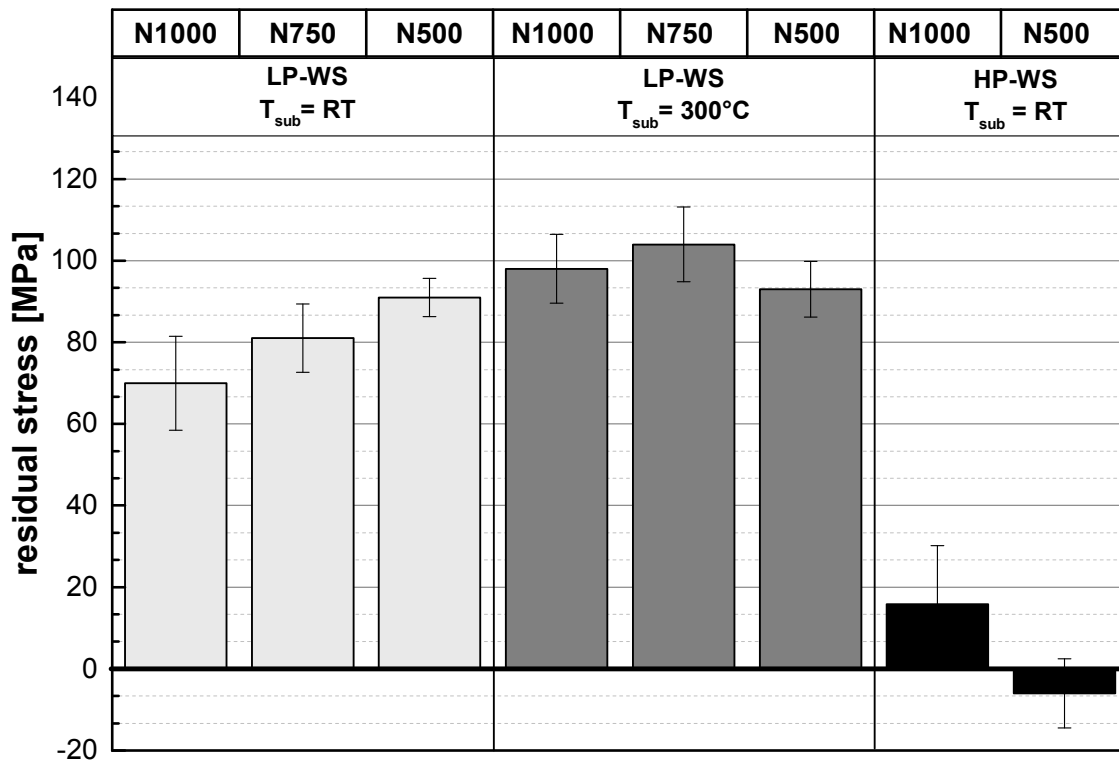


Figure 76: Stress states of the different warm sprayed coatings as obtained by XRD-analyses of the 222-atomic plain.

5.4. Electrical and Mechanical Properties

The electrical and mechanical properties were determined to analyse the influence of coating defects. Coating integrity and thus coating cohesion is a necessary pre-requisite for good cavitation resistance to avoid material and particle removal.

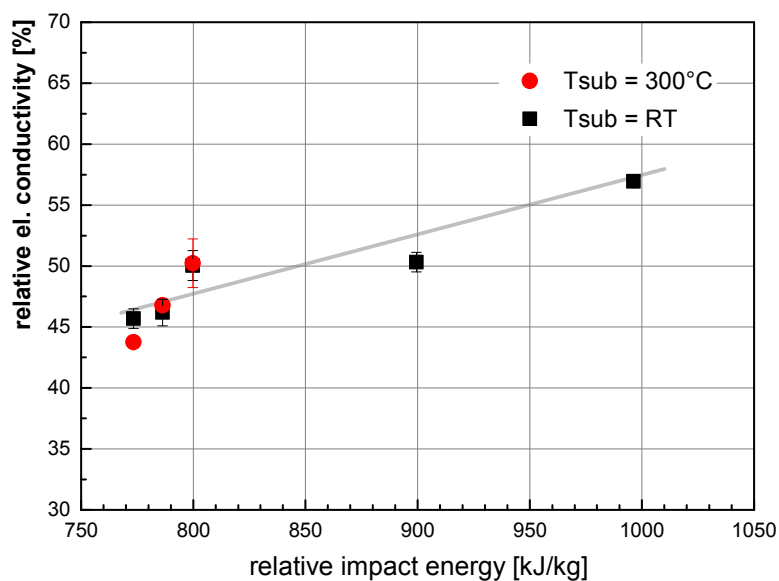


Figure 77: The electrical conductivity of warm sprayed NAB hard as a function of the relative impact energy. The electrical conductivity was set in relation to the bulk conductivity.

Figure 77 shows the relative electrical conductivity revealing an increase with impact energies. The substrate temperature does not significantly affect the coating electrical conductivity.

Figure 78 shows the influences of the relative particle impact energy and enhanced substrate temperature on coating hardness. Coating hardness is influenced by porosity and strain hardening, recrystallization and contaminations of e.g. oxygen. The results show that coating hardness reduces slightly at elevated impact conditions, although remaining within a narrow regime between 400 and 425 HV0.3. Higher thermal and/or kinetic influences allow for reducing dislocation density by recrystallization. Coatings processed on pre-heated substrates show slightly lower hardness than those sprayed on non-heated substrates.

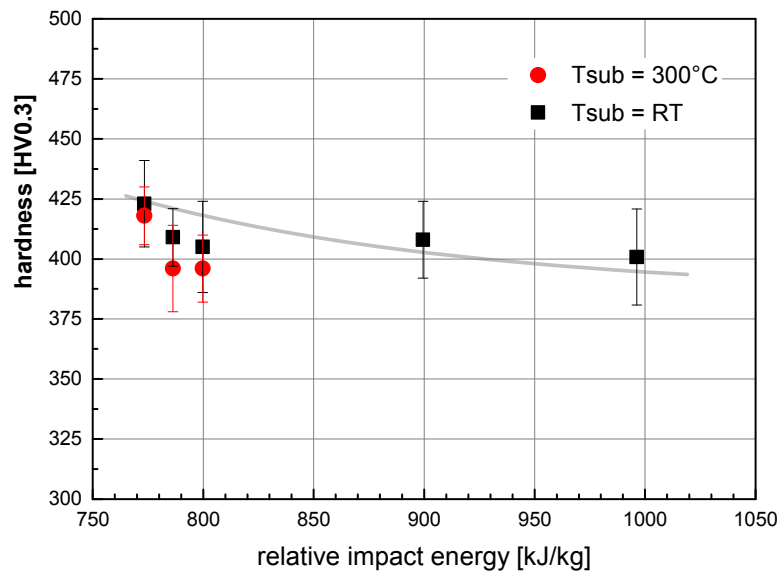


Figure 78: Coating hardness as a function of the relative impact energy showing only a minor trend. Substrate heating conditions are indicated as insert.

In contrast to coating hardness, the coating cohesive properties are highly sensitive on the relative particle impact energy. Figure 79 illustrates the ultimate tensile strength as a function of the relative particle impact energy and reveals a strong upward trend. Higher impact energies, achieved by thermal and kinetic influences, cause more deformation and promote the formation of areas of shear instabilities. Consequently, particle-particle bonding improves and leads to higher coating strengths. Higher coating temperature by pre-heated substrates could slightly enhance bonding quality.

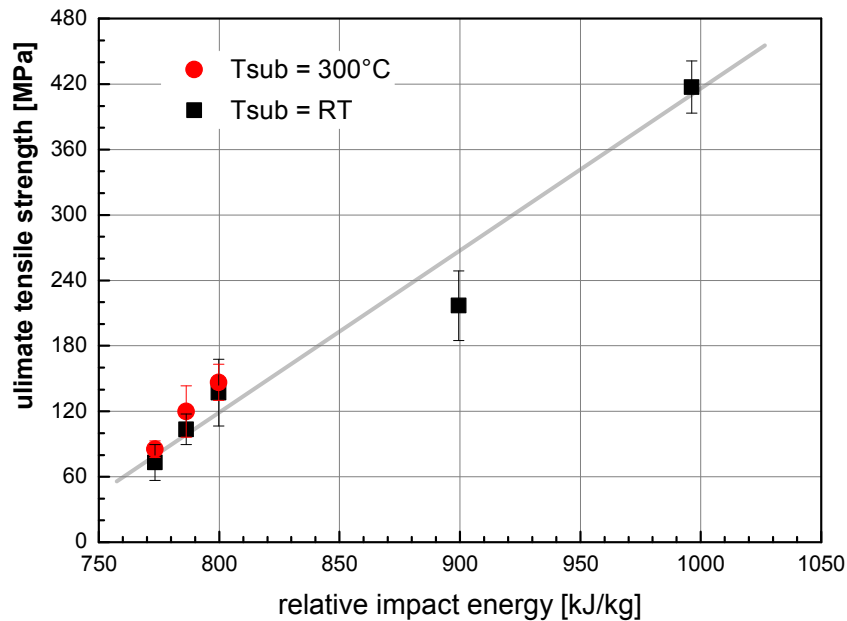


Figure 79: The figure shows that increasing the relative impact energy leads to better coating cohesion. Substrate heating conditions are indicated as insert.

5.5. Single Particle and Coating Adhesion

Good coating adhesion is a necessary criterion for final applications. Hence, single particle adhesion was tested by cavitation tests and statistically evaluated for the as-sprayed state and after 90 sec testing. Coating adhesion was tested directly.

Figure 80 summarizes the amounts of adhering particles in the as-sprayed state and after 90 sec of cavitation treatment. The chosen spray conditions consider a high nitrogen flow-rate (N1000) and thus a cold impact condition and a low nitrogen flow (N500), thus hot condition. Low flow-rates are also employed for processing coatings on heated substrate and raised combustion pressure. Spraying at cold conditions resulting in about 30 % of adhering particles, most of them of category “deformed”. Almost 50 % of these particles are removed after 90 sec of testing and only about 12 % of all particles remain on the substrate. When increasing the spray temperature by reduced nitrogen flow-rates, the majority of overall about 30 % of adhering particles changes from category “deformed” to category “semi-molten”. After 90 sec of cavitation testing, all particles are removed and hence indicate poor bonding of “semi-molten” particles. Applying the same hot condition on pre-heated substrates, the amount of adhering particles is almost 100 % and contains about 60 % of particle category “deformed” that can stick within the thermally softened substrate. However, about 30 % of the particles, mainly of this type are removed during cavitation testing. That might be attributed to the fact that larger particles are less well bonded and easily detach during testing. “Semi-molten” particles, that determine this category, are removed only to minor extent and seem to improve bonding at elevated substrate temperatures. Similar low nitrogen flow-rates but higher combustion pressures also result in nearly 100 % of adhering particles, the majority of 80 % belonging to category “semi-molten”. After 90 sec of cavitation testing, most of the particles remain on the substrate. Cavitation testing mainly removes particles of category “deformed”.

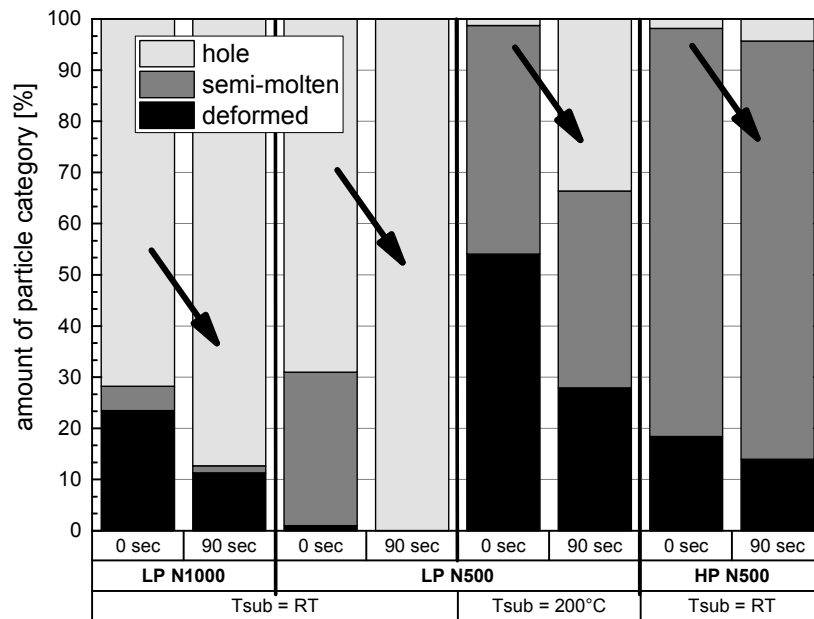


Figure 80: Adhering particles of the different categories in as-sprayed condition and after 90 sec cavitation treatment.

Figure 81 shows the coating adhesion strength of the warm sprayed NAB hard coatings. The comparison indicates quite different trends with low bond strength of LP-WS coatings on non-pre-heated substrates, high bond strength of LP-WS coatings on heated substrates and medium bond strengths for HP-WS coatings on non-pre-heated substrates. Coatings sprayed with LP-WS show a descending trend for reduced nitrogen flow-rates. A similar trend can be observed for coatings sprayed with enhanced combustion pressure, whereas the higher kinetic energy allows for improved bonding. Spraying on pre-heated substrates shows highest coating adhesion strength, but a contrary trend. Here, hotter spray conditions improve bonding.

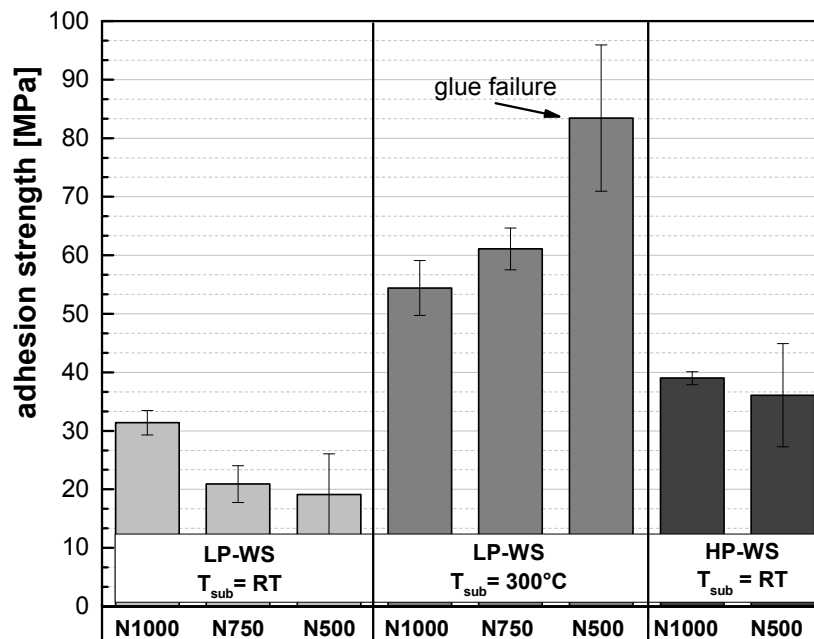


Figure 81: Adhesion strengths of warm sprayed NAB hard coatings on steel S235 substrates at different nitrogen flow-rates, combustion pressures and substrate temperatures indicating highest adhesion on pre-heated substrates.

Interestingly, the results of single particle adhesion correlates well with the coating bond strengths. Spray parameter where high amounts of particle category “deformed” remain on the substrate after cavitation testing show better coating adhesion.

5.6. Cavitation Behaviour

The cavitation erosion-rates of the warm sprayed bronze coatings were evaluated and individual damage mechanism were analysed by SEM for selected cavitation times.

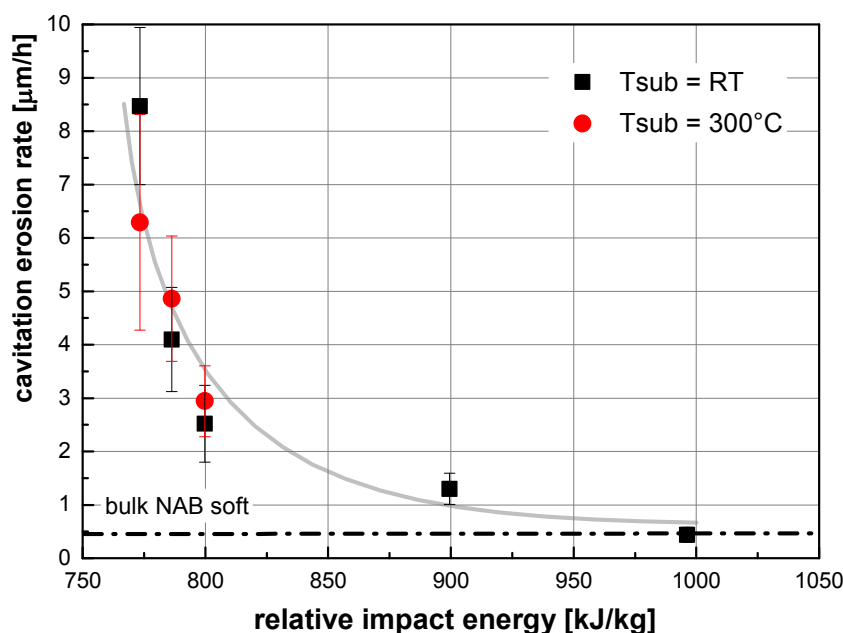


Figure 82: Cavitation erosion-rate of the warm sprayed bronze coatings as a function of the relative impact energy on pre-heated and not pre-heated substrates. For comparison, the measured cavitation rate of the respective bulk Ni-Al-bronze is given as a straight line.

Figure 82 illustrates the cavitation erosion-rates as a function of the relative particle impact energy and reveals that coatings sprayed with high impact energies show significantly lower erosion-rates than those sprayed at lower energetic conditions. At highest impact energies, the warm sprayed coating can realize bulk-like cavitation performance with a cavitation erosion-rate of $0.43 \pm 0.1 \mu\text{m/h}$. High kinetic and/or thermal energies allow for improved particle bonding and thus enhanced cohesion. An effect by increased substrate temperature is only observed for the coatings sprayed with the lowest impact energies, reducing the cavitation erosion-rate. That could be attributed to the fact that the formation of shear instabilities can be shifted from particle sides towards the substrate or already adhering layer sides. After reaching a relative impact energy of about 750 kJ/kg, the substrate temperature does not any more affect the cavitation performance.

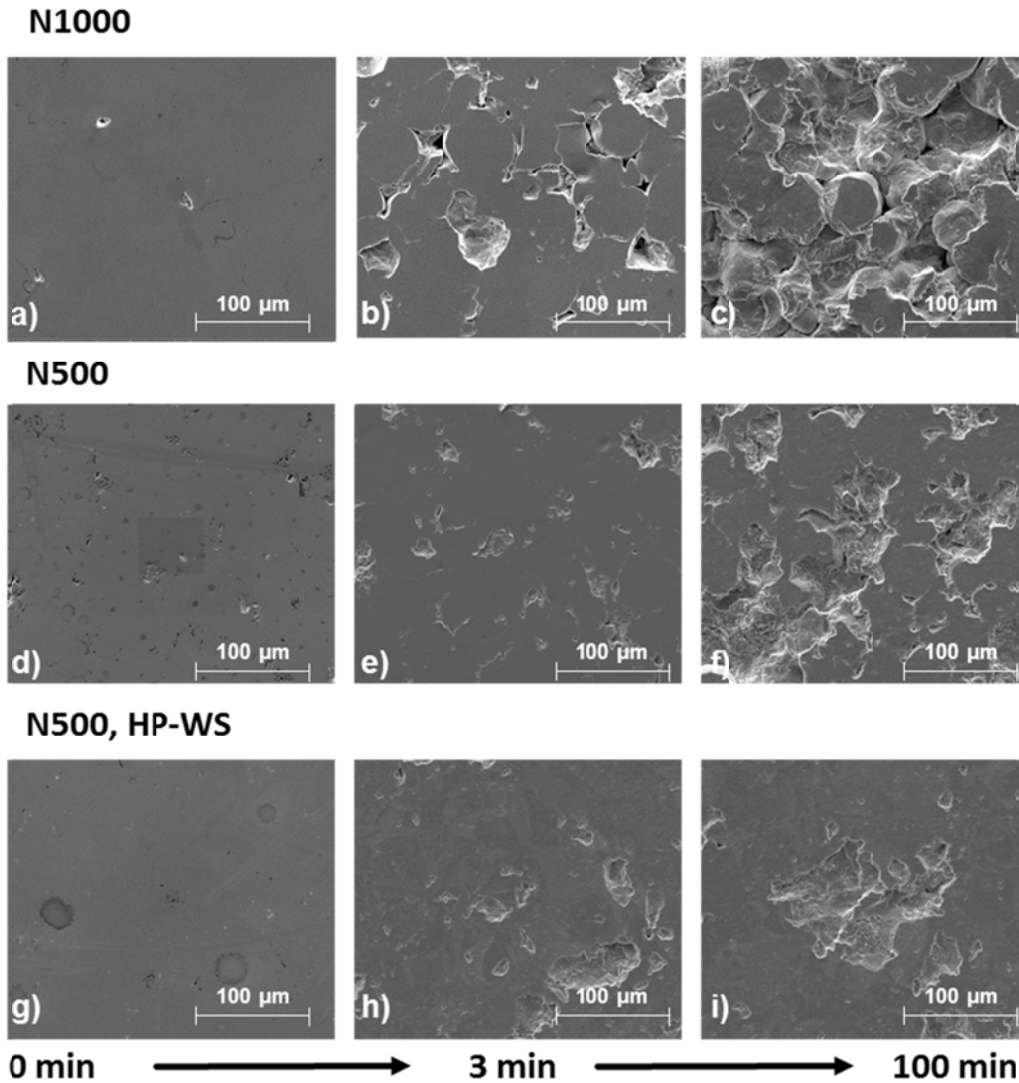


Figure 83: Surface morphologies of selected warm sprayed bronze coatings in the as-polished state and after 3 min and 100 min of cavitation testing. Individual spray and testing conditions are given in the figure.

Figure 83 shows the surface morphologies of selected cavitated specimen after 0, 3 and 100 min of cavitation testing. All coating surface morphologies illustrate dense surfaces with almost no defects prior to cavitation testing (Figure 83a-c). After 3 min, first damages occur and result in material removal whereas different wear mechanism between the different deposition conditions can be detected. The coatings sprayed with high nitrogen flow-rates (Figure 83a, d, g), suffer from completely removed particles and fracture along particle-particle interfaces. Most of the fracture seems to occur between sprayed splats. For the lower nitrogen flow-rates (Figure 83b, e, h), a significant higher amount of the originally polished surface is retained after cavitation testing. These coatings display adhering particles that are enclosed by ruptured material fractions. These topographies seem to correspond to trans-particle or inter-splat failure. Differences of wear mechanisms due to higher substrate temperatures cannot be detected and hence are not shown. For the cases of higher combustion pressures, only few particle shaped morphologies can be identified in the erosion pattern (Figure 83c, f, i), most of the material removal occurs over trans-particle fracture. As compared to low pressure warm-spraying, higher amounts of the originally prepared surface is retained.

5.7. Discussion

5.7.1. Influence of the Spray Conditions

The spray conditions comprise variations of the combustion pressure, the nitrogen flow rate and the substrate temperature. Firstly, the parameters sets determining particle impact temperature and velocity, i.e. combustion pressure and nitrogen flow rate, will be discussed and are summarized within the particle impact energy concept. Later, the influence of the substrate temperature will be considered.

Particle Impact Energy

The particle impact temperature and velocity can be transferred into a particle impact energy concept as introduced by Assad et al. for cold spraying [ASS16] and described in the previous chapters. For warm spraying of Ni-Al-bronze this energy concept allows for describing coating formation processes and for predicting coating properties, in a similar manner as the coating quality parameter η for cold gas spraying [KRE16, ASS11]. However, the results also showed that the concept has limits when side reactions come into play. Recrystallization and thus the reduction of residual stresses occur mainly after spraying as well as oxidation that cannot be explained by the particle impact energy concept.

Nevertheless, most coating properties can be discussed on the basis of the particle impact energy concept. The results in the previous chapters are already described as a function of the relative particle impact energy, assuming the velocity and temperature of particles with a mean diameter of 30 μm . Higher impact energies, either thermal or kinetic, allow for reduced porosity and enhanced coating properties like elevated tensile strengths, reduced cavitation erosion-rates as well as better electrical conductivity. These clear correlations confirm the hypothesis that both hotter and faster impact conditions improve particle deformability and thus coating formation. However, the concept might have limits for temperatures above the melting point and for too high impact energies that might be destructive or spread molten particles without adhering. A slight descending trend can be observed for the deposition efficiency, which reduces at high relative impact energies above 850 kJ/kg. In the present study, the mechanisms are similar to cold gas spraying since the bronze particles impact mainly in a solid state (compare chapter 5.1). Only small particles exhibit semi-molten fractions that influence coating formation. The higher deformation at elevated impact energies enhance the formation of adiabatic shear instabilities between adhering particles and improve coating cohesion [ASS16]. In addition, smaller and semi-molten particles can easily close pores and act as a kind of binder. Hence, less crack nuclei by non-bonded interfaces are present that could contribute to material removal by the cavitation treatment. In consequence, the damage mechanism changes from whole particle removal to fracture of particle parts with increasing impact energy. Highest particle impact energies could provide almost bulk like properties with respect to cavitation resistance.

The residual stresses turn from tensile for low-pressure warm sprayed coatings into marginal compressive stresses for an elevated combustion pressure. The tensile stresses base mainly on the thermal misfit between coating and substrate [LUZ11, ASS16, SAL14]. Compressive stresses, originating from the mechanical deformation during particle impact, might be reduced by recrystallization since the substrate and coating temperatures reach the recrystallization temperature of about 240 °C even for high nitrogen flow-rates. Elevated

combustion pressures might increase the mechanical influence and superimpose the thermal misfit and recrystallization.

The coating hardness remains within a narrow regime, which indicates the influence of recrystallization. The influence of the spray conditions on coating oxidation illustrates that the hotter spray conditions lead to higher oxide contents, which is attributed to the hotter gas stream but also to enhanced substrate temperatures. The particle temperatures are rather similar, but as compared to low-pressure warm spray, the particles of high-pressure warm spray are exposed to the gas jet for shorter times, resulting in slightly lower oxide contents. Hence, oxidation occurs mainly at the hot substrate, as described in literature [KUR08, KIM09, DAV14].

Regarding coating adhesion, the particle velocity and temperature need to be considered separately. The particle temperature determines the degree of thermal softening or even partial melting. Low nitrogen flow-rates increase the particle temperatures and thus result in enhanced thermal softening of the feedstock powder. Hence, the hotter particles show a high flattening ratio but cause low deformation to the substrate. Consequently less adiabatic shear instabilities arise on the substrate side contributing to coating adhesion. Moreover, more pronounced jets at particle sides are not necessarily in contact to the substrate surface. As compared to the particle temperature, the particle velocity has a higher influence on particle adhesion. Coatings sprayed with high-pressure warm spray show better adhesive strengths. An elevated particle velocity can generate larger areas of shear instabilities and thus improve bonding [ASS16].

An influence of the different spray parameters on the crystallographic coating structures could not be observed. As compared to the feedstock powder, all coating structures show a reduction of martensite. Similar to cold gas spraying (chapter 4.8.3), the martensite seems to be partly converted by strain-induced transformation processes as introduced in literature for MCrAlY [BOR14].

Substrate Pre-Heating

This part aimed to enhance coating properties by reducing amounts of non-bonded interfaces and gain a high cavitation resistant and good adhering coating. Hence, the influence of elevated substrate temperatures was examined.

The results demonstrate that cohesive properties like ultimate tensile strength, electrical conductivity and the cavitation performance show only minor differences between pre-heated and not pre-heated specimen [WAT14]. Figure 84 shows the recorded substrate temperatures for the first few minutes of coating deposition. Already after 4 to 6 passes (out of more than 40) the substrate temperature of not-pre-heated experiments reaches a steady temperature regime between 220 °C and 240 °C. Probably, the substrate surface temperature is even higher since the measurements were conducted within the substrate, applying air cooling to the specimen. Tests without air-cooling showed substrate temperatures of 300 °C for the cold (N1000) and 340 °C for the hot (N500) spray conditions. These observations allow for the conclusion that pre-heating mainly affects the first impacting particles on the substrate, as observed by Villa et al. for cold gas spraying of titanium [VIL15, LIS13]. For coating formation only a gain of 60 °C to 80 °C in temperature would contribute to differences in coating properties.

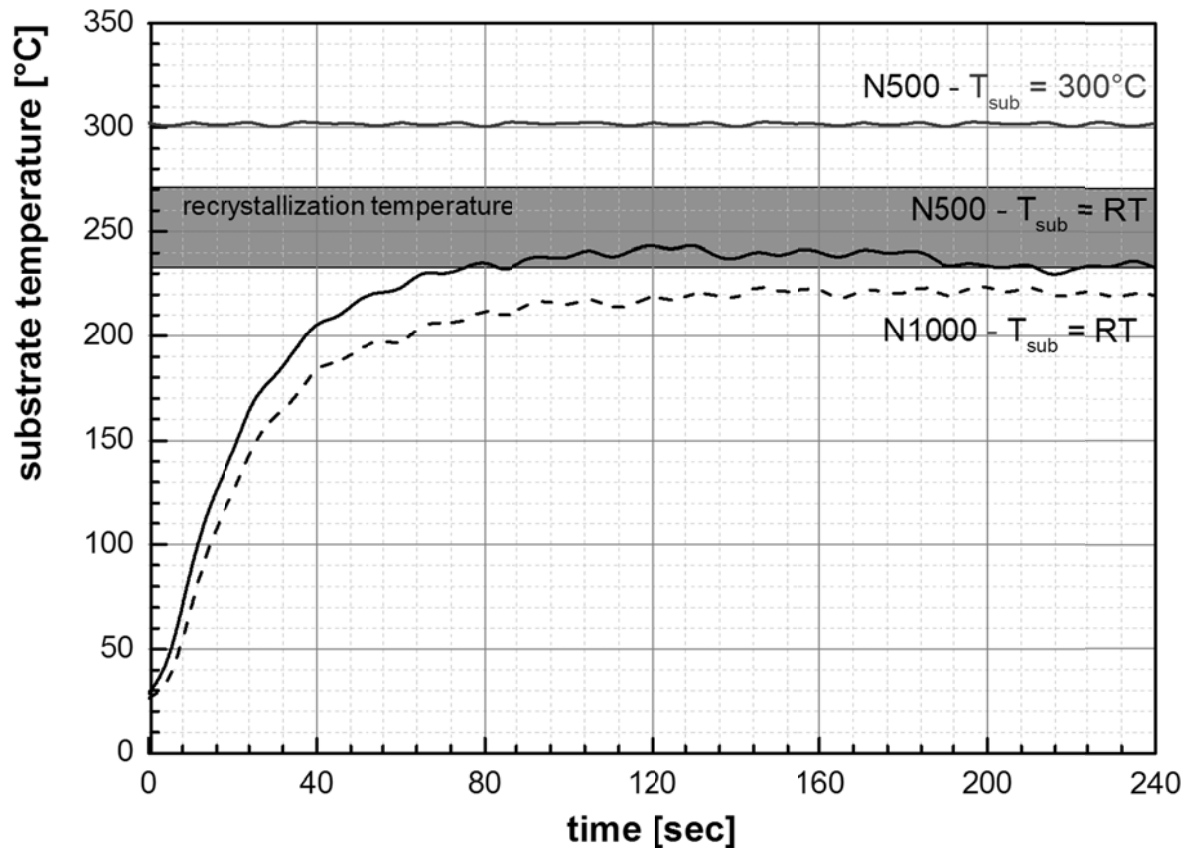


Figure 84: Substrate temperatures plotted over the time during spraying. The steady state coating temperature could reach the recrystallization temperature regime.

The benefits of substrate pre-heating for depositing the first layer were proven by observing elevated amounts of adhering particles on the wipetest samples and the better bond strengths. The thermally softened substrate allows for enhanced formation of adiabatic shear instabilities on the substrate side and improves bonding. This was observed for the cavitated wipe-test specimen, but also for the coating adhesion tests. Understanding the adhesive properties is rather complex, and has to consider effects by different nitrogen flow-rates on pre-heated and not pre-heated substrates. On not pre-heated substrates the hotter spray conditions reduce adhesion strength whereas on pre-heated substrates the adhesion improves at elevated spray temperatures. This may be explained by the complex relation between the particle and the substrate strength. If both partners exhibit equal strength upon impact, areas of shear instabilities would occur equally at both sides and contribute to bonding. If both sides have a high strength, particles decelerate faster and pronounced areas of shear instabilities arise in shorter time scales in a very small and confined area [KLA16]. If one partner is softer, the area of shear instability and thus the necessary requisite for bonding is less confined and might reduce adhesion. This is in line with the results of this study. Spraying with cold conditions (N1000) on cold substrates leads to better adhesion. The particles keep a higher strength and cause more deformation and areas of shear instabilities in the contact zone to the substrate. In contrast, spraying with hotter conditions, particles of lower strength carry most of the deformation and only barely deform the substrate. Adiabatic shear instabilities occur most prominently on particle sides, and are not necessarily in contact to the surface, which results in lower adhesion strength. When using pre-heated substrates, substrate and particle strength at higher particle temperatures suit better and result in a more uniform distribution of shear instabilities at common interfaces.

Summing up, best conditions for coating adhesion can be realized when particles and substrate have a similar strength at adjusted temperatures.

Besides adhesion, the elevated substrate temperature seems to affect the oxide content within the coating. Probably all layers suffer from oxidation effects and the substrate temperature is about 60 to 80 °C degrees hotter for the experiments with substrate heating. Hence, even after spraying the stored heat would contribute to oxidation.

As compared to non-pre-heated substrates, pre-heating causes slightly higher coating stresses and a slightly reduced coating hardness at otherwise same spray conditions. The results vary within a narrow regime since the substrate temperature within all experiments exceeded the recrystallization temperature (compare Figure 84). Nevertheless, the temperature difference between pre-heated and not pre-heated substrates might accelerate diffusion and recrystallization, and thus explain the slightly higher tensile stresses and reduced coating hardness.

5.7.2. Properties with Influence on Cavitation Performance

The results show that warm spraying can provide highly cavitation resistant coatings with close to bulk properties. For analysing the critical influences on cavitation performance, selected correlations between coating properties and the cavitation-rates are displayed in Figure 85.

As expected, the correlations show that a high cohesive strength (Figure 85a) is essential for attaining a high cavitation resistance. Dependencies of the ultimate tensile strength agree well with those of the electrical conductivity (Figure 85b). The correlation to strength is confirmed by SEM micrographs of the cavitated surfaces (Figure 83). At low cohesive properties, whole particles are removed and fracture occurs mainly at particle-particle interfaces. In contrast, coatings with a high cohesive strength are more cavitation resistant and show only minor losses by whole particle removal. On the one hand, the cavitation performance is dominated by the bonding of particles. On the other hand, the feedstock, means the actual materials properties, become more prominent and can turn out to be the dominating factor, if excellent bonding and coating cohesion can be facilitated. Concomitantly, porosity and non-bonded areas play an equally important role, since non-bonded particle-particle interfaces act as crack nucleation sites and contribute to material loss [HOU14, BAR05, TAN03, TAN05, AL-02]. Figure 85d shows the relation between cavitation resistance and oxide contents, not revealing observable trends. Probably the oxide content is too low or the oxides are too small and finely dispersed to influence cavitation performance. The correlation with the residual stress in Figure 85e illustrates separate trends for low-pressure and for high-pressure warm spraying. Both trends display better cavitation performance at lower stresses. Comparing high-pressure and low-pressure warm spray trends, the higher kinetic energy and thus coating cohesion seems to superimpose effects by compressive stresses. The correlation to the coating hardness as shown in Figure 85f, not allows for deriving certain trends. The regime between 395 HV0.3 and 423 HV0.3 is quite narrow and represents mainly influences by recrystallization, instead of material hardening.

Summing up, coating cohesion is the most important coating property that determines its cavitation resistance. Good coating cohesion is only obtained in the absence of non-bonded internal interfaces and pores.

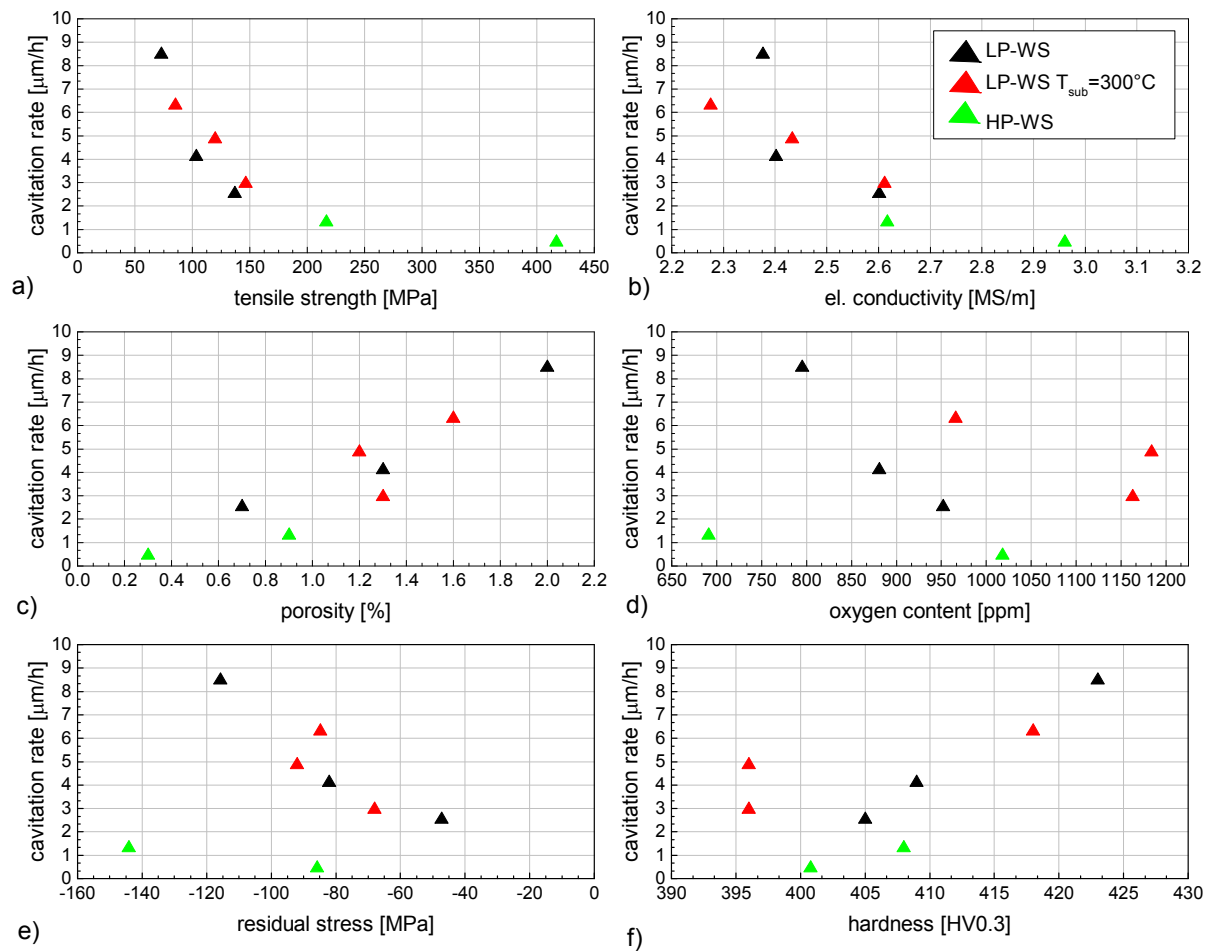


Figure 85: Correlations of cavitation rates with tensile strength (a), electrical conductivity (b), porosity (c), oxygen content (d), residual stress (e) and the coating hardness (f).

6. High Velocity Oxy-Fuel Spraying of Ni-Al-Bronze

High velocity oxy-fuel spraying was used as a reference method, using mainly liquid impact conditions in contrast to cold spraying or warm spraying.

6.1. Simulation

Within this project, as before for warm spraying, particle temperatures and velocities, as calculated by computational fluid dynamics, were calculated and supplied by Hiroshi Katanoda from Kagoshima University, Kagoshima / Japan. Information on particle impact conditions should supply a better understanding of coating formation. The simulations focussed on the influences of using air or nitrogen as cooling gas and the development of particle temperature and velocity at spray distances of 250, 300 and 350 mm. The simulations considered that the oxygen content of air as cooling gas completely participates in combustion. In real conditions that might be not fulfilled, resulting in lower λ -values, thus temperatures should be treated rather as an upper estimate. The oxy-fuel ratio λ was kept at $\lambda = 0.63$ and not varied in the simulations. Here the literature allows forecasting general trends by varying oxy-fuel ratios [KRE00B, KRE03]. Highest flame temperatures are expected for $\lambda = 0.8$. Lower or higher oxy-fuel ratios, rich or lean combustion, result in lower temperatures. In the present study, λ was varied between 0.5 and 0.8. A variation in the lean regime ($\lambda > 0.8$) would have the risk by the excess of oxygen [KRE03].

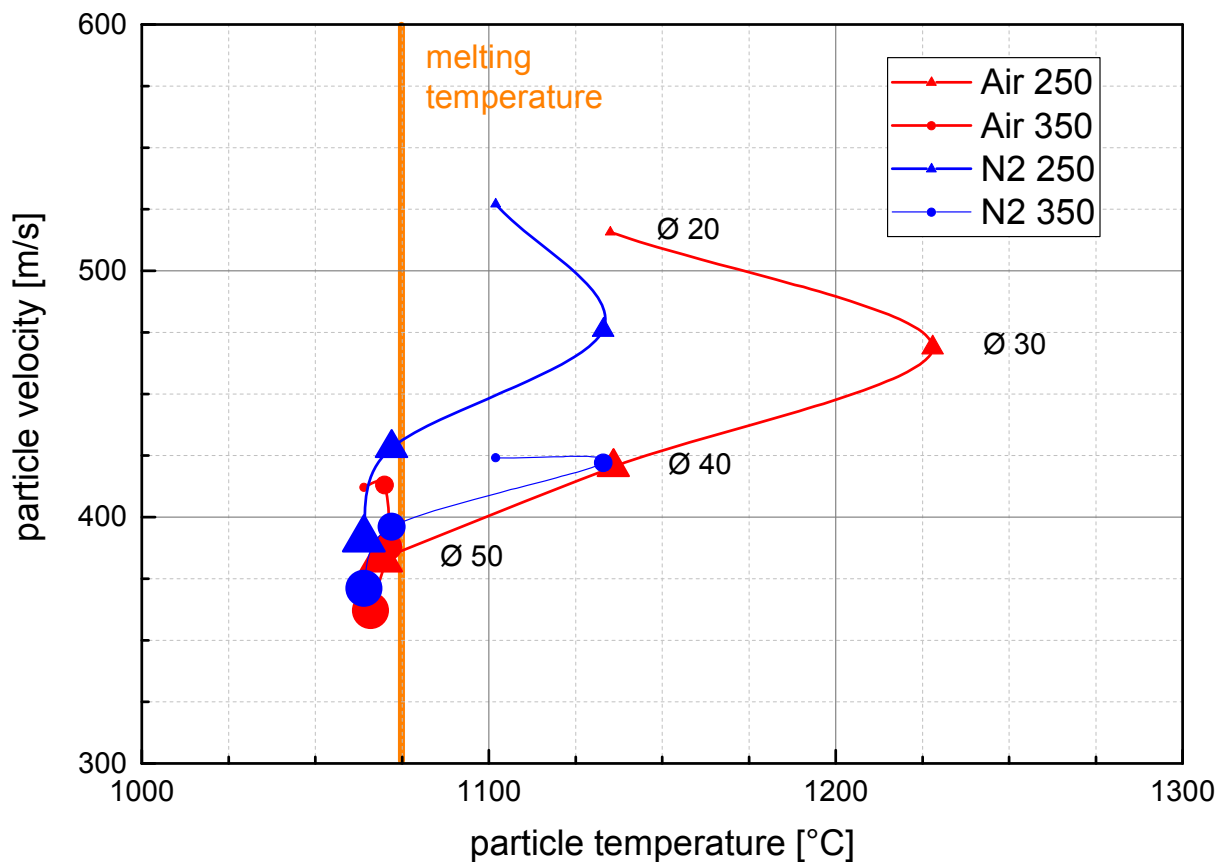


Figure 86: Calculated particle impact conditions during HVOF-spraying with nitrogen or air as cooling gas at spray distances of 250 and 350 mm, respectively.

Simulation results considering the influences by spray distance and cooling gases on particle velocity and temperature are illustrated in Figure 86. The algorithms used for cold spraying,

cannot be applied to thermal spraying, since respective η -values for liquid impacts reach infinity. The calculation reveal that operating at $\lambda = 0.63$ results in particle temperatures in a narrow regime to the melting temperature. A short spray distance of 250 mm for both air and nitrogen as cooling-gas allow for exceeding the melting temperature. Spraying with nitrogen instead of air as cooling gas results in lower particle temperatures. The particle velocities are similar for both cooling gases. Spraying at a distance of 350 mm, the particle temperatures and velocities are similar and vary within a narrow regime for all particle sizes. The particle temperatures are close around the melting temperature. Generally, bigger particles reach lower temperatures and velocities than smaller ones. For a spray distance of 250 mm, particles with a size of 30 μm achieve highest particle temperatures.

More details on particle heating and cooling over the axial path through the nozzle and the free jet are given in Figure 87a and b by calculated fractions of molten particle for different particle sizes of air-cooled (a) and nitrogen-cooled conditions (b). Both figures illustrate rapid heating and melting of particles with sizes below 50 μm . Large particles of 50 μm and larger do not melt completely within the process and stay in a semi-molten state. After a certain distance from the nozzle exit, particles begin to cool down and to solidify. Very small particles below 10 μm cool very rapidly within the gas stream and impinge in the solid state. Particles with sizes between 20 to 40 μm cool less rapid and impinge semi-solid. Particles of around 30 μm reach highest temperatures and own enough thermal inertia to keep the molten state until impacting. The observed trends concern both, the air and the nitrogen cooled conditions. The comparison nevertheless shows that the overall lower temperature by using nitrogen as cooling gas should result in a lower molten particle fraction than the use of air.

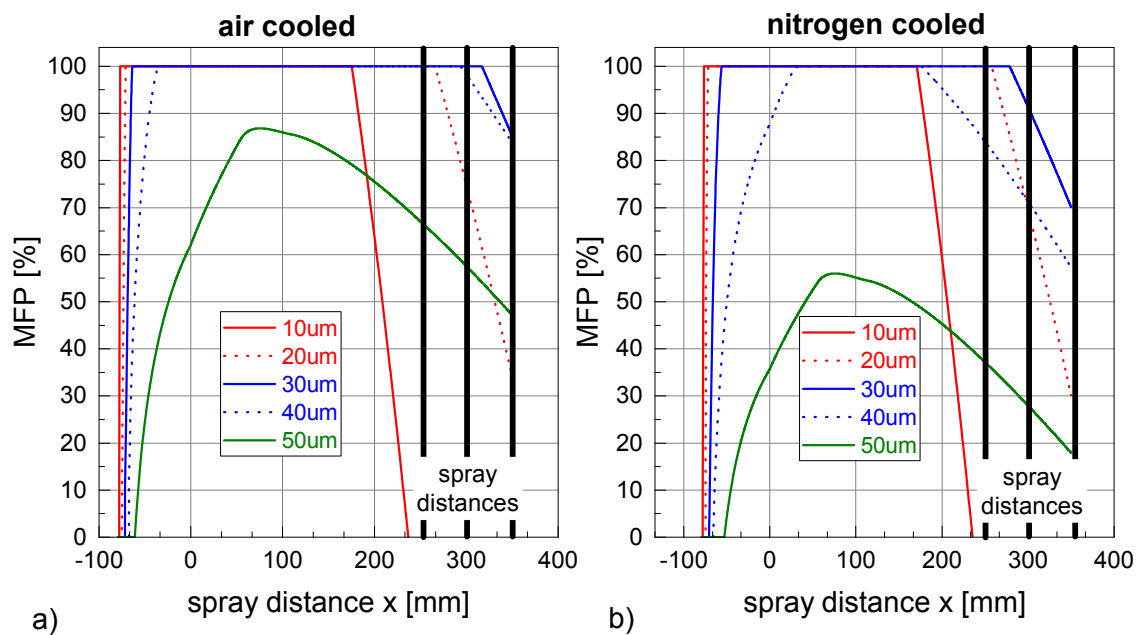
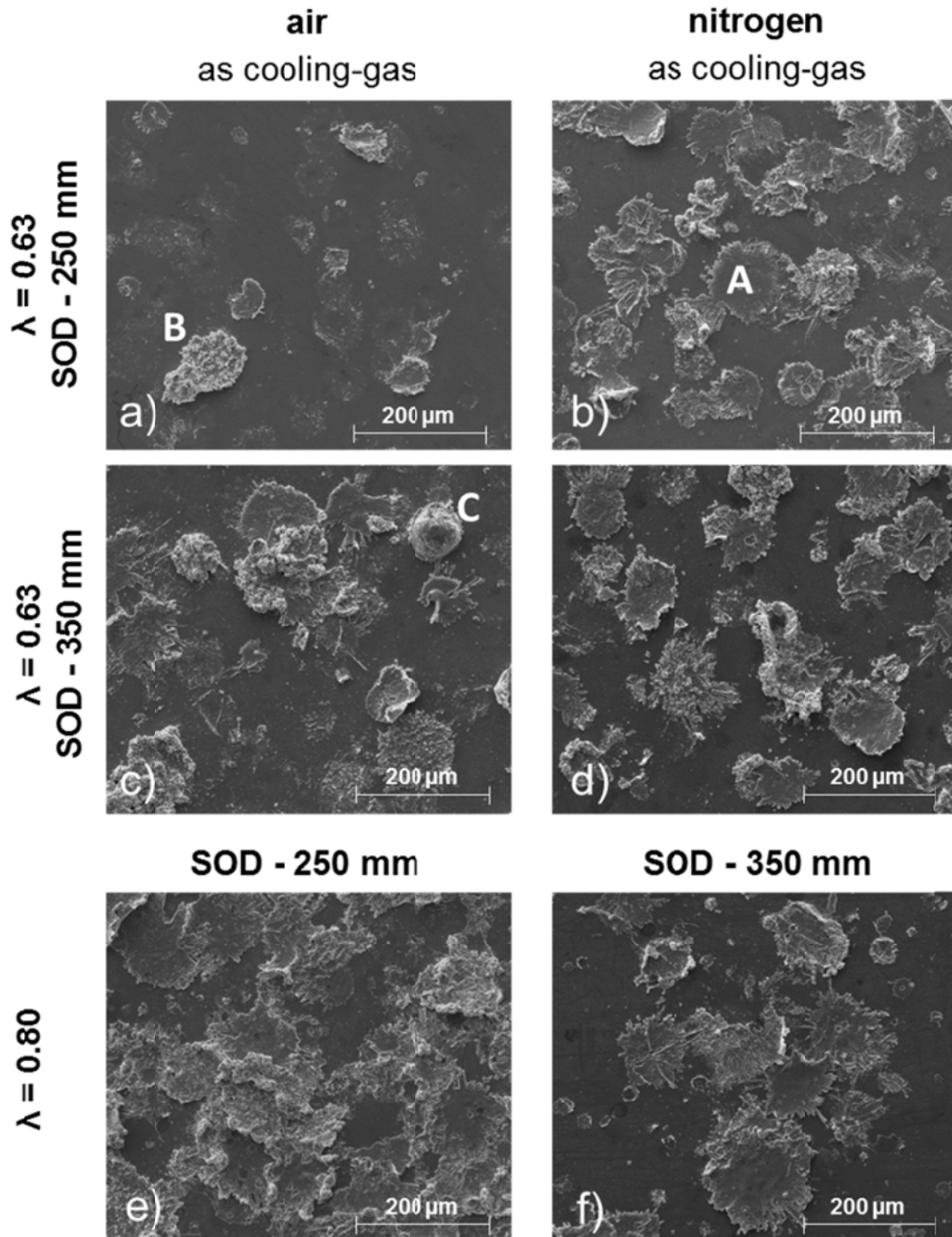


Figure 87: Calculated molten fraction particle over the axial path through nozzle and free-jet showing the difference between air (a) and nitrogen (b) as cooling gas. Both simulations show that particles above 50 μm are not completely molten and that particle smaller than 20 μm cool rapidly in the free-jet. The powder injection was 200 mm before the nozzle exit.

6.2. Particle Impact Behaviour and Deposition Efficiency

The impact morphologies of the HVOF sprayed NAB hard particles were evaluated by SEM to analyse particle deformation and to understand coating formation and respective properties. In particular, information regarding the molten fraction particle can be derived. Figure 88 shows typical particle impact morphologies of NAB hard particles sprayed with air or nitrogen as cooling gas for spray distances of 250 mm and 350 mm at $\lambda = 0.63$.



For Figure 88: Particle impact morphologies of HVOF-sprayed NAB hard particles on steel GL-A at various spray conditions. The left column concerns the use of air as cooling gas, the right one the use of nitrogen.

For coatings sprayed with $\lambda = 0.8$, the stand-off distance for air as cooling gas is 250 mm and for nitrogen as cooling gas is 350 mm. The different impact morphologies can be distinguished into type A (completely molten), type B (partially molten) and type C (solid

impacts). Figure 88a shows NAB hard particles sprayed with air as cooling gas at a spray distance of 250 mm and a $\lambda = 0.63$. The surface shows few adhering particles on the substrate which occur as partially molten with minor solid fractions within the molten matrix (type B). However, many bright splats indicate impacts of bronze particles that left minor remnants on the substrate. When increasing the spray distance to 350 mm (Figure 88c) and thus decrease particle impact temperatures, almost all particles adhere on the substrate. Most of the morphologies appear as semi-molten. In addition to that, also highly flattened and almost completely molten particles of type A are present that show frayed rims and spread bronze material around them. Besides molten or semi-molten particles, some particles seem to impact in the solid state (type C). Spraying with nitrogen as cooling gas at a spray distances of 250 mm (Figure 88b), most particles adhere on the substrate and indicate semi-molten morphologies (type B) with fringes. Spraying at 350 mm stand-off distance does not reveal significant differences regarding splat formation (Figure 88d), most particles being molten or semi-molten. Also at this spray distances, in comparison to experiments with air as cooling gas, more splats adhere on the substrate and indicate more homogeneous viscous deformation. At elevated oxygen-fuel ratios ($\lambda = 0.8$) and thus higher spray temperatures, Figure 88e and f show more molten impact morphologies (type A). Splats sprayed with air as cooling gas (SOD: 250 mm) indicate rather rough surfaces. In contrast, the impacted particles sprayed with nitrogen as cooling gas (SOD: 350 mm) illustrate to some extent more uniform and flat splat surfaces. However, all adhering splat would contribute to coating formation.

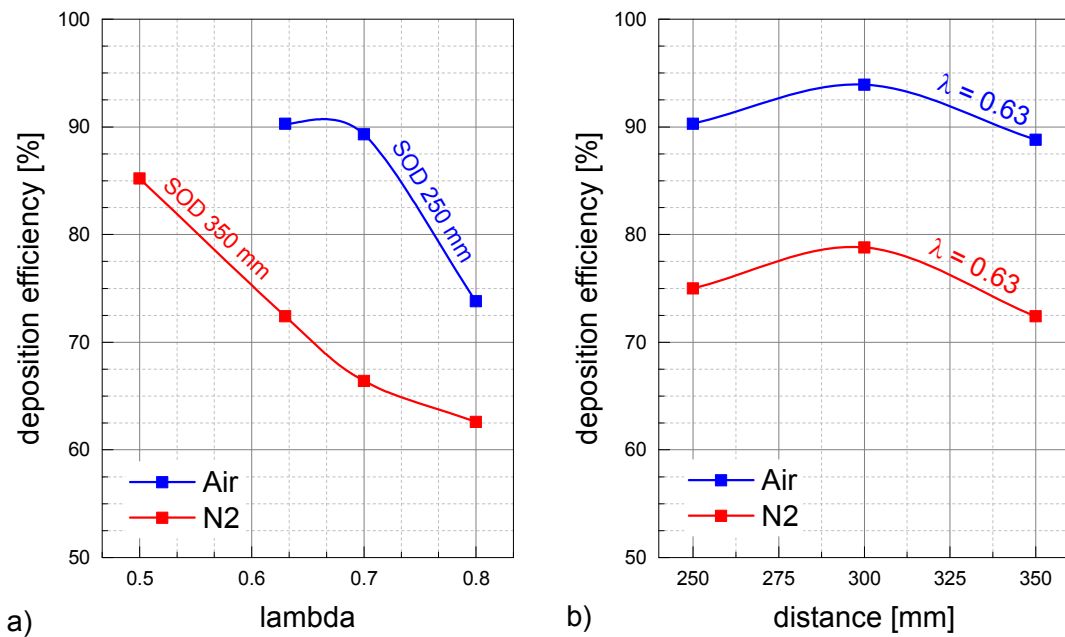


Figure 89: Coating deposition efficiency of HVOF sprayed NAB hard coatings as a function of λ and the spray distance for nitrogen and air as cooling gas.

The measured coating deposition efficiencies of the HVOF-sprayed NAB hard coatings are shown in Figure 89a and b as a function of λ and the spray distance for nitrogen and air as cooling gas. The influence of λ (a) shows higher deposition efficiencies when spraying with air as cooling gas as compared to the use of nitrogen as cooling gas. For both cooling gases, increased λ -values reduce the deposition efficiency. Hotter and faster particle impact conditions might cause splashing and hence reduce the amount of adhering particle fractions. The influence of the spray distance in Figure 89b illustrates a maximum at a spray distance of 300 mm. Here the particle temperatures seem to play a role. The deposition

efficiency at too short spray distances could suffer from molten or highly semi-molten particles that spread upon impact. At too high spray distances, the deposition efficiency may be influenced by already solidified particles that do not adhere on the substrate or previous layers.

6.3. Coating Microstructures, Phase Composition and Residual Stresses

Coating microstructures were examined to understand coating formation processes focusing on particle deformation and coating cohesion. Thus, also coating defects like porosity and oxygen content were analysed, as well as electrical conductivity, coating phase contents and residual stresses.

Figure 90 shows selected microstructures of HVOF-sprayed coatings by using air or nitrogen as cooling gas for different spray distances and variations of the oxygen-to-fuel ratio. Figure 90a displays the microstructure of a coating sprayed with a low oxygen-fuel ratio ($\lambda = 0.63$) at a short spray distance of 250 mm. The microstructure contains partly molten and completely molten particles accompanied by pores (black) and oxides (grey). Partly molten and the few solid impacted particles show a high flattening ratio and are surrounded by minor amounts of oxides. The pores show different sizes but occur mainly above semi-deformed and thus hard particles. In between, areas occur shattered with numerous small pores. When using the same oxygen-fuel ratio but nitrogen as cooling gas and thus colder spray conditions, the microstructure appears to some extent more homogeneous and less porous (Figure 90b). Few larger particles exhibit low deformation and seem to impact in the solid state. Smaller particles appear molten and allow for closing gaps and pores. Nonetheless, areas containing small pores are detectable too. When increasing the spray distance, the coating sprayed with air as cooling gas (Figure 90c) shows a similar amount of pores and non-bonded areas as at a shorter distance. Some large particles that impacted in the solid state exhibit cracks. In contrast to this microstructure, the one sprayed with nitrogen as cooling gas at a spray distance of 350 mm is more homogeneous and contains only a small amount of pores and oxides (Figure 90d), although the impact conditions are within a comparable regime according to calculations.

Coatings sprayed at $\lambda = 0.80$ appear more homogeneous but darker as compared to those sprayed with lower λ -values. Probably more oxygen is dissolved within the bronze. For both cooling gases, the microstructures contain only molten or highly semi-molten particles, flattened to a high degree. Hence, the microstructure appears very dense, although minor amounts of pores are detectable. It should be noted here, that the contrast by optical microscopy not allows for a clear distinction of pores and oxides. Especially, the coating sprayed with nitrogen as cooling gas displays higher amounts of pores and oxides.

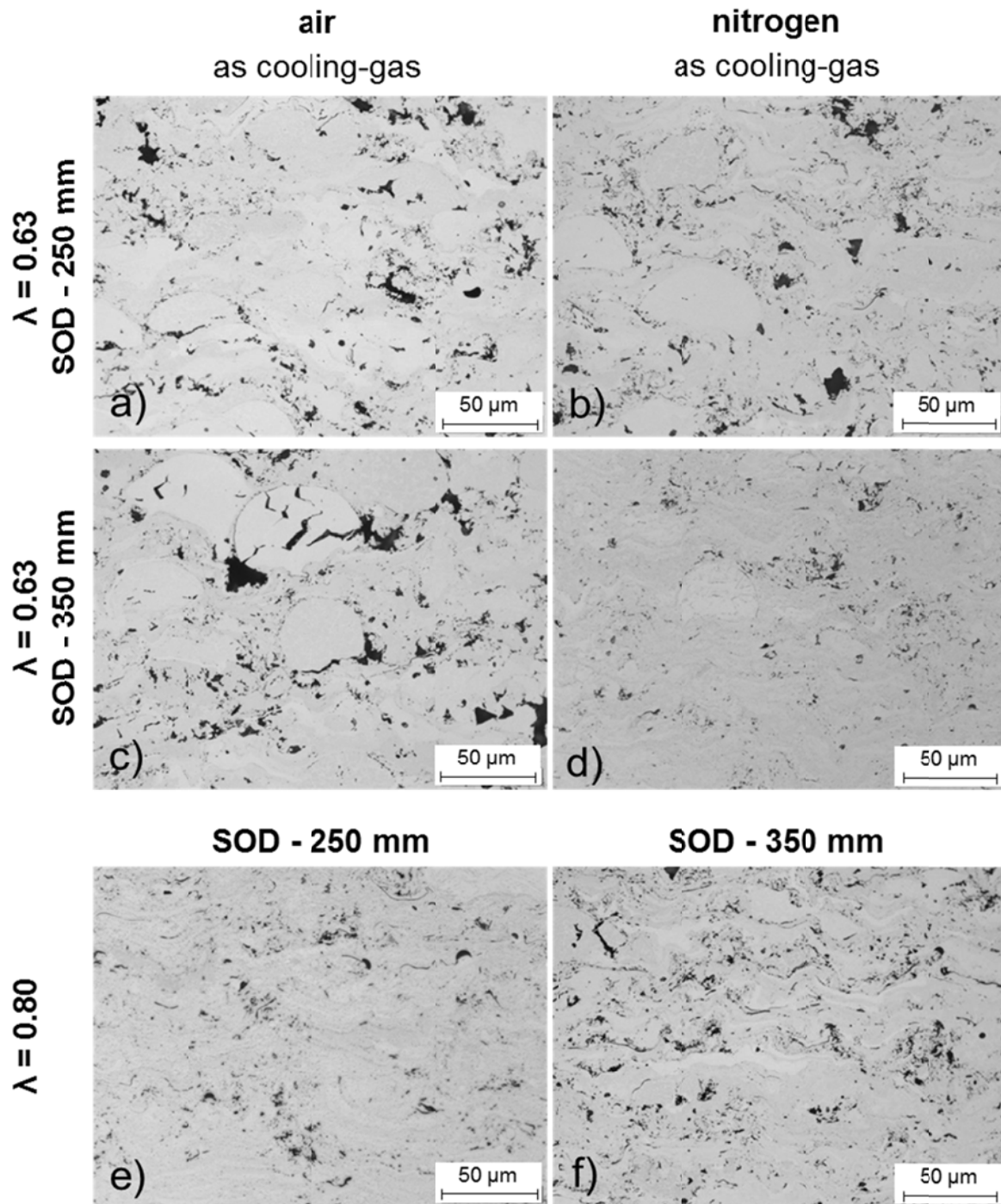


Figure 90: Microstructure of HVOF-sprayed NAB hard coatings sprayed at different spray distances and oxygen-fuel ratios with air and nitrogen as cooling gases.

The measured porosities are presented in Figure 91a and b for coatings sprayed with air or nitrogen as cooling gas. Nitrogen cooled coatings allow for up to 7-times lower porosities at similar spray conditions than those sprayed with air as cooling gas. For both types of cooling gas, the porosity reduces with increasing $\lambda = 0.65$ to $\lambda = 0.80$. At too high temperatures, a superimposed formation of oxides might disturb the formation of dense coatings. Higher process temperatures enhance particle melting and by liquid impacts closing of gaps. Figure 91b illustrates that porosity roughly decreases with increasing spray distances, showing a maximum for air cooling at a spray distance of 300 mm. The lowest porosity is obtained for a spray distance of 350 mm for both types of cooling gases. The differences in porosity might be attributed to the individual degree of molten fractions particles and the pick-up of oxygen during flight.

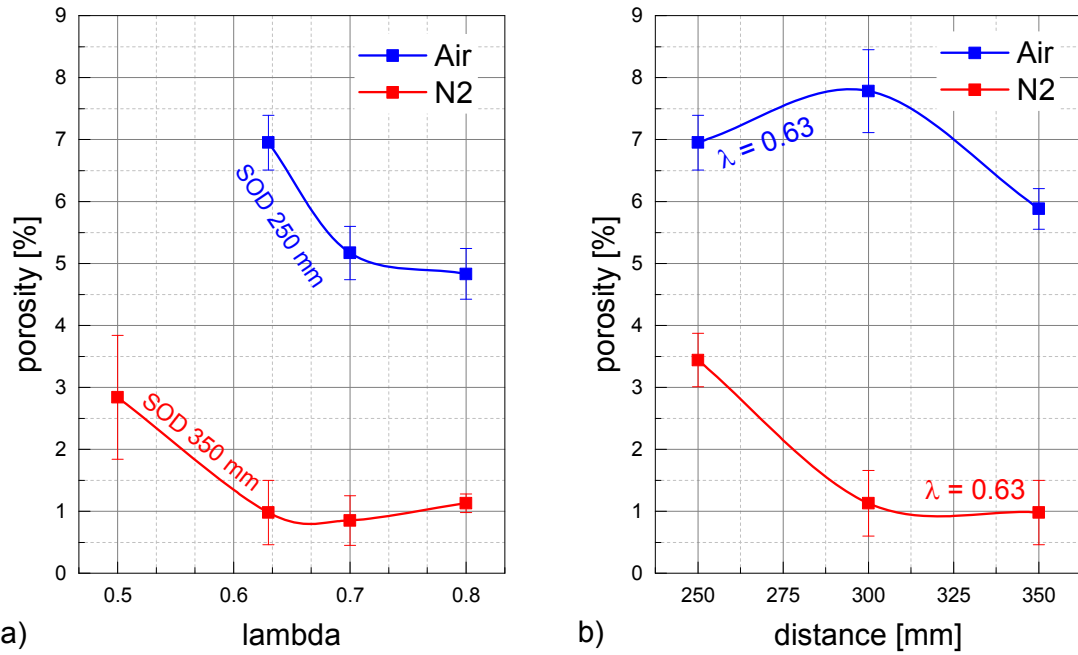


Figure 91: Porosity of the HVOF-sprayed NAB hard coatings produced at different spray distances and oxygen-fuel ratios with air and nitrogen as cooling gases.

The oxygen content of the HVOF-sprayed coatings is shown in Figure 92 as a function of λ (a) and the spray distance (b) for air and nitrogen as cooling gases. Both figures (a, b) show a higher oxygen content than those processed with nitrogen. Oxygen from the cooling gas, that not participates in combustion allows for enhanced oxidation within the hot flame. Spraying at elevated λ -values close to stoichiometric conditions increases process temperatures and enforces oxidation (a). In contrast, the spray distances (b) do not affect the oxide content. That might be attributed to oxidation mainly occurring in the hottest part of the flame.

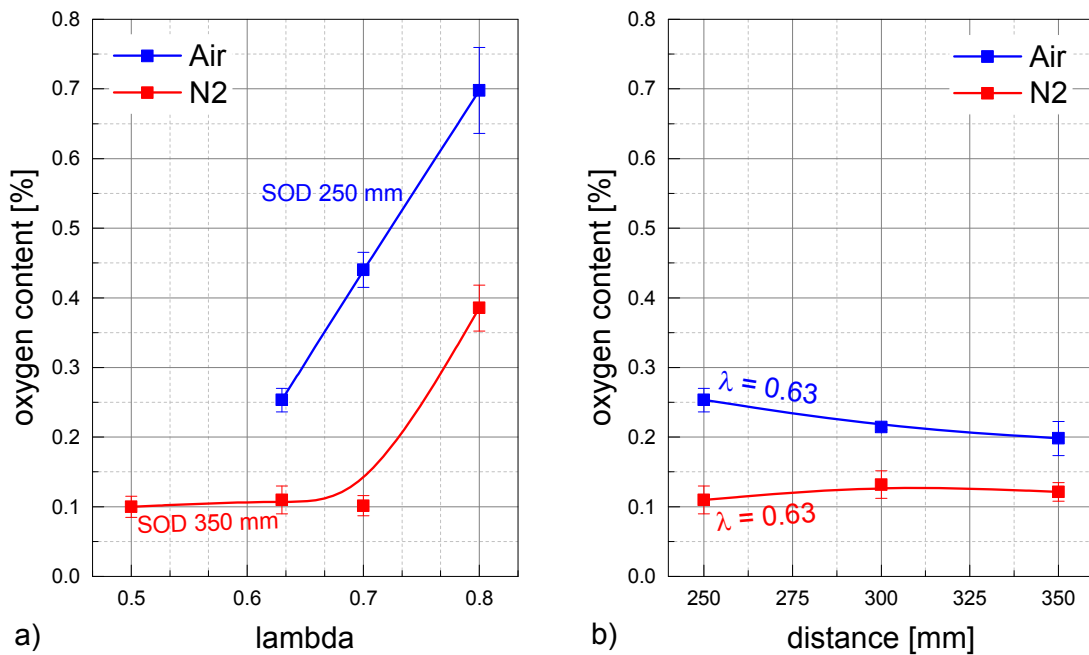


Figure 92: Oxygen content of the HVOF-sprayed NAB hard coatings produced at different spray distances and oxygen-fuel ratios with air and nitrogen as cooling gases.

The electrical conductivity is a general indicator for coating defects like pores, non-bonded areas, microstructural changes and contamination.

Figure 93 illustrates the electrical conductivity of the HVOF-sprayed NAB hard coatings sprayed over different oxygen-fuel ratios and spray distances for the different cooling gases. The results show comparable values for coatings sprayed with nitrogen and air as cooling gases. Applying higher λ -values and thus hotter flame temperatures provides improved electrical conductivity but a drop after the maximum at λ -values above 0.7. The contamination of oxygen might superimpose the effect that reduced members of pores and non-bonded areas reduce the electrical conductivity for higher λ -values. In contrast, the electrical conductivity as a function of the spray distance does not reveal any stronger variations and for both cooling gases remains within a narrow regime.

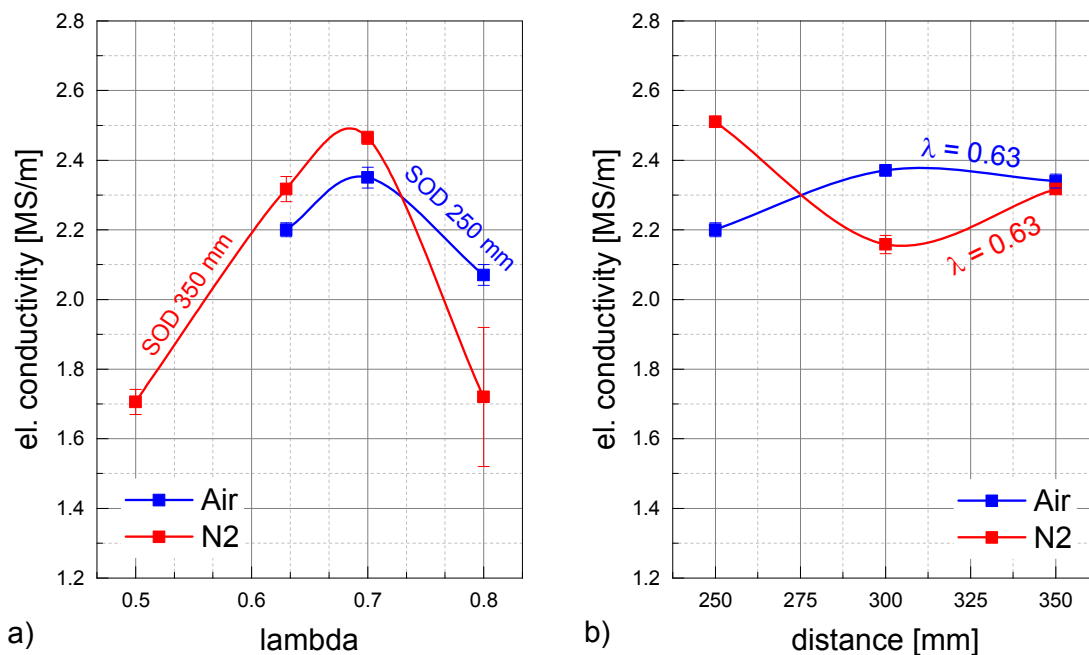


Figure 93: *Electrical conductivity of the HVOF-sprayed NAB hard coatings produced at different spray distances and oxygen-fuel ratios with air and nitrogen as cooling gases.*

Figure 94 shows the XRD-pattern of NAB-hard powder in comparison to the HVOF-sprayed coatings for different λ -values. The comparison between the powder and coating generally demonstrates that the martensite fractions are slightly reduced, but to less extend than for cold spraying or warm spraying. This may arise from remaining martensite fractions or by re-formation during rapid solidification on the substrate or already coated layers. Interestingly, the fraction of the γ_2 -phase rises with increasing λ only for nitrogen as cooling gas, probably higher process temperatures support the diffusion process and thus the formation of the γ_2 -phase. A comparable but less pronounced trend could be observed over the spray distance for both air and nitrogen cooled spray conditions (not shown). In addition, the XRD-pattern shows a peak widening from powder-pattern to coating-pattern since more lattice defects arise.

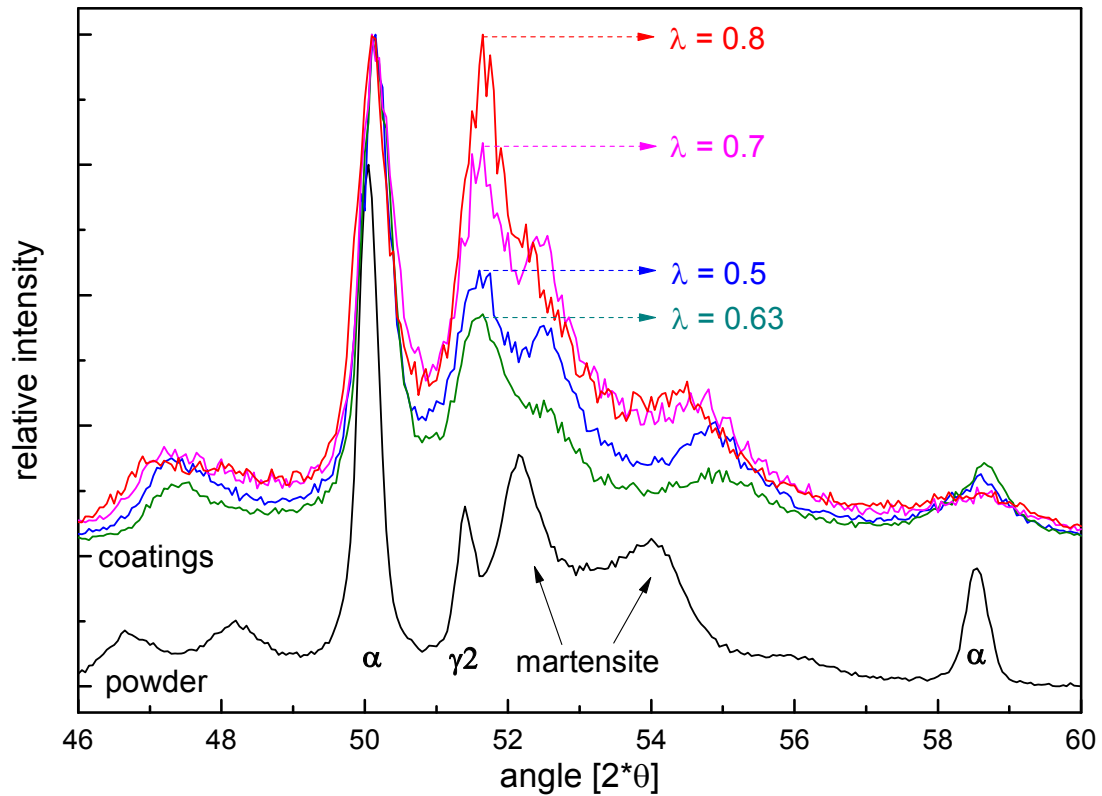


Figure 94: XRD-pattern between as-atomized powder (NAB hard) and HVOF-sprayed coatings with different λ -values at a spray distance of 350 mm and nitrogen as cooling gas.

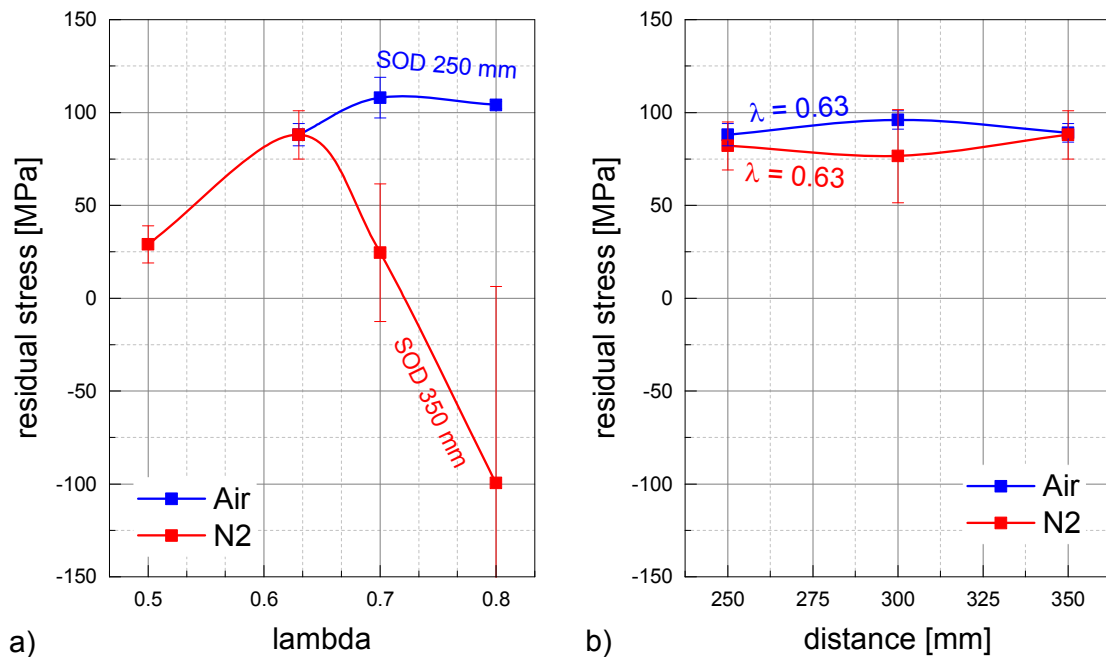


Figure 95: Residual stresses of the α -phase 222-lattice plane of the HVOF-sprayed NAB hard coatings produced at different spray distances and oxygen-fuel ratios with air and nitrogen as cooling gases.

The peak shifts of the α and γ_2 -phase allow for determination of residual stresses as shown in Figure 95a and b. For most of the spray conditions, residual stresses are tensile due to the mostly liquid impact and are rather similar for both cooling gases. Except at increased λ -values above 0.63 for nitrogen cooled conditions, the stress development indicates a trend from tensile to compressive stresses whereas air cooled conditions remain rather constant.

The phase analyses revealed a phase transformation towards the γ_2 -phase which has a lower physical density as compared to the α -solid-solution with increasing λ -values, resulting in reduced and slightly compressive stresses. The influence of the spray distance in Figure 95b shows minor influences on residual stresses.

6.4. Mechanical Properties

For distinguishing different influences on coating cavitation performance, the coating hardness and thus the resistance against plastic deformation as well as the coating cohesion were determined.

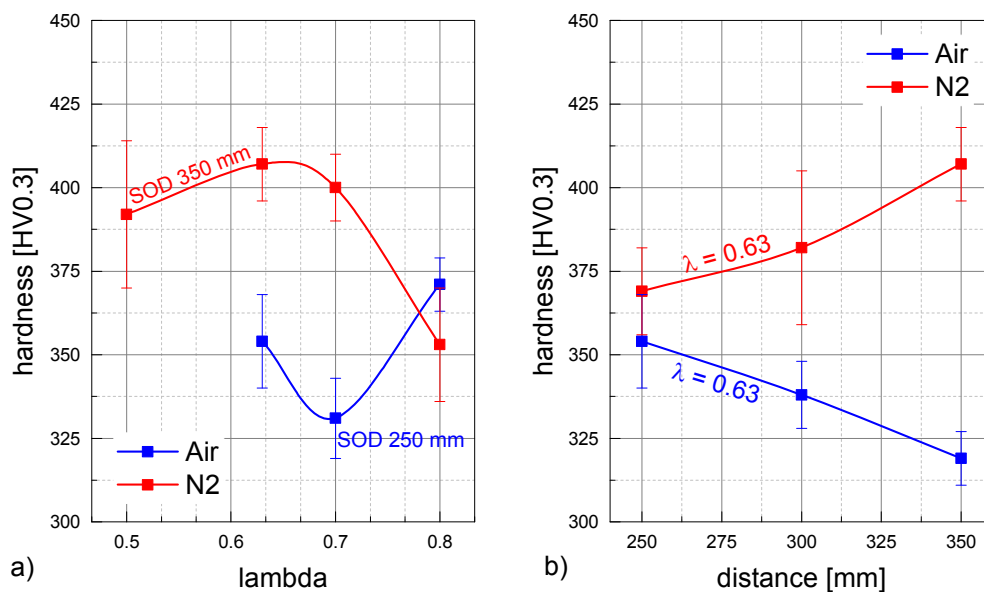


Figure 96: Hardness of the HVOF-sprayed NAB hard coatings produced at different spray distances and oxygen-fuel ratios with air and nitrogen as cooling gases.

Figure 96a and b show the coating hardness for different oxygen-fuel ratios and spray distances by cooling with air or nitrogen. When increasing the oxygen-fuel ratio in Figure 96a, different trends for air and nitrogen as cooling gas can be identified. Using nitrogen as cooling gas, an increasing λ -value shows a maximum hardness at about $\lambda = 0.66$ whereas using air as cooling gas results in a minimum at $\lambda = 0.70$. The trends in Figure 96b show that an increasing hardness with spray distance for nitrogen as cooling gas, whereas the hardness decreases with increasing spray distances for air as cooling gas. For interpreting the different trends, it should be considered that reduced porosity, increased oxide content or work hardening would enhance hardness. Lower porosity at larger spray distance together with work hardening might explain the trends using nitrogen as cooling gas. The results for air as cooling gas are to a higher content superimposed by oxidation and porosity distribution.

As a measure for coating cohesion, the coating ultimate tensile strengths is plotted in Figure 97a and b versus the oxygen-fuel ratio and spray distance for cooling gases air and nitrogen. In general, the coatings sprayed with nitrogen as cooling gas show higher tensile strength as compared to coatings sprayed with air as cooling gas. Increased λ -values (Figure 97a) and thus elevated flame and particle temperatures cause higher tensile strengths. Moreover, Figure 97b shows that strength increases with spray distances. Spraying with air as cooling gas results in slightly higher strengths at lower spray distances. The increase of strength with

λ and probably also spray distance can possibly be explained by reduced porosity and reduced amounts of non-bonded interfaces.

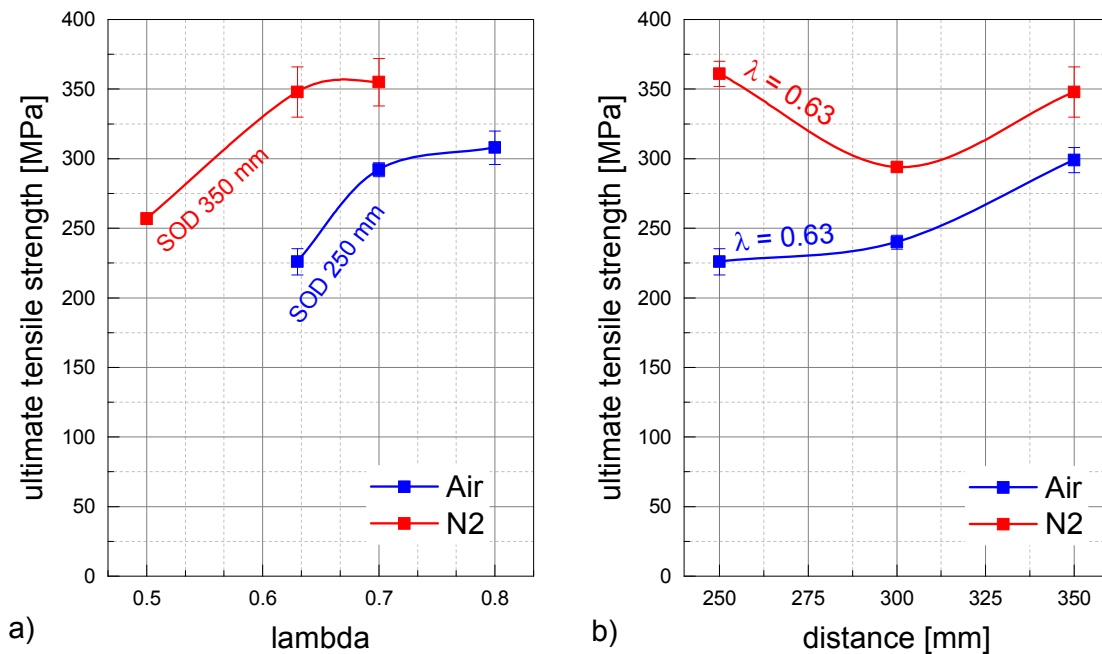


Figure 97: Ultimate tensile strength of the HVOF-sprayed NAB hard coatings produced at different spray distances and oxygen-fuel ratios with air and nitrogen as cooling gases.

6.5. Cavitation Behaviour

Analyses of the cavitation resistance were performed in defined time intervals to derive the cavitation rate from mass losses of the HVOF-sprayed coatings in accordance with ASTM G32-10 indirect method. For understanding the cavitation mechanism SEM analyses of surface topographies were subsequently applied. In Figure 102 a selection of surface morphologies after 100 min cavitation testing of HVOF-sprayed coatings is given. Figure 102a shows the surface morphology of a HVOF-sprayed NAB hard coating with air as cooling gas at a short spray distance of 250 mm after 100 min of cavitation testing. The surface is rough and reveals only few remaining areas of the polished surface but many deep holes by inter-splat failure. On the one hand, the microstructure displays unmolten and still spherical particles that show no material removal by the cavitation treatment. On the other hand some areas display a completely ruptured surface where no indication of single particles is detectable. Here material removal might occur by fatigue behaviour. At a larger spray distance of 350 mm (Figure 102c), the surface displays more of the original remaining polished surface areas and less remaining spherical particles. Some deeper craters are evident. Most of the material removal occurs by trans-particle failure, probably by fatigue. Figure 102b and d) illustrate surface morphologies of the same spray conditions as Figure 102a and c) but for using nitrogen as cooling gas. The surface morphologies show less material loss and more of the original polished areas than for the air cooled conditions. Here, no holes or whole removed particles are detectable. Similar to that, the morphologies in Figure 102e and f show for the elevated oxy-fuel ratio $\lambda = 0.80$ a rather homogeneous material removal, mainly on small length scales by trans-particle failure, probably by fatigue. In the direct comparison, the sample processed with air as cooling gas shows more events of complete particle removal.

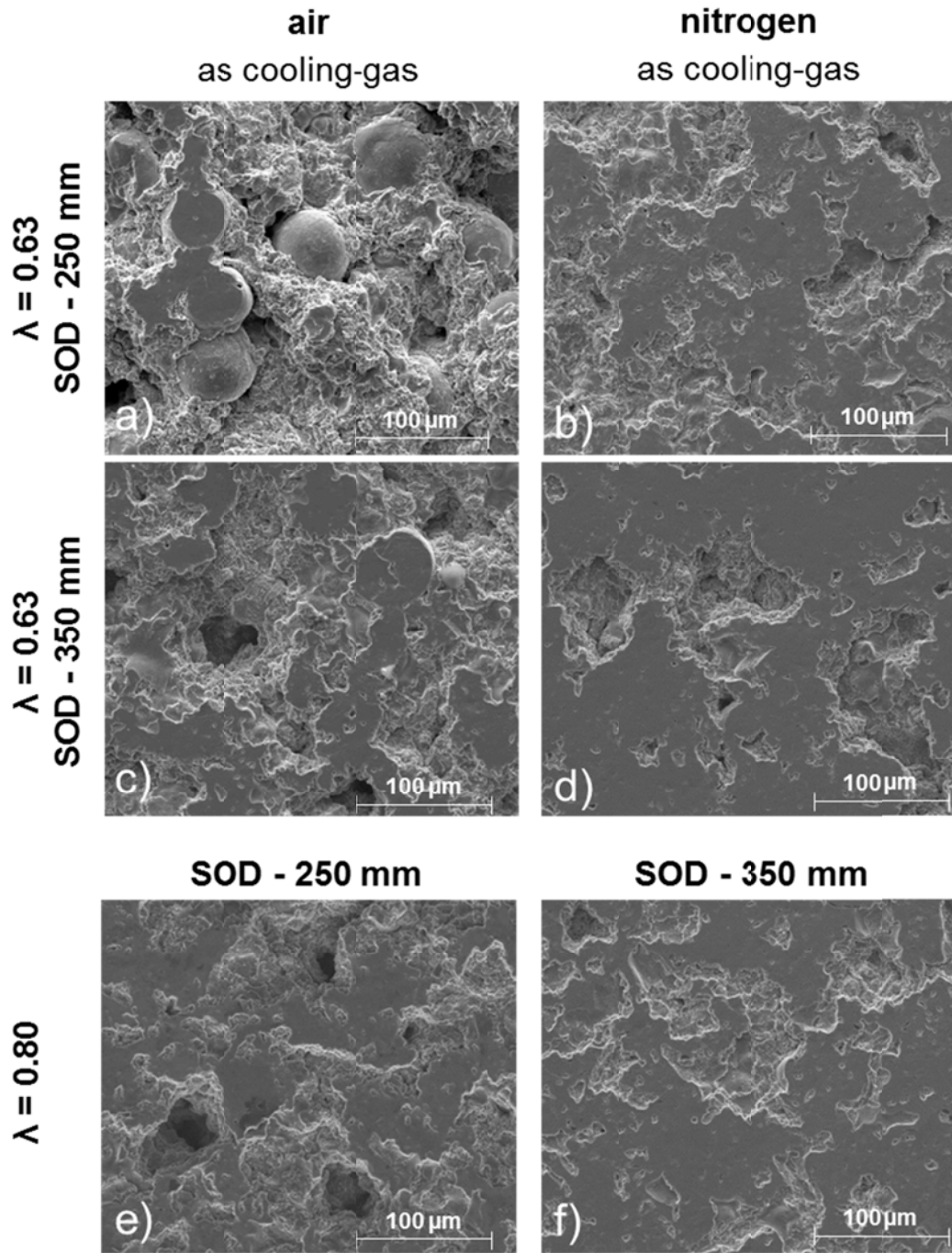


Figure 102: Surface morphologies after 100 min of cavitation treatment of HVOF-sprayed NAB hard coatings sprayed under variation of cooling gas, spray distance and oxygen-fuel ratios.

The cavitation erosion-rates are summarized in Figure 103a and b. The figures confirm the observations by SEM and reveal higher cavitation erosion-rates and hence elevated material losses for air as cooling gas. The cavitation rates decrease with increasing λ and increasing spray distance and indicate that hotter impact conditions are favourable. The higher cavitation rates by using air as cooling gas can be attributed to effectively lower temperatures and the presence of oxides.

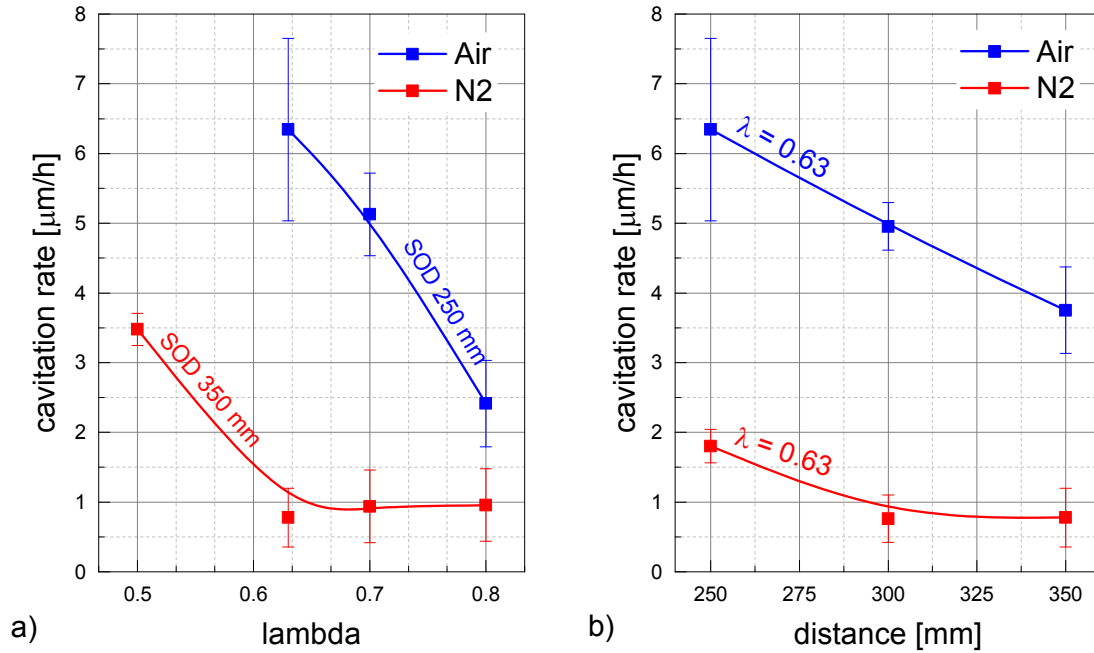


Figure 103: Cavitation erosion-rates of the HVOF-sprayed NAB hard coatings sprayed at different oxygen-fuel ratios, spray distances and cooling gases.

6.6. Coating Adhesion

Good coating adhesion is the necessary requisite for applications. Results on adhesive strength of NAB hard HVOF-sprayed coatings are summarized in Figure 98a and b. The figure indicates good adhesion for all spray conditions with strengths around 40 MPa. Coatings sprayed with nitrogen as cooling gas show generally a higher adhesive strength and different trend than those sprayed with air as cooling gas. As illustrated in Figure 98a, the adhesion strength by using air as cooling gas decreases for enhanced λ -values. For spraying with nitrogen as cooling gas, the bond strength increases until reaching a maximum at $\lambda = 0.7$. Too hot spray conditions seem to reduce adhesion strengths, either by surface oxidation or too fluid flow of impinging droplets. An increase of spray distance results in a higher bond strength for using nitrogen as cooling gas and in slightly lower bond strength by using air. The different trends again seem to be a matter of particle / droplet impact temperatures and associated flow, as well as oxidation.

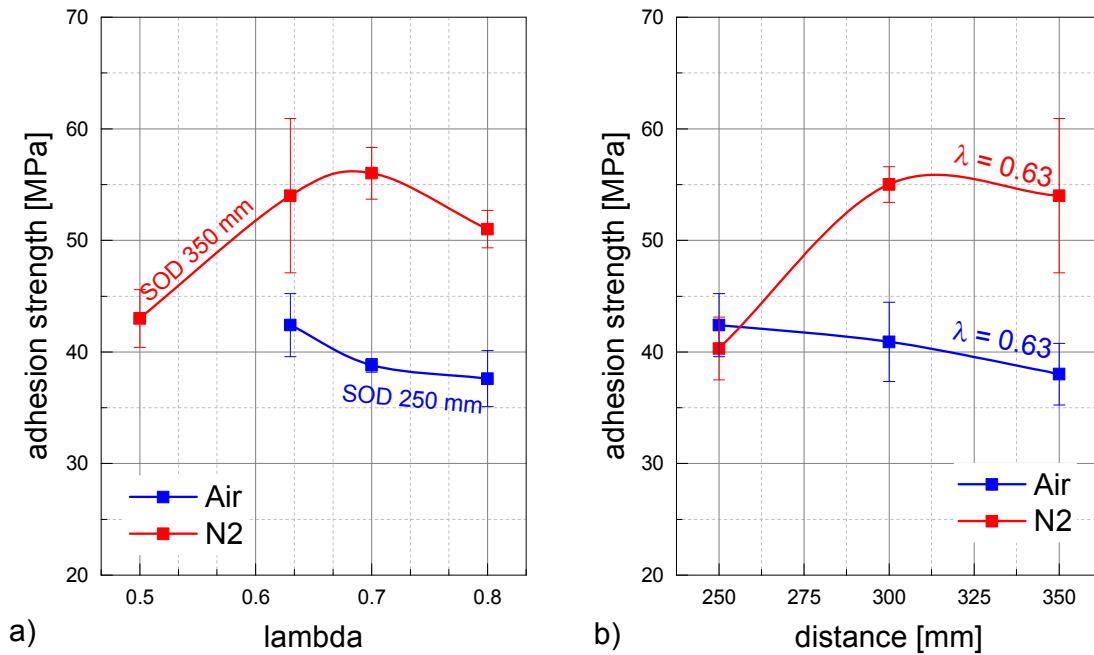


Figure 98: Coating adhesion of the HVOF-sprayed NAB hard coatings sprayed at different oxygen-fuel ratios, spray distances and cooling gases.

6.7. Discussion

6.7.1. Influence of the Spray Conditions

The results of the different HVOF-spray parameters sets are based on the oxy-fuel ratio λ , the spray distance and the cooling gases air and nitrogen. These parameter sets result in different coating properties, as will be discussed in the following paragraphs.

Influence of the Oxy-Fuel ratio λ

The normalized oxy-fuel ratio λ was varied from 0.5 to 0.8 within this study. The stoichiometric conditions, means optimal combustion, is at $\lambda = 1.0$ whereas highest flame temperatures are achieved at $\lambda = 0.8$ [RIC00]. The used range of λ -values should mainly influence spray temperatures and only slightly varying the gas velocities [KAW06]. In the results, this was proven for both nitrogen and air cooled spray conditions during HVOF spraying. In agreement with literature [LI04], too hot conditions reduce the coating deposition efficiency [LI04]. Liquid and fast impacting droplets might splatter and thus reduce the amount of adhering feedstock. For high λ -values, the single particle impact morphologies showed only few semi-molten fractions. Also within the coating microstructures, almost no semi-molten particles are detectable. Furthermore, for hotter spray conditions, the microstructures occur more homogeneous with fewer pores but include increasingly more dark areas that might be attributed to oxides as described in literature. The measured oxygen content confirms that by showing a drastic rise at $\lambda = 0.65$. This influences and reduces the electrical conductivity and seems to affect the residual stresses by volume or phase changes. Higher flame temperatures also result in increased substrate temperatures, allowing for diffusion and decomposition of supersaturated α -bronze. γ_2 -precipitations having a lower density than α -bronze then cause compressive stresses in the coating, being superimposed to the tensile stresses by thermal shrinkage. Elevated λ -values of up to 0.8 allow for enhanced inter-splat bonding and to ensure increasing coating strength. Probably

enhanced diffusion and liquid flow into pores and gaps provide improved cohesion as shown in literature for metal coatings [FAU14]. The improved inter-splat cohesion and thus coating strength determines the cavitation properties. The results demonstrate that the cavitation mechanism turns to show more trans-splat failure by fatigue and removal of coating fractions at higher flame temperatures. A higher oxide content which might enhance material removal, in this parameter regime is outbalanced by the high coating strength. In summary, cavitation properties close to bulk properties can be obtained by well-tuned HVOF spray conditions.

Influence of the cooling Gases Nitrogen and Air

The results of the coatings sprayed with comparable parameter sets in terms of λ revealed significant differences for using nitrogen or air as cooling gas. Probably two different aspects need to be considered. The experimental results reveal higher powder temperatures for coatings sprayed with nitrogen as cooling gas in comparison to the use of air in contrast to simulated impact conditions. Coatings sprayed with nitrogen as cooling gas showed more particle flattening (compare microstructures), lower deposition efficiencies and reduced porosity as well as higher tensile strength and thus improved cavitation performance. The schematic in Figure 99 summarizes the different effective gas flows to support possible explanations. Air or nitrogen as cooling gases were supplied with a flow-rate of 360 l/min, whereas 20 % of the air flow was considered to participate within the combustion process. For balancing the overall amount, to respective λ -values the individual oxygen flows were respectively reduced. This results in lower effective nitrogen flows and probably lower chamber pressure, in consequence reducing flame temperature [RIC00]. Moreover, the layout of the DJ2700 spray gun direct the cooling gas as shielding around the particles and along the nozzle walls. Not being ideally mixed in the combustion chamber, it can be assumed that not all of the oxygen is participating in combustion. The above argument might explain the offset of $\Delta\lambda \sim 0.1$ for significant rises in coating properties for using nitrogen instead of air as cooling gas. Moreover, the presence of oxygen in the shielding flow around particles could enhance oxidation. This could explain the higher oxygen content of coatings sprayed with air instead of nitrogen as cooling gas. This combination of reduced flame temperatures and enhanced contamination can explain the reduced coating properties by spraying with air instead of nitrogen as cooling gas.

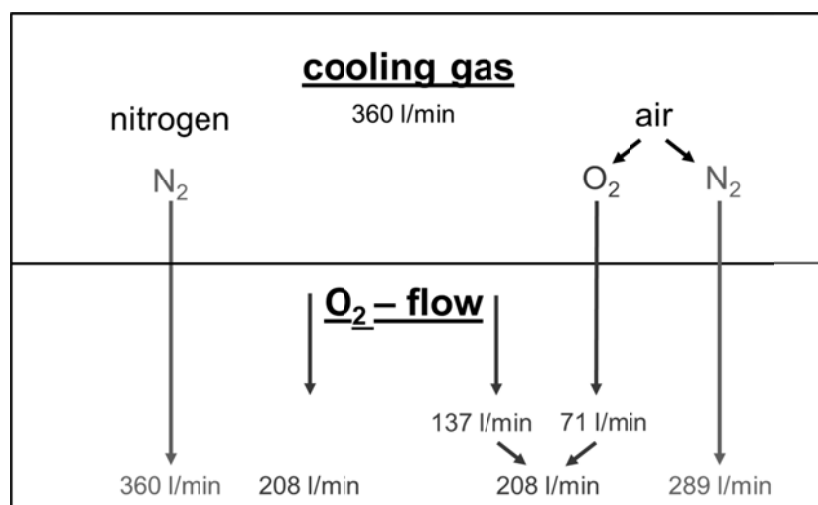


Figure 99: Schematic summarizing the different influences by cooling gas types on overall effective gas flow for the example of $\lambda = 0.63$. Tuning spray parameters in a way that 20 % of air as cooling gas participates in combustion by reduced pure oxygen flows, the effective nitrogen flow is lower than by using directly nitrogen as cooling gas.

Spray Distance

Apart from the oxygen to fuel ratios and the type of cooling gas, also the spray distance influences impact conditions and thus coating properties. By residence times in the expanding gas jet, particles cool down and decelerate more for larger spray distances, smaller particles are more affected than larger ones. At a spray distance of about 350 mm, the velocities and temperatures of the particles for the given size distributions get rather similar. Molten particles cool down and re-solidify to a regime around the melting temperature. Hence, for longer spray distances, coating formation occurs more homogeneous, as observed in coating microstructures for both cooling gases, than for shorter spray distances. For all spray distances, particles around 30 μm in diameter retain the highest thermal energy, since smaller particles cool rapidly and large particles do not reach as high temperatures (compare the molten fraction particle in Figure 87). The single impact morphologies do not reveal any nameable differences in deformation behaviour since all single impact particle impact conditions were close to the melting temperature. For higher spray distances, more particles do adhere. The electrical conductivity and the ultimate tensile strength as a measure for the bonded area and vary slightly with spray distance. This is caused by decreasing porosity and thus improved coating cohesion. Slightly colder and more homogeneous particle impact conditions at larger spray distances might avoid too much particle splattering and thus improve bonding between splats. Better bonding allows for enhanced cavitation performances as observed for cold gas spraying and warm spraying. The reduction of splattering by increasing spray distance might also explain slightly better bond strength by increased spray distance.

6.7.2. Properties with Influence on Cavitation Performance

The results of the HVOF-sprayed NAB coatings demonstrate that the coating formation processes is rather complex. For possible understanding, a couple of influences have to be considered, in addition to those known from cold gas spraying and warm spraying. In particular, the mainly liquid impact and oxidation within the process determine possible coating properties. For distinguishing the different influences, Figure 100 correlates the coating cavitation rates with several coating properties. The results show that similar to cold gas spraying and warm spraying, the coating cohesion as represented by the coating strength (a), and the amount of crack nuclei like pores (c) indicate almost linear correlations. Similar is reported in literature for WC-CO-Cr with HVOF sprayed coatings [KUM16]. As observed by the surface topography after cavitation testing, coatings with high strength most prominently show fatigue damage and removal of coating fractions instead of whole particle removal. The relation between cavitation rate and electrical conductivity (b) does not show any correlation, since the oxide content seems to play a major role for electron mobility. Interestingly, the HVOF-sprayed coatings show a rather good cavitation resistance despite the oxygen contents, and thus no clear correlation to the amount of contamination. Hotter spray parameter sets allow for enhanced melting and cohesion but in parallel enhance oxidation. Closing of large gaps and cracks seems to superimpose the influence of very small and well-distributed oxides within the coating.

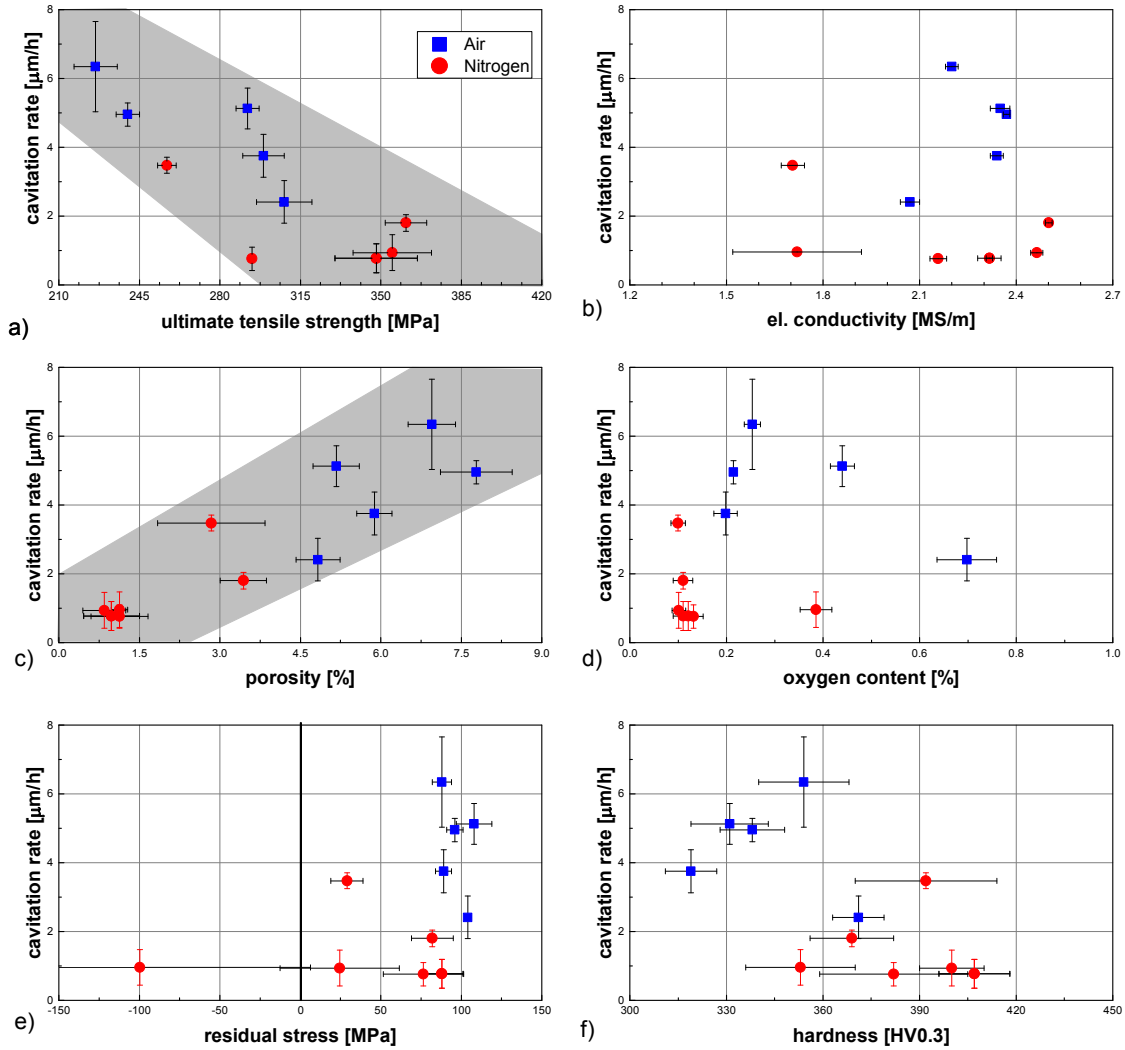


Figure 100: Correlations between the different cavitation-rates and several coating properties of HVOF-spray NAB coatings with air and nitrogen as cooling gases.

On a first view, Figure 100e might indicate low compressive stresses improve cavitation resistance. Looking into detail, residual stresses are quite complex and are not the main factor determining cavitation. Within a small region within the tensile regime, high differences in cavitation performance can be obtained. Interestingly, coating hardness shows a wide distribution and no clear trend, in contrast to initial assumptions.

Summing up, the cavitation performance is mainly determined by the reduction of internal cracks and of non-bonded interfaces, i.e. good bonding between splats. Hence, the cavitation resistance correlates well with increasing strength and decreasing coating porosity. Porosity and thus crack nuclei reduce the coating cohesion.

7. Comparison between different Spray Techniques and Annealing Conditions

7.1. General Aspects

The results demonstrate that good coating properties similar to that of bulk material and thus good cavitation resistance can be achieved by using high parameter sets in cold spraying and warm spraying, or well-tuned parameters in HVOF- spraying. Similar results can also be obtained by post heat-treatments, as applied to cold-sprayed coatings that were sprayed at sub-optimum conditions. Figure 101 compares optimized mean cavitation-rates of NAB samples. Attempts to use other bronze materials as CuMn13Al8Fe3Ni3, CuNi15Sn8 and CuSn10 to improve inter-particle bonding in cold spray also resulted in rather good coating qualities, which, however, in the end are not competitive enough against the use of NAB as feedstock. In the following section, for each technique, individual differences are worked out to derive needed pre-requisites for processing coatings of good quality.

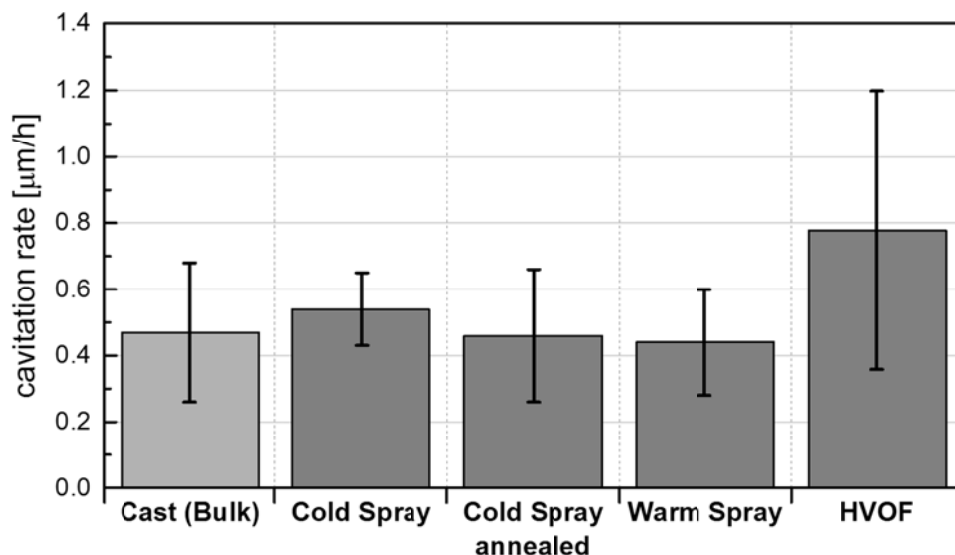


Figure 101: Best attainable cavitation rates of thermally or kinetically sprayed coatings as well as of coatings in comparison to that of bulk NAB-bronze as reference.

The rather similar cavitation resistance of bulk NAB and respective coatings, processed with various spray techniques is obtained by quite different microstructural features. Figure 102 shows the optimized coating microstructures and the respective coating surface morphologies after 100 min of cavitation treatment in comparison to that of cast bulk material for the different used spray methods. The cast material shows the typical NAB microstructure with rather large grain sizes and finely dispersed precipitations. The surface topography after cavitation treatment displays plastic deformation and many spots that indicate material losses, mainly occurring at grain boundaries. In contrast, the microstructure of the cold-sprayed and warm-sprayed coatings both show smaller grains, since due to solid impacts, the single particles retain their grain-refined features, as obtained by the rapid solidification during the powder atomization process. The microstructures indicate only very low amounts of oxides. In contrast to bulk material, the surface after cavitation testing shows almost no plastic deformation. Cavitation damage occurs through trans-particle failure. For the annealed cold-sprayed coating, originally processed with lower parameter sets, several larger pores can be observed after 100 min of cavitation test which are due to carving out

initially more loosely bonded material. Nevertheless, remaining particles are well bonded and cavitation causes mainly trans-particle failure. In contrast to cold spraying and warm spraying, the microstructure of HVOF-sprayed exhibits mainly liquid impacts with high amounts of pores and oxides that might act as crack nuclei under external loads. Nevertheless, these defects only slightly reduce the cavitation resistance by about 0.3 $\mu\text{m}/\text{h}$ as compared to the cold and warm sprayed coatings. The coating cohesion is rather high, and the cavitation damages mechanism shows that only splat fractions are removed.

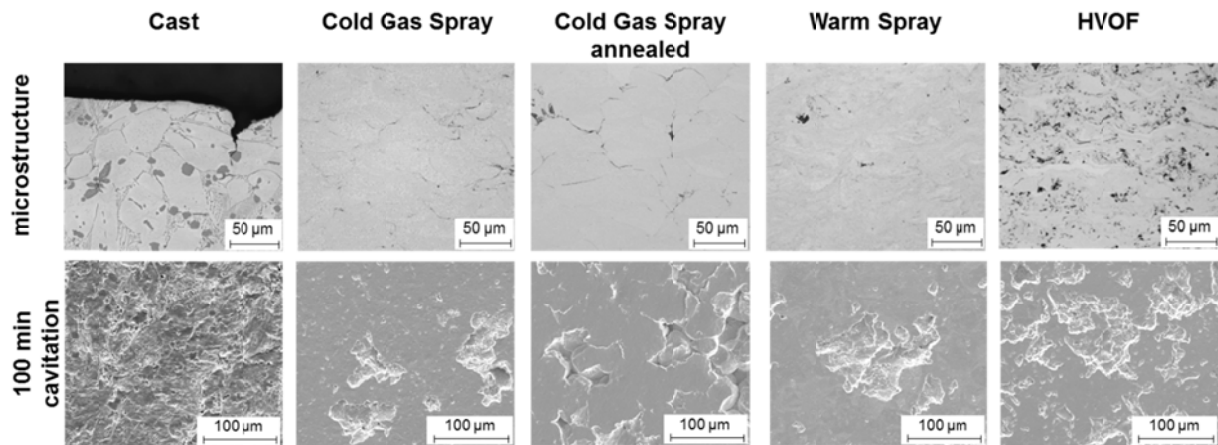


Figure 102: Coating microstructures and surface topographies after 100 min of cavitation testing for optimized coatings processed by kinetic and thermal spraying as well as the kinetic spraying, as well as the cold sprayed sample after heat-treatment in comparison to those of cast bulk material.

The rather discordant appearance of microstructures and surface damage is due to different crystallographic structures, and in consequence mechanical behaviour. The different structures as observed by XRD are compared in Figure 103. The cast bulk material contains mainly α -phase solid solution and probably κ -precipitations. In contrast, the by gas atomization rapidly cooled powder contain high amounts of martensitically transformed β_1 -high temperature structures. This fraction reduces during thermal and kinetic spraying as observed for cold spray, warm spray and HVOF spray. Interestingly the degree of degradation of martensite into α -phase depends on the spray technique. High kinetic energy allow for converting the martensite partly by stress-induced transformations, as observed for 316L and MCrAlY by Borchers et al. [BOR08, BOR14]. In contrast, the mainly thermal HVOF-process results in a relatively high amount of martensite. Although the particles melt, the martensite probably re-forms during rapid solidification upon impact, as observed by [BOR08]. Fine microstructures and dispersed martensite probably guarantee the needed high strength for good cavitation resistance, and compensate the lack of deformability in comparison to bulk NAB.

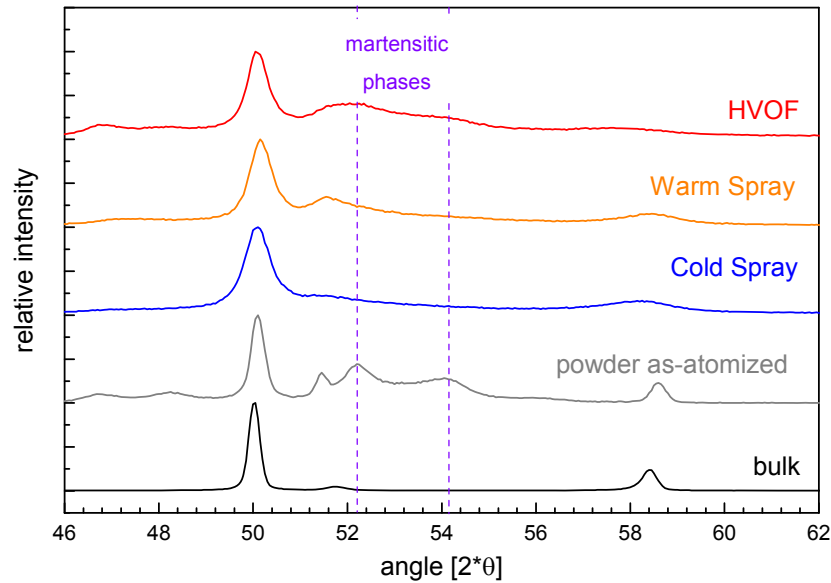


Figure 103: XRD-pattern of kinetically and thermally sprayed coatings within this study in comparison to the bulk material and the feedstock powder.

The results for all used spray methods showed that the coating properties correlate most prominently with the coating strength and the porosity but indicate individual differences. As shown in Figure 104a and b, the different kinetic and thermal spray techniques indicate, as expected, similar trends but interestingly quite different slopes or dependencies for thermally or kinetically sprayed coatings for both coating strength and porosity. On the one hand, the HVOF sprayed coatings show a higher cavitation rate at similar coating strengths and, on the other hand, lower cavitation rates at higher porosities as compared to cold sprayed and warm sprayed coatings. The major difference between the three spray methods concerns the particle impact condition, since cold sprayed and warm sprayed coatings are most prominently formed by solid particle impacts, whereas HVOF sprayed coatings are formed

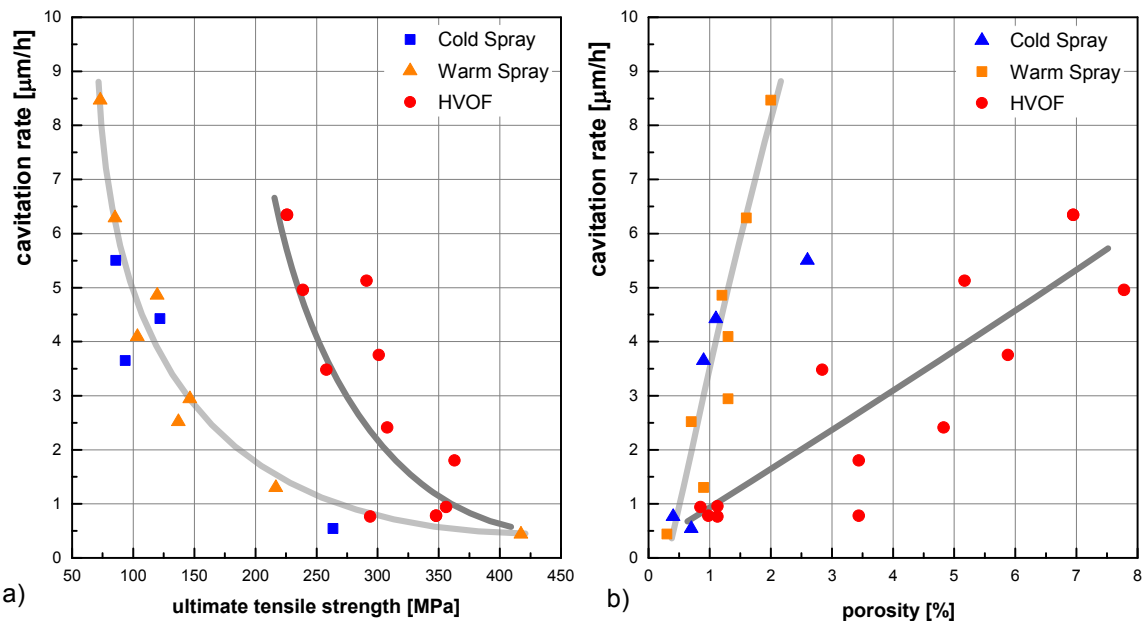


Figure 104: Correlation of the coating cavitation rates with the coating strength and porosity for the different kinetic and thermal spray methods.

liquid droplets under much hotter particle impact conditions. As already discussed in chapter 6.7.1 and 6.7.2, HVOF sprayed coatings suffer from an up to 8 times higher oxide content than warm sprayed coatings and an up to 20 times higher oxide content than the cold sprayed coatings. These brittle oxides can act as crack nuclei and consequently reduce coating cavitation resistance. In contrast, the HVOF-sprayed coatings can yield higher porosities at similar cavitation rates. Probably, the high degree of deformation of the molten droplets can cause intimate bonding between adhering splats, despite some remaining porosity and oxides, thus hindering that whole particles are removed.

7.2. Energetic Considerations

The following chapter aims to provide a more use a general basis to compare different spray parameter sets and methods to predict possible coating properties. For revealing possible problems of concepts so far used for solid impacts, the particle impact conditions for the different methods are summarized together with critical conditions for bonding in Figure 105. So far, for cold spraying the coating quality parameter η has been established, providing the opportunity to compare spray parameter sets and predict coating properties. This concept fails by approaching the melting temperature resulting in η -values striving towards infinity. As in this study applied to warm spray, considering the overall impact energy supplies a more general concept that reveals clear trends on coating properties. For HVOF spraying no uniform parameter has been developed, so far, probably due to many side effects that hinder clear correlations.

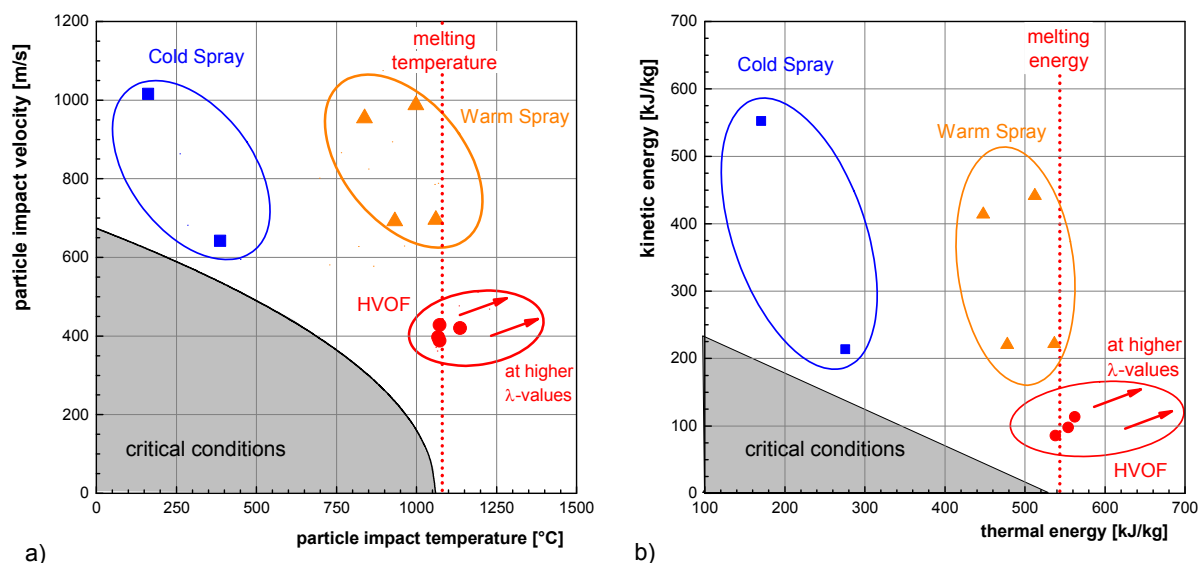


Figure 105: Impact conditions of NAB for the different spray methods in terms of particle temperatures and velocities (a) and respective thermal and kinetic energies (b) in comparison to respective critical velocities (a) and critical impact energies (b).

Figure 105 compares the attainable impact conditions in terms of critical velocity and critical impact energy. For providing more experimental evidence, Figure 106 summarizes the measured cavitation rates and strengths for the different spray methods as a function of the relative particle impact energy. The particle impact conditions including the critical conditions for bonding are transformed from particle temperature and velocity into thermal and kinetic energy as shown in Figure 105a to b. The data points correspond to selected spray parameters to display the particle impact regime for each spray method. For HVOF-spraying, the regime displays the impact conditions for $\lambda = 0.63$ with air and nitrogen as cooling gas.

The arrows indicate the particle impact regime when considering higher λ -values and thus hotter spray conditions. Comparing the critical velocity and critical energy concepts, no significant differences get obvious. Not being obvious on the first view, the energy concept allows for comparing the different spray methods. Here, the kinetic and thermal impact energies as introduced for warm spraying in chapter 1.2 in equation 3 can be considered. In comparison to cold spraying (500 to 750 kJ/kg), warm spraying and HVOF-spraying (650 to 1000 kJ/kg) show the highest particle impact energies. Although showing low kinetic impact energies, for HVOF-spraying a latent heat of fusion of about 214 kJ/kg has to be added since particles impact in a mainly molten state.

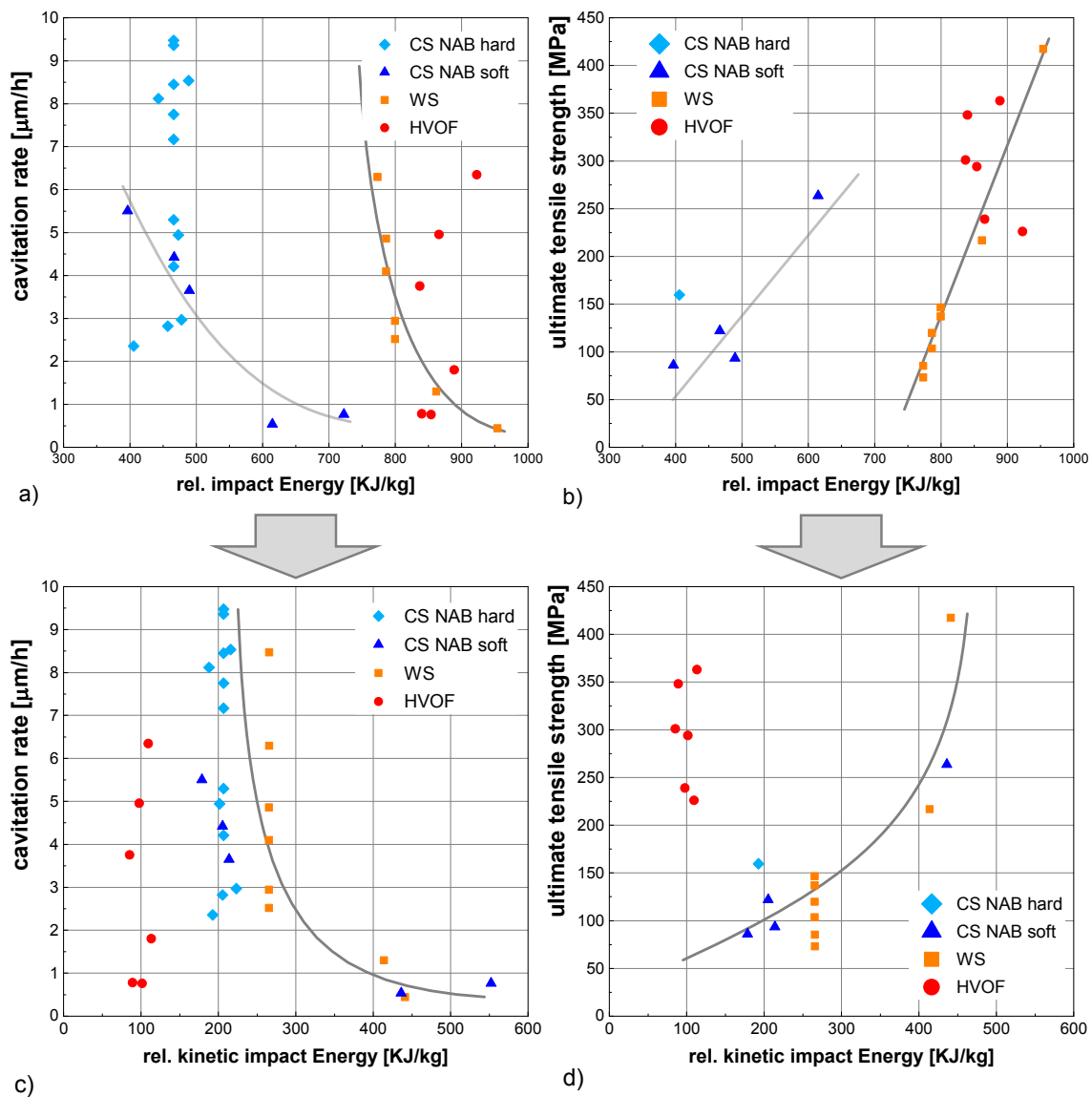


Figure 106: Correlation between the coating cavitation rates and the ultimate tensile strength of the different spray techniques used in this study with the relative impact energies, incorporating kinetic and thermal contributions (a and b) in comparison to only kinetic impact energies (c and d). The impact energies are calculated for a mean particle diameter of 30 μm . The latent heat of fusion of 214 kJ/kg is included within the calculated energies for HVOF-spraying since particles impact mainly in a molten state.

In Figure 106a and b the cavitation rates and ultimate tensile strengths NAB coatings processed by the different spray techniques are plotted over the particle impact energy. The diagrams illustrate clear trends of improved coating performance by increased impact

energies for cold spraying with NAB soft and warm spray of NAB hard. The comparison of absolute energies needed for certain properties nevertheless differs between both. As compared to warm spraying, in cold spraying, lower particle impact energies are required to achieve similar results. As discussed in chapter 4.8.3, the data of the cold sprayed NAB hard coatings scatter over wide range within a close impact condition regime, probably due to the high powder strength and dominating secondary influences. The data of HVOF-sprayed coatings show no distinct trend, due to the superimposed effects by oxidation. Nevertheless, they range down close to that of bulk material cavitation rates and achieve almost bulk strength. The impact energy regime of HVOF-spraying is highest, due to the high fraction of molten phase, with about constant kinetic energy. It may be concluded that by reducing the side effects in HVOF-spraying, warm spraying and HVOF could both process coatings of similar good and almost bulk-like cavitation resistance and strengths. Within the same optimized energy regime, as compared to cold spraying, warm-sprayed and HVOF-sprayed coatings were processed with higher particle impact energies, resulting in similarly high cavitation resistance and strength as optimized cold-sprayed coatings.

For analysing the differences between cold spraying and warm spraying, the coating properties were correlated with the kinetic impact energy, as shown in *Figure 106c* and *d*. The correlation shows one common clear trend for both, warm-sprayed and cold-sprayed coating properties. This indicates that the high thermal energies as used in warm spraying are not necessarily required to form cavitation resistant and high strength coatings. Possibly, the local heating of the solid particle outer rim by deformation is sufficient for adequate particle bonding and good coating properties. These findings are in good agreement to estimates of Schmidt et al. for particle melting energies [SCH09], identifying bonding by local deformation and heating as energetically favourable. Surplus thermal energy as in HVOF or in even hotter thermal spray techniques are not required and can even be detrimental due to low the low melt viscosity upon impact and concomitant splattering, thus reducing deposition efficiency.

8. Conclusion

In the present thesis, Ni-Al-bronze coatings were sprayed by cold gas spraying, warm spraying and HVOF-spraying to obtain cavitation resistant coatings and to identify influencing factors that determine the damage mechanisms. To overcome the limitations of cold gas spraying by too high powder strength, some batches of the Ni-Al-bronze powder were annealed to reduce disturbing martensite contents and to thus lower the respective particle strength. Furthermore, bronzes with lower strength were cold-sprayed as a compromise: due to intrinsic lower resistance against deformation an increased amount of bonded areas is achieved, thus increasing structural cavitation resistance, however, at the expense of the material's inherent lower cavitation resistance. In addition, the cold sprayed Ni-Al-bronze coatings were optimized by applying various heat-treatments and studying their influence on coating performance. For analysing and comparing the properties of the coatings obtained by different kinetic and thermal spray techniques, the new concept of particle impact energy is successfully introduced.

From these different studies, the following can be concluded:

Conclusions focusing on Coating Properties

- Cavitation resistant coatings with a performance similar to bulk Ni-Al-bronze can be obtained by all applied spray techniques. In case of cold spray coatings sprayed with nitrogen as process gas, heat treatments can tune the needed quality.
- All optimized coatings showed good bond strength greater 30 MPa, especially substrate pre-heating resulted in improved adhesion strengths.
- Coating cohesion, i.e. strength was determined as the key factor for cavitation resistance. Inhomogeneities like non-bonded interfaces, oxides or large precipitations act as crack nuclei and accelerate cavitation damages.
- Cavitation damage mechanisms were identified as (i) whole particle removal for coatings with low strength and (ii) trans-particle or trans-splat failure for coatings with high strength, i.e. good internal cohesion.
- Coating hardness played a negligible role within all as-sprayed coatings, although being a measure of the resistance against plastic deformation. The hardness remains within a narrow regime that probably does not allow for obtaining clear trends.
- For cold gas spraying within the investigated parameter range, the intrinsic material properties have a higher influence on cavitation resistance than the amount of bonded interfaces. Porous coatings based of high strength bronze still show a better cavitation performance than dense coatings based on low strength bronze.

Conclusions focussing on Powder and Coating Heat-Treatments

- Ni-Al-bronze powder heat treatment at 650 °C for 7 h eliminates the disturbing martensite content within the NAB powder feedstock and thus lowers particle strength to values similar to that of the respective bulk material.

- Cold gas spraying of heat-treated Ni-Al-bronze powders show a highly improved deformability upon impact as compared to as-atomized feedstock powder
- Applying heat-treatment for 1 h at 500°C onto coatings that were cold-sprayed with annealed Ni-Al-bronze powder results in a cavitation performance similar to that of bulk material. Annealing has to meet a compromise between surface diffusion increasing the amount of bonded areas and volume diffusion that causes grain coarsening and precipitate growth, i.e. over-aging.

Conclusions focussing on the Coating Quality Parameter η and the Particle Impact Energy Concept

- Cold gas spraying with increased η -values up to 1.7 results in improved coating properties.
- The newly introduced particle energy concept provides the opportunity to compare coating properties of different thermal or kinetic spray techniques by one single parameter.
- Higher particle impact energies in warm spraying resulted in improved coating performances. An upper limit could not be determined yet.
- Warm-sprayed coatings were processed at higher thermal energies than cold-sprayed coatings. The comparison of attainable coating properties at similar particle impact energies revealed that such high thermal energies are not necessarily required to form high quality coatings. Thermal softening of the outer shell of single particles as attained by deformation is sufficient enough, and conceivably energetically more efficient than heating of the whole particle.
- Deriving clear trends of the particle impact energy for HVOF-sprayed coatings remains difficult since side reactions like oxidation highly influence coating properties. However, the total impact energy is highest among the investigated technologies and most probably much higher than necessary.

9. Literature

- [AL-02] Al-Hashem, A.; Riad, W., The role of microstructure of nickel–aluminium–bronze alloy on its cavitation corrosion behaviour in natural seawater, In: *Materials Characterization*, Vol. 48, No. 1 (2002), p. 37-41.
- [ALK01] Alkhimov A, Kosarev V, Klinkov S., The Features of Cold Spray Nozzle Design, In: *Journal of Thermal Spray Technology*, Vol. 10, No. 2 (2001), p.375-381.
- [ALK90] Alkhimov, A. P.; Kosarev, V. F.; Papyrin, A. N., A Method of Cold Gas-Dynamic Deposition, In: *Soviet Physics Doklady*, Vol.35, No. 12 (1990), p.1047-1049.
- [ALK94] Alkimov A, Papyrin A, Kosarev V, Nesterovich N., Gas-Dynamic Spray Method for Applying a Coating, US-Patent 5,302414, 1994.
- [ARA13] Arabgol Z, Assadi H, Schmidt T, Gärtner F, Klassen T., Analysis of Thermal History and Residual Stress in Cold-Sprayed Coatings, In: *Journal of Thermal Spray Technology*, Vol. 23, No.1-2(2013), p.84-90.
- [ASS03] Assadi, H., Gärtner, F., Stoltenhoff, T., Kreye, H., Bonding mechanism in Cold Spraying, In: *Acta Materialia*, Vol. 51 (2003), p. 4379-4394.
- [ASS11] Assadi, H., Schmidt, T., Richter, H., Kliemann, J.-O., Binder, K., Gärtner, F., Klassen, T., Kreye, H., On Parameter Selection in Cold Spraying, In: *Journal Thermal Spray Technology*, Vol. 20 (2011), p.1161-1176.
- [ASS15] Assadi, A., Irkhin, I., Gutzmann, H., Gärtner, F., Schulze, M., Villa Vidaller, M., Klassen, T., Determination of plastic constitutive properties of microparticles through single particle compression, In: *Advanced Powder Technology*, Vol. 26 (2015), p.1544-1554.
- [ASS16] Assadi, H., Kreye, H., Gärtner, F., Klassen, T., Cold spraying - A materials perspective, In: *Acta Materialia*, Vol. 116 (2016), p. 382-407.
- [BAR05] Barik, R.C, Erosion and erosion–corrosion performance of cast and thermally sprayed nickel–aluminium bronze, In: *Wear*, Vol. 259, No. 1-6 (2005), p.230-242.
- [BOR08] Borchers, C., Schmidt, T., Gärtner, F., Kreye, H., High strain rate deformation microstructures of stainless steel 316L by cold spraying and explosive powder compaction, In: *Applied Physics A*, Vol. 90 (2008), p.517-526.
- [BOR14] Borchers, C., Stoltenhoff, T., Hahn, M., Schulze, M., Assadi, H., Suryanarayana, Gärtner, F., Klassen, T., Strain-induced phase transformation of CoNiCrAlY alloys, In: *Advanced Engineering Materials*, Vol. 17. No. 5 (2014), p. 723-731.
- [BOU02] Bourne, N.K, On the collapse of cavities, In: *Shock Waves*, Vol. 11, No. 6 (2002), p.447-455.
- [BRE13] Brennen, C., Cavitation and bubble dynamics, In: Cambridge University Press, 2013.
- [BRO93] Browning, J.A., Thermal Spray Method Utilizing In-Transit Powder Particle Temperatures Below Their Melting Point, US Patent 5,271,965, 1993.

- [BRO94] Browning, J.A., Thermal Spray Method and Apparatus for Optimizing Flame Jet Temperature, US Patent 5,330,798, 1994.
- [BUT73] Butrymowicz, D.B., Manning, J.R., Read, M.E., Diffusion In Copper And Copper Alloys, Part II. Copper-Silver And Copper-Gold Systems, In: Journal of Physical and Chemical Reference Data 3, No. 2 (1974), p.527.
- [CAR09] Carlton, J.: Rudder - Propeller - Hull Interaction: The Results of Some Recent Research, In-Service Problems and Their Solutions, In: First International Symposium on Marine Propulsors (2009), Trondheim/Norway.
- [CHA07] Champagne, V.K., The Cold Spray Materials Deposition Process: Fundamentals and Applications, Cambridge, Woodhead; 2007.
- [CIN13A] Cinca, N., López, E., Dosta, S., Guilemany, J., Study of stellite-6 deposition by cold gas spraying. In: Surface and Coatings Technology, Vol. 232 (2013), p.891-898.
- [CIN13B] Cinca, N.; Guilemany, J.M, Structural and properties characterization of stellite coatings obtained by cold gas spraying. In: Surface and Coatings Technology, Vol. 220 (2013), p.90–97.
- [CRA04] Crawmer, D.E., Coating Structures, Properties, and Materials, In: Davis, J.R., ed. Handbook of Thermal Spray Technology, Materials Park, ASM International (2004), p 47-53.
- [CZI10] Czichos, H. K., Tribologie-Handbuch, Wiesbaden: Vieweg+Teubner Verlag / GWV Fachverlage, 2010.
- [DAV04] Davis, J.R., Handbook of Thermal Spray Technology, Materials Park, ASM International; 2004.
- [DEU16] Data sheet CuSn10, Deutsches Kupferinstitut, https://www.kupferinstitut.de/fileadmin/user_upload/kupferinstitut.de/de/Documents/Shop/Verlag/Downloads/Werkstoffe/Datenblaetter/Bronze/CuSn10-C.pdf, downloaded: 26.09.2016.
- [DYK98] Dykhuizen, R., Smith, M., Gas Dynamic Principles of Cold Spray, In: Journal of Thermal Spray Technology, Vol. 7, No. 2 (1998), p.205-212.
- [ERN13] Ernst, K., Braeutigam, J., Gärtner, F., Klassen, T., Effect of Substrate Temperature on Cold-Gas-Sprayed Coatings on Ceramic Substrates, In: Journal of Thermal Spray Technology, Vol. 22 (2013), p.422-432.
- [FAU01] Fauchais P, Vardelle A, Dussoubs B., Quo Vadis in Thermal Spraying?, In: Journal of Thermal Spray Technology, Vol. 10. No. 1 (2001), p.44-66.
- [FAU14] Fauchais, P., Heberlein, J., Boulos, M., Thermal spray fundamentals, 2014.
- [GAE05] Gärtner F, Stoltenhoff T, Schmidt T, Kreye H., The Cold Spray Process and Its Potential for Industrial Applications, In: Journal of Thermal Spray Technology, Vol. 15, No. 2 (2006), p.223-232.
- [GAE06] Gärtner, F., Stoltenhoff, T., Voyer, J., Kreye, H., Riekehr, S., Kocak, M., Mechanical Properties of Cold-Sprayed and Thermally Sprayed Copper Coatings, In: Surface & Coatings Technology, Vol. 200 (2006), p. 6770-6782.

- [GAE06A] Gärtner, F., Richter, H.J., HVOF spraying with powder and wire, In: Conference Proceedings, 7th HVOF-Kolloquium (2006), Erding, p.39-56.
- [GIL99] Gilmore, D., Dykhuizen, R., Neiser, R., Roemer, T., Smith, M., Particle Velocity and Deposition Efficiency in the Cold Spray Process, In: Journal of Thermal Spray Technology, Vol. 8, No. 4 (1999), p.576-582.
- [GL09] Klassifikations- und Bauvorschriften II, Werkstoffe und Schweißtechnik (2009), download from rules.dnvgl.com/docs/pdf/gl/maritimerules/gl_ii-1-2_d.pdf, 26.07.2016.
- [GL12] Klassifikations- und Bauvorschriften I Schiffstechnik 2012, download from rules.dnvgl.com/docs/pdf/gl/maritimerules2016Jan/gl_i-2-4_d.pdf 26.07.2016.
- [GRI15] Grigoriev, S., Okunkova, A., Sova, A., Bertrand, P., Smurov, I., Cold spraying: from process fundamentals towards advanced applications, In: Surface Coating Technology, Vol. 268 (2015), p.77-84.
- [HAN10] Hanke S, Fischer A, Beyer M, dos Santos J., Cavitation erosion of NiAl-bronze layers generated by friction surfacing, In: Wear, Vol. 273, No. 1 (2011), p.32-37.
- [HAT07] Hattori, S., Tainaka, A., Cavitation erosion of Ti–Ni base shape memory alloys, In: Wear Vol, 262. No. 1-2 (2007), p.191-197.
- [HOE11] Hoehle, H.-M.; Nestler, M. C.: Oberflächen für längere Lebensdauer und höhere Energieeffizienz, In: Wasser und Abwasser – Sulzer Technical Review, 2011.
- [HOU14] Hou, G., Zhao, X., Zhou, H., Lu, J., An, Y., Chen, J., Yang, J., Cavitation erosion of several oxy-fuel sprayed coatings tested in deionized water and artificial seawater, In: Wear, Vol 111, No. 1 (2014), p.81-92.
- [HUS09] Hussain T, McCartney D, Shipway P, Zhang D., Bonding Mechanisms in Cold Spraying: The Contributions of Metallurgical and Mechanical Components, In: Journal of Thermal Spray Technology, Vol. 18, No. 3 (2009), p. 364-379.
- [INS16] Data sheet – CuNi15Sn8, Institut Europeen du Cuivre, <http://copperalliance.fr/le-cuivre/les-alliages/les-cupro-nickels/cuni15sn8>, downloaded: 26.09.2016.
- [IRI08] Irissou, É, Legoux, J.-G, Ryabinin, A, Jodoin, B, Moreau, C., Review on Cold Spray Process and Technology: Part I, In: Journal of Thermal Spray Technology, Vol. 17, No. 4 (2008), p. 495-516.
- [IVO06] Ivosevic, M., Cairncross, R.A., Knight, R., 3D Predictions of Thermally Sprayed Polymer Splats : Modeling Particle Acceleration, Heating and Deformation on Impact with a Flat Substrate, In: International Journal of Heat and Mass Transfer, Vol. 49, No.19-20 (2006), p. 3285-3297.
- [JEA14] Jeandin, M., Rolland, G., Descurninges, L., Berger, M., Which powders for cold spray?, In: Surface Engineering, Vol. 30, N. 5 (2014), p.291-298.
- [KAT03] Katanoda, H., Kazuyasu, M., Analysis of Particle Behavior in High-Velocity Oxy-Fuel Thermal Spraying Process, In: Journal of Thermal Science, Vol.12, No 3 (2003), p.279-282.
- [KAT06A] Katanoda, H., Yamamoto, H., Matsuo, K., Numerical simulation on supersonic flow in High-Velocity Oxy-Fuel thermal spray gun, Journal of Thermal Science, Vol. 15, No. 1 (2006), p.65-70.

- [KAT06B] Katanoda, H., Quasi-One-Dimensional Analysis of the Effects of Pipe Friction, Cooling and Nozzle Geometry on Gas/Particle Flows in HVOF Thermal Spray Gun, In: Materials Transactions, Vol. 47, No. 11 (2006), p. 2791-2797.
- [KAT08] Katanoda, H., Kiriaki, T., Tachibanaki, T., Kawakita, J., Kuroda, S., Fukuhara, M., Mathematical Modeling and Experimental Validation of the Warm Spray (Two-Stage HVOF) Process, In: Journal of Thermal Spray Technology, Vol. 18, No. 3 (2009) p.401-410.
- [KAT09] Katanoda, H., Kiriaki, T., Tachibanaki, T., Kawakita, J., Kuroda, S., Fukuhara, M., Mathematical Modeling and Experimental Validation of the Warm Spray process, In: Journal of Thermal Spray Technology, Vol. 18, No. 3 (2009), p.401-410.
- [KAT11] Katanoda, H., Morita, H., Komatsu, M., Kuroda, S., Experimental and Numerical Evaluation of the Performance of Supersonic Two-Stage High-Velocity Oxy-Fuel Thermal Spray (Warm Spray) Gun, In: Journal of Thermal Science, Vol. 20, No. 1 (2011), p.66-92.
- [KAT13] Katanoda, H., Sun, B., Ohno, N., Fukanuma, H., Kuroda, S., Watanabe, M., Ohashi, O., Design and Development of High-Pressure Warm Spray Gun, In: Conference Proceedings, Thermal Spray (2013), Busan/Republic of Korea, ASM International, p.196-199.
- [KAW06] Kawakita, J., Isoyama, K., Kuroda, S., Yumoto, H., Effects of deformability of HVOF sprayed copper particles on the density of resultant coatings, In: Surface & Coatings Technology, Vol. 200 (2006), p.4414-4423.
- [KAY16] Kay, C.M., Karthikeyan, J., High pressure cold spray. Materials Park: ASM International, 2016.
- [KIM09A] Kim, K., Watanabe, M., Kuroda, S., Thermal softening effect on the deposition efficiency and microstructure of warm sprayed metallic powder, In: Scripta Materialia, Vol. 60 (2009), p. 710-713.
- [KIM09B] Kim, K., Watanabe, M., Kuroda, S., Jetting-Out Phenomenon Associated with Bonding of Warm-Sprayed Titanium Particles onto Steel Substrate. Journal of Thermal Spray Technology. 2009;18(4):490-499.
- [KLA16] Klassen, T., Gärtner, F., Assadi, H., Process Science of Cold Spray, In: Kay Karthikeyan J, ed. High-Pressure Cold Spray - Principles and Applications, Materials Park, ASM International, Ch. 2 (2016), p. 1-50.
- [KLI05] Klinkov, S., Kosarev, V., Rein, M., Cold spray deposition: Significance of particle impact phenomena, In: Aerospace Science and Technology, Vol. 9, No. 7 (2005), p.582-591.
- [KOR09A] Kornev, N., Propellertheorie, Aachen: Shaker; 2009.
- [KOR09B] Korobov, Y., Deposition of protective coatings by means of supersonic flame spraying, In: Thermal Engineering, Vol. 56, No. 2 (2009), p.142-146.
- [KRE00A] Kreye, H., Stoltenhoff, T., Cold spraying - a study of process and coating characteristics, In: Thermal Spray - Surface Engineering via Applied Research, C.C. Berndt, Ed., ASM International, Materials Park, OH, 2000, p. 419-422.
- [KRE00B] Kreye, H., Gärtner, F., Kirsten, A., Schwetzke, R., High Velocity Oxy-Fuel Flame Spray, State of the Art, Prospects and Alternatives, In Conference Proceedings, 5th HVOF-Kolloquium (2000), Erding, p.5-16.

- [KRE03] Kreye, H., Gärtner, F., Richter, H.J., High Velocity Oxy-Fuel Flame Spraying – State of the Art, new Developments and Alternatives, In: Conference Proceedings, 6th HVOF-Kolloquium (2003), Erding, p.5-17.
- [KRE14] Krebs, S., Gärtner, F., Klassen, T., Cold Spraying of Cu-Al-Bronze for Cavitation Protection in Marine Environments, In: Materialwirtschaft und Werkstofftechnik, Vol. 45, No. 8 (2014), p.708-717.
- [KRE15] Krebs, S., Gärtner, F., Klassen, T., Cold Spraying of Cu-Al-Bronze for Cavitation Protection in Marine Environments, In: Journal of Thermal Spray Technology, Vol. 24, No. 1 (2015), p.126-135.
- [KRE16] Krebs, S., Kuroda, S., Katanoda, H., Gärtner, F., Klassen, T., Araki, H., Frede, S., Warm Spraying of high strength Ni-Al-bronze for cavitation protection, In: Conference Proceedings, International Thermal Spray Conference, Shanghai / China, 2016, p.144-150.
- [KRO09] Kroemmer, W., Heinrich, P., Kreye, H., High Velocity Oxy-Fuel Flame Spraying: past - present - future, In: Conference Proceedings, 8th HVOF-Kolloquium (2009), Erding, p.9-16.
- [KUM05] Kumar, R.K., Boy, J., Zatorski, R., Stephenson, L.D., Thermal Spray and Weld Repair Alloys for the Repair of Cavitation Damage in Turbines and Pumps: A Technical Note, In: Journal of Thermal Spray Technology, Vol. 14, No. 2 (2005), p. 177-182.
- [KUM16] Kumar, R.K., Kamaraj, M., Seetharamu, S., Pramod, T., Sampathkumaran, P., Effect of Spray Particle Velocity on Cavitation Erosion Resistance Characteristics of HVOF and HVOF Processed 86WC-10Co4Cr Hydro Turbine Coatings, In: Journal of Thermal Spray Technology, Vol. 25, No. 1 (2016), p.1217-1230.
- [KUR08] Kuroda, S., Kawakita, J., Watanabe, M., Katanoda, H., Warm spraying—a novel coating process based on high-velocity impact of solid particles, In: Science and Technology of Advanced Materials, Vol. 9, No. 3 (2008), p.033002.
- [KUR11] Kuroda, S., Watanabe, M., Kim, K., Katanoda, H., Current Status and Future Prospects of Warm Spray Technology, In: Journal of Thermal Spray Technology, Vol. 20, No. 4 (2011), p.653-676.
- [KWO00] Kwok, C.T., Man, H.C., Cheng, F.T., Cavitation erosion and pitting corrosion behaviour of laser surface-melted martensitic stainless steel UNS S42000, In: Surface and Coatings Technology, Vol. 126, No. 2-3 (2000), p. 238-255.
- [LAE13] Laepple, Volker, Werkstofftechnik Maschinenbau. Theoretische Grundlagen und praktische Anwendungen, In: Bibliothek des technischen Wissens, 4th ed., Haan-Gruiten, Europa-Lehrmittel, 2013
- [LEE15] Lee, C., Kim, J., Microstructure of Kinetic Spray Coatings: A Review, In: Journal of Thermal Spray Technology, Vol. 24, No 4 (2015), p.592-610.
- [LI06] Li, W.Y., Li, C.J., Liao, H., Effect Of Annealing Treatment On The Microstructure And Properties Of Cold-Sprayed Cu Coating, In: Journal of Thermal Spray Technology, Vol. 15, No. 2 (2006), p.206-211.
- [LIS13] List, A., Lyphout, C., Villa, M., Gärtner, F., Mechanical Properties of Cold-Sprayed Ti-6Al-4V Coatings, In: Conference Proceedings, International Thermal Spray Conference, Busan / Korea, 2013, p. 155 – 160.

- [LON04] Longo, F.N., Postcoating Operations, In: Davis, J.R., ed. Handbook of Thermal Spray Technology, Materials Park, ASM International (2004), p. 128-131.
- [LUZ11] Luzin, V., Spencer, K., Zhang, M., Residual stress and thermo-mechanical properties of cold spray metal coatings, In: Acta Materialia 59 (2011), p.1259–1270.
- [LV15] Lv, Y., Hu, M., Wang, L., Xu, X., Han, Y., Lu, W., Influences of heat treatment on fatigue crack growth behaviour of NiAl bronze (NAB) alloy, In: Journal of Materials Research, Vol. 30, No. 20 (2015), p.3041-3048.
- [MAN02] Mann, B.S., Arya, V., An Experimental Study to Correlate Water Jet Impingement Erosion Resistance and Properties of Metallic Materials and Coatings, In: Wear, Vol 253 (2002), p.650–661.
- [MAT16] Product data sheet of Matthey Lamineries – CuNi15Sn8, http://www.matthey.ch/fileadmin/user_upload/downloads/fichetechnique/DE/BF158_T3_C.pdf, downloaded: 26.09.2016.
- [MEI00] Meigh, H., Cast and Wrought Aluminium Bronzes, Properties, Processes and Structure, In: IOM Communications Ltd., London, 2000.
- [MEN11] Meng, X.M., Zhang, J.B., Han, W., Zhao, J., Liang, Y.L., Influence Of Annealing Treatment On The Microstructure And Mechanical Performance Of Cold Sprayed 304 Stainless Steel Coating In: Applied Surface Science, Vol. 258, No. 2 (2011), p.700-704.
- [MOL13] Molak, R., Araki, H., Watanabe, M., Katanoda, H., Ohno, N., Kuroda, S., Warm Spray Forming of Ti-6Al-4V, In: Journal of Thermal Spray Technology, Vol. 23, No. 1-2 (2013), p.197-212.
- [MOR13] Morita, T., Kuroda, S., Murakami, H., Katanoda, H., Sakamoto, Y., Newman, S., Effects of Initial Oxidation on Beta Phase Depletion and Oxidation of CoNiCrAlY Bond Coatings Fabricated by Warm Spray and HVOF Processes, In: Surface and Coatings Technology, Vol. 221, No. 25 (2013), p.56-69.
- [MOR14] Moridi, A., Hassani-Gangaraj, S.M., Guagliano, M., Dao, M., Cold spray coating: Review of material systems and future perspectives, In: Surface Engineering, Vol. 30 (2014), p.369-395.
- [NOR97] Norman, A.F., Eckler, K., Gärtner, F., Moir, S.A., Zambon, A., Greer, A.L., Ramous E., The application of microstructure-selection maps to droplet solidification, In: Materials Science and Engineering, Vol. 226 (1997), p.48-52.
- [OER12] Oertel, H., Prandtl - Führer durch die Strömungslehre: Grundlagen und Phänomene, 13., 2012. Wiesbaden, Springer Fachmedien, 2012.
- [PAP06] Papyrin, A., Kosarev, V., Klinkov, S., Alkhimov, A., Fomin, V.M., In: Cold Spray Technology, Elsevier, 2006.
- [PAP88] Papamoschou, D., Roshko A., The compressible turbulent shear layer: an experimental study, In: Journal Fluid Mechanics, Vol. 197, No. 1 (1988), p.453.
- [PLE66] Plesset, M.S., Devine, R.E., Effect of exposure time on cavitation damage, In: Journal of Basic Engineering, Vol. 88 (1966), p. 691-705.

- [PLE71] Plesset, M.S., Chapman, R.B., Collapse of an initially spherical vapour cavity in the neighborhood of a solid boundary, In: Journal of Fluid Mechanics, Vol. 47 (1971), p.283-290.
- [RIC00] Richter, H.J., May, G., Fluid Mechanic and Thermal Aspects of High Velocity Spraying, In: Conference Proceedings, 5th HVOF-Kolloquium (2000), Erding, p.19-28.
- [RIC97] Richman, R.H., McNaughton, A Metallurgical Approach to Improved Cavitation-Erosion Resistance, In: Journal of Materials Engineering and Performance, Vol. 6, No. 5 (1997), p. 633–641.
- [RIG04] Riggs, W., Introduction to Testing and Characterization, In: Davis, J.R., ed. Handbook of Thermal Spray Technology, Materials Park, ASM International (2004), p. 217-223.
- [SAL14] Saleh, M., Luzin, V., Spencer, K., Analysis of the residual stress and bonding mechanism in the cold spray technique using experimental and numerical methods, In: Surface and Coating technology, Vol. 252 (2014), p.15-28.
- [SCH06A] Schmidt, T., Gärtner, F., Assadi, H., Kreye, H., Development of a generalized parameter window for cold spray deposition, In: Acta Materialia, Vol. 54 (2006), p.729-742.
- [SCH06B] Schwetzke, R., Kroemmer, W., Heinrich, P., Influencing factors for HVOF-spraying, In: Conference Proceedings, 7th HVOF-Kolloquium (2006), Erding, p.57-63.
- [SCH09] Schmidt, T., Assadi, H., Gärtner, F., Richter, H., Stoltenhoff, T., Kreye, H., Klassen, T., From Particle Acceleration to Impact and Bonding in Cold Spraying, In: Journal of Thermal Spray Technology, Vol. 18, No. 5-6 (2009), p.794-808.
- [SHA95] Shalaby, H. M., Al-Hashem, A., Al-Mazeedi, H., Abdullah, A., Field And Laboratory Study Of Cavitation Corrosion Of Nickel Aluminium Bronze In Sea Water, In: British Corrosion Journal, Vol. 30, No. 1 (1995), p.63-70.
- [SHI04] Shi, D., Li, M., Christofides, P., Diamond Jet Hybrid HVOF Thermal Spray: Rule-Based Modeling of Coating Microstructure. In: Industrial & Engineering Chemistry Research, Vol. 43, No. 14 (2004), p.3653-3665.
- [SHI05] Shi, H., Fan, J., Zhang, J.G., Le, H., Peng, Y., Jin, B.Z., Mi, X., Influence of Aging Treatment on the Microstructure and Properties of Spray Formed CuNi15Sn8 alloy, In: Materials Science Forum, Vols. 475-479 (2005), p.2831-2834.
- [SIN12] Singh, H., Sidhu, T. S., Kalsi, S. B. S., Cold spray technology: future of coating deposition processes, In: Frattura ed Integrità Strutturale, Vol. 22 (2012), p.69.
- [SOM10] Sommer K, Heinz R, Schöfer J., Verschleiß metallischer Werkstoffe, Wiesbaden: Vieweg+Teubner Verlag / Springer Fachmedien, 2010.
- [STE06] Stella, J., Schüller, E., Heßing, C., Hamed, O.A., Pohl, M., Stöver, D., Cavitation erosion of plasma sprayed NiTi coatings, In: Wear, Vol. 260 (2006), p.1020-1027.
- [STO02] Stoltenhoff, T., Kreye, H., Richter, H., An Analysis of the Cold Spray Process and Its Coatings, In: Journal of Thermal Spray Technology, Vol. 11, No. 4(2002), p.542-550.
- [STO06] Stoltenhoff, T., Borchers, C., Gärtner, F., Kreye, H., Microstructures and key properties of cold-sprayed and thermally sprayed copper coatings. In: Surface and Coatings Technology, Vol.200, No. 16-17 (2006), p.4947-4960.

[TAN03] Tan, K.S, Wood, R., Stokes, K., The slurry erosion behaviour of high velocity oxy-fuel (HVOF) sprayed aluminium bronze coatings, In: Wear Vol. 255, No. 1-6 (2003), p.195–205.

[TAN05] Tan, K.S., Solid particle erosion–corrosion behaviour of a novel HVOF nickel aluminium bronze coating for marine applications - correlation between mass loss and electrochemical measurements, In: Wear, Vol. 258, No. 1-4 (2003), p.629-640.

[VIL15] Villa Vidaller, M., Haußler, F., Assadi, H., Gärtner, F., Influence of Substrate on Cold Sprayed Titanium Coatings, In: Conference Proceedings, International Thermal Spray Conference (2015), Long Beach/USA, p.1047-1054.

[VYA77] Vyas, B., Preece, C. M., Cavitation erosion of face centered cubic metals, In: Metallurgical Transactions, Vol. 8, No. 6, p. 915-923.

[WAN13] Wang, Q., Zhang, M., Review on recent research and development of cold spray technologies, In: Key Engineering Materials, Vol. 533 (2013), p.1–52.

[WAT13] Watanabe, M., Brauns, C., Komatsu, M., Kuroda, S., Gärtner, F., Klassen, T., Katanoda, H., Effect of N₂ flow-rate on microstructure and mechanical properties of metallic coatings by warm spray deposition, In: Surface & Coatings Technology, Vol. 232 (2013), p.587-599.

[WAT14] Watanabe, Y., Yoshida, C., Atsumi, K, Yamada, M., Fukumoto, M., Influence of Substrate Temperature on Adhesion Strength of Cold-Sprayed Coatings, In: Journal of Thermal Spray technology (2014).

[WIE06] Wielage, B., Wank, A., Pokhmurska, H., Grund, T., Rupprecht, C., Reisel, G., Development and trends in HVOF spraying technology, In: Surface and Coatings Technology, Vol. 201, No. 5 (2006), p. 2032-2037.

[WON11] Wong, W., Irissou, E., Ryabinin, A., Legoux, J., Yue, S., Influence of Helium and Nitrogen Gases on the Properties of Cold Gas Dynamic Sprayed Pure Titanium Coatings, In: Journal of Thermal Spray Technology, Vol. 20, Nos.1-2 (2010), p.213-226.

[WOO06] Wood, R.J.K., Erosion-corrosion interactions and their effect on marine and offshore materials, In: Wear, Vol. 261 (2006), p.1012-1023.

[WU00] Wu, S.K., Lin, H.C., Yeh, C.H., A comparison of the cavitation erosion resistance of NiTi alloys, SUS304 stainless steel and Ni-based self-fluxing alloy, In: Wear, Vol. 244 (2000), p.85-93.

[WU06] Wu, J., Fang, H., Yoon, S., Kim, H., Lee, C., The rebound phenomenon in kinetic spraying deposition, In: Scripta Materialia, Vol. 54, No. 4 (2006), p.665-669.

[XIO04] Xiong, T., Gu, C., Zhang, W., Wu, M., Wu, J., Jin, H., Li, T., Study of Aluminium Bronze Coating By Cold Spray Process, In: Conference Proceedings, International Thermal Spray Conference, Osaka, 2004.

[XU16] Xu, X., Wang, H., Lv, Y., Lu, W., Sun, G., Investigation on Deformation Behavior of Nickel Aluminum Bronze by Neutron Diffraction and Transmission Electron Microscopy, In: Metallurgical And Materials Transactions, Vol. Vol. 47, No. A (2016), p. 2081-2092.

[YU13] Yu, M., Li, W., Wang, F., Suo, X., Liao, H., Effect of particle and substrate preheating on particle deformation behaviour in cold spraying, In: Surface and Coatings Technology, Vol. 220 (2013), p.174-178.

[ZAM98] Zambon, A., Badan, A., Eckler, K., Gärtner, F., Norman, A.F., Greer, A.L., Herlach, D.M. Ramous, E., Microstructure and Phase Selection in Containerless Processing of Fe-Ni Droplets, In: Acta Materialia, Vol. 46 (1998), p.4657- 4670.

[ZHA05] Zhang, D., Shipway, P., McCartney, D., Cold Gas Dynamic Spraying of Aluminum: The Role of Substrate Characteristics in Deposit Formation, In: Journal of Thermal Spray Technology, Vol. 14, No. 1(2005), p.109-116.

[ZUC02] Zuckerwar, A., Handbook of the speed of sound in real gases, Amsterdam: Academic Press; 2002.